

Inaugural dissertation
for
obtaining the doctoral degree
of the
Combined Faculty of Mathematics, Engineering and Natural
Sciences of the
Ruprecht - Karls - University
Heidelberg

Presented by
M.Sc. Nuria Vaquero Siguero
born in: Madrid, Spain. 18th of September 1996
Oral examination: 7th of February 2025

Unveiling the Complexity of Colorectal Cancer Heterogeneity. From Clonal Evolution to Cancer Stem Cells

Referees:

Prof. Dr. Sergio P. Acebrón

Prof. Dr. Andreas Trumpp

A mis padres.
Una muesca más.

TABLE OF CONTENT

TABLE OF CONTENT	
FIGURES	
TABLES.....	
ABBREVIATIONS.....	
SUMMARY.....	
ZUSAMMENFASSUNG	
INTRODUCTION.....	1
The mammalian intestine	1
Embryonic origin of the intestinal epithelium.....	1
Adult intestinal architecture and function	1
Adult intestinal stem cells	2
Intestinal stem cell programs.....	4
Intestinal regeneration and plasticity.....	4
Intestinal stem cell niche	6
Colorectal cancer	8
Epidemiology.....	8
Aetiology	9
CRC Stages	9
Pathogenesis and genetics of CRC.....	12
CRC treatments.....	13
Molecular classification of CRC	14
Models of CRC progression	16
<i>In vitro</i> modelling of CRC	16
<i>In vivo</i> modelling of CRC	17
Genetically engineered mouse models.....	17
Transplantation models	17
CRC heterogeneity	18
Genetic ITH as a driving force in CRC progression	18
Modelling tumour evolution	20
The Cancer Stem Cell model.....	21
Tools to study the stemness	21
CSC in CRC	23
Metastasis initiating cells	25
CSCs and therapy response	26
Targeting foetal-like CSCs	27
AIMS OF THE THESIS	29

RESULTS	31
Chapter I: Understanding clonal dynamics during CRC progression	31
Organoid systems as a tool to study CRC intra-tumour heterogeneity	31
Multicolour LeGO optical barcoding system	33
Generation of the 21 LeGO barcoded clones	34
Deciphering the colour code at a single-cell level of a LeGO barcoded mixed population by flow cytometry	34
<i>In vitro</i> characterization of the LeGO barcoded VKPN clones	35
The LeGO system reveals niche-dependent clonal selection	38
Chapter II: Defining the role of foetal-like cancer cells in CRC progression	41
Characterization of LGR5 ⁺ cells in <i>Apc</i> wild-type (<i>Apc</i> ^{wt}) CRC	41
<i>Apc</i> mutant (<i>Apc</i> ^{mut}) tumours have higher <i>Lgr5</i> -expression levels than <i>Apc</i> ^{wt} tumours	41
Generation of <i>Lgr5</i> -iCaspase9-tdTomato knock-in MTOs.	42
tdTomato labels LGR5 ⁺ cells	43
LGR5 solely marks CSCs in <i>Apc</i> ^{mut} tumours <i>in vitro</i> and <i>in vivo</i>	44
High <i>Lgr5</i> expression is required to induce iCaspase9 dimerization by AP-20187 treatment.	47
Characterization of foetal-like CSCs in CRC	49
Identification of foetal-like intestinal marker genes associated with tumour aggressiveness in CRC	49
TROP2 surface expression marks foetal-like CRC cells in mouse and human CRC ..	51
TROP2 and LGR5 define distinct cancer cell populations	51
TROP2 marks foetal-like CRC cells with stem cell properties	54
<i>In vitro</i> <i>Tacstd2</i> expression level in VAKPS MTOs is sufficient to induce iCaspase9 dimerization by AP-20187 treatment.	58
<i>In vivo</i> <i>Tacstd2</i> expression level in VAKPS MTOs is not sufficient to induce iCaspase9 dimerization by AP-20187 treatment.	61
TROP2 ⁺ cells fuel CRC tumour growth	62
Generation of a GEMM to lineage trace TROP2-expressing cells.	62
<i>In vitro</i> transformation of TcT small intestine-derived organoids to carry the CRC-associated oncogenic mutations	65
<i>In vitro</i> lineage tracing of TROP2 ⁺ cancer cells	67
Understanding the role of TROP2 ⁺ cells during CRC progression.	70
TROP2 ⁺ cells are the metastasis-initiating cells (MICs) in CRC	70
TROP2 levels are increased in response to chemotherapy treatment.	73
Defining the role of TROP2 in CRC progression	77
TROP2 is a driver of tumour initiation in CRC	77
TROP2 is a driver of metastasis in CRC.	80
DISCUSSION	81

Tumour heterogeneity as a driver of CRC progression	81
Clonal evolution in CRC	81
Modelling clonal evolution in CRC: current limitations	82
LeGO optical barcoding system reveals niche-dependant clonal selection in CRC.....	83
Immune-cancer clones crosstalk and their influence on tumour progression and metastatic potential	83
Phenotypic features associated with selective somatic mutations	83
Defining and targeting CSC in CRC	84
LGR5 and TROP2 define a different subset of CSCs in CRC	84
LGR5 marks CSCs in CRC with high WNT pathway activation	84
Foetal-like CRC cells presents stem cell properties	85
Targeting CRC cell plasticity	85
Establishment of a new model to trace foetal-like CSCs.....	86
TROP2 is associated with tumour aggressiveness	87
TROP2 ⁺ cell as the metastasis initiating cell in CRC	87
TROP2 has a functional role in CRC initiation and metastasis	88
TROP2 expression is enhanced upon chemotherapy expression. A new therapeutic window that can be exploit in the clinics	89
TROPHIT1: an investigator-initiated phase II/III multicentre randomized clinical trial for metastatic CRC	90
CONCLUSIONS.....	91
Understanding clonal dynamics during CRC progression	91
Defining the role of foetal-like cancer cells in CRC progression	91
MATERIALS AND METHODS	93
Organoid Culture	93
Mouse Tumour-derived organoids.....	93
Small intestine epithelial organoids	93
Patient-derived organoids.....	94
Vectors and cloning strategies	94
CRISPR/Cas9 Knock-Out vectors	95
Human TROP2 overexpressing vector	96
CRISPR/Cas9 knock-in vectors.....	97
pSpCas9(BB)-sgRNA-2A-GFP plasmid construction	97
HR180- <i>Lgr5</i> -iCaspase9-T2A-tdTomato and HR180- <i>Tacstd2</i> -iCaspase9-T2A-tdTomato donor plasmids construction	97
LeGO vectors	98
Electroporation.....	99
CRISPR/Cas9 knock-out generation and selection	99
CRISPR/Cas9 knock-in generation and selection	100

Generation of <i>Kras</i> ^{G12D} mutant small intestine-derived organoids.....	102
Lentiviral production, organoid transduction and selection	102
Lentiviral production	102
Organoid transduction and selection	103
Single cell dissociation of organoids	103
Clonogenicity assays	104
<i>In vitro</i> drug treatment.....	104
<i>In vitro</i> lineage tracing.....	104
Organoid and tumour cryopreservation.....	104
Tumour dissociation.....	105
FACS and flow cytometry analysis.....	105
DNA extraction.....	106
RNA extraction from cell pellets and tumour tissue	106
RNA extraction from sorted cells.....	106
cDNA synthesis	107
Real-Time Quantitative PCR (RT-qPCR)	107
10x single-cell RNA sequencing.....	109
Analysis of public datasets.....	109
Gene sets, scores and enrichment analysis	110
Kaplan-Meier plots from publicly available datasets.....	110
Western Blot	110
Histology.....	111
Tissue processing	111
Haematoxylin & Eosin	111
Immunohistochemistry (IHC)	111
Immunofluorescence (IF).....	112
Histological analysis	113
Mouse Experiments	113
<i>Tacstd2</i> ^{CreERT2} GEMM generation	113
Mouse Lines.....	114
Mouse Genotyping	114
Murine Colonoscopy-Guided Mucosal Injection.....	115
Subcutaneous injection and tumour monitoring	116
Intrasplenic injection and tumour monitoring.....	116
<i>In vivo</i> AP-20187 treatment.....	116
<i>In vivo</i> lineage tracing.....	116
Statistical analysis	117
Schemes and illustrations	117

Contributions.....	117
BIBLIOGRAPHY	119
ACKNOWLEDGEMENTS	129
AGRADECIMIENTOS.....	129

FIGURES

Figure 1. The adult intestinal epithelium.	2
Figure 2. Intestinal homeostasis.	3
Figure 3. Intestinal stem cell programs.	4
Figure 4. Intestinal stem cell dynamics during intestinal regeneration.	6
Figure 5. WNT signalling pathway.	7
Figure 6. CRC staging.	10
Figure 7. Evolutionary pathways of CRC tumorigenesis.	13
Figure 8. Molecular classifications of CRC.	15
Figure 9. CRC clonal evolution models.	19
Figure 10. Sources of CRC heterogeneity.	21
Figure 11. Methodologies used for characterization of stem cells.	23
Figure 12. CSC dynamics.	25
Figure 13. CSC dynamics during CRC progression.	26
Figure 14. SG mode of action.	28
Figure 15. VKPN mouse tumour-derived organoids.	31
Figure 16. The principle of the multicolor LeGO optical barcoding system.	32
Figure 17. Generating 21 uniquely LeGO barcoded clones: the binomial coefficient formula.	33
Figure 18. Generation of 21 LeGO optically barcoded VKPN clones.	36
Figure 19. Gating strategy and Boolean analysis for quantification of the 21 different LeGO barcoded VKPN clones in a mixed population.	37
Figure 20. Characterization of the 21 LeGO optically barcoded VKPN clones.	38
Figure 21. In vitro clonal competition of the 21 LeGO optically barcoded VKPN clones.	38
Figure 22. Engraftment capacity of the VKPN MTO model.	39
Figure 23. Clonal analysis <i>in vivo</i> revealed niche dependencies.	40
Figure 24. <i>Apc</i> ^{mut} tumours are enriched for the adult ISC program.	41
Figure 25. VAKPS MTOs have elevated <i>Lgr5</i> -expression levels compared to VKPN MTOs.	42
Figure 26. Generation of <i>Lgr5</i> -iCaspase9-tdTomato (LiCT) knock-in MTO lines.	43
Figure 27. tdTomato signal identifies LGR5 ⁺ cells.	44
Figure 28. Generation of the VAKPN ^{LiCT} MTO line.	44
Figure 29. <i>Apc</i> ^{mut} MTOs exhibit higher number of LGR5-tdTomato ⁺ cells as well as elevated LGR5-tdTomato protein level compared to <i>Apc</i> ^{wt} MTOs.	45
Figure 30. LGR5-tdTomato ⁺ cell population has higher organoid formation capacity than LGR5-tdTomato ⁻ cell population in <i>Apc</i> ^{mut} MTOs <i>in vitro</i>	46
Figure 31. LGR5-tdTomato ⁺ cell population has higher tumour-initiating capacity than LGR5-tdTomato ⁻ cell population in <i>Apc</i> ^{mut} tumours <i>in vivo</i>	47
Figure 32. High <i>Lgr5</i> expression level are required to induce iCaspase 9 dimerization by AP-20187 treatment.	48
Figure 33. Expression profiles of genes from the foetal ISC signature in human CRC.	50
Figure 34. TROP2 expression correlates with poor overall survival and lower disease-free survival in CRC.	50
Figure 35. TROP2 surface expression positively correlates with higher tumour stage in MTOs.	51
Figure 36. TROP2 expression marks foetal-like cancer cells in human and murine CRC.	52
Figure 37. TROP2 expression does not mark adult ISCs in human and murine CRC.	53

Figure 38. TROP2 and LGR5 mark distinct cancer cell populations in CRC.	53
Figure 39. TROP2 ⁺ cells have higher organoid formation capacity than TROP2 ⁻ cells in MTOs and PDOs <i>in vitro</i> .	55
Figure 40. TROP2 marks a stem-like cancer cell population <i>in vivo</i> in <i>Apc</i> ^{wt} tumours.	56
Figure 41. LGR5 marks CSCs only in <i>Apc</i> ^{mut} CRCs whereas TROP2 marks the CSCs in <i>Apc</i> ^{wt} “low WNT” CRCs.	57
Figure 42. Generation of Tacstd2-iCaspase9-tdTomato (TiCT) knock-in VAKPS and VKPN lines.	59
Figure 43. tdTomato reports TROP2 ⁺ cells in VAKPS ^{TiCT} MTOs.	60
Figure 44. Selective ablation of TROP2 ⁺ cells <i>in vitro</i> .	60
Figure 45. TROP2 expression levels are not sufficient to induce iCaspase 9 dimerization by AP-20187 treatment <i>in vivo</i> .	61
Figure 46. Generation of the <i>Tacstd2</i> ^{CreERT2} mouse line.	63
Figure 47. Generation of the <i>Tacstd2</i> ^{CreERT2} ; <i>Rosa26</i> ^{LSL-tdTomato} (TcT) mouse line.	63
Figure 48. tdTomato labels TROP2 ⁺ cells in the TcT GEMM.	64
Figure 49. Lineage tracing of TROP2 ⁺ cells in small intestine-derived organoids.	65
Figure 50. Genetic modification of TcT small intestine-derived organoids to generate TcT-AKP tumour organoids.	66
Figure 51. Genetic modification of TcT small intestine-derived organoids to generate TcT-KPN tumour organoids.	67
Figure 52. Lineage tracing analysis of TROP2 ⁺ cells in TcT-AKP organoids.	68
Figure 53. The <i>Rosa26</i> ^{tdTomato} allele is still functional in the TcT-KPN MTO line.	68
Figure 54. TcT-KPN MTO line has low expression level of TROP2.	69
Figure 55. <i>In vivo</i> lineage tracing analysis of TROP2 ⁺ TcT-AKP cells.	69
Figure 56. TROP2 ⁺ cells mark the invasive front and micro-metastases.	71
Figure 57. TROP2 marks cancer cells with high metastatic potential in VAKPS and VKPN models.	72
Figure 58. Liver metastases derived from the different sorted cell populations (LGR5 ⁻ /TROP2 ⁻ , LGR5 ⁺ /TROP2 ⁻ , LGR5 ⁻ /TROP2 ⁺ , LGR5 ⁺ /TROP2 ⁺) restored tumour heterogeneity.	73
Figure 59. TROP2 expression levels increase after chemotherapy in MTOs.	74
Figure 60. TROP2 does not mark drug-persistent cells.	75
Figure 61. Heterogeneous expression of TROP2 across human CRC patients.	76
Figure 62. TROP2 expression level increase after chemotherapy treatment in PDOs. A.	76
Figure 63. Generation of TROP2 KO VAKPS MTO lines.	77
Figure 64. TROP2 deficiency leads to a decrease in the organoid formation capacity <i>in vitro</i> .	78
Figure 65. TROP2 deficiency leads to a decrease in the tumour-initiation capacity and tumour growth <i>in vivo</i> .	79
Figure 66. Generation of TROP2 overexpressing MTO lines.	79
Figure 67. TROP2 overexpression increases organoid formation capacity <i>in vitro</i> .	79
Figure 68. TROP2 is involved in CRC metastasis.	80
Figure 69. Revised cancer stem cell model in CRC.	85
Figure 70. Stem cell dynamic in CRC progression.	88
Figure 71. Stem cell dynamics upon therapeutic treatment.	90
Figure 72. SG as a third line treatment for mCRC.	90

TABLES

Table 1. TNM tumour staging protocol.	12
Table 2. Culture media conditions used for the different MTOs.	93
Table 3. sgRNA sequences used for generating CRISPR/Cas9 KO organoid lines.	95
Table 4. Program used for the annealing of the sgRNAs and shRNA oligo sequences.	96
Table 5. Sequence of the primers used for amplification of the <i>TACSTD2</i> cDNA amplification.	96
Table 6. Sequences of the primers used for the generation of the EV control plasmid.	97
Table 7. sgRNA sequences used for generating CRISPR/Cas9 Knock-in organoid lines.	97
Table 8. Oligo sequences used for the insertion of the AflII restriction site in the HR180-LGR5-iCT vector.	98
Table 9. Primer sequences for the amplification of the homology arms.	98
Table 10. LeGO vectors.	99
Table 11. Nepagene program used for organoid electroporation.	99
Table 12. Primer sequences for specific validation of the KO efficiency.	100
Table 13. Primers used for the specific integration of the iCT and GFP cassettes.	101
Table 14. Primers used for the validation of the Ruby-Puromycin resistant cassette removal.	102
Table 15. Primer sequences used for the amplification of the Kras ^{G12D} mutant sequence.	102
Table 16. Vectors used for the lentiviral.	103
Table 17. Filter configuration on the BD LSR Fortessa to analyze the LeGO optically barcoded cells.	105
Table 18. Reaction mixture for cDNA synthesis.	107
Table 19. Reaction mixture for RT-qPCR.	108
Table 20. RT-qPCR program.	108
Table 21. Primer sequences used for RT-qPCR.	109
Table 22. TBS-T buffer composition	111
Table 23. List of the Western Blot antibodies used.	111
Table 24. List of the primary antibodies used for histology.	112
Table 25. List of the biotinylated secondary antibodies used for IHC.	112
Table 26: List of the fluorescent secondary antibodies used for IF.	113
Table 27. Primer sequences used for specific integration PCR.	114
Table 28. Primer sequences for specific mouse allele genotyping.	115
Table 29. PCR programs used for specific mouse allele genotyping.	115

ABBREVIATIONS

4-OHT	4-hydroxytamoxifen
ADC	Antibody-drug conjugate
AJCC	American Joint Committee on Cancer
APC	Adenomatous polyposis coli
B	EBFP2
BAC	Bacterial Artificial Chromosome
BlastR	Blasticidin resistance
BME	Cultrex reduced growth factor basement membrane
BMP	Bone morphogenetic protein
bp	Base pair
Cas9	CRISPR-associated protein 9
CBC	Crypt base columnar
CID	Chemically-induced dimerizer
CIN	Chromosomal instability
CMS	Consensus molecular subtype
CRC	Colorectal cancer
CRSIPR	Clustered regularly interspaced short palindromic repeats
CSC	Cancer stem cell
CTC	Circulating tumour cell
DFS	Disease-free survival
DNA	Deoxyribonucleic acid
DT	Diphtheria toxin
DTA	Diphtheria toxin subunit A
DTR	Diphtheria toxin receptor
E	Embryonic day
EGF	Epidermal growth factor
EGFR	Epidermal growth factor receptor
EMA	European Medicines Agency
ERT2	Estrogen receptor
ES	Embryonic stem
FACS	Fluorescence-activated cell sorting
FAP	Familial adenomatous polyposis
FDA	Food and Drug Administration
FP	Fluorescent protein
Fw	Forward
G	eGFP
gDNA	Genomic DNA
GEMM	Genetically engineered mouse model
GFP	Green fluorescent protein
GOI	Gene of interest
HA	Homology arm
Het	Heterozygous
HNPCC	Hereditary non-polyposis colon cancer
iCMS	Intrinsic CMS
iCT	Inducible Caspase9-tdTomato

IF	Immunofluorescence
IHC	Immunohistochemistry
ISC	Intestinal stem cell
K	dKatushka2
KO	Knock-out
LeGO	Lentiviral gene ontology
LGR5	Leucine-rich repeat-containing G-protein-coupled receptor 5
LiCT	<i>Lgr5</i> -iCaspase9-tdTomato
LSL	LoxP-STOP-LoxP
Ly6a	Lymphocyte antigen 6 family member A
mCRC	Metastatic colorectal cancer
MIC	Metastasis-initiating cell
MSI	Microsatellite instable
MSS	Microsatellite stable
MTO	Mouse tumour-derived organoid
Mut	Mutant
N1ICD	Notch1 intracellular domain
NeoR	NemomycinResistance
O	mOrange
O/N	Overnight
OS	Overall survival
P	Post-natal day
PDO	Patient-derived organoid
PNK	Polynucleotide Kinase
PuroR	Puromycin resistant
RIPA	Radioimmunoprecipitation Assay
RNA	Ribonucleic acid
RT-qPCR	Real-Time Quantitative PCR
Rv	Reverse
S	T-Sapphire
SB	Sleeping beauty
scRNA	Single-cell RNA
SG	Sacituzumab Govitecan
sgRNA	single guide RNA
shRNA	Short hairpin RNA
SPP1	Secreted Phosphoprotein 1
TA	Transit-amplifying
TACSD2	Tumour associated calcium signal transducer 2
TBS-T	Tris-buffered saline-Tween20
TGF- β	Transforming growth factor- β
TIC	Tumour-initiating cell
TiCT	<i>Tacstd2</i> -iCaspase9-tdTomato
TME	Tumour microenvironment
TROP2	Trophoblast antigen 2
TSG	Tumour suppressor gene
V	Venus
wt	Wild-type

SUMMARY

Colorectal cancer (CRC) is one of the main contributors to cancer-related fatality. Patient survival highly depends on tumour stage at diagnosis, as the 5-year overall survival rate drops drastically from ~64% for patients diagnosed in stage I–II to 12% for patients diagnosed in stage IV. Thus, ~90% of CRC related deaths are associated with metastatic disease that does not respond to currently available systemic treatments. Emerging evidence suggests that inter- and intra-tumour heterogeneity significantly contributes to cancer progression and therapy-resistance. In this PhD thesis, I focus on two main sources of intra-tumour heterogeneity: clonal dynamics and stem cell hierarchy.

During CRC progression, the tumour ecosystem is subjected to continuous evolution. However, the patterns of clonal dynamics and their dependence on the surrounding environment are not yet well understood. To investigate this, I used an optical barcoding system (LeGO) in mouse tumour-derived organoids to longitudinally track individual clones in different environments. My findings revealed a key bottleneck both *in vitro* and *in vivo*, suggesting that clonal selection plays a major role during CRC progression. Moreover, my results indicate that clonal selection is highly influenced by the tumour microenvironment, which critically contributes to tumour heterogeneity and has implications for therapeutic intervention.

Furthermore, CRC cells are hierarchically organized with cancer stem cells (CSCs) at the apex, initiating and fuelling tumour growth. LGR5 has been suggested as the marker for CSCs in CRC. However, a significant number of CRCs present none or few LGR5⁺ cells. LGR5⁺ CSCs become absent during metastasis initiation and therapy response. Instead, a foetal intestinal stem cell program is reactivated. In this thesis, I propose TROP2 as a marker for these foetal-like CSCs in CRC and functionally characterized them. My findings suggest a mutually exclusive distribution of LGR5⁺ and TROP2⁺ CSC populations in both, mouse and human CRC, implying that they represent distinct CSC populations. I demonstrated that while LGR5 marks CSCs in *Apc^{mut}* CRCs, TROP2 marks CSCs in *Apc^{wt}* (WNT-low, serrated) CRCs. Furthermore, TROP2 expression is associated with advanced tumour stages and poor prognosis. Here, I showed that, in CRC, TROP2 marks the cells located at the tumour invasive front as well as the metastasis-initiating cell. Additionally, TROP2 gain-of-function and loss-of-function experiments revealed its direct, but yet unknown, role in CRC progression. Finally, TROP2 represents a promising therapeutic target in CRC due to the potent therapeutic activity of the TROP2 antibody-drug conjugated, Sacituzumab Govitecan (SG). Thus, we have launched a multicentre randomized investigator-initiated trial (phase II/III; NCT06243393) to test SG as a 3rd line treatment versus standard-of-care in metastatic CRC patients.

ZUSAMMENFASSUNG

Darmkrebs ist eine der Hauptursachen für krebsbedingte Todesfälle. Die Überlebensrate der Patienten hängt in hohem Maße vom Tumorstadium bei der Diagnose ab. Die Fünf Jahres Überlebensrate sinkt drastisch von ~64 % bei Patienten die in Stadium I-II diagnostiziert werden, auf 12 % bei Patienten, die in Stadium IV diagnostiziert werden. Folglich sind ~90 % der Todesfälle im Zusammenhang mit Darmkrebs auf eine metastasierte Erkrankung zurückzuführen, die auf die derzeit verfügbaren systemischen Behandlungen nicht anspricht. Neue Erkenntnisse deuten darauf hin, dass die Heterogenität zwischen und innerhalb des Tumors wesentlich zum Fortschreiten des Krebses und zur Therapieresistenz beiträgt. In dieser Dissertation konzentriere ich mich auf zwei Hauptfaktoren der Heterogenität innerhalb des Tumors: die klonale Dynamik und die Stammzellenhierarchie.

Während des Fortschreitens von Darmkrebs ist das Ökosystem des Tumors einer kontinuierlichen Evolution unterworfen. Die Muster der klonalen Dynamik und ihre Abhängigkeit von der Umgebung sind jedoch noch nicht gut verstanden. Um dies zu untersuchen, habe ich ein optisches Barcoding-System (LeGO) in Organoiden aus Mäusetumoren entwickelt, um einzelne Klone in verschiedenen Umgebungen zu verfolgen. Meine Ergebnisse zeigen, dass es sowohl *in vitro* als auch *in vivo* einen Engpass gibt, der darauf hindeutet, dass die klonale Selektion eine wichtige Rolle bei der Progression von Darmkrebs spielt und dass die klonale Selektion stark von der Mikroumgebung des Tumors beeinflusst wird. Diese Faktoren tragen entscheidend zur Heterogenität des Tumors bei und haben Auswirkungen auf die therapeutische Intervention.

Darüber hinaus sind Darmkrebszellen hierarchisch organisiert, wobei Krebsstammzellen an der Spitze stehen, die das Tumorwachstum initiieren und vorantreiben. LGR5 wurde als Marker für Krebsstammzellen in Darmkrebs identifiziert. Eine beträchtliche Anzahl von Darmkrebserkrankungen weist jedoch keine oder nur wenige LGR5⁺-Zellen auf. Außerdem sind LGR5⁺ Krebsstammzellen bei der Metastasierung und beim Ansprechen auf die Therapie reduziert. Stattdessen wird das fötale intestinale Stammzellprogramm reaktiviert. In dieser Arbeit schlage ich TROP2 als Marker für diese fötalen Darmstammzellen in Darmkrebs vor und charakterisiere sie funktionell. Meine Ergebnisse deuten auf eine sich gegenseitig ausschließende Verteilung von LGR5⁺ und TROP2⁺ Krebsstammzell-Populationen sowohl im Darmkrebs der Maus als auch des Menschen hin, was bedeutet, dass sie unterschiedliche Krebsstammzell-Populationen darstellen. Ich konnte zeigen, dass LGR5 Krebsstammzellen in *Apc*^{mut}-Karzinomen markiert, während TROP2 Krebsstammzellen in *Apc*^{wt} Karzinomen (WNT-niedrig, serratiert) markiert. Außerdem wird die TROP2-Expression mit fortgeschrittenen Tumorstadien und einer schlechten Prognose in Verbindung gebracht.

Hier konnte ich zeigen, dass TROP2 bei Darmkrebs die Zellen markiert, die sich an der invasiven Front des Tumors befinden, sowie die Zellen, die die Metastasierung einleiten. Darüber hinaus zeigten Experimente zum Funktionsgewinn und -verlust von TROP2 seine direkte, aber bisher unbekannte Rolle bei der Progression von Darmkrebs. Außerdem stellt TROP2 ein vielversprechendes therapeutisches Ziel bei Darmkrebs dar, da der konjugierte TROP2-Antikörper Sacituzumab Govitecan (SG) eine starke therapeutische Aktivität aufweist. Daher haben wir eine multizentrische, randomisierte Studie (Phase II/III; NCT06243393) gestartet, um SG als Drittlinienbehandlung im Vergleich zur Standardtherapie bei Patienten mit metastasiertem Darmkrebs zu testen.

INTRODUCTION

The mammalian intestine

Embryonic origin of the intestinal epithelium

The intestinal epithelium originates from the endoderm, one of the three primary germ layers formed during gastrulation. At embryonic day (E) 9 in mice and gestational weeks 3-7 in humans, the foetal gut is characterised by a pseudostratified, nearly flat epithelium. Around E14.5 in mice and gestational week 9 in humans, this epithelium undergoes significant remodelling and rapid proliferation, ultimately resulting in the development of the mature adult intestine (Kim et al., 2007; Kolev and Kaestner, 2023). This developmental process is tightly controlled by WNT and Hedgehog signalling programs (Kolev and Kaestner, 2023). Indeed, in the adult intestinal epithelium, foetal intestinal programs are suppressed. However, during intestinal disorders such as cancer or colitis, there is a reactivation of these foetal-like programs. This reversion is marked by the dedifferentiation of adult epithelial cells into progenitor-like cells that express foetal markers, facilitating regeneration and repair processes (Fey et al., 2024; Viragova et al., 2024).

Adult intestinal architecture and function

The adult human intestine, with a surface area exceeding 30 m², is the second largest epithelium in our body, surpassed only by the skin (Gehart and Clevers, 2019). The mammalian intestine is a complex and vital organ of the gastrointestinal tract responsible for the digestion and absorption of nutrients and the protection from external pathogens. It extends from the end of the stomach to the anus and is divided into two segments: the small intestine and the large intestine (Kolev and Kaestner, 2023). The small intestine, divided in duodenum, jejunum and ileum, is mainly responsible for the final steps of food digestion and nutrient uptake. The large intestine, comprising the caecum, colon and rectum, plays a crucial role in water reabsorption and the formation of faeces (Kolev and Kaestner, 2023).

The intestinal function is achieved through the millions of crypt-villus units, the complex and specialised microscopic structures in which the intestine is organised. Each of these units consists of a villus, a finger-like protrusion, surrounded by multiple invaginations in the epithelial wall called crypts (**Figure 1**). The length of the villus decreases along the intestinal tract being the longest in the duodenum (>1mm) and absent in the colon. These structures increase the surface area of the intestine, facilitating nutrient absorption. Due to its extensive surface, the intestinal epithelium is also exposed to many insults such as toxins or pathogens.

In order to minimise exposure to such hazards, intestinal cells have a very short lifespan, lasting only 3-5 days. This rapid turnover of mature intestinal cells is maintained by the adult intestinal stem cells (ISCs) (Gehart and Clevers, 2019).

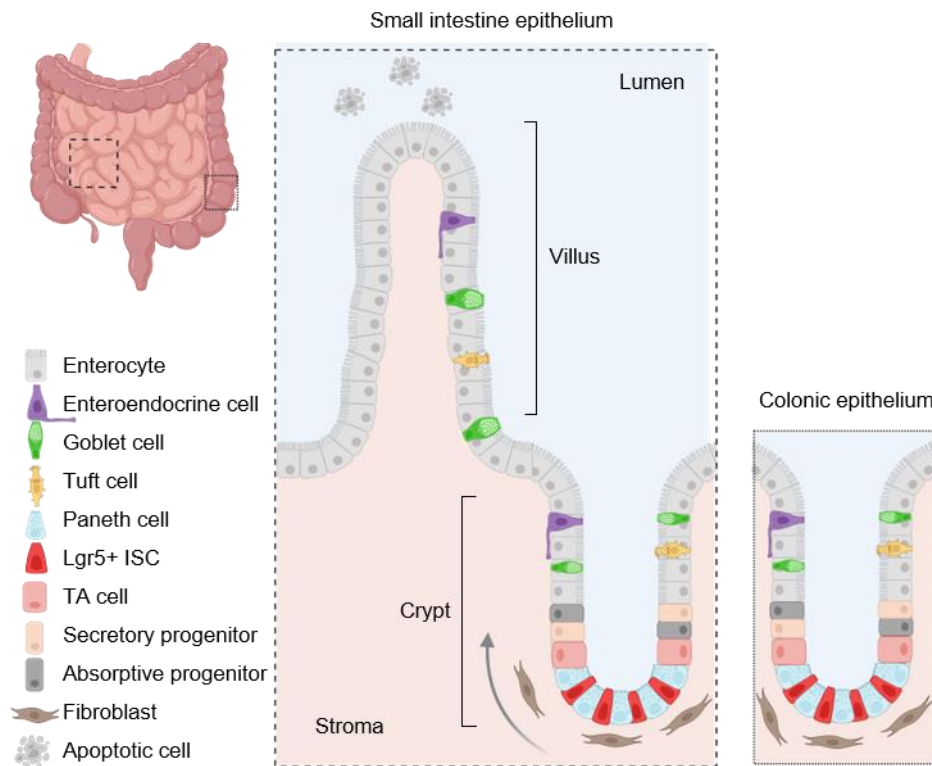


Figure 1. The adult intestinal epithelium. The small intestinal epithelium is organised in millions of villus-crypt structures whereas the colonic epithelium only contains crypts. In both epitheliums the LGR5⁺ ISCs are located at the bottom of the crypt intercalated with the Paneth cells. ISCs give rise to all the specialised cells of the intestinal epithelium. This progeny is gradually pushed out of the crypt base. Upon reaching the villus tip (in the small intestine) or the crypt tip (in the colon), these cells undergo anoikis and are subsequently shed into the intestinal lumen for clearance. ISC, intestinal stem cell; TA, Transit-amplifying.

Adult intestinal stem cells

The ISCs, also known as crypt base columnar (CBC) cells, are multipotent stem cells located at the crypt base (**Figure 1**). These long-lived, rapidly proliferating cells possess self-renewal capabilities and are responsible for generating all cell types within the intestinal epithelium. For decades, cumulative evidence suggested the presence of an intestinal precursor cell. However, the lack of unique ISC markers hindered their functional identification. It was not until 2007 when the advent of lineage tracing technology revealed that ISCs are marked by leucine-rich repeat-containing G-protein-coupled receptor 5 (*Lgr5*) expression (hereafter LGR5⁺ ISCs) (Barker et al., 2007). The generation of the *Lgr5*^{eGFP-IRES-CreERT2}; *Rosa26*^{lacZ} genetically engineered mouse model (GEMM) revealed the stem cell capacity of these cells as they generate ribbons of cells emanating from the crypt base towards the villi within five days (**Figure 2A**). These ribbons contained all the different cell types of the intestinal epithelium (Barker et al., 2007).

ISCs divide to produce either additional ISCs or transit-amplifying (TA) cells, which are short-lived progenitors that undergo several rounds of division. As this progeny differentiates into specialised intestinal epithelial cells (enterocytes, goblet cells, tuft cells, enteroendocrine cells and Paneth cells) they are gradually pushed out of the crypt towards the tip of the villus (**Figure 1 and 2B**). Upon reaching the villus tip, typically within 3-5 days, these cells undergo anoikis and are subsequently shed into the intestinal lumen for clearance (**Figure 1**). Notably, Paneth cells are the only differentiated cells that do not follow this upward migration; instead, they remain interspersed among the ISCs at the crypt base (Gehart and Clevers, 2019).

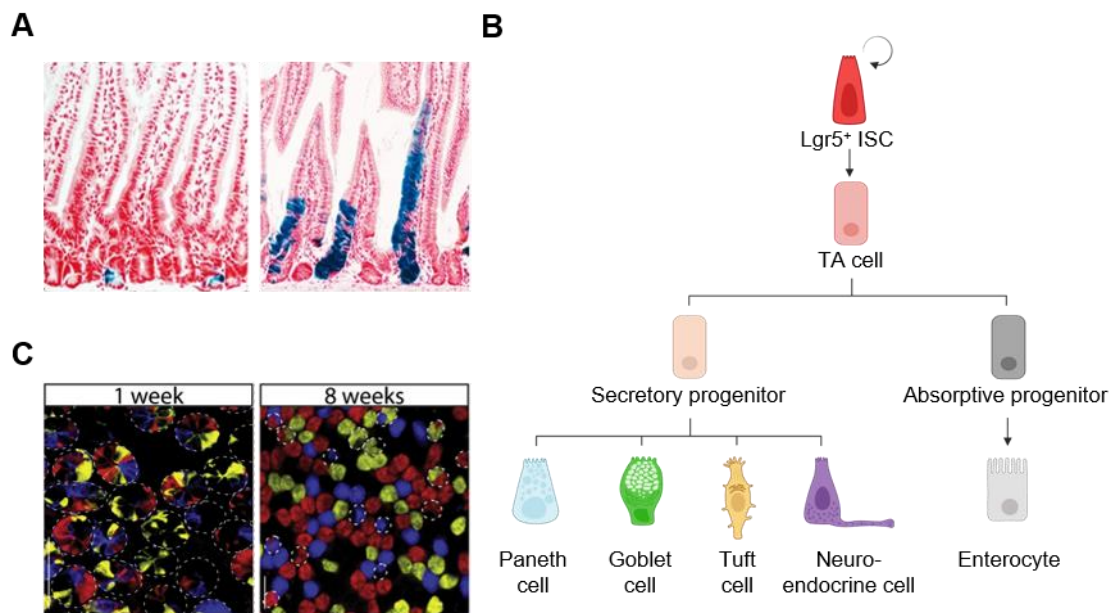


Figure 2. Intestinal homeostasis. **A.** Immunohistochemistry images showing the LacZ reporting activity (left) one day and (right) five days after tamoxifen induction in the small intestine of the *Lgr5*^{EGFP-IRES-CreERT2}; *Rosa26*^{lacZ} GEMM. Images from (Barker et al., 2007). **B.** Schematic representation of the intestinal stem cell hierarchy. TA, transit amplifying. **C.** Whole-mount image of the small intestine after one and eight weeks of the *Rosa26*^{Confetti} allele activation. Images from (Snippert et al., 2010).

Adult stem cells can divide symmetrically or asymmetrically. In symmetric divisions, a stem cell produces two identical daughter cells, both of which have the same cell-fate, either remaining as stem cells or undergoing differentiation. In contrast, asymmetric divisions result in one stem daughter cell and one differentiated daughter cell. The choice between symmetric and asymmetric division is regulated by various intrinsic factors such as the orientation of the mitotic spindle and extrinsic factors such as the microenvironment (Barker, 2014; Morrison and Kimble, 2006). To gain deeper insights into how LGR5⁺ ISCs divide and maintain the epithelial homeostasis Snippert *et al.* performed fate-mapping experiments in the *Ah*^{Cre}; *Rosa26*^{Confetti} GEMM. In this model, Cre expression induces recombination of the Confetti cassette and cells are stochastically labelled by one of the four fluorescent proteins encoded by this allele. These experiments revealed that LGR5⁺ ISCs symmetrically divide and daughter cells stochastically adopt either ISC or TA cell fate. Furthermore, the observation that over time the intestinal crypt

became monochromatic indicated that in homeostasis intestinal crypts drift towards clonality (Snippert et al., 2010) (Figure 2C).

Intestinal stem cell programs

The Clevers lab set out to further characterise LGR5⁺ ISCs. Utilising the *Lgr5*^{CreERT2} GEMM allowed for the successful isolation of LGR5⁺ ISCs, which were marked by the expression of the Green Fluorescent Protein (GFP) (Barker et al., 2007). This approach enabled detailed transcriptomic profiling of these stem cells, leading to the establishment of a distinct adult ISC signature. This signature consists of 384 genes such as *Lgr5*, *Ascl2*, *Axin2*, *Smoc2* and *Olfm4* that were highly expressed in these cells (Munoz et al., 2012) (Figure 3).

Embryonic development of the intestine has been characterised in great detail. Interestingly, until E16, no sign of adult ISCs was observed in the foetal intestinal epithelium (Garcia et al., 2009; Kim et al., 2007). These findings paved the way to explore the intestinal stem cell signatures present at early developmental stages. Taking advantage of the 3D *in vitro* culture systems, Mustata et al. established cultures of the murine intestine at different developmental stages (Mustata et al., 2013). Interestingly, foetal-derived 3D *in vitro* cultures had a spheroid-like morphology compared to the organoid with crypt-like protrusions generated from adult mouse intestines. Additionally, a transcriptional comparison of E16-18 and post-natal day (P) 0 intestinal 3D cultures showed 317 up-regulated (i.e., *Lymphocyte antigen 6A* (*Ly6a*)/ Stem cell antigen-1 (SCA-1), *Annexin A1* (*Anxa1*), *Clusterin* (*Clu*), *tumour-associated calcium signal transducer 2* (*Tacstd2*)/trophoblast cell-surface antigen 2 (TROP2)) (hereinafter foetal ISC program) and 179 downregulated genes (Mustata et al., 2013) (Figure 3).

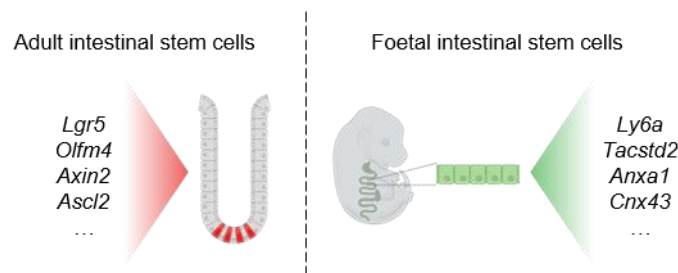


Figure 3. Intestinal stem cell programs. Intestinal stem cells are defined by two different stem cell programs depending on the developmental stage.

Intestinal regeneration and plasticity

Maintaining the intestinal homeostasis is crucial to avoid perturbations that can lead to gastrointestinal diseases such as chronic inflammation or tumorigenesis. To do so, LGR5⁺ ISCs ensure swift cellular turnover as well as the maintenance of the ISC pool in the crypts (Barker et al., 2007).

Many studies have interrogated the molecular programs underlying epithelial regeneration upon injury. Strikingly, transcriptomic profiling of the intestinal epithelium during colonic regeneration revealed that the LGR5⁺ ISC programs are highly suppressed after injury (Fazilaty et al., 2021; Metcalfe et al., 2014). Intestinal damage can occur in different forms ranging from an acute inflammation caused by viral, bacterial, parasitic infections, antibiotics, chemotherapy or irradiation, to a chronic inflammatory condition such as Crohn's disease (Figure 4). Tian et al. investigated the physiological relevance of depleting LGR5⁺ ISCs in the intestine. To do so, they generated the *Lgr5*^{DTR-eGFP} GEMM. In this GEMM, the diphtheria toxin receptor (DTR) is expressed under the control of the *Lgr5* promoter. Upon administration of the diphtheria toxin (DT), *Lgr5*-expressing cells will be selectively depleted. Short-term LGR5⁺ ISC depletion did not affect intestinal homeostasis as the TA cells located in the +4 position of the intestinal crypt, marked by *Bmi1* expression, dedifferentiate to restore the stem cell pool compensating the LGR5⁺ ISC loss (Tian et al., 2011). On the other hand, persistent ablation of LGR5⁺ ISCs compromised intestinal regeneration, suggesting that the LGR5⁺ ISCs, regardless if they are pre-existent or newly replenished by dedifferentiation of the +4 cells, are indispensable for maintaining intestinal homeostasis (Tan et al., 2021).

To model a more physiological scenario to study intestinal regeneration, other strategies such as helminth infection, the use of radiation or the administration of the DSS in the drinking water have been implemented to induce acute or chronic colitis. This, combined with marker-based lineage tracing studies further demonstrated that progenitor cells from the absorptive (ALPI1⁺ cells) (Tetteh et al., 2016) and secretory lineages (ATOH1⁺ cells) (Tomic et al., 2018) as well as quiescent label-retaining cells (CLU⁺ cells) (Ayyaz et al., 2019) can dedifferentiate and serve as source of regeneration of the LGR5⁺ ISC pool upon injury (summary in (Hageman et al., 2020)).

Single-cell RNA (scRNA) sequencing has been instrumental to reveal that injury-responsive epithelial cells acquire a transient foetal-like ISC program, while suppressing the differentiation lineages and adult ISC (Ayyaz et al., 2019; Karo-Atar et al., 2022; Nusse et al., 2018; Yui et al., 2018). This primitive foetal program endows the cells with proliferative and plastic traits to regenerate the intestinal epithelium. More importantly, this is a transient state, thus it is strictly regulated to ensure that adult intestinal programs are restored once the integrity of the intestinal epithelium is repaired (reviewed elsewhere (Fey et al., 2024; Viragova et al., 2024)) (Figure 4).

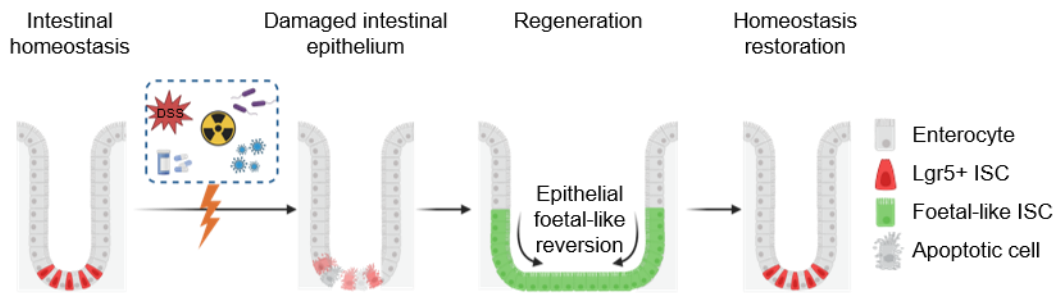


Figure 4. Intestinal stem cell dynamics during intestinal regeneration. LGR5⁺ ISCs are ablated upon intestinal damage induced by insults such as radiation, inflammation, or chemotherapeutics. In turn, foetal-like ISCs reappear to regenerate the intestinal epithelium and restore homeostasis. DSS, dextran sulphate sodium.

Intestinal stem cell niche

Maintenance and protection of the ISCs needs to be ensured for proper intestinal function. Hence, ISCs are strategically positioned at the crypt base within a highly regulated microenvironment known as the ISC niche. This niche is primarily supported by Paneth cells and fibroblasts, which secrete or present various molecules establishing a gradient within the crypt. The proliferation of ISCs is governed by three key signalling pathways, WNT, Notch, and Epidermal growth factor (EGF), all of which promote cell division while inhibiting differentiation. Contrary, the bone morphogenetic protein (BMP) pathway is actively suppressed in ISCs to maintain their undifferentiated state (Beumer and Clevers, 2021).

WNT signalling

The canonical WNT signalling pathway is an evolutionary conserved pathway crucial for various developmental processes. Within the intestinal epithelium, WNT plays a central role in promoting ISC proliferation and stemness (Clevers and Nusse, 2012). In the absence of WNT stimuli, the APC-destruction complex triggers the proteasomal degradation of β -catenin, the key signalling molecule in this pathway. Contrary, when WNT ligands are present, secreted by the ISC microenvironment, they bind to the WNT receptor complex Frizzled-LRP5/6, leading to the stabilisation of β -catenin. Stabilised β -catenin translocates to the nucleus, where it functions as a transcriptional co-activator of the TCF/LEF transcriptional complex, driving the expression of target genes essential for ISC functions (Li et al., 2012) (Figure 5). Blocking the WNT signalling pathway in the intestine using TCF4 knock-out (KO) mice resulted in the absence of proliferative cells in the intestinal crypts, suggesting that WNT signalling pathway is indeed needed for ISC proliferation (van Es et al., 2012).

One of the WNT targets is RNF43, a negative regulator of the WNT signalling pathway. To keep the pathway active and sustain stemness, the presence of the WNT agonist R-spondin is essential. R-spondin, secreted by the ISC microenvironment, binds to the surface proteins RNF43 and LGR5. Upon binding, LGR5 facilitates the internalisation and degradation of

RNF43, thereby ensuring that WNT signalling remains "ON". This continuous activation of WNT signalling is crucial for maintaining the proliferative capacity and stemness of intestinal stem cells. On the other hand, dysregulation of this signalling pathway which results in the hyperactivation of the WNT signalling pathways, leads to intestinal tumour formation (Clevers and Nusse, 2012).

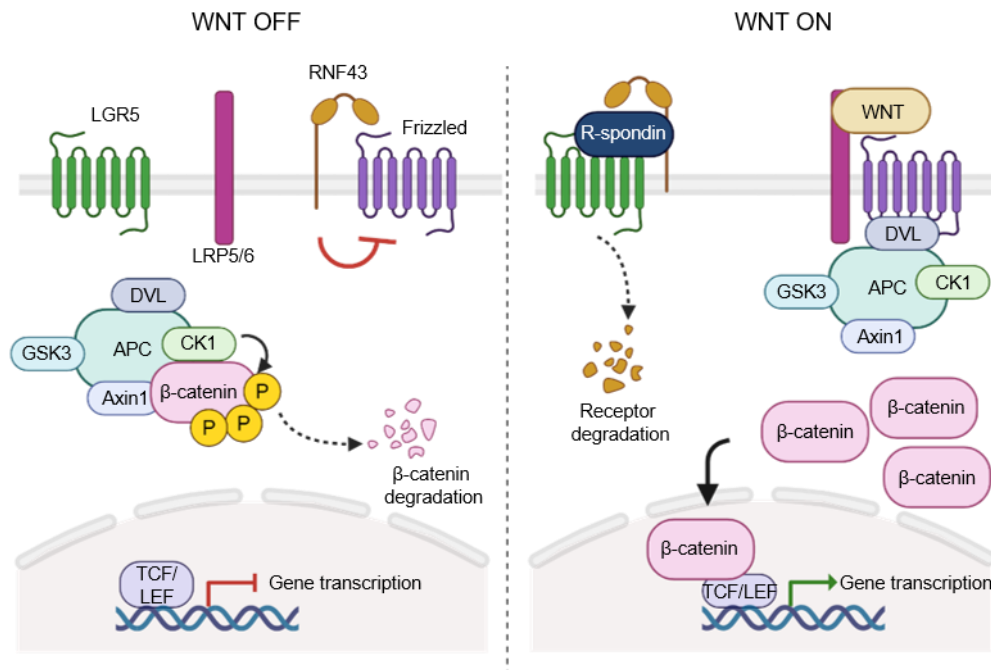


Figure 5. WNT signalling pathway. In the absence of the WNT ligand, β-catenin is degraded and the WNT signalling pathway remains "OFF". Once WNT binds to the Frizzled/LRP5/6 complex β-catenin is stabilised and is translocated to the nucleus where it will drive the transcription of WNT target genes.

Notch signalling

In the intestine, Notch signalling plays a crucial role in maintaining stemness by inhibiting differentiation into secretory lineages. This signalling pathway requires direct cell-to-cell interaction, where one cell expresses Notch ligands (such as DLL1/4) and the adjacent cell expresses Notch receptors (such as Notch1). Within the ISC niche, Paneth cells are the primary source of Notch ligands, while ISCs predominantly express Notch receptors. Upon ligand-receptor binding, Notch1 undergoes cleavage by γ-secretase, releasing the Notch1 intracellular domain (N1ICD). The N1ICD then translocates to the nucleus where it associates with the transcription factor RBPJ to initiate the transcription of target genes that reinforce stem cell identity and inhibit differentiation (Gehart and Clevers, 2019).

EGF signalling

The EGF signalling pathway regulates proliferation of ISCs but is not essential in maintaining stem cell identity. The ligand, EGF, is secreted by Paneth and mesenchymal cells from the ISC niche. Its receptor, the ERBB1, is a tyrosine kinase receptor highly abundant on

the ISCs. Upon activation, ERBB1 initiates a downstream signalling cascade activating the PI3K/AKT and MAPK pathways, leading to an increased survival and proliferative properties ([Hassan and Seno, 2022](#)). Hyperactivation of the EGF signalling pathway is a strong driver of intestinal tumorigenesis ([Fearon and Vogelstein, 1990](#)). To prevent this, the pathway is tightly regulated in the ISCs through the co-expression of ERBB1 and LRIG1. LRIG1 is a negative regulator that modulates EGF signalling, thereby maintaining appropriate levels of cell proliferation and preventing unchecked growth ([Gehart and Clevers, 2019](#)).

BMP signalling

The BMP signalling pathway is a critical pathway involved in cell differentiation. Therefore, BMP activity needs to be repressed in the ISC niche. This is achieved by secretion of BMP antagonists such as Gremlin1/2 or Noggin, which are secreted by the mesenchymal cell located in the ISC niche ([Gooding and Leedham, 2020](#)). Aberrant expression of Grem1 resulted in ectopic crypt formation and polyposis ([Davis et al., 2015](#)).

Colorectal cancer

Epidemiology

Colorectal cancer (CRC) accounts for ~10% of all diagnosed-cancer cases (1.9 million new cases in 2020) being the third most diagnosed cancer type and the second leading cause of cancer-related mortality worldwide (1 million deaths in 2020). CRC occurs more frequently in developed countries and is associated with known risk factors, including alcohol consumption, smoking, obesity, sedentariness and Western diets. Due to early detection programmes and lifetime changes the incidence rate of advanced CRC has stagnated, although on a high level ([Dekker et al., 2019](#); [Siegel et al., 2023](#)). Indeed, it was estimated that by the age of 70, half of the Western population develops an adenomatous polyp. A portion of these polyps will advance to cancer, with the lifetime risk of developing CRC estimated to be around 5% ([Radtke and Clevers, 2005](#)).

Approximately 15%-30% of CRC patients present with metastases at the time of diagnosis, and around 20%-50% of CRC patients with initially localised disease will eventually develop metastases. The liver is the most common site for these metastases, followed by the lungs, peritoneum, distant lymph nodes and brain ([Cervantes et al., 2023](#)). The 5-year overall survival rate for CRC lies at ~64% with drastic variations depending on tumour stage at the time of diagnosis being 90% for early-stage CRC and decreasing to 12% for metastatic CRC (mCRC). Consequently, ~90% of CRC deaths are related to metastasis ([Cardoso et al., 2022](#)).

Aetiology

CRC, similar to other cancer types, is a genetic disease. This gene-centric model of cancer postulates that CRC arises from the accumulation of different mutations in specific genes (oncogenes, tumour suppressor genes (TSG) and DNA repair-related genes) (Vogelstein et al., 2013). The selective fitness provided by these alterations will determine the adaptive potential of a given cancer cell (Fearon, 2011). Based on the origin of these mutations, CRC are categorised into sporadic, familial or inherited (Dekker et al., 2019; Marmol et al., 2017):

- Sporadic CRC, which make up about 70% of all CRC cases, is caused by point mutations that occur during a person's lifetime and are not associated with inherited syndromes. These mutations affect individual cells and their progeny, leading to a heterogeneous molecular pathogenesis. (Marmol et al., 2017)
- Familial CRC, which accounts for 25% of CRC cases, refers to a heterogeneous group of CRC patients who have at least one relative with CRC history but whose germline mutation is unknown or unspecific (Armelaio and de Pretis, 2014; Marmol et al., 2017).
- Inherited CRC accounts for the remaining 5% of CRC cases and occurs due to inherited mutations in one allele of a specific CRC driver gene. Sporadic acquisition of a mutation on the other allele will trigger tumorigenesis (Armelaio and de Pretis, 2014). Inherited CRC can be further subdivided into:
 - Familial adenomatous polyposis (FAP) (~1% of all CRC cases) is a polyposis variant characterised by the formation of high numbers of potentially malignant polyps in the colon due to the presence of a germline mutation in the adenomatous polyposis coli (*APC*) gene.
 - Hereditary non-polyposis colon cancer (HNPCC) (~2-3% of all CRC cases), mainly caused by Lynch syndrome, is linked to mutations in DNA repair genes such as *MSH2*, *MLH1*, *MLH6*, *PMS1*, and *PMS2*. Loss of the DNA repair machinery leads to accumulation of DNA mutations and ultimately tumorigenesis.

CRC Stages

The American Joint Committee on Cancer (AJCC) has established a tumour staging protocol, known as the TNM system, world-wide utilised in medical oncology for classifying the extent of cancer spread. This system evaluates three critical components:

- T: stands for the extent and size of the primary tumour.
- N: indicates the degree of tumour dissemination into lymph nodes.

- M: indicates the presence of distant metastases

By assigning specific values to each component, the TNM staging system allows for precise characterization of cancer stages, ranging from Stage 0 (*in situ* tumour) to Stage IV (advanced metastatic disease) (**Figure 6**) (**Table 1**). This systematic approach aids in determining prognosis, ultimately contributing to more effective and personalised patient care. However, this grading system does not consider important aspects such as the genetics of CRC which are well known to have a great impact in treatment response.

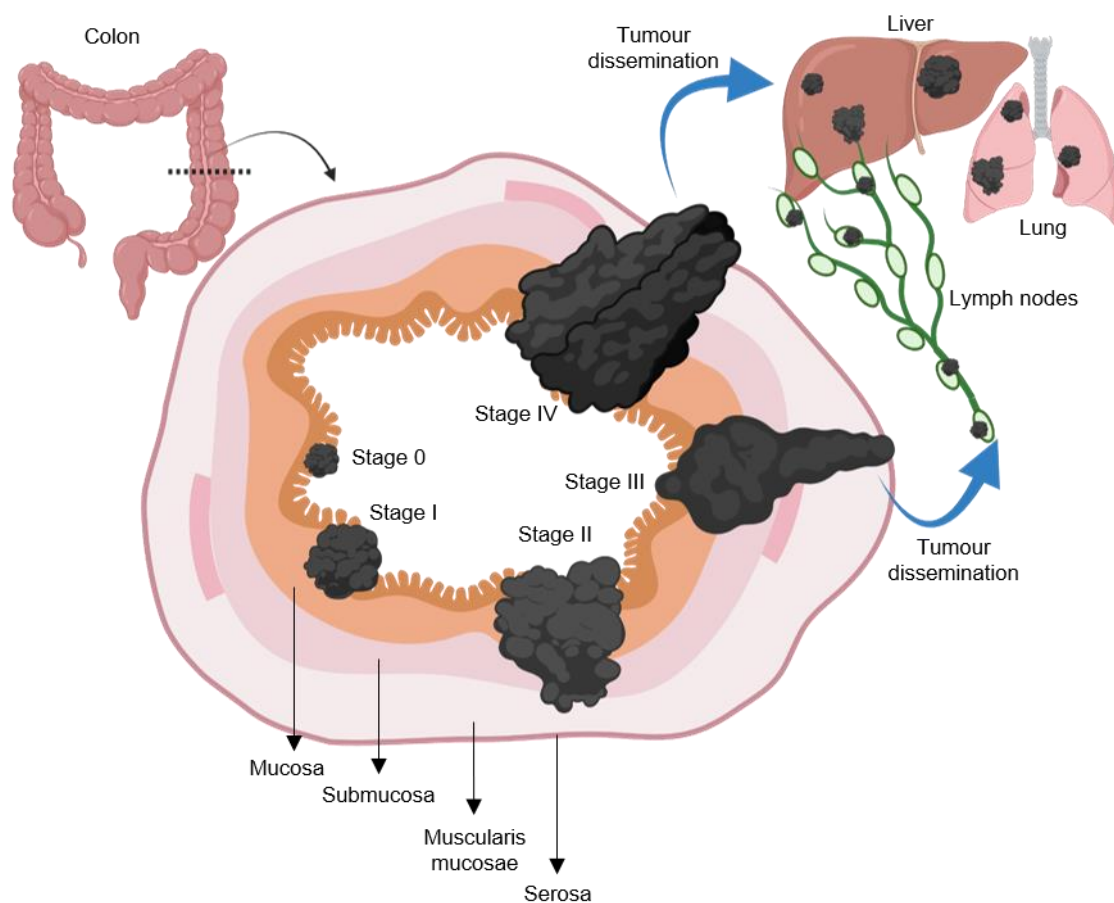


Figure 6. CRC staging. CRC can be clinically divided in 5 stages based on the tumour invasiveness and dissemination. While stage 0-II CRC differ in the grade of invasiveness but are non-metastatic, stage III CRC presents lymph node dissemination and stage IV is characterised by tumour dissemination into distant organs.

Tumour Stage	TNM Staging System	Description
0	Tis, N0, M0	Early stage CRC. <i>In situ</i> carcinoma that has not grown beyond the colonic muscularis mucosa (Tis). It has not spread to nearby lymph nodes (N0) or to distant sites (M0).
I	T1/T2, N0, M0	The cancer has grown into the submucosa (T1), and it may also have grown into the muscularis propria (T2). It has not spread to nearby lymph nodes (N0) or to distant sites (M0).

IIA	T3, N0, M0	The cancer has grown into the outermost layers of the colon but has not gone through them (T3). It has not spread to nearby lymph nodes (N0) or to distant sites (M0).
IIB	T4a, N0, M0	The cancer has grown through the wall of the colon but has not grown into other nearby tissues or organs (T4a). It has not yet spread to nearby lymph nodes (N0) or to distant sites (M0).
IIC	T4b, N0, M0	The cancer has grown through the wall of the colon and is attached to or has grown into other nearby tissues or organs (T4b). It has not yet spread to nearby lymph nodes (N0) or to distant sites (M0).
IIIA	T1/T2, N1/N1c, M0	The cancer has grown into the submucosa (T1), and it may also have grown into the muscularis propria (T2). It has spread to 1-3 nearby lymph nodes (N1) or into fatty areas near the lymph nodes (N1c). It has not spread to distant sites (M0).
	T1, N2a, M0	The cancer has grown into the submucosa (T1). It has spread to 4-6 nearby lymph nodes (N2a). It has not spread to distant sites (M0).
	T3/T4a, N1a-b/N1c, M0	The cancer has grown into the outermost layers of the colon (T3) or through the wall of the colon (T4a) but has not reached nearby organs. It has spread to 1-3 nearby lymph nodes (N1a-b) or into fatty areas near the lymph nodes (N1c). It has not spread to distant sites (M0).
IIIB	T2/T3, N2a, M0	The cancer has grown into the muscularis propria (T2) or into the outermost layers of the colon (T3). It has spread to 4-6 nearby lymph nodes (N2a). It has not spread to distant sites (M0).
	T1/T2, N2b, M0	The cancer has grown into the submucosa (T1), and it might also have grown into the muscularis propria (T2). It has spread to 7 or more nearby lymph nodes (N2b). It has not spread to distant sites (M0).
	T4a, N2a, M0	The cancer has grown through the wall of the colon but has not reached nearby organs (T4a). It has spread to 4-6 nearby lymph nodes (N2a). It has not spread to distant sites (M0).
IIIC	T3/T4a, N2b, M0	The cancer has grown into the outermost layers of the colon (T3) or through the wall of the colon (T4a) but has not reached nearby organs. It has spread to 7 or more nearby lymph nodes (N2b). It has not spread to distant sites (M0).
	T4b, N1/N2, M0	The cancer has grown through the wall of the colon and is attached to or has grown into other nearby tissues or organs (T4b). It has spread to at least 1 nearby lymph node or into fatty areas near the lymph nodes (N1 or N2). It has not spread to distant sites (M0).
	T4b, N1/N2, M0	The cancer has grown through the wall of the colon and is attached to or has grown into other nearby tissues or organs (T4b). It has spread to at least 1 nearby lymph node or into fatty areas near the lymph nodes (N1 or N2). It has not spread to distant sites (M0).
IVA	Any T, Any N, M1a	The cancer may or may not have grown through the wall of the colon (Any T). It might or might not have spread to nearby lymph nodes. (Any N). It has spread to 1 distant organ or distant set of lymph nodes, but not to distant parts of the peritoneum (M1a).
IVB	Any T, Any N, M1b	The cancer may or may not have grown through the wall of the colon (Any T). It might or might not have spread to nearby lymph nodes (Any N). It has spread to more than 1 distant organ or distant set of lymph nodes, but not to distant parts of the peritoneum (M1b).
IVB	Any T, Any N, M1c	The cancer may or may not have grown through the wall of the colon (Any T). It might or might not have spread to nearby lymph nodes (Any N). It has spread to

	distant parts of the peritoneum, and may or may not have spread to distant organs or lymph nodes (M1c).
--	---

Table 1. TNM tumour staging protocol. Table adapted from <https://www.cancer.org/cancer/types/colon-rectal-cancer/detection-diagnosis-staging/staged.html>

Pathogenesis and genetics of CRC

In CRC, initial dysplasia of the mucosa is followed by the formation of adenomas, some of which will progress to aggressive adenocarcinomas that can ultimately invade and metastasize distant organs such as liver or lungs (Turajlic and Swanton, 2016). Each of these steps can be triggered by accumulation of different genomic alterations which are accompanied by morphological changes of the intestinal epithelium (Fearon and Vogelstein, 1990). In CRC these alterations have been elucidated in great detail and can be divided into three different developmental routes (Figure 7):

- The adenoma-to-carcinoma 'classical' model (80% of all CRC): In this model tumours develop in a stepwise manner with an initial mutation in the *APC* gene that will induce transformation of the intestinal epithelium into a tubular adenoma. Subsequent gain-of-function mutations in the RAS pathway or loss-of-function mutations in TSGs such as *TP53* or in the transforming growth factor- β (TGF- β) signalling pathway will trigger the further progression into an invasive carcinoma that can ultimately metastasize (Fearon, 2011; Fearon and Vogelstein, 1990). These tumours are microsatellite stable (MSS) and present chromosomal instability (CIN) (Dekker et al., 2019).
- Serrated neoplasia pathway (10-20% of all CRC): This model differs from the 'classical' model in that CRC is not initiated by *APC* mutations. Instead, these tumours originate from *KRAS* or *BRAF* oncogenic mutations. Tumours are usually located in the right side of the colon and present a flat and serrated morphology, hindering its detection by routine colonoscopy (Aiderus et al., 2024). Additional loss-of-function mutations in *TP53* are needed for further progression into an invasive carcinoma (JE et al., 2015). Furthermore, a recent study has shown that activation of the Notch1 signalling is required for CRC metastasis (Jackstadt et al., 2019). While *KRAS* mutant CRC are MSS and CIN, a significant proportion of *BRAF* mutant CRC acquire additional mutation in the DNA repair machinery thus turning into microsatellite instable (MSI) tumours (Aiderus et al., 2024).
- MSI CRC (2-7% of all CRC): Lynch syndrome accounts for the 95% of all MSI CRC tumours. In this model, inherited alteration in the DNA repair machinery genes leads to accumulation of mutations and lately hypermutated tumours (Dekker et al., 2019).

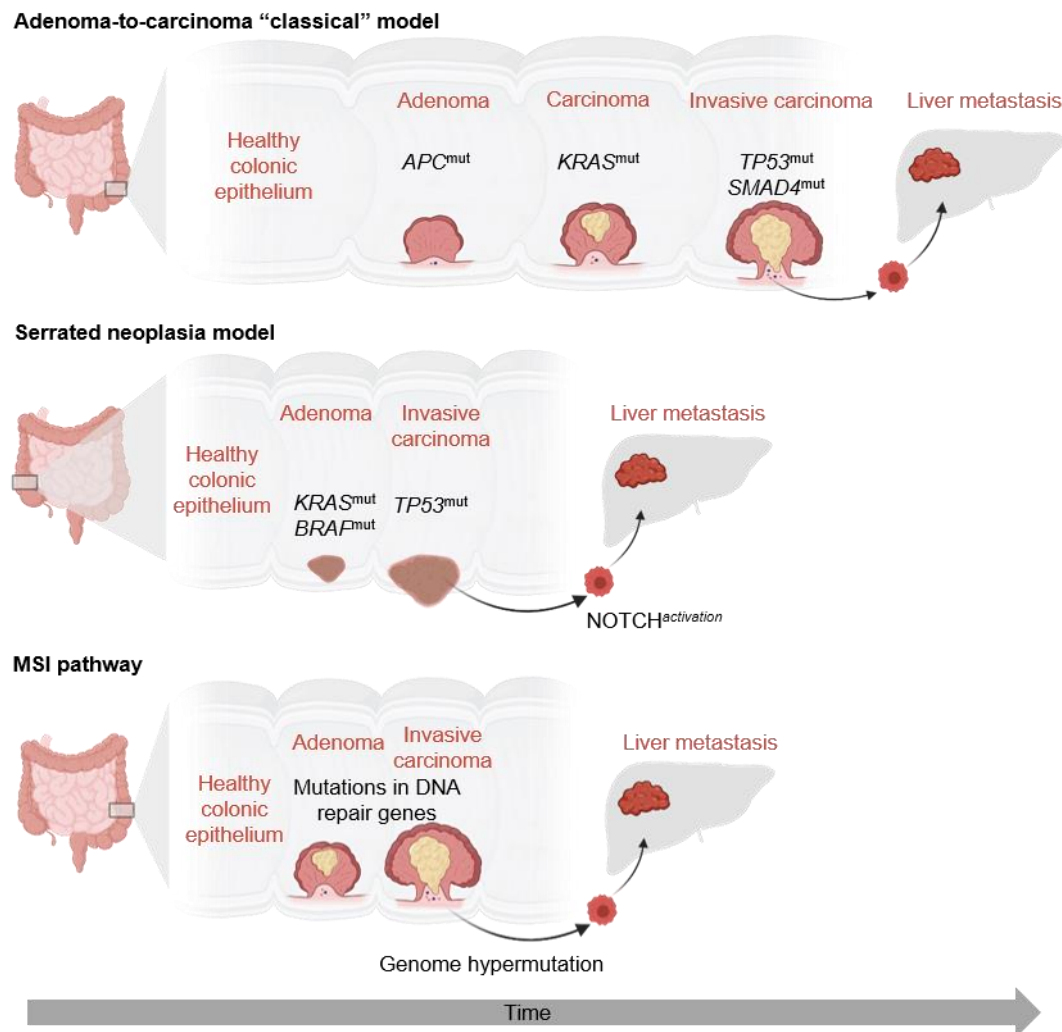


Figure 7. Evolutionary pathways of CRC tumorigenesis. Schematic representation of the three different CRC developmental routes from tumour initiation to metastatic progression by acquisition of different mutational profiles.

CRC treatments

CRC treatment strategies are multifaceted and tailored to the stage of the disease, tumour molecular profile and patient characteristics. The standard-of-care for CRC patients is surgical resection of the primary tumour, which can be curative in early-stage CRC. However, after resection, 20-40% of the patients will develop metastasis due to an early dissemination of tumour cells. Patients with metastatic disease or high risk of metastasis receive a combination of surgery and systemic treatments including chemotherapy and/or targeted therapy which is administered in a neoadjuvant or adjuvant setting (Dekker et al., 2019; Sanchez-Gundin et al., 2018). The chemotherapy agents most frequently used include 5-fluorouracil (5-FU) and leucovorin combined with oxaliplatin (FOLFOX) or with irinotecan (FOLFIRI) which aim to control tumour growth by attacking mainly the proliferative tumour cells. Nevertheless, chemotherapy efficacy is limited by its high systemic toxicity and low tumoural cell-specific selectivity, issues that can be mitigated through the combination with targeted therapies (Avolio and Trusolino, 2021).

Among the numerous genetic alterations identified in CRC, only *KRAS*, *NRAS*, *BRAF*, *HER2* and MSI status, are used to guide treatment decisions. For instance, the epidermal growth factor receptor (EGFR) inhibitors cetuximab and panitumumab are used in combination with chemotherapy as a first- and second-line treatment in patients with *KRAS* or *NRAS* wild-type CRC (Avolio and Trusolino, 2021; Douillard et al., 2010; Karapetis et al., 2008). Another example is the anti-VEGF antibody bevacizumab, which is used in combination with chemotherapy as a first-line treatment in patients with *KRAS* or *NRAS* mutant CRC (Hurwitz et al., 2004; Saltz et al., 2008). Unlike in melanoma, *BRAF* mutant CRC show poor response to *BRAF* inhibitors as monotherapy. However, combining cetuximab with the *BRAF* inhibitor Encorafenib as a second-line treatment has shown better response in *BRAF*^{V600E} metastatic CRC (Cervantes et al., 2023). Identification of *HER2* amplification after failure of first-line treatment guides the treatment regimen towards *HER2* inhibition regimens (Cervantes et al., 2023). Additionally, since 2017, immune check blockade with anti-PD-L1/PD-1 or anti-CTLA4 antibodies has been used as a first-line treatment in MSI CRC patients with successful results (Cervantes et al., 2023).

Despite these interventions, the response to treatment is not always durable, with high stage-dependent relapse rates posing a significant challenge. Hence, further improvement and research is necessary. Understanding of the fundamental biology of CRC has significantly increased over the past years, yet therapy resistance remains as one of the major challenges. One of the main reasons for the treatment failure is the high degree of inter- and intra-tumour heterogeneity (ITH).

Molecular classification of CRC

In the clinics, it is crucial to classify patients depending on the molecular and mutational profile of the tumour to tailor the best therapy regimen. To provide a unified subtyping of CRC an international consortium stratified CRC into four consensus molecular subtypes (CMSs) (CMS1-4) attending to the molecular profile of over 5.000 CRC patient samples (Guinney et al., 2015). CMS1 accounts for 14% of all CRCs and it is characterised by high MSI and strong immune cell infiltration, making it susceptible to immune check inhibition. CMS2, or the canonical subtype, represents 37% of CRCs and shows high WNT- and MYC- signalling. These tumours are generally more responsive to standard chemotherapy regimens. CMS3, or the metabolic subtype, accounts for 13% of all CRC and is defined by metabolic dysregulation, caused by *KRAS* mutations and hence increased MAPK activity. 23% of CRC patients belong to the CMS4 or mesenchymal subtype, which present the worst prognosis. These tumours are marked by high stromal infiltration and TGF- β rich environments. The remaining 13% tumours

present mixed features which might represent a transition between phenotypes or high degree of ITH (Guinney et al., 2015) (Figure 8A).

In 2022, the single-cell intrinsic CMS (iCMS) stratification model was proposed thanks to the advances in single-cell sequencing. iCMS2 is associated with CIN whereas iCMS3 comprises tumours with high MSI and tumours with low copy number variations (Joanito et al., 2022). This classification helped to segregate the CMS4 subtype into the two iCMS subtypes, having the one in the iCMS2 group a better prognosis. However, this classifier failed in providing more granularity in the CMS2 and CMS3 subtypes, which were assigned to the iCMS2 and iCMS3, respectively (Dunne and Arends, 2024; Joanito et al., 2022) (Figure 8B).

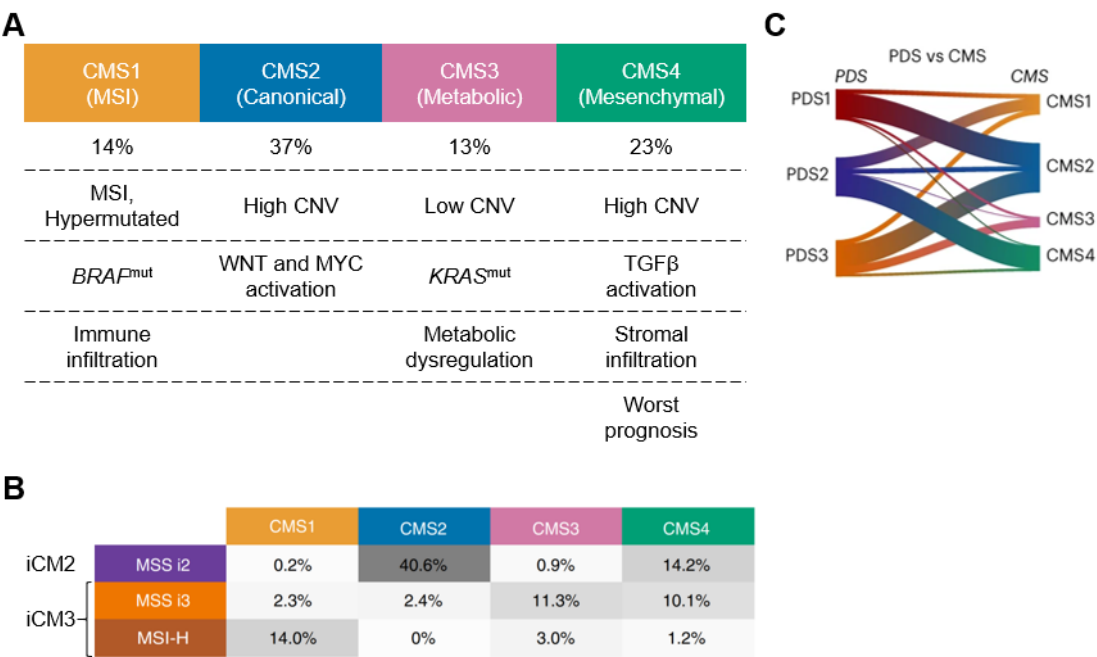


Figure 8. Molecular classifications of CRC. **A.** CMS classification of CRC reflecting the genomic and biological differences across subtypes. Adapted from (Guinney et al., 2015). **B.** Table showing the percentage of patients from the CMS cohort broken down into the iCMS classification. Adapted from (Joanito et al., 2022). **C.** Sankey plot showing CMS–PDS alignment from the FOCUS cohort. Adapted from (Malla et al., 2024).

Recently, a new stratification approach based on gene ontology and pathway activation analysis revealed a set of three pathway-derived subtypes (PDS), offering valuable insights into tumour biology that extends beyond the mutational status and with closer link to clinical phenotypes. The PDS1 subtype (26% of CRC) is characterised by high WNT and MYC signalling activation, thus, fast-cycling cancer stem cells (CSCs) (marked by *LGR5* expression). The PDS2 subtype (31% of all CRC) is enriched for immune and TGF-β signalling pathways activation and is associated with regenerative and foetal-like intestinal signatures (marked by *ANXA1* expression). The PDS3 subtype (30% of all CRC) is devoid of activation of the above-mentioned proliferation and stemness features and appears to be enriched for

differentiation markers. Unlike the iCMS subtyping, the PDS system stratified the CMS2 patients in two different groups PDS1 and PDS3 ([Malla et al., 2024](#)) (**Figure 8C**).

Tumour stratification gives in-depth insights into the molecular features of individual tumours, enabling the prediction of therapy response and patient outcomes. However, these classifications are just a vague summary of the spectrum of tumours bearing roughly the same phenotype. The boundaries between different CMSs are blurred and patients are often not assigned to any subtype. Furthermore, due to the high ITH in CRC, tumours frequently show traits of different subtypes in different tumour areas.

Models of CRC progression

***In vitro* modelling of CRC**

2D adherent cell lines are used in cancer research as a tool to gain insights into CRC progression and response to treatments. Indeed, they are cost-effective, easy to handle and compatible with a wide range of experimental techniques. However, these models were underrepresenting the wide ITH and histopathological features observed in CRC tumours ([Lannagan et al., 2021](#)).

In 2009, the field of CRC research was revolutionised with the establishment of 3D cultures from the healthy intestinal epithelium ([Sato et al., 2009](#)). Moreover, advances in CRISPR/Cas9 genomic editing allowed the modelling of CRC progression by inducing CRC driving mutations in genes such as *APC*, *TP53*, *SMAD4* and *KRAS* into these 3D organoid cultures, closely resembling the human disease ([Fearon and Vogelstein, 1990](#); [Gostimskaya, 2022](#)). Importantly, these advancements have led to the establishment of comprehensive biobanks of CRC organoids from human and murine origin, which serve as powerful tools to study the implication of different genetic alterations in CRC progression and therapeutic responses ([Ooft et al., 2019](#); [Yao et al., 2020](#)). Contrary to the 2D adherent cell lines, 3D cultures were proven to recapitulate histopathological and transcriptional features present *in vivo* as well as a higher degree of heterogeneity within the culture. However, a pressing drawback was still the absence of the tumour microenvironment (TME). This was circumvented by utilising co-culture systems in which tumoural organoids are grown in the presence of mesenchymal and/or immune cells, mimicking the physiological interactions between cancer cells and the TME ([Neal et al., 2018](#)). In summary, these 3D models allow the *in vitro* modelling of CRC advancing our understanding of the disease and the development of targeted therapies.

***In vivo* modelling of CRC**

Genetically engineered mouse models

GEMMs are undoubtedly the most powerful tool to study CRC progression as they accurately resemble the genetic complexity, heterogeneity and native microenvironment observed in the human disease. The first mouse model of CRC was developed in the 1990s and harbours a mutation in the *Apc* gene (i.e. *Apc*^{Min/+}). Spontaneous loss of heterozygosity in the remaining allele results in the formation of polyps, benign tumours that can later on progress to carcinomas (Moser et al., 1993).

The introduction of inducible CreERT2–*LoxP* technology in the 2000s significantly advanced the capabilities of GEMMs. This system allows for the targeted deletion of specific genomic regions that are flanked by *loxP* sites upon administration of tamoxifen, leading to the deletion or expression of genes within the tissue of interest. In this context, the CreERT2 transgene is driven by a tissue-specific promoter, enabling precise genetic modifications that can mimic the alterations seen in human CRC (Nagy, 2000). Later advancements crossing *Lgr5*^{eGFP-IRES-CreERT2} (Barker et al., 2007) or *villin1*^{CreERT2} (Madison et al., 2002) GEMMs with various mouse lines carrying CRC-related genetic alterations, such as *Apc*^{fl/fl}, *Trp53*^{fl/fl}, *Kras*^{G12D/+}, *BRAF*^{V637e/+}, *Smad4*^{fl/fl} or *Rosa26*^{Notch1CD/+}, allow to model different stages of CRC progression. When these GEMMs carry up to two of these genetic alterations, adenomas develop, with some eventually progressing into invasive carcinomas (Jackstadt and Sansom, 2016). Introducing a third or fourth genetic alteration increases tumour aggressiveness, allowing the study of later stages of CRC (Jackstadt et al., 2019; Tauriello et al., 2018). Yet, many of these models exhibit long latencies and low penetrance of metastasis, with animals often succumbing to high tumour burden before metastasis can develop. This limitation hinders the study of later metastatic stages of CRC. To overcome this limitation transplantation models are employed.

Transplantation models

While *in vitro* systems provide valuable insights, they often fall short of replicating key aspects of the tissue architecture and the drug pharmacodynamics and pharmacokinetics. These elements are essential for understanding tumour progression and patient outcomes. To address these limitations, transplantation models have been developed, enabling the inoculation of human- or mouse-derived CRC cells and organoids into murine hosts (McIntyre et al., 2015).

Subcutaneously transplantation models are frequently employed to evaluate tumour formation potential and drug efficacy. In these models, tumours grow in the dorsal region of the animals, making them easy to monitor over time. However, subcutaneous tumours hardly metastasize. Conversely, orthotopic transplantation offers a more physiologically relevant approach by allowing the study of primary tumour formation within the intestinal environment, as well as the spontaneous development of metastasis (McIntyre et al., 2015). For instance, Fumagalli *et al.* established an orthotopic model by transplanting patient-derived organoids (PDOs) into the caecal wall of immunocompromised mice, which provides a more accurate representation of tumour behaviour in a native setting (Fumagalli et al., 2017). Recent innovations in transplantation techniques like the colonoscopy-guided mucosal injection, have further reduced the invasiveness of the procedure and facilitated tumour monitoring (Chen et al., 2020; Jackstadt et al., 2019).

Overall, these advancements enable longitudinal studies of CRC progression, allowing researchers to assess the impact of genetic alterations on tumour dynamics and TME. Additionally, to model CRC metastasis more effectively, other transplantation strategies with higher penetrance are utilised. For example, spleen and tail vein injections are commonly employed to study liver and lung metastases, respectively (Jackstadt and Sansom, 2016; Tauriello et al., 2018). However, it is important to note that these models may not fully capture critical bottlenecks of metastasis, such as tumour invasion and extravasation.

Overall, by integrating organoid technology with sophisticated transplantation models, researchers can gain deeper insights into the complexity of CRC biology, ultimately paving the way for improved therapeutic strategies and patient outcomes.

CRC heterogeneity

Genetic ITH as a driving force in CRC progression

From an evolutionary perspective, tumours are dynamic ecosystems composed of a large number of different cancer cell populations that evolve differently and accumulate diverse somatic alterations (clones). In addition, within these clones, new genetic diversity emerges (subclones). Thanks to high-throughput genomic sequencing technologies, tumour genetic diversity has been used as a tool to yield quantitative insights in terms of tumour evolution and clonal dynamics (Turajlic et al., 2019). To date, two models of tumour evolution have been proposed:

- The linear progression model. In 1990, Fearon and Vogelstein postulated the linear progression model of CRC (Fearon and Vogelstein, 1990). In this model tumours

develop in a stepwise manner, as afore-described (**Figure 7**) (Fearon, 2011; Fearon and Vogelstein, 1990). Within this model, sequential acquisition of new driver mutations is followed by selective sweeps and clonal expansion, indicating that tumours have a monoclonal nature and ITH is only a transitory event that occurs during clonal competition (Turajlic et al., 2019) (**Figure 9A**).

- The 'Big Bang model'. This model predicts that tumours originally appear as an expansion of multiple subclones that are equally fit and that this ITH is an inherent feature in CRC. Thus, tumours present a polyclonal nature where most cancer cells harbour shared clonal alterations (public mutations), which are required for malignant transformation, i.e. *APC*. In addition, subclonal alterations (private mutations) are acquired at early stages and remain pervasive during tumour growth (Sottoriva et al., 2015) (**Figure 9B**).

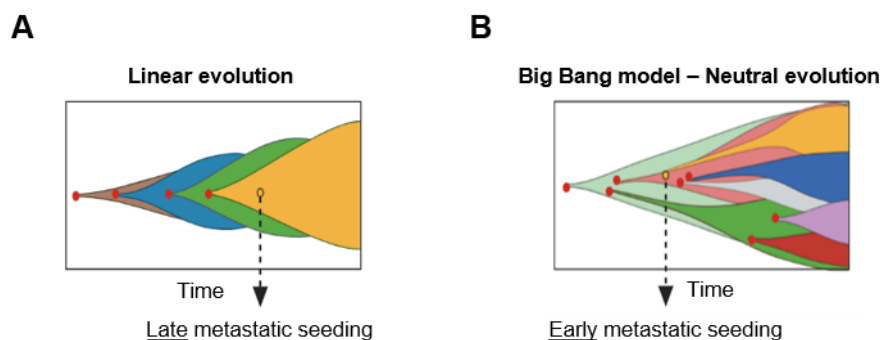


Figure 9. CRC clonal evolution models. Schematic illustrations of the two models of CRC evolution: **A**. Linear evolution and **B**. Neutral evolution models.

For decades it was assumed that metastasis is the latest event during tumour progression. Only evolutionary advanced CRC cells present beneficial traits to escape and survive in hostile environments different from the colon and therefore, the ones involved in the metastatic seeding (Massague and Obenauf, 2016) (**Figure 9A**). Conversely, analysis of the genomic divergence between the primary tumour and paired metastasis revealed that, in most of the cases, metastatic lesions only shared the truncal mutations with the primary lesion. Nonetheless, they differ in the subclonal alterations that appear later during evolution, suggesting that in 80% of the cases metastasis is an early event during tumorigenesis in CRC, lung and breast cancer (Hu et al., 2019; Hu et al., 2020; Sottoriva et al., 2015) (**Figure 9B**). This theory supports the early presence of 'born to be bad' clones with high invasive potential in the primary tumour (Sottoriva et al., 2015). Nevertheless, not all tumours metastasize, and it remains elusive which molecular features confer these 'born to be bad' clones with the abilities to early escape and disseminate to distant organs.

Furthermore, Hu *et al.* investigated the phylogeny of paired tumour samples (primary tumour and matched lymph node and distant metastasis) of a cohort of 20 CRC patients finding

a recurrent pattern in which distant metastasis are genetically less diverse whereas draining lymph node metastases samples had multiclonal origins (Hu et al., 2019). Interestingly, a similar scenario was observed when analysing the genetic diversity in liver metastasis samples in treatment-naïve and post-treatment settings indicating an additional bottleneck through which the tumour-resistant cells develop (Hu et al., 2019; Hu et al., 2020; Reiter et al., 2020).

Modelling tumour evolution

DNA barcoding has been extensively used for the study of clonal dynamics (Gerrits et al., 2010; Lu et al., 2011; Peikon et al., 2017). Here, DNA barcodes are integrated in the genome of a large scale of founder cells so that each targeted cell will carry a unique and identifiable mark that will be inherited to the daughter cells (Bhang et al., 2015; Lu et al., 2011). The complexity of the library will depend on the length and variable sites of the DNA barcode (Kebschull and Zador, 2018; Peikon et al., 2017; Winters et al., 2017). Moreover, these vectors have been also engineered to include other cassettes such as Cre recombinase or sgRNAs to induce specific genomic alteration to the targeted cells (Winters et al., 2017). These approaches have enabled to uncover the pre-existence of therapy resistance clones in non-small cell lung cancer (Bhang et al., 2015; Foggetti et al., 2021) as well as to interrogate the fitness power of different panels of tumour suppressor genes in lung adenocarcinoma (Rogers et al., 2017). Yet, DNA barcoding has some caveats: i) recovery of the cells for posterior functional characterization is not possible; ii) the spatial resolution is missing and iii) it will allow to study tumour evolution only at the clonal level.

To overcome these limitations, recombinase-based *in vivo* lineage tracing systems were first developed to visualise the nervous system network with the Brainbow mice. These mouse models present transgenes with different fluorescent proteins flanked by incompatible *Lox* variants. Upon Cre activation, random recombination of the *lox* sites and the orientation of the inserted cassettes will give rise to a mosaicism of differently labelled cells (Livet et al., 2007). The Confetti mouse is the most used multicolour lineage tracing system *in vivo*. This model allows discriminating up to four different colours (GFP, YFP, RFP or CFP) (Snippert et al., 2010). Another less used mouse model is the Rainbow, which consists of three tandem Rainbow copies yielding expressions of up to ten different colour codes (Wollny et al., 2016). The power of this approach is the maintenance of the spatial context, which allows the study of clonal evolution in the native environment (Fumagalli et al., 2020a; Wollny et al., 2016). Yet, the reduced number of combinations possible limits the multiplexing capacity of the study.

The Cancer Stem Cell model

ITH was thought to be merely caused by genetic alterations occurring during tumour evolution. However, single cell multi-omic technologies have uncovered a high degree of phenotypic heterogeneity among cancer cells harbouring the same mutational profile (Tirosh et al., 2016). The CSC model has become prominent as a non-genetic source of ITH explained by diverse differentiation states along the evolutionary trajectory, which are not defined by genetic changes but by different epigenetic or transcriptional programs (Gavish et al., 2023; Kreso and Dick, 2014). The CSC model states that tumours are organised in a hierarchical manner where a specific cancer cell population, known as CSC, initiates and fuels tumour growth and is responsible for therapy resistance and metastasis (Batlle and Clevers, 2017) (Figure10).

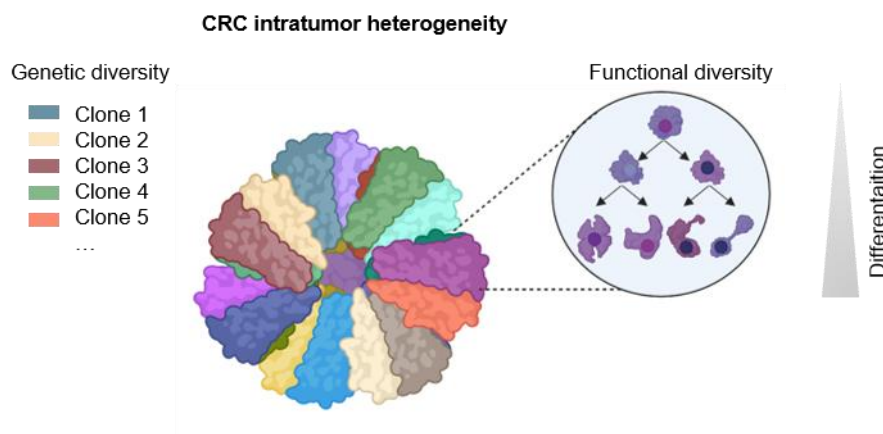


Figure 10. Sources of CRC heterogeneity. Image representation of the two sources of CRC heterogeneity: genetic diversity and functional diversity (differentiation state).

Tools to study the stemness

To determine the stemness potential of specific cell populations, the scientific community have developed various methodologies that mainly rely on the identification of marker genes exclusively expressed in those cells. Some of the most commonly used tools include:

- Transplantation assays. The putative stem cell population is first isolated by fluorescence-activated cell sorting (FACS) based on the expression of a marker gene and subsequently transplanted at limited dilutions in secondary recipient mice. If transplanted cells can reconstitute the tissue and maintain long-term function, it provides evidence of their stemness properties. Another alternative is the seeding of these cells in Matrigel *in vitro* to assess the spheroid formation capacity (Loh and Ma, 2024) (Figure 11A). In the past, this method required the availability of antibodies

against the protein of interest as well as its cell surface expression. Genetic engineering strategies overcome this limitation by locating a fluorescent reporter gene under the control of the promoter of the gene of interest, enabling the identification of the cells regardless of protein localization while also maintaining cell viability (Cortina et al., 2017b; Shimokawa et al., 2017). Matter of actual debate are the immune deficiency status of the recipient mice, and the injection site. Overall, transplantation-based approaches are the “gold standard” assay used to assess the tumour-initiation capacity (TIC) of the cell; however, the stem cell niche is disrupted and therefore this method needs to be complemented with additional approaches (Loh and Ma, 2024).

- Lineage tracing. Lineage tracing is a powerful method for tracking the progeny of a putative stem cell in its native microenvironment over time. Two elements are required: (1) an inducible recombinase system such as Cre-ERT2 recombinase whose sequence is introduced in the genome under the transcriptional control of the promoter of the marker gene of interest (GOI); (2) a reporter gene (i.e. fluorescent protein (FP) or lacZ) that is regulated by a constitutive promoter but whose expression is initially blocked by a *LoxP*-STOP-*LoxP* cassette located upstream of the reporter sequence. Upon tamoxifen administration, recombination occurs at the *loxP* sites in cells expressing the GOI and thus, the Cre-ERT2, resulting in the removal of the STOP codon. This activation allows for the expression of the reporter gene in the targeted cell and its progeny, thereby enabling the tracking of cell lineages over time (Batlle and Clevers, 2017) (**Figure 11B**).
- Lineage ablation. Lineage ablation is another valuable approach for evaluating the stem cell potential of a putative stem cell within its native microenvironment. This strategy involves the introduction of a suicide gene sequence under the control of the promoter of the marker gene of interest to selectively induce cell death (Loh and Ma, 2024) (**Figure 11C**). When the diphtheria toxin subunit A (DTA) suicide gene is employed, apoptosis is triggered in any cell expressing the gene at any time (Lange et al., 2019; Plummer et al., 2017). Alternatively, targeted cell ablation can be achieved using a pro-caspase9 or DTR sequence, where cell death is induced upon administration of a chemically-induced dimerizer (CID) (Clackson et al., 1998; Kemper et al., 2012) or DT (Saito et al., 2001), respectively. This method allows for precise manipulation of specific cell populations, providing insights into the functional role of stem cells in tissue maintenance and regeneration.
- Single-cell profiling. Single-cell profiling techniques enable the analysis of gene expression profiles at the individual cell level. By analysing the transcriptomes of single

cells, stem cell populations can be inferred and their developmental trajectories can be reconstructed (Loh and Ma, 2024).

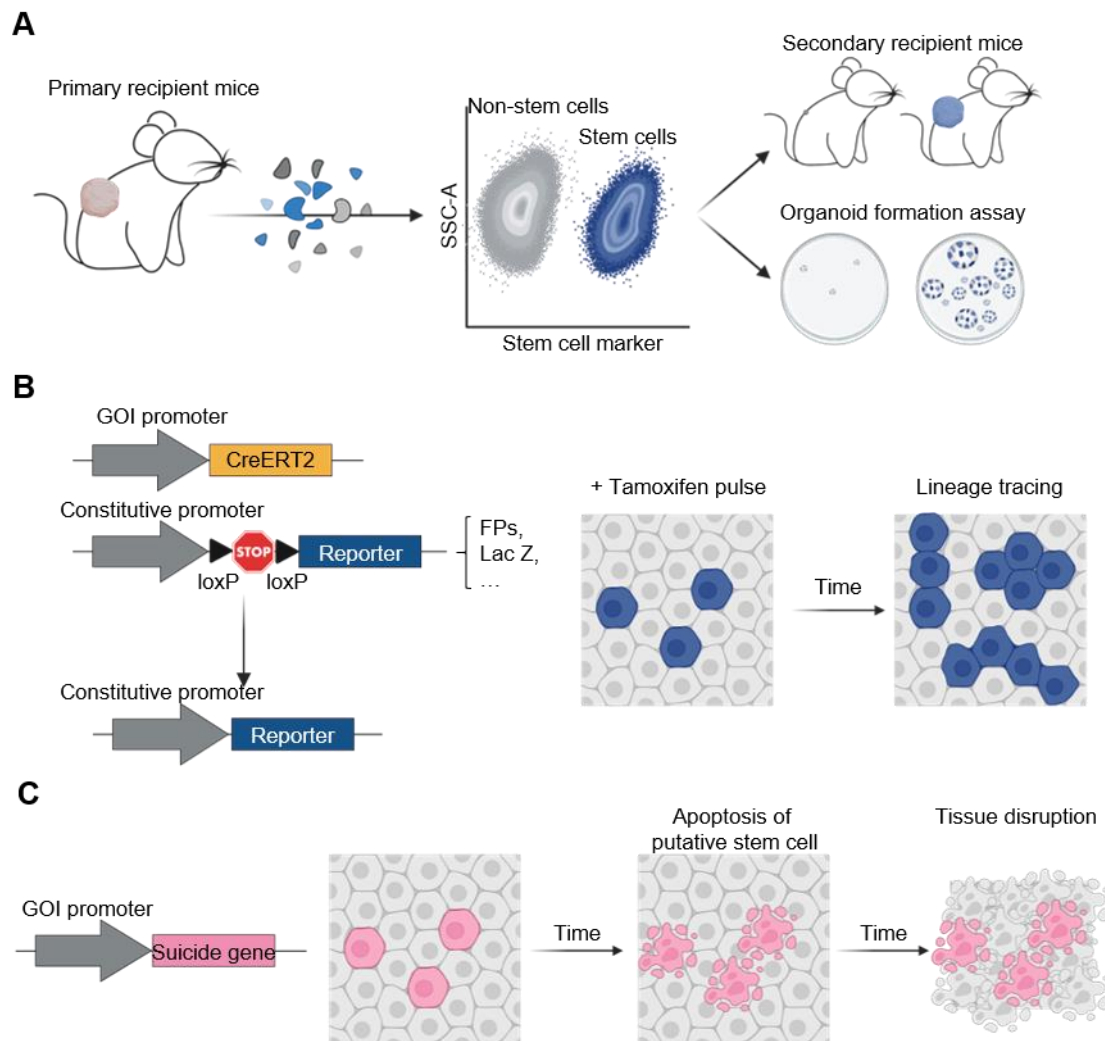


Figure 11. Methodologies used for characterization of stem cells. **A.** Tumour or organoid formation assays from FACS separated stem cells and non-stem cells. **B.** Lineage tracing experiments to assess the capacity of putative stem cells to fuel tumour growth. **C.** Ablation of putative stem cells to assess the effect on tissue maintenance or tumour growth.

CSC in CRC

Most tumour cells often retain transcriptomic features of their healthy tissue counterparts (Gavish et al., 2023). Indeed, in CRC, LGR5⁺ cancer cells were found to be the cell of origin of CRC (Barker et al., 2009). Furthermore, in 2017, three different laboratories demonstrated the dependency of CRC primary tumours on LGR5⁺ tumour cells, reinforcing the CSC role of LGR5⁺ cells (hereinafter LGR5⁺ CSCs) (Cortina et al., 2017a; de Sousa e Melo et al., 2017a; Shimokawa et al., 2017). Importantly, upon complete ablation of the CSC pool, the non-CSCs were able to de-differentiate into a stem cell, providing a proof-of-concept of the

plasticity of tumour cells (de Sousa e Melo et al., 2017a). Altogether, LGR5 has been broadly recognised as “the CSC marker” in CRC.

The above described work on CSCs has been solely conducted in models that recapitulate the classical route of CRC progression (*APC* mutant (*APC*^{mut}) models) (Cortina et al., 2017a; de Sousa e Melo et al., 2017a; Fumagalli et al., 2020a; Shimokawa et al., 2017). Overall, these models are characterised by aberrant activation of WNT signalling, including *Lgr5* levels (Merlos-Suarez et al., 2011; Munoz et al., 2012; Shimokawa et al., 2017). Therefore, these models might be the ones relying on *Lgr5* expression for maintaining the CSC hierarchy. However, a significant number of CRC present none or few LGR5⁺ cells (Morral et al., 2020) raising the possibility of the presence of alternative CSC programs in these LGR5^{low} or LGR5⁻ tumours.

In line with this hypothesis, another study explored the CSC model beyond *Lgr5* expression. By studying the functional properties of the tumour cells, Morral et al. defined two zones within the tumour defined by different biosynthetic capabilities. While the periphery of the tumour was characterised by highly biosynthetic cancer cells, this capacity was lost as the cells differentiated towards the inner core of the tumour. Interestingly, these findings were independent of *Lgr5* expression but rather dependent on POLR1A (Morral et al., 2020).

Recently, there has been an increasing interest in the foetal ISC program in the context of CRC (Mustata et al., 2013). This program, absent in the healthy intestinal epithelium, is reactivated upon cellular stresses in adult tissues (Ayyaz et al., 2019; Bala et al., 2023; Karo-Atar et al., 2022; Mzoughi et al., 2023; Nusse et al., 2018; Yui et al., 2018). Thus, as cancer is a wound that never heals, the induction of the foetal ISC program found in CRC is not surprising (Bala et al., 2023; Mzoughi et al., 2023; Vasquez et al., 2022). Transcriptional profiling of human and murine CRCs has indicated that tumours with low WNT activation like CMS4 tumours are enriched for foetal ISC programs. Serrated adenomas, which are *APC*-proficient tumours driven by *KRAS* or *BRAF* oncogenic mutations, are also enriched for foetal ISC signatures while showing lower levels of WNT pathway activation and adult ISC programs (Chen et al., 2021; Kawasaki et al., 2020; Leach et al., 2021; Vasquez et al., 2022). In addition to the genetic background of CRCs, other cell-extrinsic factors such as the TME or therapeutic stresses can modulate the CSC phenotype (Vasquez et al., 2022) (extensively reviewed in our review (Fey et al., 2024)). Interestingly, these two stem cell programs define two different CSC populations that can co-exist within a tumour indicating a continuum between both stem cell states influenced by cell-intrinsic and -extrinsic factors (Vasquez et al., 2022) (**Figure 12**). However, the stem cell potential of foetal-like CSCs and their role in tumour progression remains elusive.

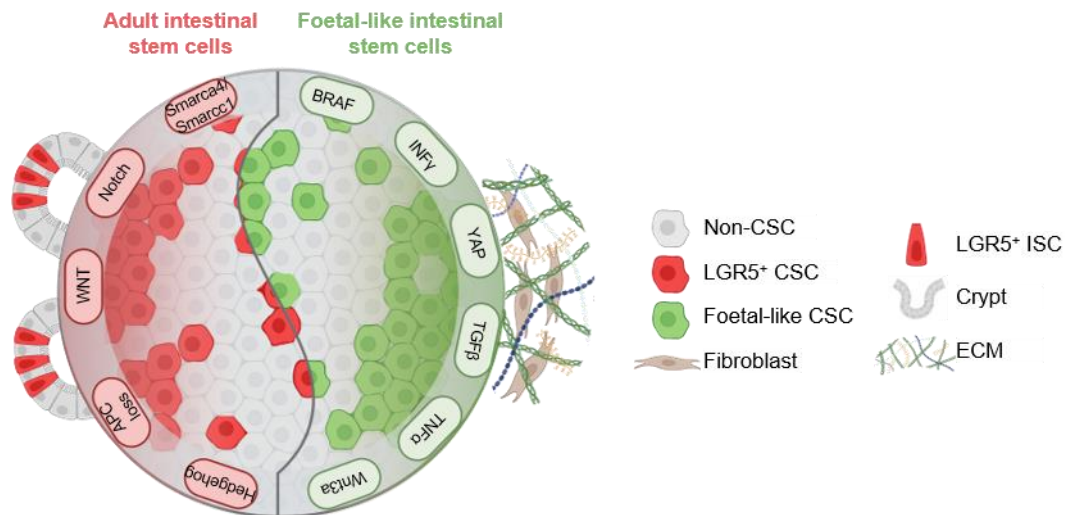


Figure 12. CSC dynamics. Schematic illustrations of adult CSCs (LGR5⁺ CSC) (red) and foetal-like CSCs (green), switching between the stem cell phenotypes through intrinsic and extrinsic cues within a plastic continuum. Figure adapted from (Fey et al., 2024).

Metastasis initiating cells

Metastasis is the primary cause of CRC-associated fatalities. Analysis of primary tumours alongside their matched metastases has uncovered highly conserved mutational patterns (Hu et al., 2019; Hu et al., 2020; Sottoriva et al., 2015), suggesting that the key drivers of metastasis may be influenced by non-genetic factors. Indeed, CSCs have been put forward as the origin of metastasis (Loh and Ma, 2024). Nevertheless, complete ablation of LGR5⁺ CSCs resulted in primary tumour shrinkage (de Sousa e Melo et al., 2017a; Shimokawa et al., 2017), yet they did not affect formation of metastases (de Sousa e Melo et al., 2017a). Furthermore, when LGR5⁺ CSCs were deleted in established metastases, there was a significant reduction in metastatic burden (de Sousa e Melo et al., 2017a). Taken together, LGR5⁺ CSC ablation experiments suggested that LGR5⁺ CSCs play distinct roles at different stages of CRC progression, being dispensable for tumour and metastatic outgrowth but indispensable in the metastatic seeding.

Insights into the stem cell plasticity during CRC progression revealed that the tumour invasive front and circulating tumour (CTCs) cells are LGR5⁻, reinforcing the theory that LGR5⁺ CSCs are not involved in the metastatic seeding (Fumagalli et al., 2020a). Further research to define the metastasis initiating cell (MIC) have identified *L1CAM* and *EMP1* expression in the invasive tumour front (Canellas-Socias et al., 2022; Ganesh et al., 2020) (Figure 13). These invasive cells are associated for regenerative programs observed during colitis (Ganesh et al., 2020) and highly enriched for genes associated with poor prognosis (Canellas-Socias et al., 2022), respectively.

Furthermore, analysis of micro- and macro-metastatic lesions have shown that EMP1⁺ cells are indeed enriched in the micro-metastatic setting, while still remaining negative for LGR5 (Figure 13). Nevertheless, restoration of the LGR5⁺ CSC pool was crucial for the progression into macro-metastasis (Canellas-Socias et al., 2022; Fumagalli et al., 2020a; Heinz et al., 2022) (Figure 13). Single-cell analysis of matched primary tumours identified the transcription factor PROX1 as a key regulator of stem cell plasticity during metastasis (Moorman et al., 2023). These metastases were characterised by an enrichment of squamous and neuroendocrine transcriptional programs, preceded by an enrichment of the foetal ISC program, ultimately resulting in poor patient outcomes. In humans, micro-metastases can remain dormant for years before eventually progressing to macro-metastases. YAP signalling plays a pivotal role in the early stages of the metastatic process. However, its downregulation is necessary for the subsequent progression to macro-metastases, as it facilitates further dedifferentiation into the LGR5⁺ state (Heinz et al., 2022). While it has been established that YAP signalling activates the foetal ISC gene program, the exact role of this program in metastatic seeding remains unclear. Moreover, the stringent regulation of YAP signalling might explain why models exhibiting constitutive YAP overexpression have shown that increased YAP activity can actually suppress CRC progression and metastasis (Cheung et al., 2020). Taken together, these findings underscore the intricate complexity of the metastatic process and reinforce the idea that cellular plasticity, rather than genetic alterations, is the primary driver of CRC progression.

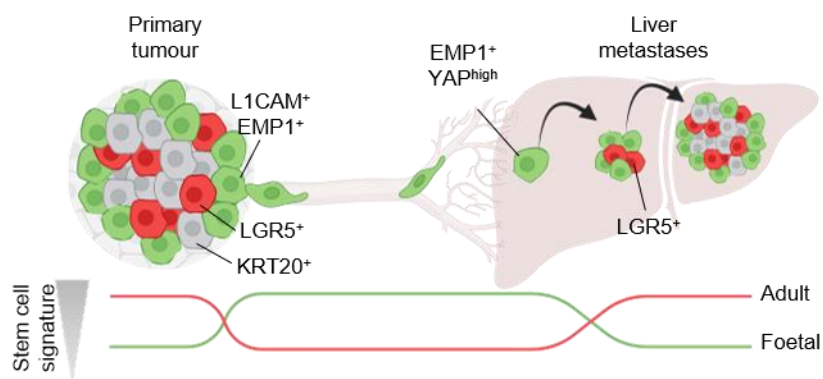


Figure 13. CSC dynamics during CRC progression. CRC cells that leave the primary tumour are reprogrammed into a regenerative/foetal ISC program and are characterised by L1CAM and EMP expression (green cells). These cells enter circulation and seed to distant organs such as the liver (metastasis). In order to progress into a macro-metastasis, LGR5⁺ CSCs (red cells) need to reappear.

CSCs and therapy response

Therapeutic approaches for treating CRC include surgical resection, chemotherapy, targeted therapy and immunotherapy (Dekker et al., 2019; Sanchez-Gundin et al., 2018). CSCs are believed to significantly drive treatment failure (Loh and Ma, 2024). Sequencing analyses have revealed that drug persister cells downregulate adult ISC programs during

chemotherapy treatment. These drug persister cells adopt a transient state that resembles the foetal ISC program ([Alvarez-Varela et al., 2022](#); [Vasquez et al., 2022](#)). These cells can also be identified by their expression of the RNA-binding protein MEX3A ([Alvarez-Varela et al., 2022](#)).

Furthermore, a cancer cell population marked by LGR5 and p27 was shown to be resistant to chemotherapy and drive tumour relapse through deactivation of YAP signalling ([Ohta et al., 2022](#)). Another study has suggested that the induction of the foetal ISC program was attributed to *TP53* status in CRCs. *TP53*-proficient tumour acquired foetal traits upon DNA damage caused by chemotherapeutic treatment, predicting a poor patient prognosis ([Sole et al., 2022](#)).

Analysis of the FOxTROT cohort, consisting of matched CRC tumour samples before and after chemotherapy selective pressure also revealed a switch towards a foetal ISC program. Indeed, tumours with higher capacity to adapt to selective pressures by switching stem cell programs showed the poorest therapy response ([Vasquez et al., 2022](#)).

Taken together, foetal ISC signatures are a recurring theme across all the aforementioned studies, suggesting a possible but yet undefined role of this program in therapy response. Therefore, efforts to selectively target CRC cells enriched with foetal ISC programs may represent a promising therapeutic strategy.

Targeting foetal-like CSCs

Therapy regimens that suppress foetal programs have not been yet described in the literature. Thus, targeting therapy against specific foetal stem cell markers seems to be the best therapeutic approach. When assessing specific markers of the foetal-stem cell signature they mostly either have no human homologue (*Ly6a*) or show very broad expression in the immune cell (*Spp1*) and stromal cell (*Cnx43*, *Aqp5*, *Krt7*) compartments ([Mustata et al., 2013](#)).

TROP2 is a transmembrane glycoprotein initially identified in mouse trophoblasts that is also part of the foetal ISC signature ([Cubas et al., 2009](#); [Lipinski et al., 1981](#); [Mustata et al., 2013](#)). TROP2 functions as a calcium signalling transducer, capable of signalling through multiple pathways. TROP2 expression is restricted to a small set of adult epithelial tissues such as skin and lung, with no expression in the healthy intestine. However, TROP2 has been widely found to be expressed in multiple epithelial carcinomas such as triple negative breast cancer, urothelial carcinomas, lung cancer and CRC ([Shvartsur and Bonavida, 2015](#)). Although the role of TROP2 is only sparsely understood, TROP2 expression has been

associated with poor patient prognosis. Overall, TROP2 represents an attractive target for therapeutic interventions.

Interestingly, the Food and Drug Administration (FDA) and European Medicines Agency (EMA) recently approved Sacituzumab Govitecan (SG), an antibody-drug conjugate (ADC) against TROP2 for the treatment of breast and urothelial cancers. SG contains a humanised TROP2 antibody (hRS7) linked to the cytotoxic agent SN38, the active metabolite of irinotecan. Upon the hydrolysis of the payload, SN38 induces cell death through inhibition of topoisomerase 1, preventing DNA repair ([Kopp et al., 2023](#)) (**Figure 14**). SG has shown significant clinical success in trials for unresectable locally advanced or metastatic triple-negative breast tumours in patients who have undergone two or more prior systemic therapies (ASCENT; ClinicalTrials.gov: NCT02574455) ([Bardia et al., 2021](#)). Additionally, the TROPiCS-02 study in patients with locally advanced or metastatic hormone receptor-positive, HER2-negative breast cancer demonstrated clinically meaningful benefits of SG treatment over chemotherapy (ClinicalTrials.gov: NCT03901339) ([Rugo et al., 2023](#)). Furthermore, in patients with locally advanced or metastatic urothelial cancer who had previously received platinum-based chemotherapy and either PD-1 or PD-L1 inhibitors, SG treatment extended overall survival (TROPY-U-01; ClinicalTrials.gov: NCT03547973) ([Tagawa et al., 2021](#)). Taken together, SG might be a valuable drug to target foetal ISC in CRC and therefore, its effect in CRC should be evaluated.

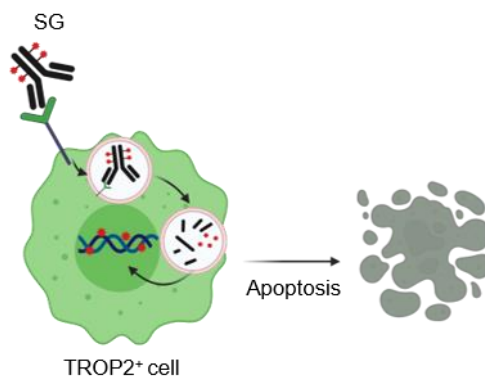


Figure 14. SG mode of action. SG will bind to TROP2 and will be internalised. Upon hydrolysis of the linker, SN38 is released and induces cell death through inhibition of topoisomerase 1, preventing DNA repair.

AIMS OF THE THESIS

The aim of this thesis is to study ITH in CRC. ITH can be divided into two dimensions. One dimension of ITH is the clonal dynamics and evolution during CRC progression. The other dimension is given by the stem cell hierarchy, which indicates diverse differentiation states of cancer cells within the tumour mass and thus, different proliferative properties, metastatic capacity and response to therapy. In this thesis I focused on the following objectives.

Chapter I: Clonal dynamics

- To establish a tool to study clonal dynamics with spatial and multiplex resolution.
- To study clonal dynamics during CRC progression.

Chapter II: Stem cell hierarchy

1. To establish versatile genetic tools to visualise, trace and ablate specific cell populations *in vitro* and *in vivo*.
2. To assess the stem cell capacity of *Lgr5*⁺ cells in *Lgr5*^{ow} tumours.
3. To identify the CSCs of *Lgr5*^{ow} tumours.
4. To study the emergence of foetal ISC programs in CRC.
5. To define a marker for the foetal ISC programs in CRC.
6. To generate a GEMM to trace foetal-like CSCs.
7. To identify the metastasis-initiating cell.
8. To study stem cell dynamics and the contribution of different stem cell populations to CRC therapy resistance.
9. To define new therapeutic approaches to target foetal-like CSCs

RESULTS

Chapter I: Understanding clonal dynamics during CRC progression

Some of the results of this chapter have been published in the journal *Cancers*. The results and figures have been adapted accordingly.

Vaquero-Siguero N*, Schleussner N*, Volk J, Mastel M, Meier J, Jackstadt R. Modeling Colorectal Cancer Progression Reveals Niche-Dependent Clonal Selection. *Cancers* (Basel). 2022;14(17):4260. Published 2022 Aug 31. doi:10.3390/cancers14174260.

**These authors contributed equally to this work.*

Organoid systems as a tool to study CRC intra-tumour heterogeneity

CRC is a highly heterogeneous disease and increasing evidences suggest that tumour heterogeneity plays a significant role in cancer progression and resistance to therapy (Hu et al., 2019; Hu et al., 2020; Reiter et al., 2020). Since the establishment of the 3D organoid cultures, tumour-derived organoids have been used as a powerful tool for dissecting the ITH in CRC. These organoids retain the genetic and phenotypic characteristics of the original tumour, making them an excellent model for investigating the complex cellular composition within tumours (Drost and Clevers, 2018).

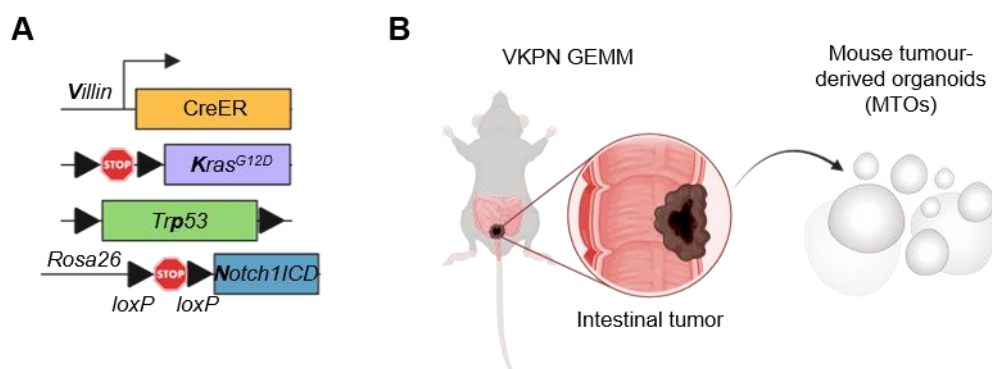


Figure 15. VKPN mouse tumour-derived organoids. A. Genetic crossing strategy for the generation of the VKPN GEMM. B. Schematic representation of the workflow for the generation of MTOs. Intestinal tumours formed in VKPN GEMMs are digested and plated in BME for establishment of MTOs. MTOs, mouse tumour-derived organoids.

Here, I set out to study CRC ITH attending to the tumour dynamics and clonal evolution in different ecosystems. Thus, I made use of a mouse tumour-derived organoid (MTO) line generated from a small intestine tumour. This tumour was originated from the *villin1*^{CreERT2}; *Kras*^{G12D/+}; *Trp53*^{fl/fl}; *Rosa26*^{Notch1ICD/+} (KPN) triple mutant GEMM (Figure 15A-B), which

generates spontaneous metastases with high stromal infiltration and transcriptional profiles associated with CMS4 (Jackstadt et al., 2019).

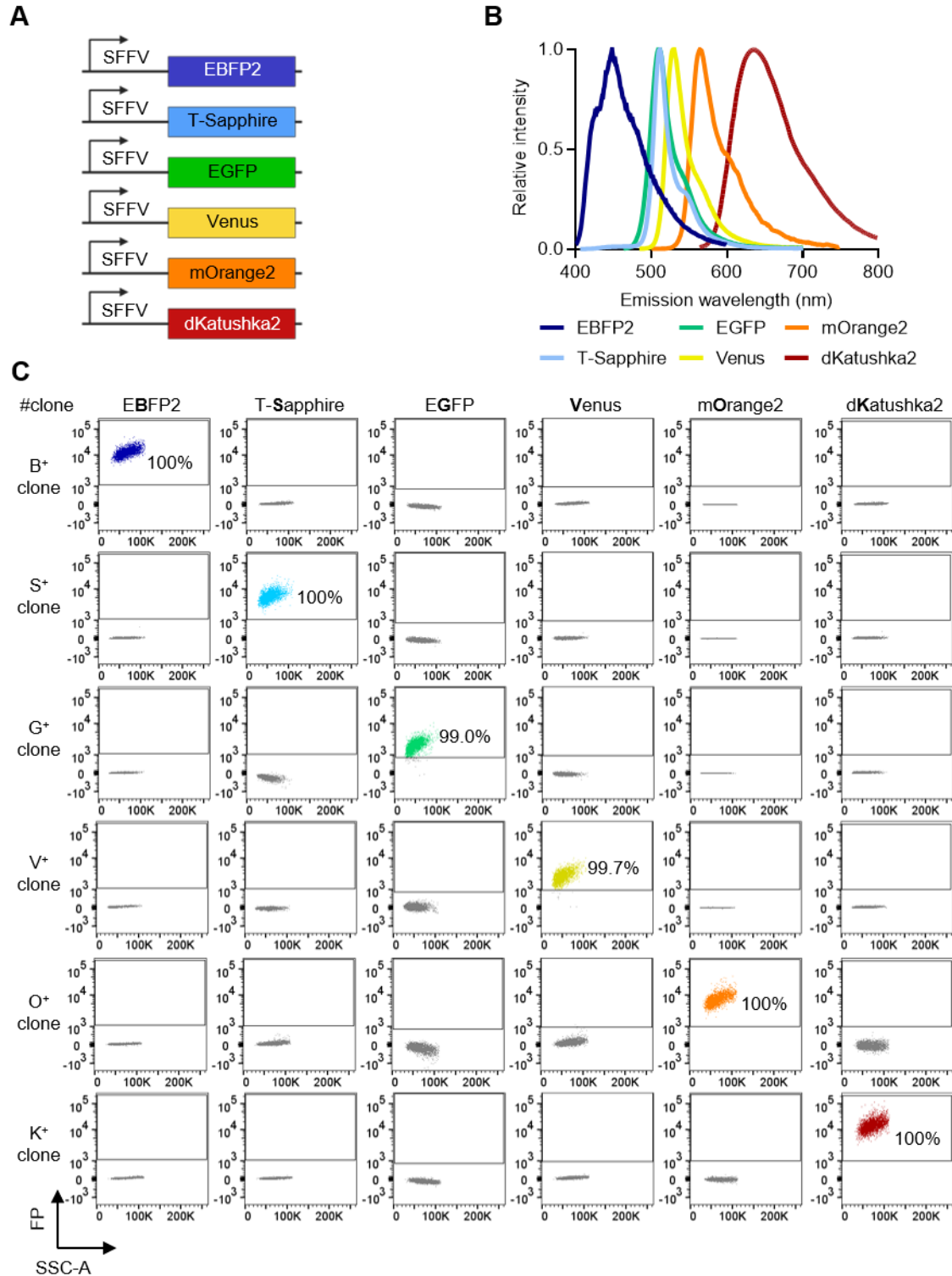


Figure 16. The principle of the multicolor LeGO optical barcoding system. **A.** Schematic overview of the 6 different LeGO vectors used for the clonal tracking. **B.** Graph depicting the emission spectra of the 6 LeGO vectors. **C.** Flow cytometry plots of the 6 different fluorescent proteins used. Every row corresponds to a clone labelled with one LeGO vector and it is specifically detected by flow cytometry. FP, fluorescent protein; B, EBFP2; S, T-Sapphire; G, EGFP; V, Venus; O, mOrange2; K, dKatushka2.

Multicolour LeGO optical barcoding system

To study ITH at the clonal resolution level, I made use of the lentiviral gene ontology (LeGO) optical barcoding system (Weber et al., 2008). This technique consists of the constitutive and stable expression of six different LeGO vectors (EBFP2, T-Sapphire, eGFP, Venus, mOrange, dKatushka2) (**Figure 16A**) whose excitation and emission wavelength allow for individual identification by flow cytometry and microscopy (**Figure 16B-C**). Importantly, contrary to traditional lineage tracing systems, this approach will allow me not only to identify metastatic and/or therapy resistance clones with spatial resolution, but also the further functional characterization of those clones. This is crucial, since the “carbon copy” I generated at the beginning of the experiments allows for a precise molecular distinction of clones and identification of changes towards metastasis or therapy resistance processes.

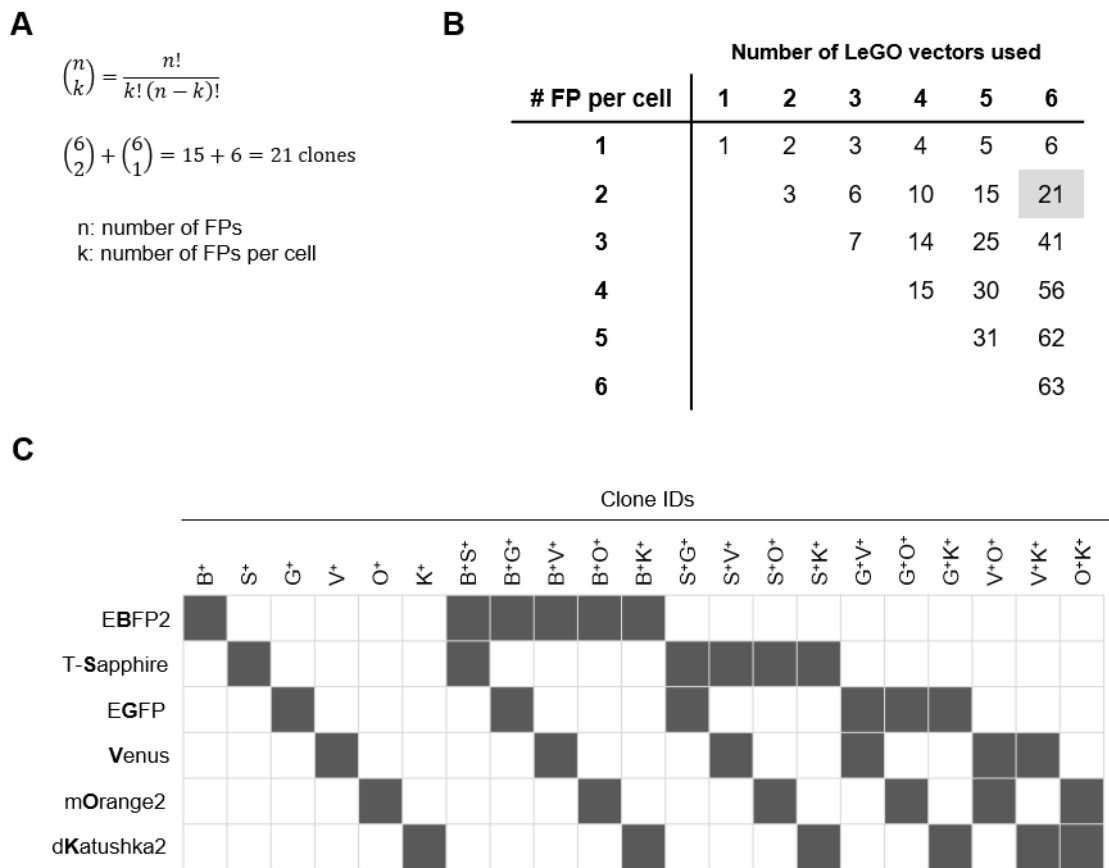


Figure 17. Generating 21 uniquely LeGO barcoded clones: the binomial coefficient formula. **A.** Example of the binomial coefficient formula to calculate the number of clones that can be uniquely labelled by using the six LeGO vectors and up to two different vectors per clone. FP, fluorescent protein. **B.** Matrix indicating the number of unique optical barcoded clones obtained by combining different numbers of LeGO vectors. Figure adapted from (Vaquero-Siguero et al., 2022). **C.** Binary readout of the 21 unique optically barcoded clones generated from the combination of one or two of the 6 LeGO vectors per cell. Grey squares indicate positivity for that fluorescent protein.

Additionally, depending on the number of the LeGO vectors used and the number of different vectors allowed per cell, the number of uniquely barcoded clones can be calculated

using the binomial coefficient formula (**Figure 17A-B**). Here, I used the 6 LeGO vectors and combined up to two different vectors per cell, which allows for the generation of 21 different clones (**Figure 17B-C**).

Generation of the 21 LeGO barcoded clones

To track the fate of single cancer cell clones during the CRC progression cascade, VKPN MTOs were transduced with the six different LeGO vectors separately (**Figure 18A**). After several rounds of passaging, cells with the integration of the fluorescent protein(s) were FACS-separated and allowed to grow into organoids. Those single cell-derived organoids were then isolated (clones) and expanded *in vitro*. A second round of lentiviral infection and FACS-sorting was performed to ultimately generate clones with 2 different LeGO fluorescent barcodes (**Figure 18A**). Importantly, stable expression of the fluorescent proteins was monitored over time for the different clones. Thus, I generated 21 different optically-barcoded clones from a VKPN MTO line that can be identified by flow cytometry and microscopy (**Figure 18A-C**). For example, the GK⁺ clone is labelled with EGFP and dKatushka2 fluorescent proteins, while being negative for EBFP, T-Sapphire, Venus and mOrange2 FPs (**Figure 18B-C**).

Deciphering the colour code at a single-cell level of a LeGO barcoded mixed population by flow cytometry.

As previously stated, each LeGO barcoded clone can be identified according to its unique colour code combination (**Figure 17C**). In order to quantify the frequency of the different barcoded clones in a mixed population by flow cytometry, a complex compensation setup and sophisticated gating strategy using the Boolean analysis method are necessary. The Boolean analysis approach allows the quantification of the different clones considering the deterministic relationship between all the clones (Mohme et al., 2017). To interrogate the sensitivity of this method, I mixed the 21 LeGO barcoded clones and performed flow cytometry analysis. First, I generated three consecutive gateings for cells, single-cells and live cells (**Figure 19A**). Subsequently, I calculated the frequency of every double-barcoded clone out of the “live cells” population by gating for the double-positive population in the flow cytometry plot for those two specific fluorescent proteins (i.e. to calculate the frequency of the BS⁺ clone out of the mixed population, I used the flow cytometry plot showing EBFP2 vs. T-Sapphire signal and draw the gate for the double-positive (EBFP2⁺ and T-Sapphire⁺) population) (**Figure 19B**). Finally, I calculated the frequency of the single-barcoded clones by removing the frequency of the double-barcoded clones containing that fluorescent protein from its total frequency (i.e. to calculate the frequency of the B⁺ clone out of the mixed population, I calculated the total frequency of EBFP2⁺ cells and subtracted the frequency of the BS⁺, BG⁺, BV⁺, BO⁺ and BK⁺

clones) (**Figure 19C**). In sum, this barcoding system allows for a sensitive and accurate identification and quantification of all the different clones present in a heterogeneous population, thus enabling the study of the clonal dynamics during tumour progression.

***In vitro* characterization of the LeGO barcoded VKPN clones**

Prior to conducting *in vivo* clonal tracking, I examined the clonal dynamics of the LeGO barcoded clones *in vitro*. Initially, the proliferation and organoid-initiation capacity of the 21 uniquely barcoded clones was assessed. To that end, each clone was individually seeded at a density of 1.000 cells per well and incubated for six days. Organoid-initiation capacity was determined based on the number of organoids formed six days after seeding. The proliferation capacity was inferred by the mean organoid size. Thus, a higher number of organoids indicated a higher organoid-initiation capacity while larger organoids suggested faster proliferation rates.

Despite originating from the same VKPN MTO line, variations in both organoid formation capacity and organoid size were observed among the different clones (**Figure 20A-C**). Furthermore, there was no apparent positive correlation between the number and area of the organoids, suggesting their independence as properties. For instance, the OK⁺ VKPN clone presented one of the smallest organoids but higher number of them. Furthermore, while the B⁺, BV⁺, SV⁺, SO⁺ OK⁺ and SK⁺ VKPN clones exhibited the highest organoid initiation capacity *in vitro*, the V⁺, BG⁺ and GO⁺ clones displayed the largest mean organoid size (**Figure 20A-B**).

Next, I set out to investigate whether clonal competition already occurred *in vitro*. To that end, I mixed the 21 LeGO barcoded VKPN clones at equal proportions and seeded them *in vitro*. The mixed population was then propagated for 14 weeks in culture and samples were taken every week to quantify the clonal dynamics over time by flow cytometry (**Figure 21A**). Strikingly, already at week 5, the V⁺ and BG⁺ clones were highly represented in the mixed population. At weeks eight and nine, these two clones constituted the majority of the culture dish. Interestingly, neither of these dominant clones were overrepresented at the start of the experiment, indicating the presence of clonal selection under *in vitro* culture conditions. At week ten, the V⁺ clone outcompeted the BG⁺ clone, being the only clone detected from week eleven onwards (**Figure 21B**). These results go in line with the prior observation that the V⁺ and BG⁺ clones were one of the clones showing larger organoids after six days in culture when seeded as single cells, indicating that these clones were more proliferative than the other clones. This intrinsic property might explain why they were highly predominant already at week five. Nevertheless, why the V⁺ overtook the BG⁺ clone needs to be elucidated as they both showed similar proliferative rates (**Figure 20B**).

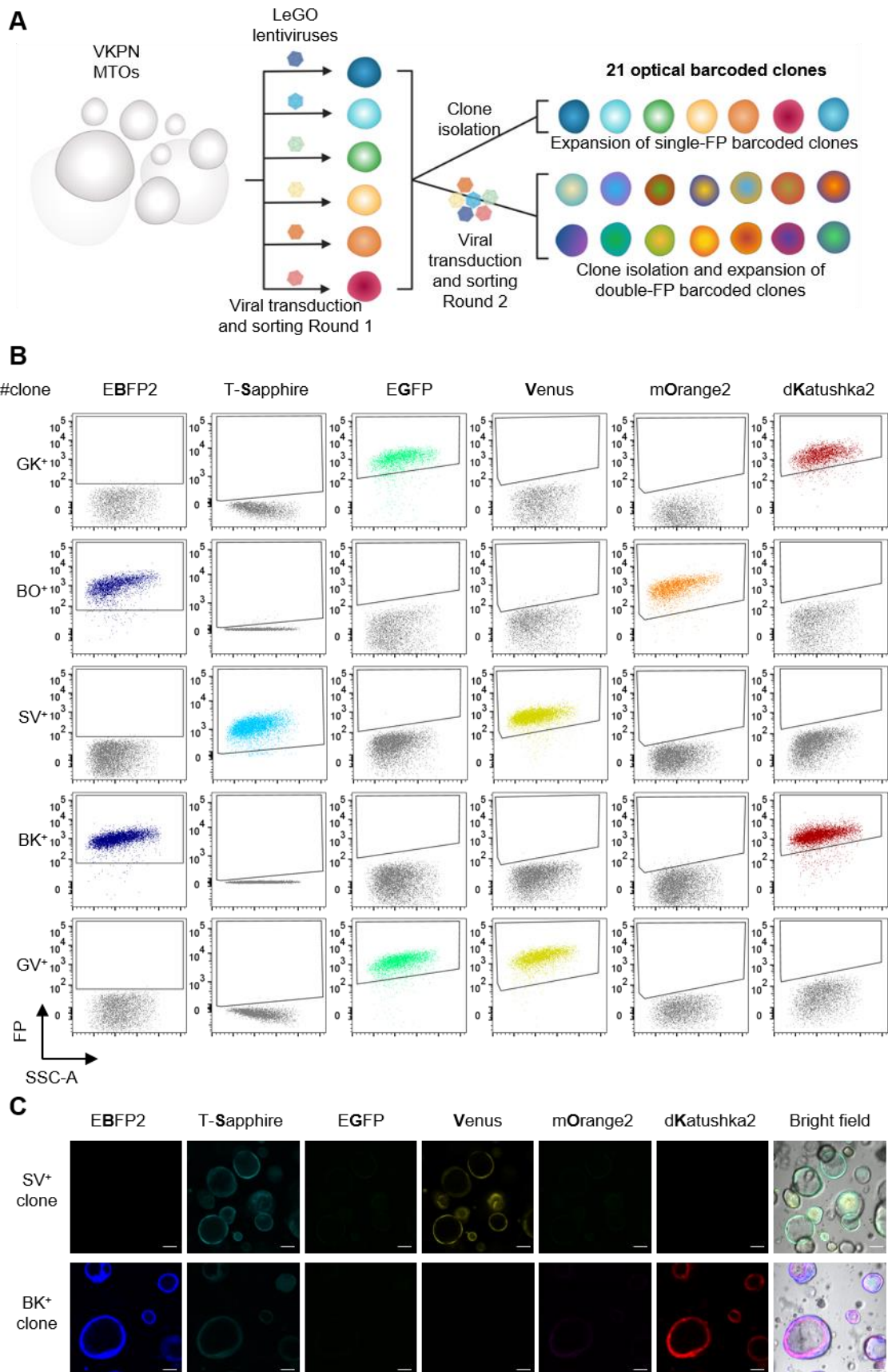


Figure 18. Generation of 21 LeGO optically barcoded VKPN clones. **A.** Workflow to generate the unique LeGO optically barcoded VKPN clones. **B-C.** Example of the identification of the double barcoded clones by **(B)** flow

cytometry and **(C)** microscopy. Every row corresponds to a clone labelled with two different LeGO vectors. B, EBFP2; S, T-Sapphire; G, EGFP, V, Venus; O, mOrange2; K, dKatushka2. Scale bar 100 μ m.

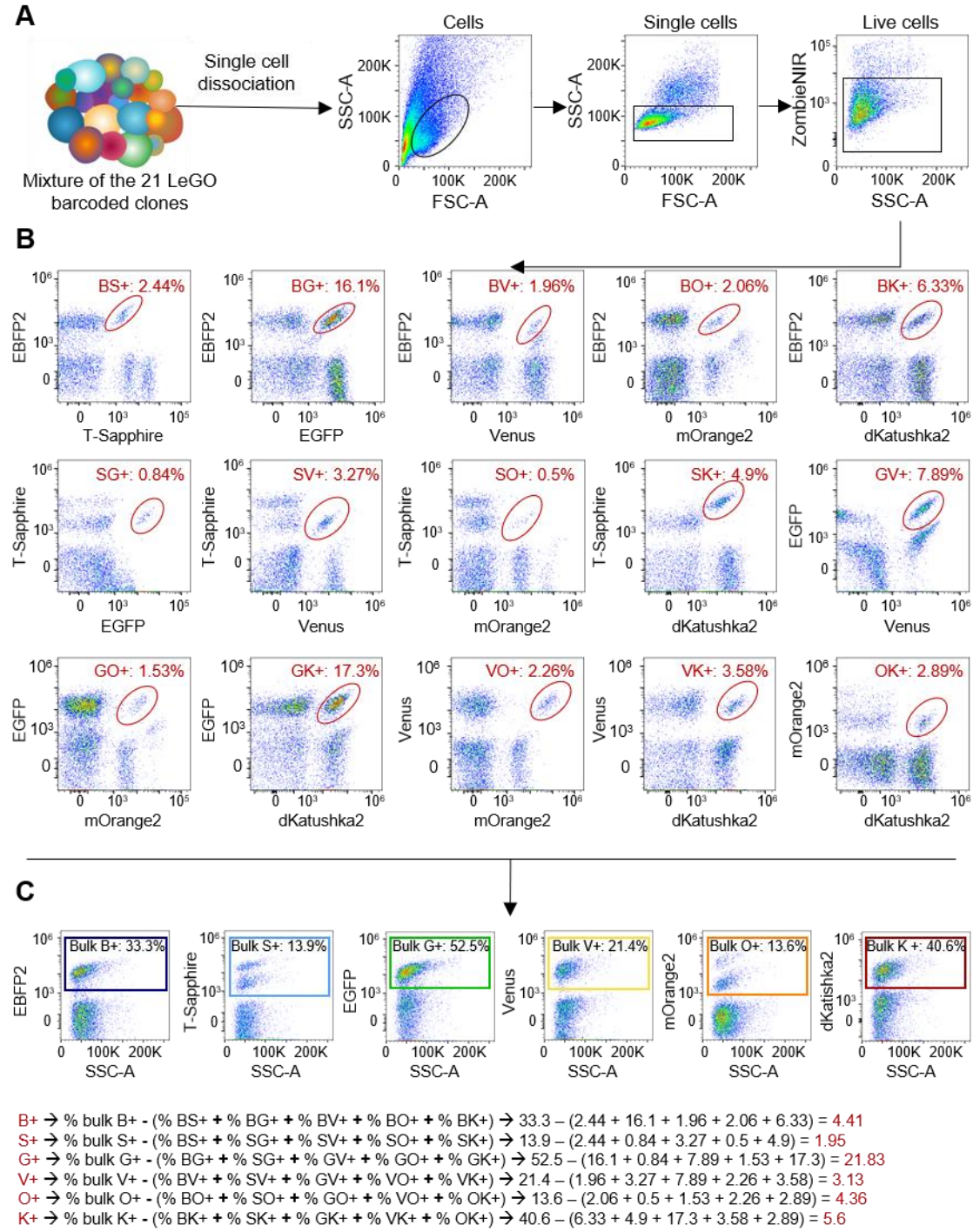


Figure 19. Gating strategy and Boolean analysis for quantification of the 21 different LeGO barcoded VKPN clones in a mixed population. A. Workflow for single-cell dissociation and consecutive gating strategy for live single-cells for posterior quantification. **B.** Flow cytometry plots for the quantification of the double-barcoded cells. **C.** Boolean analysis to infer the frequency of the six clones barcoded with only one fluorescent protein.

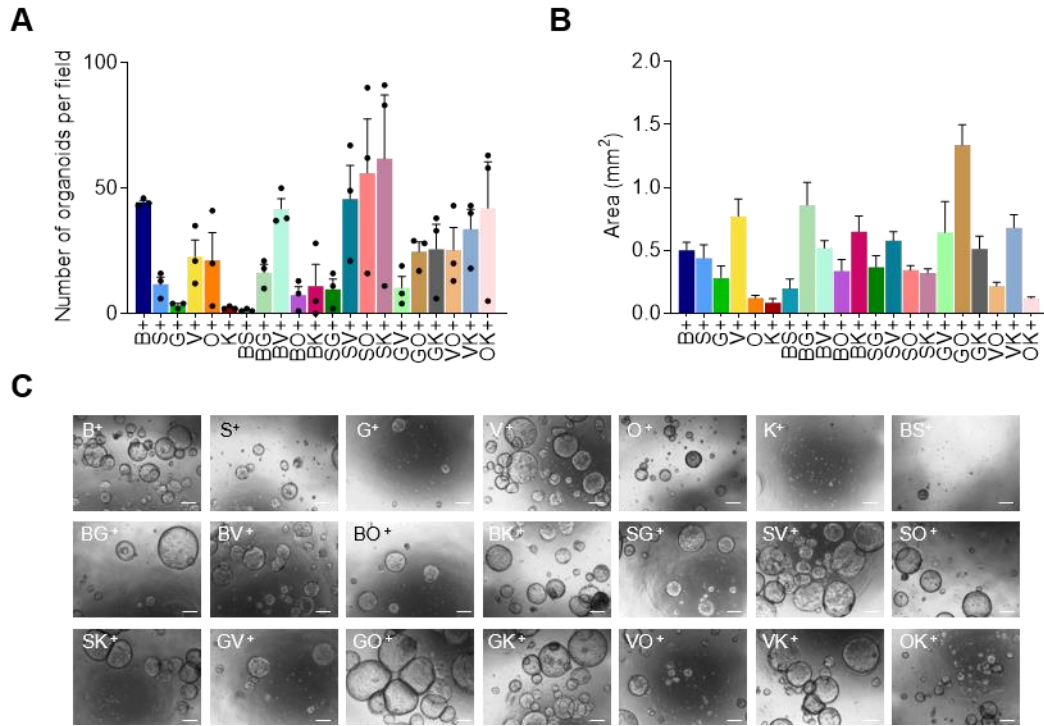


Figure 20. Characterization of the 21 LeGO optically barcoded VKPN clones. A-B. Bar graph representing (A) the number of organoids formed and (B) the mean size of the organoids formed from the 21 different LeGO barcoded VKPN clones. C. Representative images of the 21 LeGO barcoded clones. n=3 wells per clone. Scale bar 100 μ m.

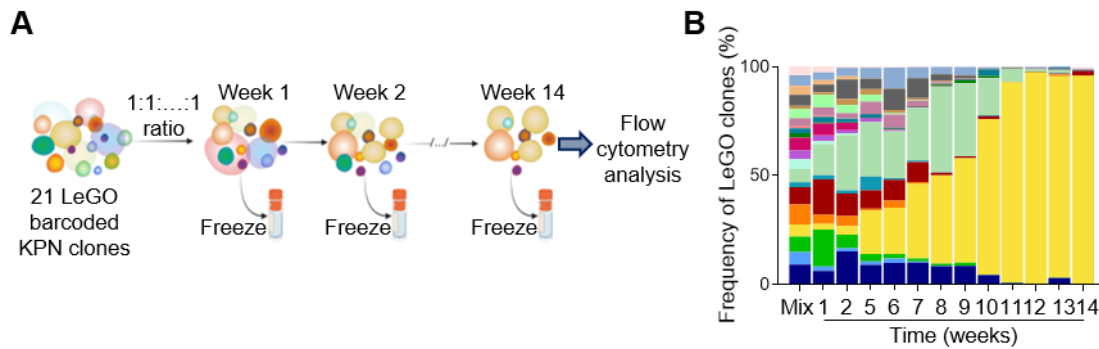


Figure 21. *In vitro* clonal competition of the 21 LeGO optically barcoded VKPN clones. A. Experimental workflow of the *in vitro* competition assay. B. Quantification of the clonal composition of the cell mix at different timepoints. First column shows the clonal composition of the mix at the time of seeding.

The LeGO system reveals niche-dependent clonal selection

To study clonal dynamics *in vivo*, I first assess the engraftment potential of the VKPN MTO line in immune-competent C57BL/6J mice. Therefore, I transplanted the VKPN parental line in different routes: subcutaneous, intracolonic and intrasplenic. The totality of the subcutaneously transplanted mice developed subcutaneous tumours (**Figure 22A**). Next, I transplanted the VKPN MTO parental line in the colonic mucosa (intracolonic injection) which better recapitulates tumour engraftment in their natural microenvironment and anatomical location. Four out of six mice developed a colonic tumour (**Figure 22B-C**). Lastly, to model

liver metastasis, I injected the VKPN parental line in the spleen. All six mice developed a significant number of macro-metastases four weeks after injection (**Figure 22D**).

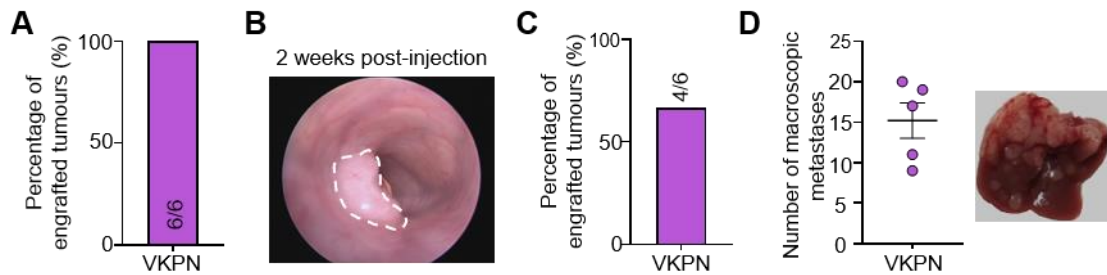


Figure 22. Engraftment capacity of the VKPN MTO model. **A.** Percentage of mice that developed subcutaneous tumours derived from the VKPN MTO parental line. **B.** Representative colonoscopy image. White dashed line indicates the tumour. **C.** Percentage of engrafted intracolonic tumours derived from the VKPN parental MTO line. **D.** Left, number of macroscopic metastases observed after 4 weeks of intrasplenic transplantation of the VKPN parental MTO line. Right, representative photo of a liver with VKPN-derived metastasis at endpoint.

Once I assessed the engraftment capacity of the VKPN MTO parental line I further investigated the clonal selection *in vivo*. To that end, I mixed the 21 LeGO barcoded VKPN clones at equal proportions and transplanted them subcutaneously in C57BL/6J mice (**Figure 23A**). Five out of the six transplanted mice developed a tumour over time (**Figure 23B**). At the endpoint, in four out of the five tumours the O⁺ clone dominated the majority of the tumour (**Figure 23C**). Interestingly, this “winning” clone was different to the one observed *in vitro*. Moreover, the one tumour showing a prevalence of a different clone, the K⁺ clone, presented the smallest tumour size and slowest proliferating rate among the subcutaneous tumours (**Figure 23B-C**).

Next, to understand the clonal selection in the native microenvironment, I mixed the 21 LeGO barcoded VKPN clones at equal proportions and transplanted them intracolonic in C57BL/6J mice. Unfortunately, none of the twelve mice (out of two independent experiments) developed any tumour in the colon (data not shown). Since the VKPN MTO parental line showed 66,6% engraftment in the colonic mucosa (**Figure 22C**), I hypothesised that the immunogenicity of the fluorescent proteins might have interfered with tumour engraftment.

Lastly, I set out to study the clonal selection during liver metastasis. For this purpose, I mixed the 21 LeGO barcoded VKPN clones at equal proportions and transplanted them into the spleen of C57BL/6J mice (**Figure 23D**). Contrary to the outcomes observed in the *in vitro* and subcutaneous *in vivo* competition assays, the B⁺ clone was the most prevalent clone observed in the liver (**Figure 23E**). Nevertheless, in this case, despite being the B⁺ clone the dominating one, a polyclonal liver metastases pattern was evident in all the mice.

Collectively, the data suggests that clonal selection is strongly influenced by the tumour microenvironment, as I assume that the TME is different in each site. The colonic mucosa

showed the most stringent clonal selection compared to the subcutaneous and liver environment. Additionally, my data indicates that this clonal selection might be also driven by the expression of the fluorescent markers, which might serve as neoantigens. Thus, further experiments in immunocompromised mice will be instrumental to interrogate the role of the immune system in this stringent clonal selection. Additionally, future multi-omic analyses are needed to define the clone-intrinsic and clone-extrinsic differences that make the V⁺, O⁺ and B⁺ clones outcompete the rest *in vitro*, subcutaneously or in the liver, respectively.

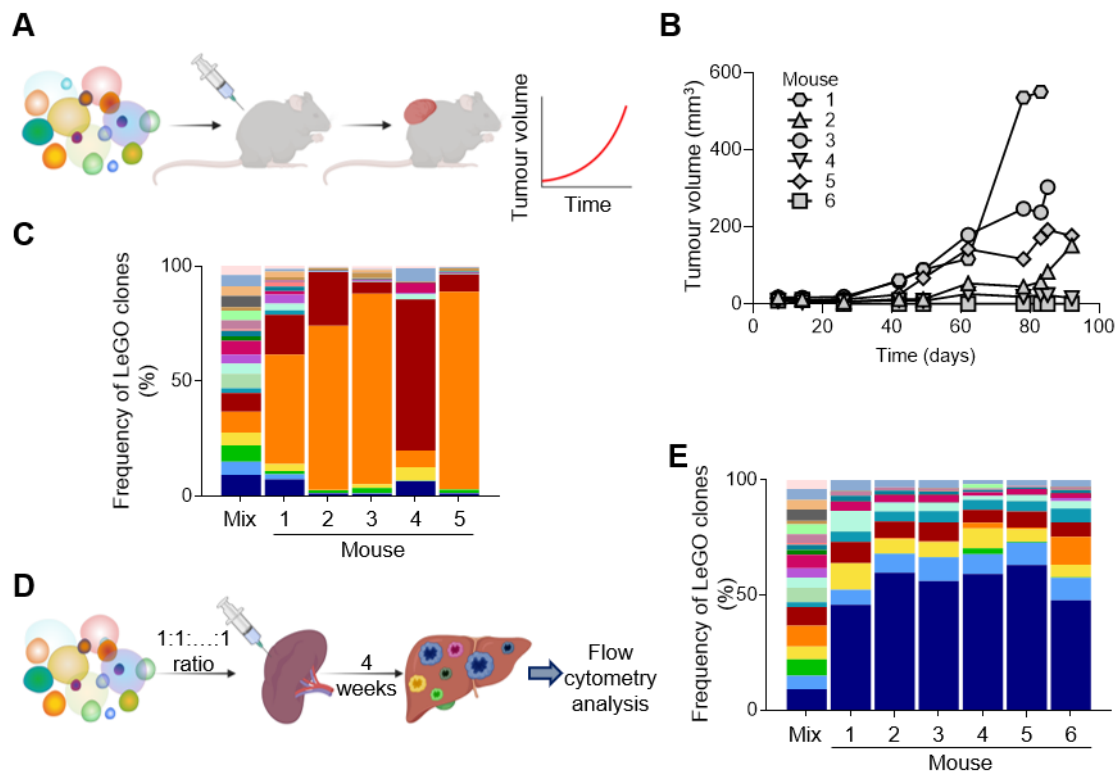


Figure 23. Clonal analysis *in vivo* revealed niche dependencies. **A.** Workflow for the study of clonal selection in subcutaneous tumours. **B.** Tumour growth of the individual subcutaneous tumours over time. **C.** Frequency of LeGO barcoded clones analysed by flow cytometry at endpoint of the subcutaneous tumours. No tumour material was recovered from mouse 6. **D.** Workflow for the study of clonal selection in liver metastases. **E.** Frequency of the LeGO barcoded clones analysed by flow cytometry at the endpoint from the liver metastases.

Chapter II: Defining the role of foetal-like cancer cells in CRC progression

Characterization of LGR5⁺ cells in *Apc* wild-type (*Apc*^{wt}) CRC

Apc mutant (*Apc*^{mut}) tumours have higher *Lgr5*-expression levels than *Apc*^{wt} tumours

LGR5 has been broadly recognized as “the CSC marker” in CRC (Cortina et al., 2017a; de Sousa e Melo et al., 2017a; Shimokawa et al., 2017). Interestingly, a significant percentage of CRCs present none or few LGR5⁺ cells (Morral et al., 2020), suggesting that CSCs are either not merely defined by *LGR5* expression or that *LGR5* expression only defines one particular subset of CSCs (Barker et al., 2009; Cortina et al., 2017a; de Sousa e Melo et al., 2017a; Shimokawa et al., 2017).

Overall, the studies performed to define LGR5⁺ cells as CSCs were based on models that recapitulate the classical route of CRC progression (*APC*^{mut} models) (Cortina et al., 2017a; de Sousa e Melo et al., 2017a; Fumagalli et al., 2020a; Shimokawa et al., 2017). These models are characterised by aberrant activation of WNT signalling, and thus, enhanced *Lgr5*-expression levels (Merlos-Suarez et al., 2011; Munoz et al., 2012; Shimokawa et al., 2017). In contrast, serrated tumours, lack *APC* alterations, having lower WNT-pathway activity (Figure 24A-B) (Borowsky et al., 2018; Jackstadt et al., 2019). Based on the importance of CSCs in tumour progression and metastasis and given the significant downregulation of the adult ISC signature in serrated (*APC*^{wt}) tumours, I aimed to define the role of LGR5⁺ cancer cells in LGR5^{low} tumours.

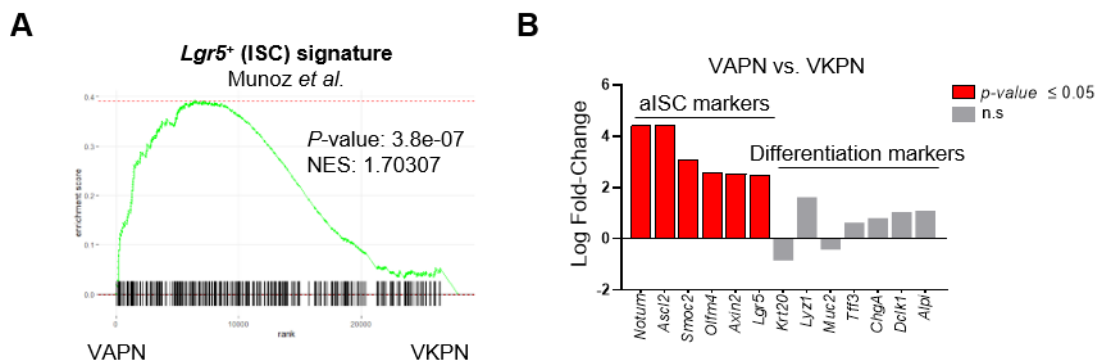


Figure 24. *Apc*^{mut} tumours are enriched for the adult ISC program. **A.** GSEA comparing the adult ISC signature in *Apc*^{mut} (*Villin*^{CreER}, *Apc*^{fl/fl}, *Trp53*^{fl/fl}, *Rosa26*^{NICD/+}, (VAPN)) versus *Apc*^{wt} (*Villin*^{CreER}, *Kras*^{G12D/+}, *Trp53*^{fl/fl}, *Rosa26*^{NICD/+} (VKPN)) tumours derived from GEMMs (Jackstadt et al., 2019). **B.** Relative expression levels of genes from the adult ISC and differentiation programs from bulk RNA sequencing data from intestinal tumours derived from APN and KPN GEMMs (Jackstadt et al., 2019). aISC, adult intestinal stem cell.

In order to validate the hypothesis, I first set out to investigate whether LGR5⁺ cells are also the CSCs in the serrated CRC subtype. For this purpose, I made use of CRC MTOs derived from GEMMs which recapitulate the classical (*Villin*^{CreER}, *Apc*^{fl/fl}, *Kras*^{G12D/+}, *Trp53*^{fl/fl}, *Smad4*^{fl/fl} (VAKPS)) or serrated (*Villin*^{CreER}, *Kras*^{G12D/+}, *Trp53*^{fl/fl}, *Rosa26*^{N1CD/+} (VKPN)) CRC subtypes (**Figure 25A**). In line with the literature, the *Apc*^{mut} (VAKPS) model presents higher *Lgr5*-expression level compared to the *Apc*^{wt} (VKPN) model (**Figure 25B**).

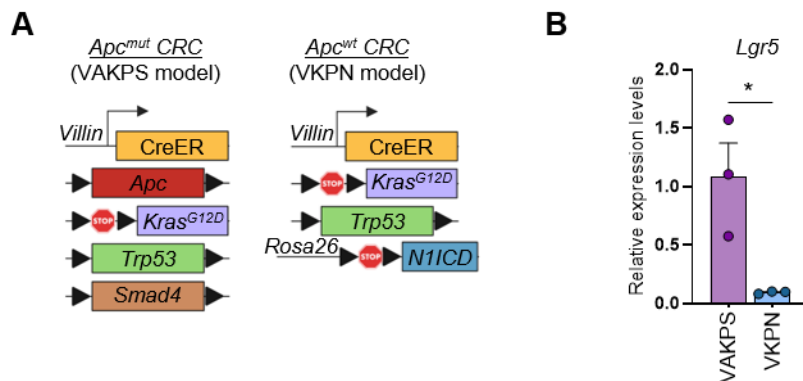


Figure 25. VAKPS MTOs have elevated *Lgr5*-expression levels compared to VKPN MTOs. **A.** Scheme of the genetic crossing strategies for the GEMMs used. MTOs from these GEMMs were generated by Dr. Rene Jackstadt. **B.** Relative expression levels of *Lgr5* in VAKPS and VKPN MTOs. Statistical analysis was performed using unpaired t-test.

Generation of *Lgr5*-iCaspase9-tdTomato knock-in MTOs.

Due to the lack of commercially available antibodies detecting LGR5, I needed to genetically modify the MTOs in order to visualize LGR5⁺ cells. Therefore, I knocked-in the tdTomato fluorescent reporter after the STOP codon of the *Lgr5* gene as previously reported (Shimokawa et al., 2017). In addition, to selectively ablate *Lgr5*-expressing cells, I introduced an inducible suicide gene (*inducible Caspase9* (*iCaspase9*)) (Shimokawa et al., 2017). Furthermore, a Ruby/Puromycin resistant (PuroR) cassette flanked by loxP sites was also inserted in the *Lgr5* locus, enabling the selection of the successfully modified cells (Shimokawa et al., 2017) (**Figure 26A**). To that end, I generated two vectors: (1) the targeting vector containing the sgRNA and the Cas9 protein sequence that will target the double strand break in the correct genomic locus and (2) the donor vector that carries the *iCaspase9*, *tdTomato* and *Ruby/PuroR* cassettes flanked by homology arms that will facilitate the homologous recombination after the DNA break in the locus of interest (**Figure 26A**).

I electroporated the VAKPS and VKPN MTOs with these plasmids and selected for positive clones with puromycin treatment four days after. Resistant clones were isolated and expanded *in vitro* for subsequent genotyping to verify the correct insertion (**Figure 26B-D**). Next, I electroporated the VAKPS^{*Lgr5*-IRES-*iCaspase9*-T2A-*tdTomato*-loxP-Ruby/PuroR-loxP} (VAKPS^{LiCT-Ruby/PuroR}) clone 1 and VKPN^{LiCT-Ruby/PuroR} clone 3 with a vector encoding for the Cre recombinase protein fused to a GFP fluorescent reporter with the aim of removing the Ruby/PuroR cassette. Two

days after electroporation I FACS separated the GFP⁺ cells and repeated the *in vitro* clonal isolation and expansion (**Figure 26B, E**). The successful removal of the Ruby/PuroR cassette was confirmed by PCR and re-sensitization to puromycin treatment (**Figure 26B, F**).

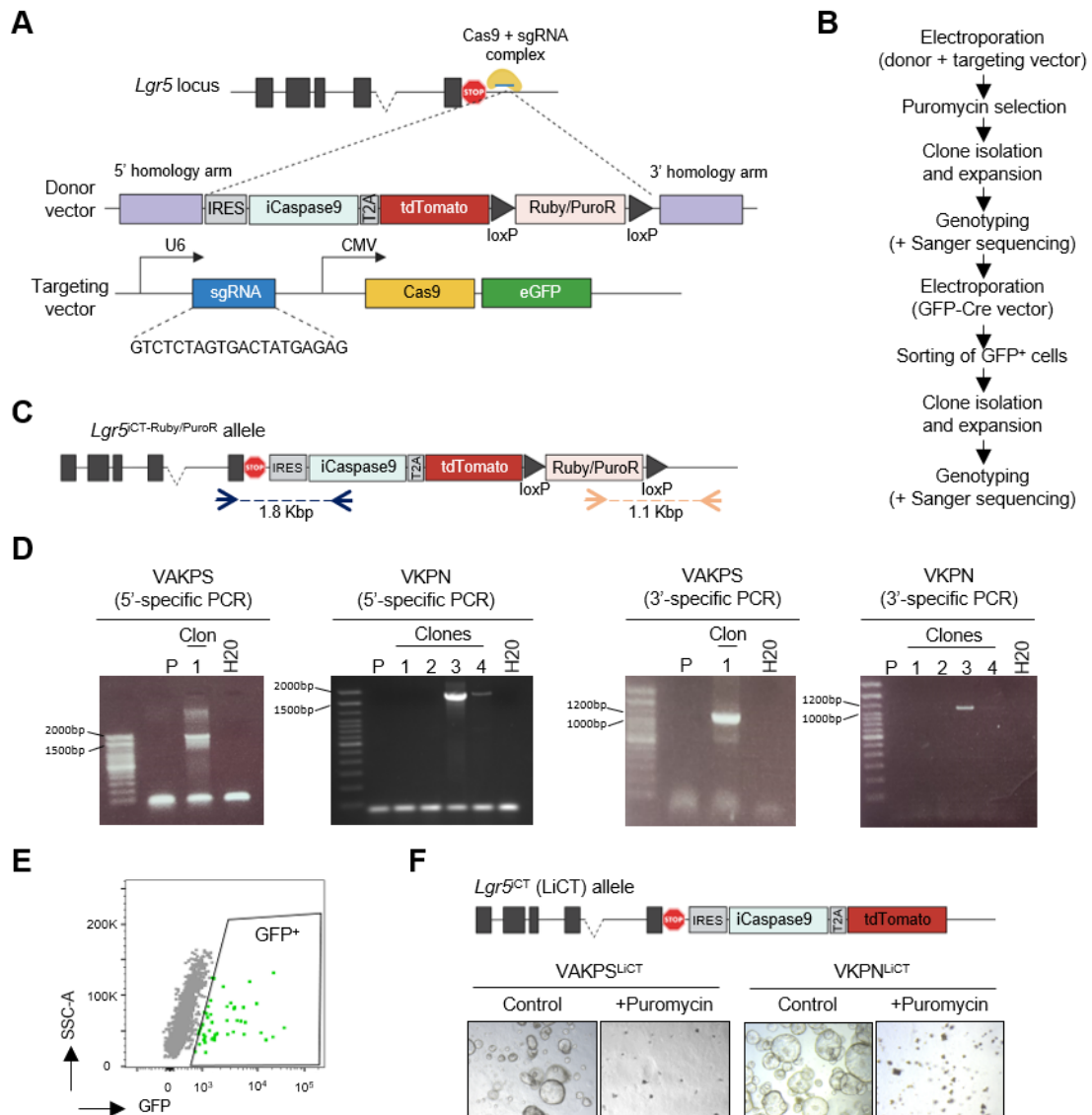


Figure 26. Generation of *Lgr5*-iCaspase9-tdTomato (LiCT) knock-in MTO lines. **A.** Scheme of the CRISPR/Cas9 strategy to knock-in the *iCaspase9-tdTomato* cassette in the *Lgr5* genomic locus. PuroR, Puromycin-resistant. **B.** Workflow for the generation of the MTO^{LiCT} lines. **C.** Scheme of the MTO^{LiCT}-Ruby/PuroR intermediate MTO line. The blue and orange arrows indicate the annealing site of the primers for the 5' and 3' specific PCR, respectively. The blue and orange dashed line indicate the PCR products for validating the specific integration of the donor sequence. **D.** PCR product of the 5' and 3' specific PCR for the generation of VAKPS^{LiCT}-Ruby/PuroR and VKPN^{LiCT}-Ruby/PuroR MTOs. **E.** FACS panel of the GFP⁺ VAKPS^{LiCT}-Ruby/PuroR MTO line three days after electroporation with the GFP-Cre vector to remove the *Ruby/PuroR* cassette. **F.** On top, scheme of the MTO^{LiCT} final allele. Below, representative images of VAKPS^{LiCT} and KPN^{LiCT} MTOs four days after puromycin treatment.

tdTomato labels LGR5⁺ cells

To validate whether tdTomato selectively labels LGR5⁺ cells in AKPS^{LiCT} and KPN^{LiCT} MTOs, I FACS separated tdTomato⁻ and tdTomato^{high} cell populations (**Figure 27A**). RT-qPCR analysis showed that tdTomato^{high}-sorted cells were enriched for *tdTomato* and *Lgr5* compared

to tdTomato⁻ sorted cells in both VAKPS^{LICT} and VKPN^{LICT} MTOs (**Figure 27B-C**). Altogether, this data indicates the successful generation of VKPN and VAKPS MTO lines with a *tdTomato* and *iCaspase9* cassettes knocked-in in the *Lgr5* genomic locus, allowing for the selective identification and ablation of *Lgr5*-expressing cells.

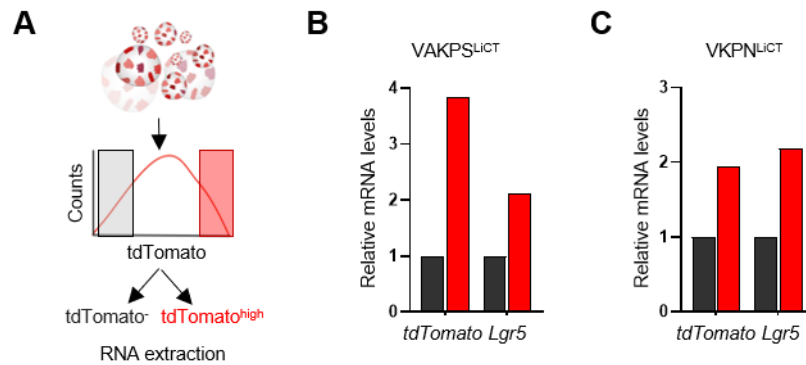


Figure 27. tdTomato signal identifies LGR5⁺ cells. **A.** Workflow scheme for FACS separation of tdTomato⁻ and tdTomato^{high} cell populations. **B-C.** RT-qPCR showing *tdTomato* and *Lgr5* mRNA expression levels of tdTomato⁻ and tdTomato^{high} sorted cell populations from **(B)** VAKPS^{LICT} and **(C)** VKPN^{LICT} MTOs.

Of note, VAKPS and VKPN genomic alterations differ not only in the *Apc* status but also in the *Smad4* status and Notch signaling level (**Figure 25A**). To rule out potential confounding variables such as *Smad4* depletion or *N1icd* overexpression, I additionally knocked-out *Apc* in VKPN^{LICT} MTOs (VAKPN^{LICT}) (**Figure 28A-B**). The *Apc*^{KO} in VKPN^{LICT} MTOs triggered the expression of ISC markers while reducing the expression of *Krt20* (differentiation marker for intestinal epithelial cells) (**Figure 28C**).

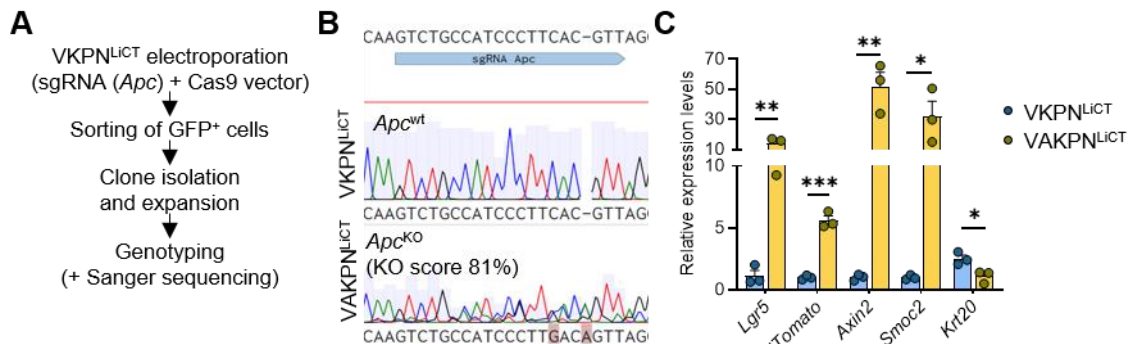


Figure 28. Generation of the VAKPN^{LICT} MTO line. **A.** Workflow scheme for the generation of the *Apc*^{KO} in the VKPN^{LICT} MTO line. **B.** Sanger sequence chromatogram confirming the *Apc*^{KO} in the VKPN^{LICT} MTO line. **C.** RT-qPCR of adult ISC markers (*Lgr5*, *Axin2*, *Smoc2*), *tdTomato* and *Krt20* (differentiation marker) from VKPN^{LICT} and VAKPN^{LICT} MTOs.

LGR5 solely marks CSCs in *Apc*^{mut} tumours *in vitro* and *in vivo*

Once I generated the CRISPR/Cas9-modified MTOs to identify LGR5⁺ cells, I first quantified the percentage of LGR5-TdTomato⁺ cells and protein levels in each MTO line. Notably, both *Apc*^{mut} lines (VAKPS^{LICT} and VAKPN^{LICT}) exhibited a higher number of LGR5-TdTomato⁺ cells as well as elevated levels of LGR5-TdTomato compared to the *Apc*^{wt}

(VKPN^{LICT}) MTO line (**Figure 29A-E**). This finding strongly suggests that *Apc* loss increases LGR5 level, corroborating previous observations (Dow et al., 2015).

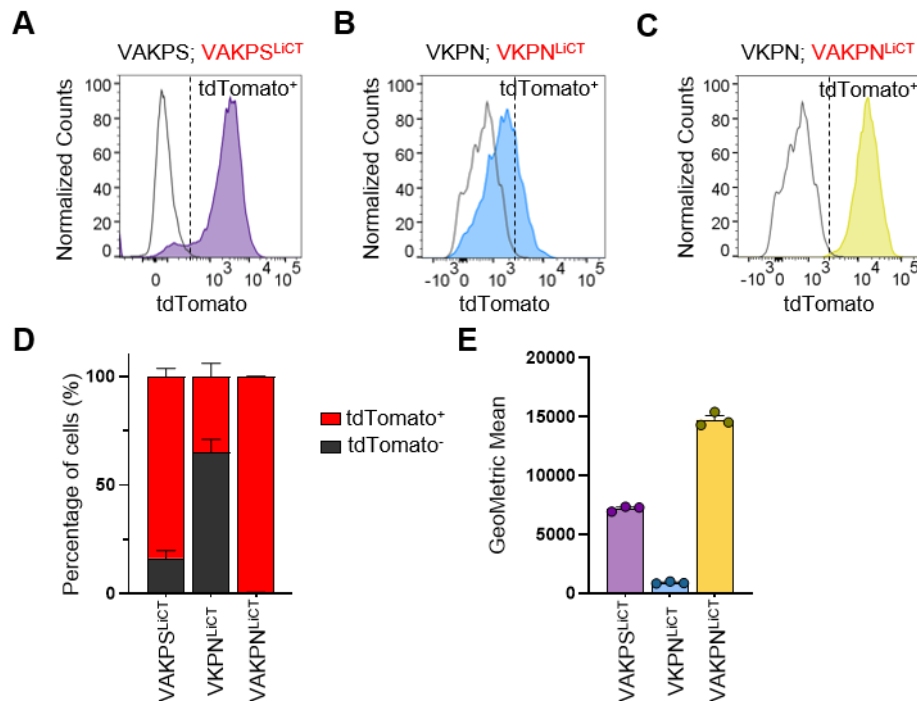


Figure 29. *Apc*^{mut} MTOs exhibit higher number of LGR5-tdTomato⁺ cells as well as elevated LGR5-tdTomato protein level compared to *Apc*^{wt} MTOs. A-C. Flow cytometry histograms of the tdTomato signal in (A) VAKPS parental and VAKPS^{LICT} MTOs (B) VKPN parental and VKPN^{LICT} MTOs and (C) VKPN parental and VAKPN^{LICT} MTOs. **D.** Percentage of tdTomato⁺ and tdTomato⁻ cells. n=3. **E.** Quantification of tdTomato signal intensity in the different MTO^{LICT} lines. n=3.

Next, I interrogated the stem cell properties of the LGR5-tdTomato⁺ cells. Thus, I performed FACS to separate the tdTomato⁻ and tdTomato⁺ (top 20%) cell populations and plated them *in vitro* to assess their clonogenic potential (**Figure 30A**). Five days after seeding, the tdTomato⁺ cells showed increased clonogenic capacity in the VAKPS^{LICT} model while no difference was observed in the VKPN^{LICT} model. Additionally, *Apc*-loss in the VKPN^{LICT} model restored the phenotype observed in the VAKPS^{LICT} MTOs (**Figure 30B-C**). Furthermore, while tdTomato⁺ cells also formed larger organoids than the tdTomato⁻ cells in the VAKPS^{LICT}, no difference was observed in the VKPN^{LICT} and VAKPN^{LICT} MTOs (**Figure 30D**). Importantly, after eight days in culture, organoids derived from both sorted cell populations displayed similar LGR5-tdTomato expression levels, restoring the heterogeneity of the parental line (**Figure 29E**).

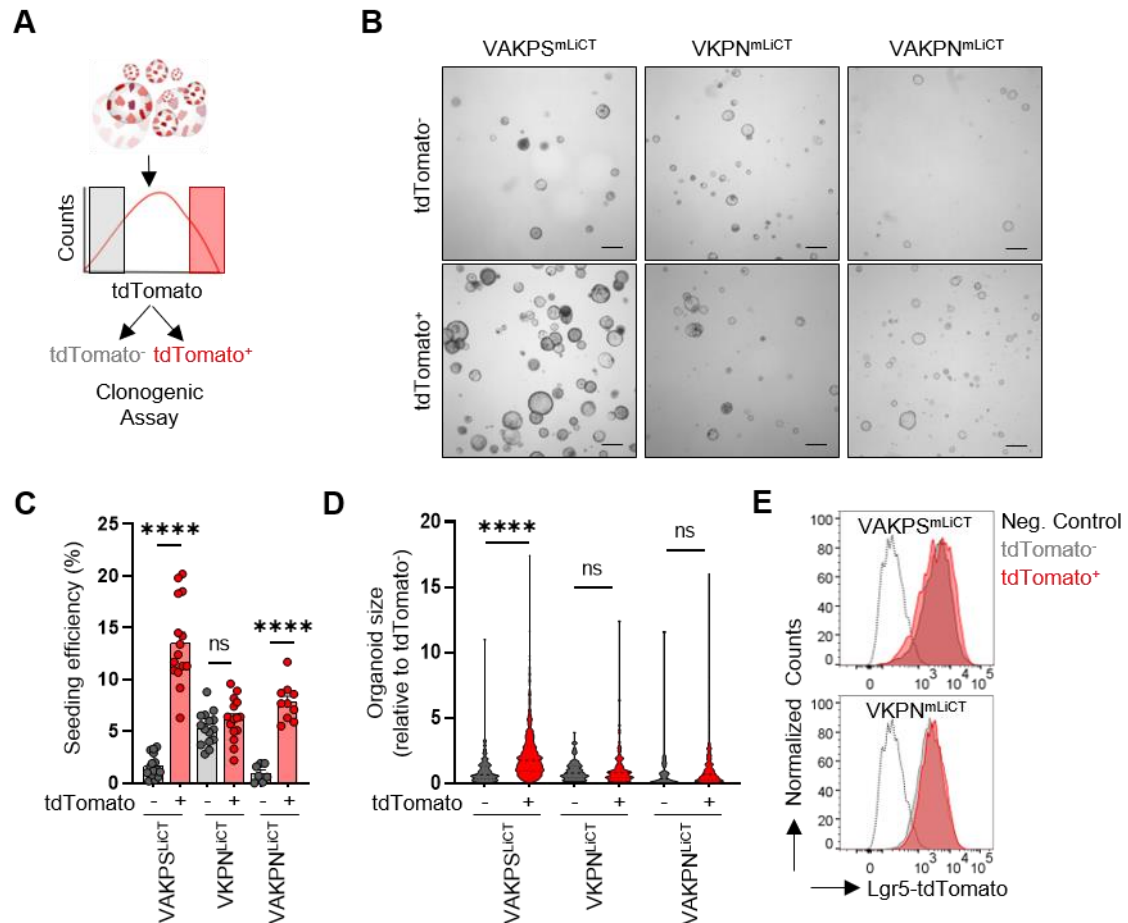


Figure 30. LGR5-tdTomato⁺ cell population has higher organoid formation capacity than LGR5-tdTomato⁻ cell population in *Apc*^{mut} MTOs *in vitro*. **A.** Workflow scheme for FACS separation of tdTomato⁻ and tdTomato⁺ cell populations for subsequent clonogenicity assays. **B.** Representative images from organoid formation assays from tdTomato⁻ and tdTomato⁺ sorted cells from VAKPS^{LiCT}, VKPN^{LiCT} and VAKPN^{LiCT} MTOs five days after seeding. Scale bar 100 μ m. **C-D.** Quantification of the (C) seeding efficiency and (D) organoid size from the organoid formation assay five days after seeding the cells. (VAKPS^{LiCT} n=15, VKPN^{LiCT} n=15, VAKPN^{LiCT} n=10 individual wells from 3 independent FACS experiments). Statistical analysis was performed using unpaired t-test. **E.** Representative flow cytometry histogram of the tdTomato signal in organoids derived from tdTomato⁻ and tdTomato⁺ sorted (top) VAKPS^{LiCT} (bottom) KPN^{LiCT} cells eight days after seeding. The parental MTO line was used as a negative control.

In line with the results observed *in vitro*, *Apc*^{mut} tumours presented higher number of LGR5-tdTomato⁺ cells (**Figure 31A-B**). To explore further the stemness properties of the LGR5⁺ tumour cells *in vivo*, I FACS separated the tdTomato⁻ and tdTomato⁺ tumor cells from subcutaneous tumours and transplanted them in the flank of secondary recipient immunodeficient NSG mice (**Figure 31C**). Similar to the *in vitro* data, tdTomato⁺ cell population had higher tumour-initiating capacities than the tdTomato⁻ cell population only in *Apc*^{mut} tumours (**Figure 31D-F**). These findings suggest that LGR5 marks CSCs only in *Apc*^{mut} CRCs whereas in *Apc*^{wt} CRCs (with low WNT-signalling activity) LGR5⁺ cells might not define the CSCs or that at least they have reduced stemness potency.

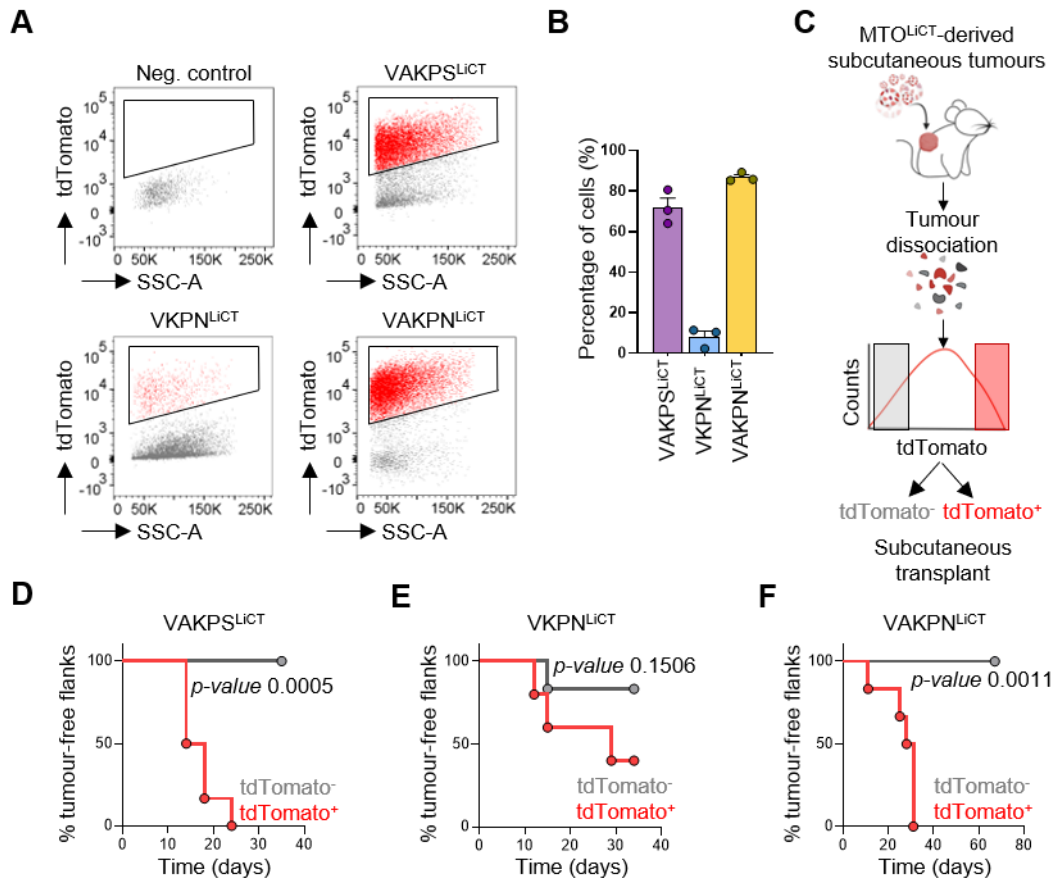


Figure 31. LGR5-tdTomato⁺ cell population has higher tumour-initiating capacity than LGR5-tdTomato⁻ cell population in *Apc*^{mut} tumours *in vivo*. **A.** Representative flow cytometry plot of tdTomato fluorescence in the CD45⁺CD31⁺EPCAM⁺ cell population from subcutaneous tumours. **B.** Quantification of the number of tdTomato⁺ cells in the CD45⁺CD31⁺EPCAM⁺ cell population from subcutaneous tumours. **C.** Workflow scheme for FACS separation of tdTomato⁻ and tdTomato⁺ cell populations derived from subcutaneous tumours for subsequent subcutaneous transplantation in the flank of secondary recipient immunodeficient NSG mice. **D-F.** Kaplan-Meier plots representing the tumour initiating capacity of LGR5-tdTomato⁻ and LGR5-tdTomato⁺ sorted cells from (D) VAKPS^{LICT}, (E) VKPN^{LICT} and (F) VAKPN^{LICT} subcutaneous transplants (n=6 mice per group). Statistical analysis was performed using the Log-rank (Mantel-Cox) test.

High *Lgr5* expression is required to induce iCaspase9 dimerization by AP-20187 treatment.

CRC cells presents high levels of plasticity (Figure 30E). Thus, to further evaluate the role of LGR5⁺ cells during CRC I took advantage of the iCaspase9 system integrated in the *Lgr5* locus along with the tdTomato reporter (Figure 32A). Here, the APAF-1 domain of the Caspase9 was replaced by a “chemical dimerizer binding domain”. Therefore, only upon treatment with the AP-20187 Chemical Inducer of Dimerization (CID) the apoptotic cascade is triggered in the *iCaspase9*-expressing cells and induces cell death (Figure 32B) (Clackson et al., 1998; Kemper et al., 2012; Shimokawa et al., 2017).

First, I assessed the ablation capacity *in vitro*. To that end, I treated the MTOs with a low (0.1 μ M) and high (1 μ M) dose of AP-20187 for 24 hours and further analysed the tdTomato levels by flow cytometry. Unfortunately, no decrease in the tdTomato signal intensity nor in the

A

MTO^{LIGT}

B

Lgr5-expressing cell

Apoptotic cell

AP-20187

C

VAKPS^{LIGT}

VKPN^{LIGT}

tdTomato GeometricMean

Untreated Vehicle 0.1 μ M 1 μ M AP-20187

D

VAKPS^{LIGT}

VKPN^{LIGT}

% tdTomato^{high} cells

Untreated Vehicle 0.1 μ M 1 μ M AP-20187

E

VAKPS^{LIGT}

VKPN^{LIGT}

VAKPN^{LIGT}

Normalized Counts

Vehicle AP-20187 (1 μ M)

tdTomato

48

Characterization of foetal-like CSCs in CRC

LGR5 is known to mark CSCs in CRC, however, the findings described above challenged this dogma. In sum, these findings showed that LGR5 marks CSCs in *Apc^{mut}* CRCs but not in *Apc^{wt}* CRCs, suggesting the presence of an alternative CSC subset in *Apc^{wt}* CRCs not marked by LGR5. Therefore, I sought to identify and define this alternative CSC pool.

I focused on the foetal ISC program (Mustata et al., 2013), which has been described to reappear in adult tissues upon stress conditions or in the context of cancer (Ayyaz et al., 2019; Bala et al., 2023; Karo-Atar et al., 2022; Mzoughi et al., 2023; Nusse et al., 2018; Vasquez et al., 2022; Yui et al., 2018). Indeed, transcriptional profiling of serrated adenomas, which are *APC*-proficient tumours, showed enrichment for foetal stem cell signatures while showing lower levels of WNT pathway activation and the adult ISC program (Chen et al., 2021; Kawasaki et al., 2020; Leach et al., 2021; Vasquez et al., 2022).

Identification of foetal-like intestinal marker genes associated with tumour aggressiveness in CRC

To ascertain the contribution of foetal-like cancer cells to CRC progression, I analysed which genes from the foetal program reappear in CRC with the aim of defining a marker gene. This marker will allow for the identification and tracking of the foetal-like cancer cells. Thus, we (in collaboration with Dr. Maria Puschhof) analysed the expression profiles of the genes from foetal ISC signature program (Mustata et al., 2013) in the TCGA-COAD cohort (<https://portal.gdc.cancer.gov/projects/TCGA-COAD>), a cohort with bulk transcriptomic data of 458 primary CRC samples. First, we mapped the 317 genes from the foetal ISC signature to their human homologues, identifying 262 genes (i.e. *Ly6a* murine gene does not have a human ortholog). Subsequently, the CRC samples were classified according to their tumour stage (I-IV) and the changes in gene expression across these stages were calculated. Of the 262 genes, 76 had at least two significant gene expression changes across CRC stages, with only 59 of these genes exhibiting a significant increase in gene expression correlating with higher tumour staging (**Figure 33A**). Given that some of these genes are lowly expressed in CRC, we compared the mean gene expression levels with the mean fold change across the different CRC stages. Intriguingly, *SPP1* (Secreted Phosphoprotein 1) and *TACSTD2* exhibited heightened expression level and a higher two-fold change in expression level that positively correlates with tumour stage (**Figure 33B-C**).

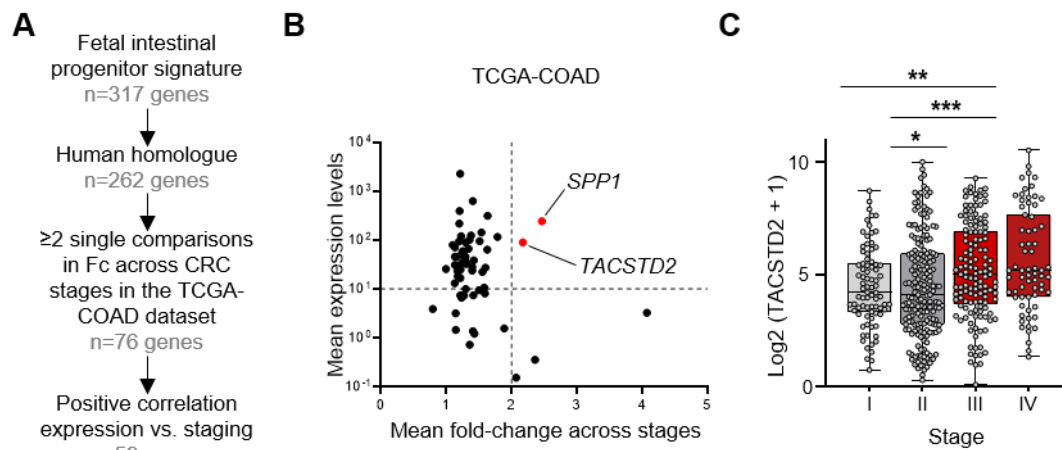


Figure 33. Expression profiles of genes from the foetal ISC signature in human CRC. **A.** Triage of the foetal ISC gene list to define a marker to identify foetal-like cancer cells. Analysis and filters for highly expressed genes and positive correlations with high tumour stages were applied. **B.** Scatter plot showing the mean expression levels of the top 59 foetal-like intestinal genes and its correlation with tumour stage in the TCGA-COAD cohort. **C.** *TACSTD2* expression levels across the different tumour stages in the TCGA-COAD cohort. Statistical analysis was performed using ordinary one-way ANOVA.

Literature analysis revealed that *SPP1* expression is restricted to tumour-associated macrophages (Qi et al., 2022). Thus, the above described analysis yields a single candidate gene to serve as a marker for foetal-like cancer cells, *TACSTD2*. *TACSTD2* encodes the TROP2 transmembrane glycoprotein, which was initially identified in mouse trophoblasts (Shvartsur and Bonavida, 2015). Indeed, TROP2 is highly abundant in a vast number of epithelial carcinomas while absent in most healthy adult tissues (Shvartsur and Bonavida, 2015; Zeng et al., 2016). Although TROP2 function is poorly described in the literature, many studies have correlated TROP2 expression with poor overall survival (OS) and short disease-free survival (DFS) in solid tumours (Zeng et al., 2016). In line with these findings, I found TROP2 expression to positively correlate with lower OS and shorter DFS in CRC (**Figure 34A-B**).

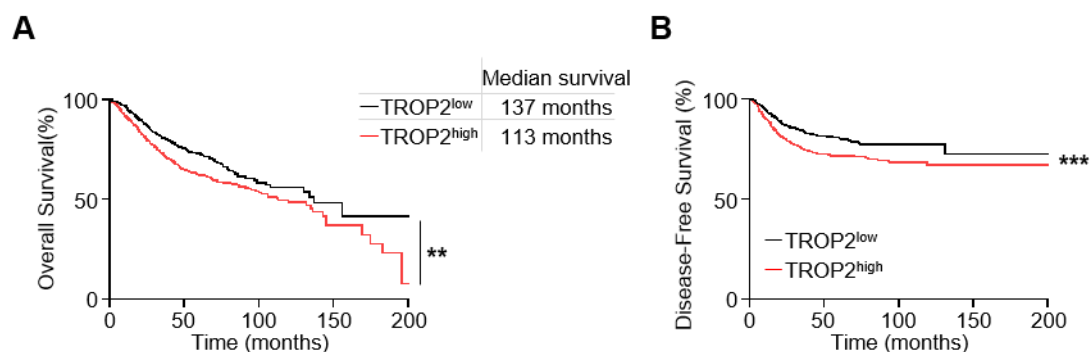


Figure 34. TROP2 expression correlates with poor overall survival and lower disease-free survival in CRC. **A-B.** Kaplan–Meier survival curve showing (A) overall survival (n= 1061) and (B) disease-free survival (n=1336) of CRC patients according to TROP2 expression levels. Statistical analysis was performed using the Log-rank (Mantel-Cox) test.

Furthermore, I assessed the expression of *Tacstd22* in several MTO models that recapitulate the different stages (denoted by the number of mutated driver genes) as well as the different routes (classical and serrated) of CRC progression. Interestingly, I observed a positive linear correlation between *Tacstd22* expression level and increased driver mutations in the MTOs (**Figure 35A-B**). Taken together, TROP2 expression level correlate with higher tumour stages in human and mouse CRC.

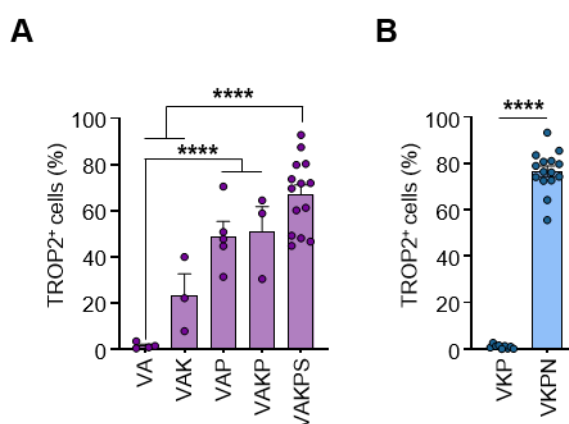


Figure 35. TROP2 surface expression positively correlates with higher tumour stage in MTOs. A-B. Percentage of TROP2⁺ cells in MTOs from the (A) classical (*Apc*^{mut}) and (B) serrated (*Apc*^{wt}) route of CRC progression. V, *Villin*^{CreER}; A, *Apc*^{fl/fl}; K, *Kras*^{G12D/+}; P, *Trp53*^{fl/fl}; S, *Smad4*^{fl/fl}; N, *Rosa26*^{N11CD/+}. Statistical analysis was performed using ordinary One-way ANOVA.

TROP2 surface expression marks foetal-like CRC cells in mouse and human CRC

Next I set out to demonstrate that TROP2 can be used as a marker for the identification of cancer cells enriched for the foetal ISC program. To that end, in collaboration with Dr. Bryce Lim, Dr. Maria Puschhof, Dr. Sigrid Fey and Manuel Mastel, we performed scRNA sequencing of subcutaneous tumors derived from PDOXs and VAKPS and VKPN MTOs. Additionally, we analysed scRNA sequencing data from the SMC and KUL publicly available datasets of human CRC specimens (Joanito et al., 2022; Lee et al., 2020). Analysis of the cancer cell compartments showed an enrichment of the foetal ISC program in the TROP2⁺ cancer cell population compared to the TROP2⁻ cancer cell population in both human (**Figure 36A-D**) and murine models (**Figure 36E-G**). Altogether, this data indicates that TROP2 can be used as a marker for foetal-like cancer cells.

TROP2 and LGR5 define distinct cancer cell populations

Interestingly, while TROP2⁺ CRC cells are enriched for the foetal ISC program in human and mouse CRC samples, TROP2⁻ CRC cells are enriched for the adult ISC program (**Figure 37A-E**). Thus, I hypothesized that CRC tumours might have different stem cell populations defined by different CSC programs, one marked by LGR5 and enriched for the

adult ISC program and another one marked by TROP2 expression and enriched for the foetal ISC program.

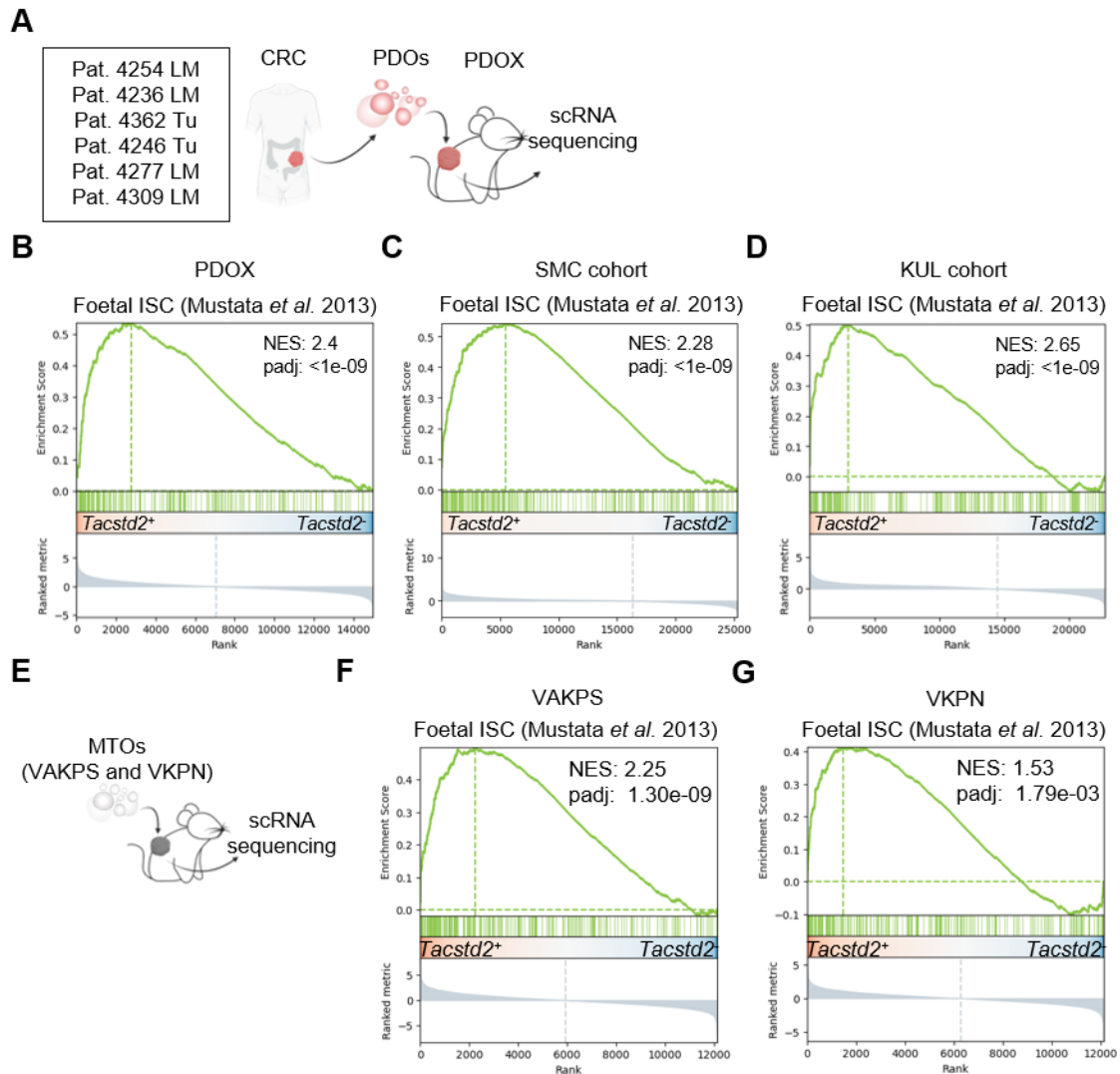


Figure 36. TROP2 expression marks foetal-like cancer cells in human and murine CRC. **A.** Schematic representation of the workflow for the generation of PDOX from six different CRC patients. PDOX, Patient-derived organoid xenographs; Pat, patient; Tu, tumour; LM, liver metastasis. **B-D.** GSEA comparing the foetal ISC signature in *TACSTD2*⁺ versus *TACSTD2*⁻ cancer cells from the **(B)** PDOX biobank, **(C)** SMC cohort and **(D)** KUL cohort (Joanito *et al.*, 2022; Lee *et al.*, 2020). **E.** Schematic representation of the workflow for the generation of subcutaneous tumours from VAKPS and VKPN MTOs. **F-G.** GSEA comparing the foetal ISC signature in *Tacstd2*⁺ versus *Tacstd2*⁻ cancer cells from **(F)** VAKPS and **(G)** VKPN subcutaneous tumours. ISC, intestinal stem cell.

To assess this, in collaboration with Dr. Bryce Lim, we analyzed the single-cell transcriptomics of 27 CRCs from two public datasets (Joanito *et al.*, 2022; Lee *et al.*, 2020). In line with my hypothesis, we observed that TROP2 and LGR5 mark distinct cell population, evidenced by their mutually exclusive distribution across and within CRC patients (**Figure 38A-B**). Furthermore, correlation analysis on the mutational status of CRC driver genes and the abundance of either TROP2⁺ or LGR5⁺ cells indicates the *APC*^{WT} CRCs are enriched for TROP2⁺ cells whereas *APC*^{MUT} CRCs are enriched for LGR5⁺ cells (**Figure 38A**).

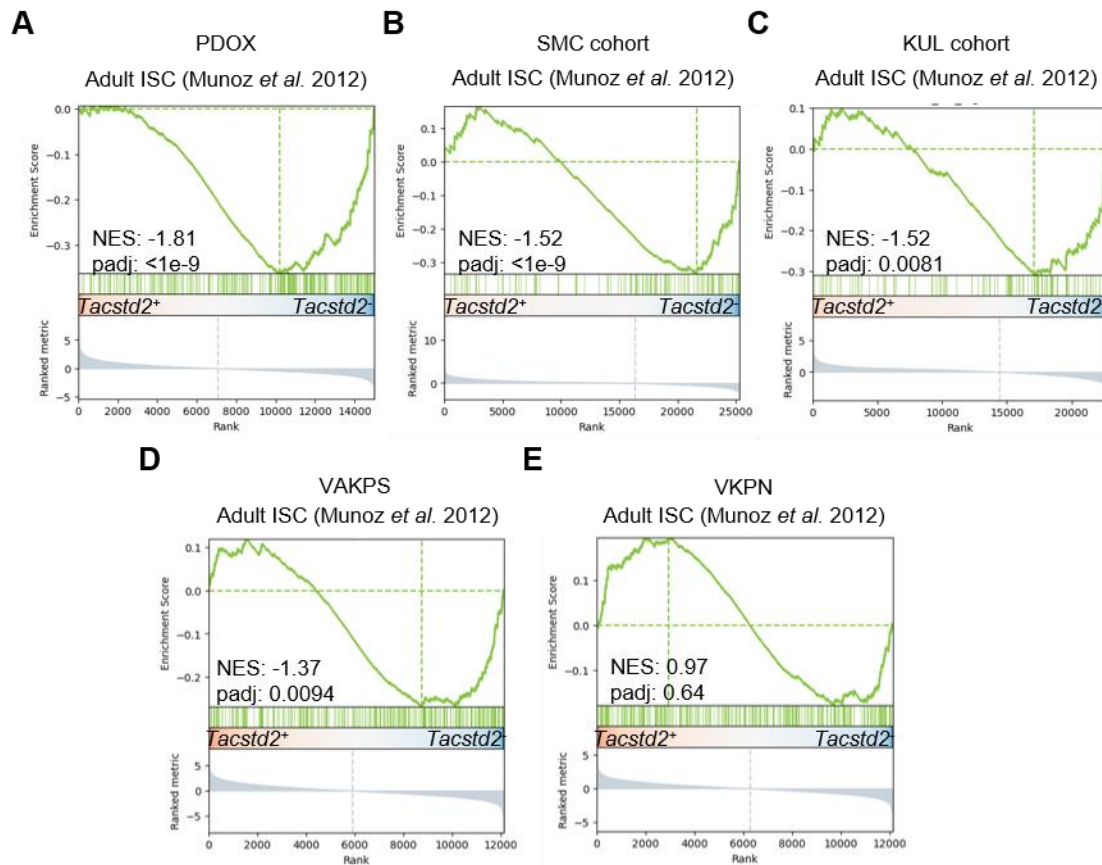


Figure 37. TROP2 expression does not mark adult ISCs in human and murine CRC. **A.** Schematic representation of the workflow for the generation of PDOX from six different CRC patients. PDOX, Patient-derived organoid xenografts; Tu, tumour; LM, liver metastases. **B-D.** GSEA comparing the adult ISC signature in *TACSTD2*⁺ versus *TACSTD2*⁻ cancer cells from the **(B)** PDOX biobank, **(C)** SMC cohort and **(D)** KUL cohort. **E.** Schematic representation of the workflow for the generation of subcutaneous tumours from VAKPS and VKPN MTOs. **F-G.** GSEA comparing the adult ISC signature in *Tacstd2*⁺ versus *Tacstd2*⁻ cancer cells from **(F)** VAKPS and **(G)** VKPN subcutaneous tumours. ISC, intestinal stem cell.

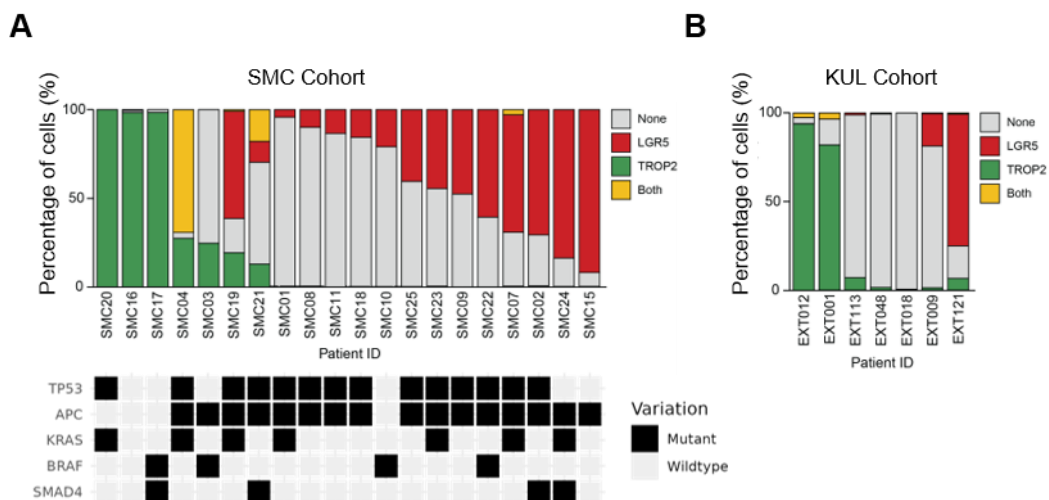


Figure 38. TROP2 and LGR5 mark distinct cancer cell populations in CRC. Percentage of tumour cells marked by LGR5⁺, TROP2⁺, LGR5⁺/TROP2⁺ and LGR5⁻/TROP2⁻ cells of each patient from the **A.** SMC and the **B.** KUL cohorts.

TROP2 marks foetal-like CRC cells with stem cell properties

The re-appearance of foetal ISC programs in CRC has been previously described (Bala et al., 2023; Mzoughi et al., 2023; Vasquez et al., 2022); however, the stem cell potential of these foetal-like CRC cells remains elusive. Thus, to define the stem cell capacity of foetal-like (TROP2⁺) CRC cells, I performed FACS to separate the TROP2⁻ and TROP2⁺ (top 20%) cell populations and plated them *in vitro* (**Figure 39A**). Interestingly, five days after seeding, TROP2⁺ cells demonstrated increased clonogenic capacity in all the different MTOs and PDOs tested, indicated by the number of organoids (**Figure 39B-D**). Furthermore, TROP2⁺ cells also formed larger organoids than the TROP2⁻ cells in all the MTOs (except VAKP) and all PDOs (**Figure 39E-F**). Of note, after seven days in culture, organoids derived from both sorted populations displayed similar TROP2 levels, restoring the heterogeneity of the parental line (**Figure 39G**).

Next, I assessed the ability of TROP2 to mark foetal-like CSCs *in vivo*. To that end, I FACS separated the TROP2⁻ and TROP2⁺ tumour cells from VAKPS and VKPN subcutaneous tumours and transplanted them in the flank of secondary recipient immunodeficient NSG mice, at serial dilutions ranging from 20 to 2.000 cells (**Figure 40A**). Of note, there were no significant differences in the number of TROP2⁺ cells across the different tumour genotypes (**Figure 40B-C**). Interestingly, TROP2⁻ cells were more capable of forming tumours after transplantation in the VAKPS model (**Figure 40D**). In contrast, in the VKPN model, TROP2⁺ cells showed an increased tumour initiating capacity (**Figure 40E**). To further confirm that the CSC pool is defined by the *Apc* status, I additionally FACS separated the TROP2⁻ and TROP2⁺ tumour cells from VAKPN subcutaneous tumours and transplanted them in the flank of secondary recipient immunodeficient NSG mice. Here, no difference in tumour initiating capacity was observed between TROP2⁻ and TROP2⁺ cells (**Figure 40F**). Furthermore, tumours developed from TROP2⁺ transplanted tumour cells were bigger than the tumours derived from TROP2⁻ cells only in the VKPN model (**Figure 40G**). Interestingly, in all three models, tumours derived from both sorted populations displayed a similar number of TROP2⁺ cells restoring the heterogeneity observed in the parental tumours (**Figure 40 H-J**). These results highlight the high levels of plasticity in CRC cells and suggest a possible dependency on TROP2⁺ cell pool restoration for tumour growth. In sum, I concluded that TROP2 marks CRC cells with stem cell properties in a subset of CRC defined by no genetic alterations in the *Apc* gene/low WNT-pathway activity.

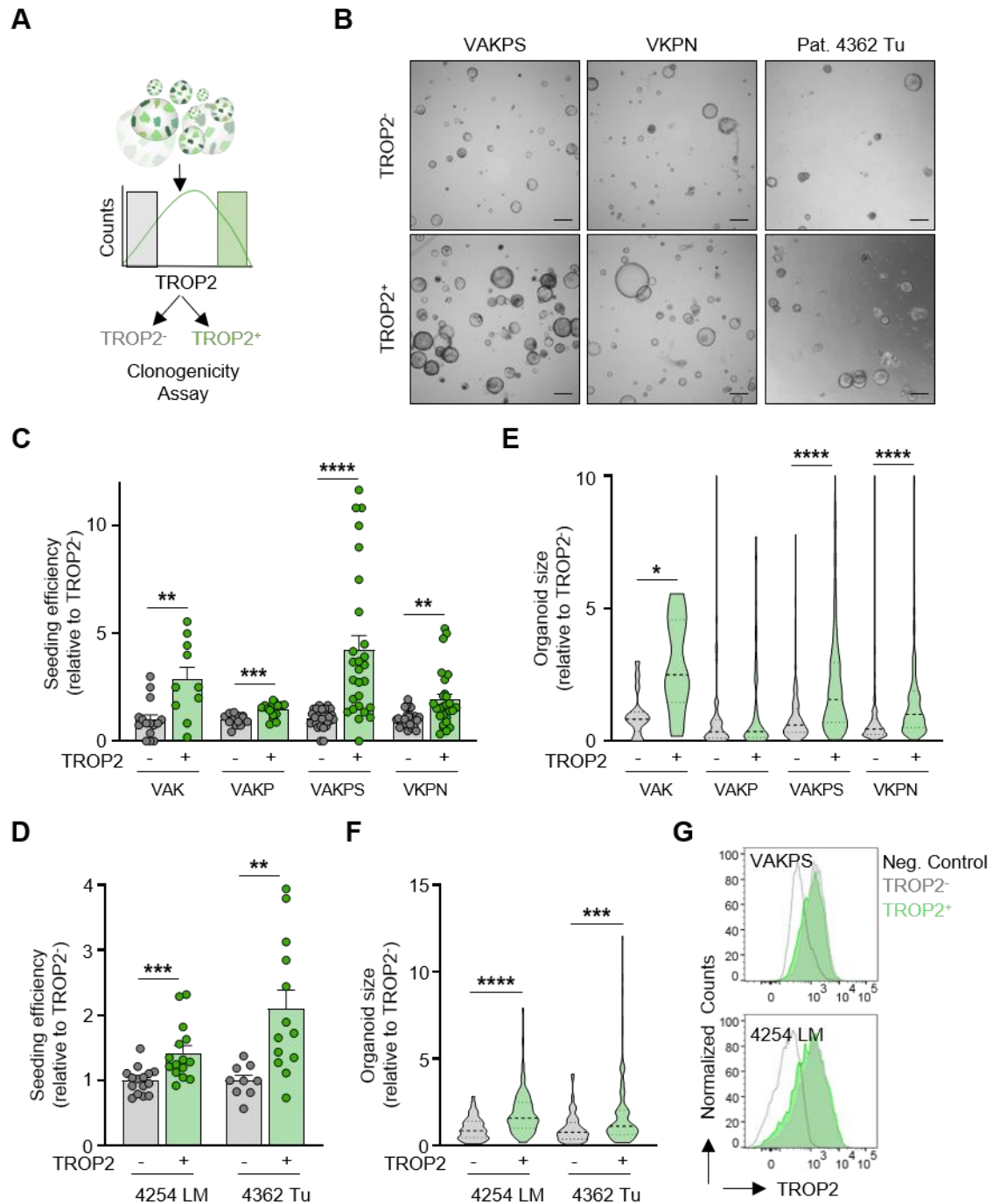


Figure 39. TROP2⁺ cells have higher organoid formation capacity than TROP2⁻ cells in MTOs and PDOs *in vitro*. **A.** Workflow scheme for FACS separation of TROP2⁻ and TROP2⁺ cell populations for subsequent clonogenic assay. **B.** Representative images from organoid formation assays from TROP2⁻ and TROP2⁺ FACS-sorted cells from VAKPS and VKPN MTOs five days after seeding and from Patient 4362 PDOs ten days after seeding. Scale bar 100µm. **C.** Quantification of the seeding efficiency from the organoid formation assay of the different MTO lines five days after seeding the cells. **D.** Quantification of the seeding efficiency from the organoid formation assay of the different PDO lines ten days after seeding. **E.** Quantification of the organoid size from the organoid formation assay of the different MTO lines five days after seeding. **F.** Quantification of the organoid size from the organoid formation assay of the different PDO lines ten days after seeding. **G.** Representative flow cytometry histogram of the TROP2 signal in organoids derived from TROP2⁻ and TROP2⁺ sorted (top) VAKPS (bottom) patient 4254 LM cells seven days after seeding. The parental cell line was used as a negative control. LM, liver metastasis. Statistical test was performed using unpaired t-test. Pat, patient; LM, liver metastasis.

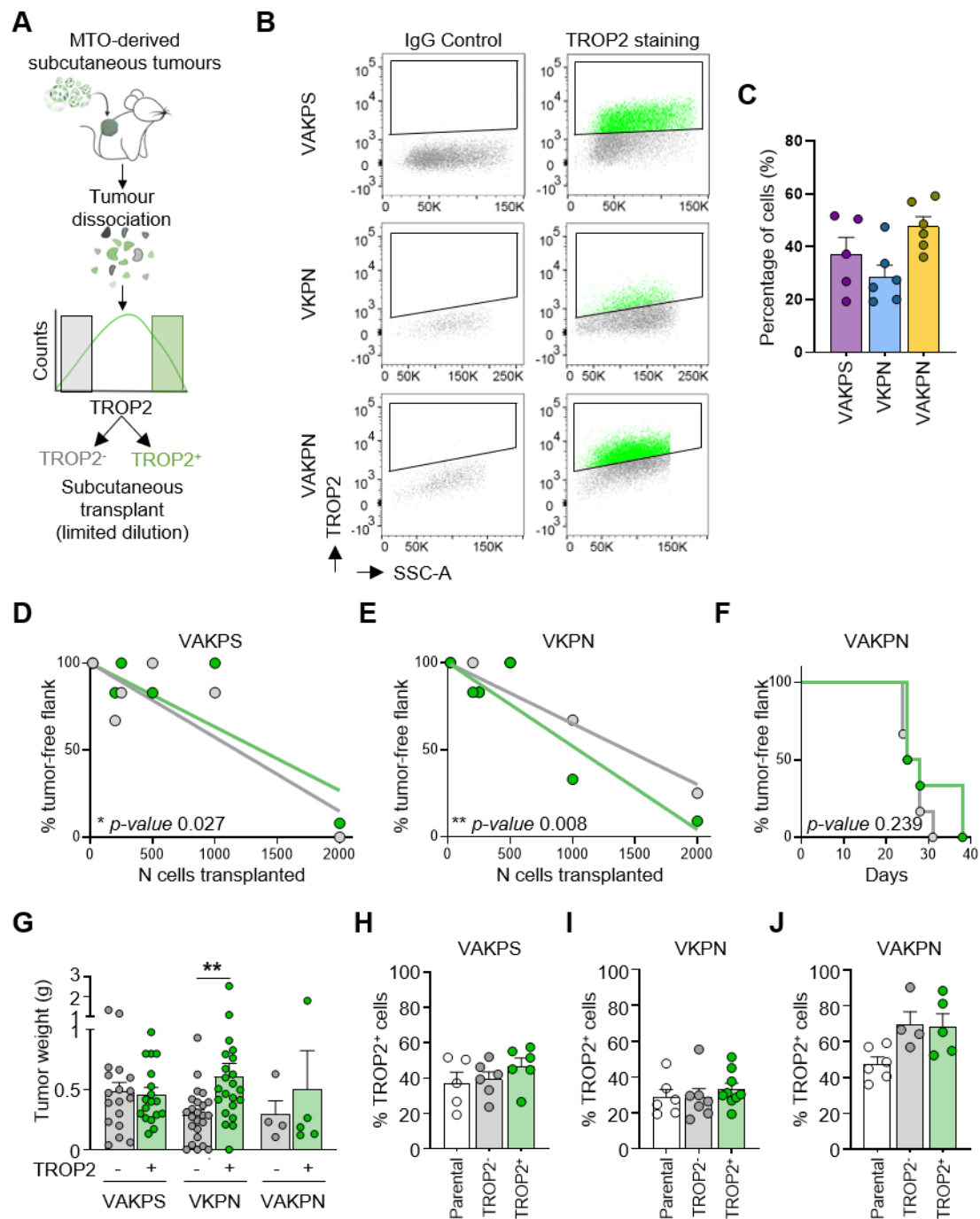


Figure 40. TROP2 marks a stem-like cancer cell population *in vivo* in *Apc*^{wt} tumours. **A.** Workflow scheme for FACS separation of TROP2⁻ and TROP2⁺ cell populations derived from subcutaneous tumours for subsequent subcutaneous transplantation in the flank of secondary recipient immunodeficient NSG mice **B.** Representative flow cytometry plot of TROP2 levels in CD45⁺CD31⁺EPCAM⁺ cells from subcutaneous tumours. **C.** Quantification of the number of TROP2⁺ cells in CD45⁺CD31⁺EPCAM⁺ cells from subcutaneous tumours. **D-E.** *In vivo* limiting dilution assay in NSG mice. Mice were subcutaneously transplanted with the indicated numbers of FACS separated TROP2⁻ or TROP2⁺ cells derived from **D.** VAKPS and **E.** VKPN tumours (n=6 mice per dilution per group). Statistical analysis was performed using Chi-square test. **F.** Kaplan-Meier plot representing the tumour initiating capacity of TROP2⁻ and TROP2⁺ sorted cells from VAKPN subcutaneous transplants (n=6 mice per group). **G.** Tumour weight in grams from the experiments in D-F. **H-J.** Percentage of TROP2⁺ tumour cells from subcutaneous tumours from the experiment in D-F. Statistical test was performed using unpaired t-test.

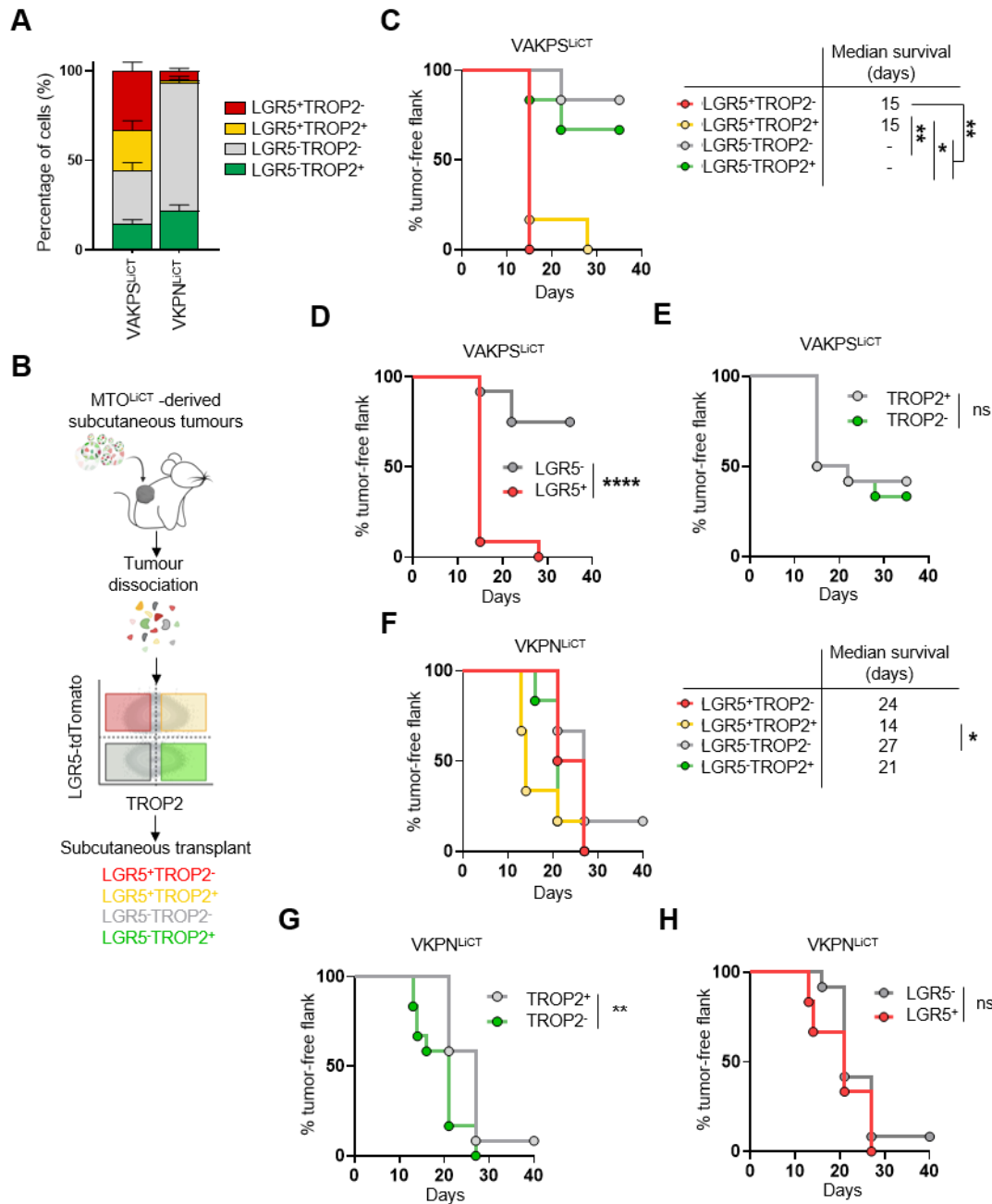


Figure 41. LGR5 marks CSCs only in *Apc*^{mut} CRCs whereas TROP2 marks the CSCs in *Apc*^{wt} “low WNT” CRCs. **A.** Percentage of LGR5⁺/TROP2⁻, LGR5⁺/TROP2⁺, LGR5⁻/TROP2⁺ cells from VAKPS^{LICT} and VKPN^{LICT} subcutaneous tumours (n=6 mice per group). **B.** Workflow scheme for FACS separation of LGR5⁺/TROP2⁻, LGR5⁺/TROP2⁺, LGR5⁻/TROP2⁻, LGR5⁻/TROP2⁺ cells populations derived from subcutaneous tumours for subsequent subcutaneous transplantation in the flank of secondary recipient immunodeficient NSG mice. **C.** Kaplan-Meier plot representing the tumour initiating capacity of LGR5⁺/TROP2⁻, LGR5⁺/TROP2⁺, LGR5⁻/TROP2⁻, LGR5⁻/TROP2⁺ sorted cells from VAKPS^{LICT} subcutaneous tumours (n=6 mice per group). **D-E.** Kaplan-Meier plot representing the tumour initiating capacity from Figure C segregated for **(D)** LGR5 or **(E)** TROP2 levels. **F.** Kaplan-Meier plot representing the tumour initiating capacity of LGR5⁺/TROP2⁻, LGR5⁺/TROP2⁺, LGR5⁻/TROP2⁻, LGR5⁻/TROP2⁺ sorted cells from VKPN^{LICT} subcutaneous tumours (n=6 mice per group). **G-H.** Kaplan-Meier plot representing the tumour initiating capacity from Figure F segregated for **(G)** TROP2 or **(H)** LGR5 protein levels. Statistical analysis was performed using the Log-rank (Mantel-Cox) test.

Analysis of the cell fraction of LGR5⁺ and TROP2⁺ CRC cells in both mouse tumour models by flow cytometry revealed that 22.2% of VAKPS subcutaneous tumour cells expressed both CSC markers (LGR5⁺/TROP2⁺) while this double positive population was a

minority in the VKPN model (1.6%) (**Figure 41A**). I hypothesized that this double positive CSC population represents a transition state. Thus, I investigated whether the double positive population (LGR5⁺/TROP2⁺) had higher stemness properties (**Figure 41B**). Analysis of the tumour-initiation capacity of the stem cell potential of the 4 different populations *in vivo* (LGR5⁻/TROP2⁻, LGR5⁺/TROP2⁻, LGR5⁻/TROP2⁺, LGR5⁺/TROP2⁺) revealed that in the VAKPS^{LiCT} model, both LGR5⁺ populations (LGR5⁺/TROP2⁻, LGR5⁺/TROP2⁺) had a higher tumour-initiating capacity than the LGR5⁻ cell populations regardless of TROP2 levels (**Figure 41C-D**). However, in line with my previous observations, when analysing these results solely according to the TROP2 expression levels, no difference in tumour initiating capacity was observed between the TROP2⁺ and TROP2⁻ populations (**Figure 41E**). Contrary, in the VKPN^{LiCT} model, both TROP2⁺ populations (LGR5⁻/TROP2⁺, LGR5⁺/TROP2⁺) had higher tumour-initiating capacity than the TROP2⁻ populations (LGR5⁻/TROP2⁻, LGR5⁺/TROP2⁻) (**Figure 41F-G**) whereas when segregating the tumours according to the LGR5 expression levels, no difference was observed (**Figure 41H**). In sum, these results showed no additional CSC potential of the double positive population (LGR5⁺/TROP2⁺) compare to the LGR5⁺/TROP2⁻ population in the VAKPS^{LiCT} or the LGR5⁻/TROP2⁺ population in the VKPN^{LiCT} model.

Taken together, I conclude that in CRC two different CSC populations exist, the LGR5⁺ CSCs enriched for the adult ISC program and the TROP2⁺ CSCs enriched for the foetal ISC program. Furthermore, my data also demonstrates that while in the *Apc*^{mut} CRCs the CSCs are marked by LGR5, TROP2 marks the CSCs in the *Apc*^{wt} “low WNT” CRCs.

***In vitro Tacstd2* expression level in VAKPS MTOs is sufficient to induce iCaspase9 dimerization by AP-20187 treatment.**

In order to block the high plasticity observed in CRC cells and further evaluate the role of TROP2⁺ cells during CRC progression, I took advantage of the iCaspase9- tdTomato system previously used for *Lgr5* (Shimokawa et al., 2017) (**Figure 26A**). Thus, this time I knocked-in the iCaspase9-tdTomato fluorescent reporter after the STOP codon of the *Tacstd2* gene (**Figure 42A-B**). After puromycin selection, resistant clones were isolated and expanded *in vitro* for subsequent genotyping to verify the correct genetic insertion (**Figure 42B-C**). Next, I electroporated the VAKPS^{Tacstd2-IRES-iCaspase9-T2A-tdTomato-loxP-Ruby/PuroR-loxP} (VAKPS^{TiCT-Ruby/PuroR}) clones 1 and 2 and VKPN^{LiCT-Ruby/PuroR} clone 3 with a vector encoding for the Cre recombinase protein fused to a GFP fluorescent reporter with the aim of removing the Ruby/PuroR cassette (**Figure 42B**). Two days after electroporation I FACS separated the GFP⁺ cells and repeated the *in vitro* subclonal isolation and expansion (**Figure 42B**). The successful removal of the

Ruby/PuroR cassette was confirmed by PCR and re-sensitization to puromycin treatment (**Figure 42B, D-E**). In sum, I generated two VAKPS^{TiCT} clones and one VKPN^{TiCT} clone.

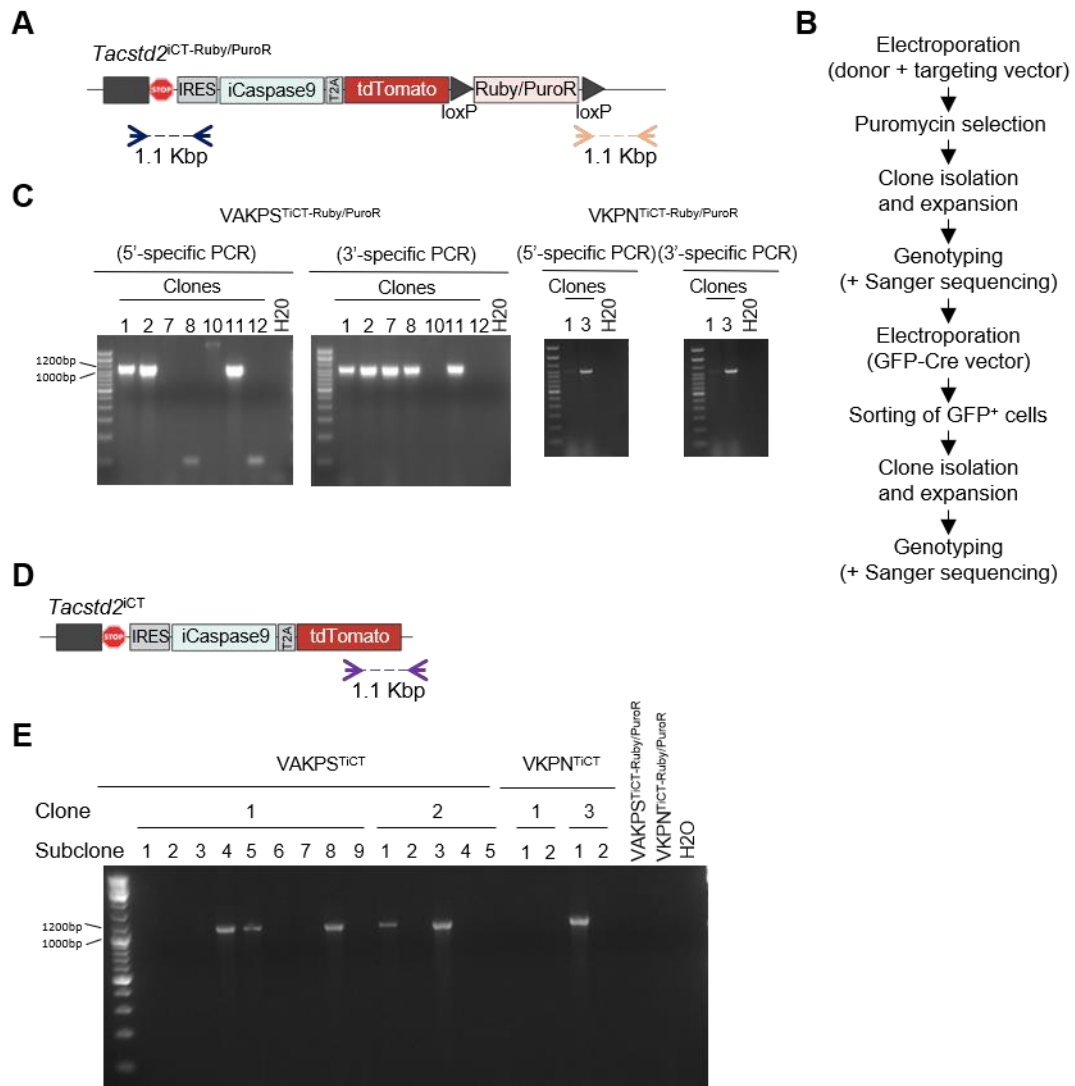


Figure 42. Generation of *Tacstd2*-iCaspase9-tdTomato (TiCT) knock-in VAKPS and VKPN lines. **A.** Scheme of the iCaspase9-tdTomato-Ruby/PuroR knock-in intermediate cassette in the *Tacstd2* genomic locus. PuroR, Puromycin-resistant. The blue and orange arrows indicate the annealing site of the primers for the 5' and 3' specific PCR, respectively. **B.** Workflow for the generation of the VAKPS^{TiCT} and VKPN^{TiCT} lines. **C.** PCR product of the 5' and 3' specific PCR for the VAKPS and VKPN MTO clones. **D.** Scheme of the *Tacstd2*^{TiCT} final allele. The purple arrows indicate the annealing site of the primers for the specific PCR to validate the removal of the Ruby/PuroR cassette. **E.** PCR product of the specific PCR shown in (C) for the VAKPS and VKPN MTO different subclones. bp, base pairs.

To validate whether tdTomato and iCaspase9 expression is restricted to TROP2⁺ cells, I analysed by flow cytometry whether TROP2⁺ cells (stained with anti-TROP2 fluorescent antibodies) were also tdTomato⁺. Out of the two VAKPS^{TiCT} clones, only clone 2 showed double positive cells (**Figure 43A**). To further validate these results, I FACS separated tdTomato⁻ and tdTomato^{high} cell populations this clone and checked the *tdTomato* and *Tacstd2* expression levels. RT-qPCR analysis showed that tdTomato^{high}-sorted cells were enriched for *tdTomato* and *Tacstd2* expression compared to tdTomato⁻ sorted cells (**Figure 43B**). Altogether, this

data indicates the successful generation of a VAKPS^{TiCT} MTO line with a *tdTomato* and *iCaspase9* cassettes knocked-in in the *Tacstd2* genomic locus, allowing for the selective ablation of *Tacstd2*-expressing cells. Unfortunately, I failed to generate the VKPN^{TiCT} MTO line as the only VKPN^{TiCT} clone obtained showed no tdTomato⁺ cells (**Figure 43C**).

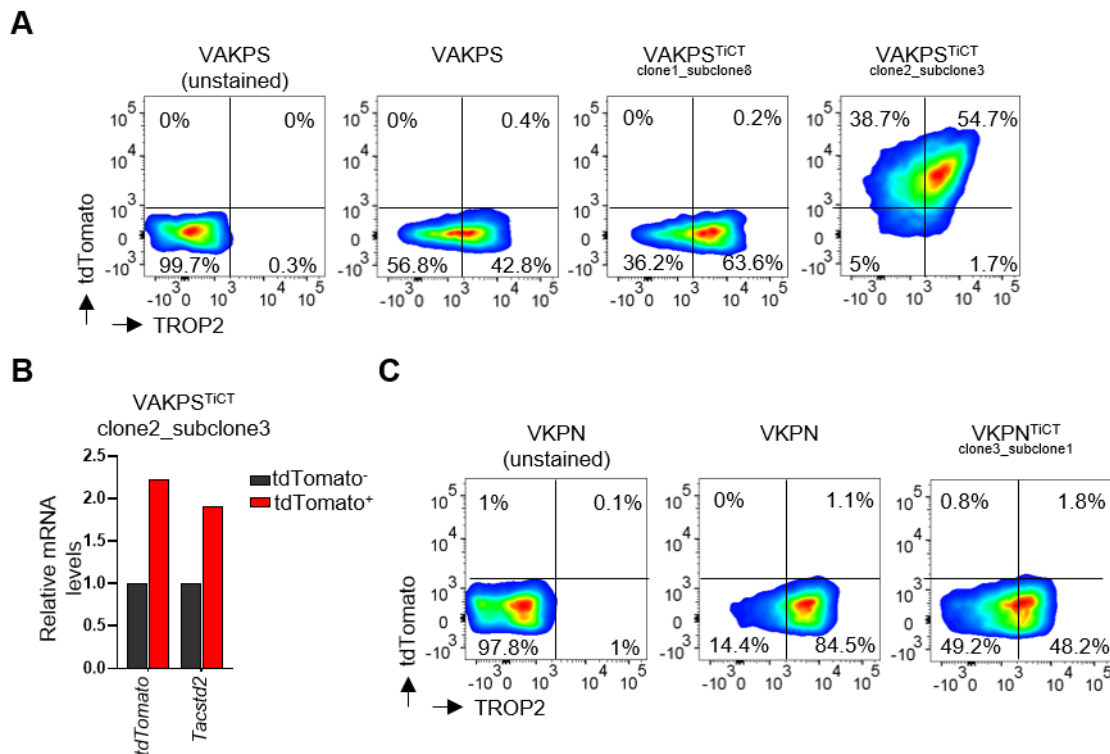


Figure 43. tdTomato reports TROP2⁺ cells in VAKPS^{TiCT} MTOs. **A.** FACS analysis showing co-expression of tdTomato and TROP2 in VAKPS^{TiCT} MTOs. **B.** RT-qPCR of *tdTomato* and *Tacstd2* mRNA expression levels of tdTomato⁻ and tdTomato⁺ sorted populations from VAKPS^{TiCT}_clone2_subclone3. **C.** FACS analysis showing absence of co-expression of tdTomato and TROP2 in the VKPN^{TiCT} MTO clone.

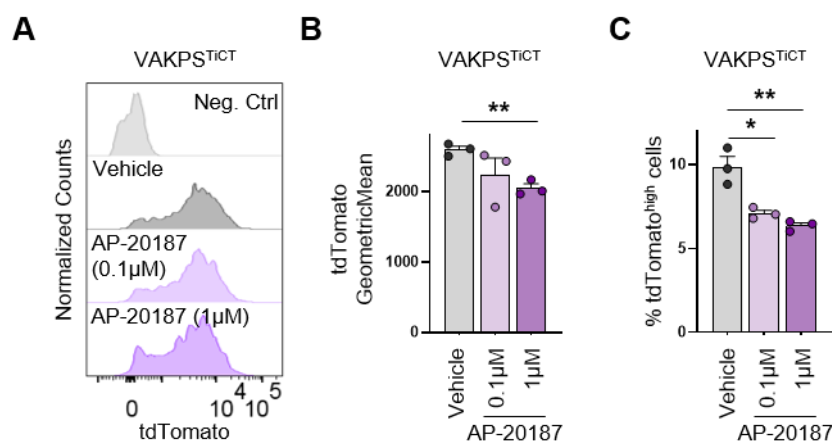


Figure 44. Selective ablation of TROP2⁺ cells in vitro. **A.** Representative flow cytometry plot of TROP2-tdTomato levels in VAKPS^{TiCT} MTOs after AP-20187 treatment for 24 hours. **B-C.** Quantification of the (B) tdTomato signal intensity and (C) percentage of tdTomato^{high} cells from VAKPS^{TiCT} MTOs after 24 hours on AP-20187. Statistical analysis was performed using unpaired t-test.

Next, I assessed the ablation capacity of TROP2⁺ cells in the VAKPS^{TiCT} MTO line *in vitro*. To that end, I treated the VAKPS^{TiCT} MTOs with a low (0.1 μM) and high (1 μM) dose of

AP-20187 for 24 hours and further analysed the tdTomato levels by flow cytometry. Interestingly, a significant decrease in the tdTomato signal intensity and the percentage of tdTomato^{high} cells was observed when treated with AP-20187 (**Figure 44A-C**).

***In vivo Tacstd2* expression level in VAKPS MTOs is not sufficient to induce iCaspase9 dimerization by AP-20187 treatment.**

Finally, to study the role of the selective depletion of TROP2⁺ cells in tumour progression I subcutaneously transplanted the VAKPS^{TiCT} MTOs and treated them with AP-20187 for ten days (**Figure 45A**). Unfortunately, no differences in tumour growth were observed (**Figure 45B**). Furthermore, when assessing the depletion levels of TROP2⁺ cells, no significant reduction of tdTomato-TROP2 nor reduction in the percentage of tdTomato-TROP2^{high} cells was observed (**Figure 45C-F**). These results might explain the absence of phenotype regarding tumour growth. Taken together, these findings suggest that the expression levels of TROP2, and thus, iCaspase9 levels, are not sufficient to induce apoptosis upon AP-20187 treatment.

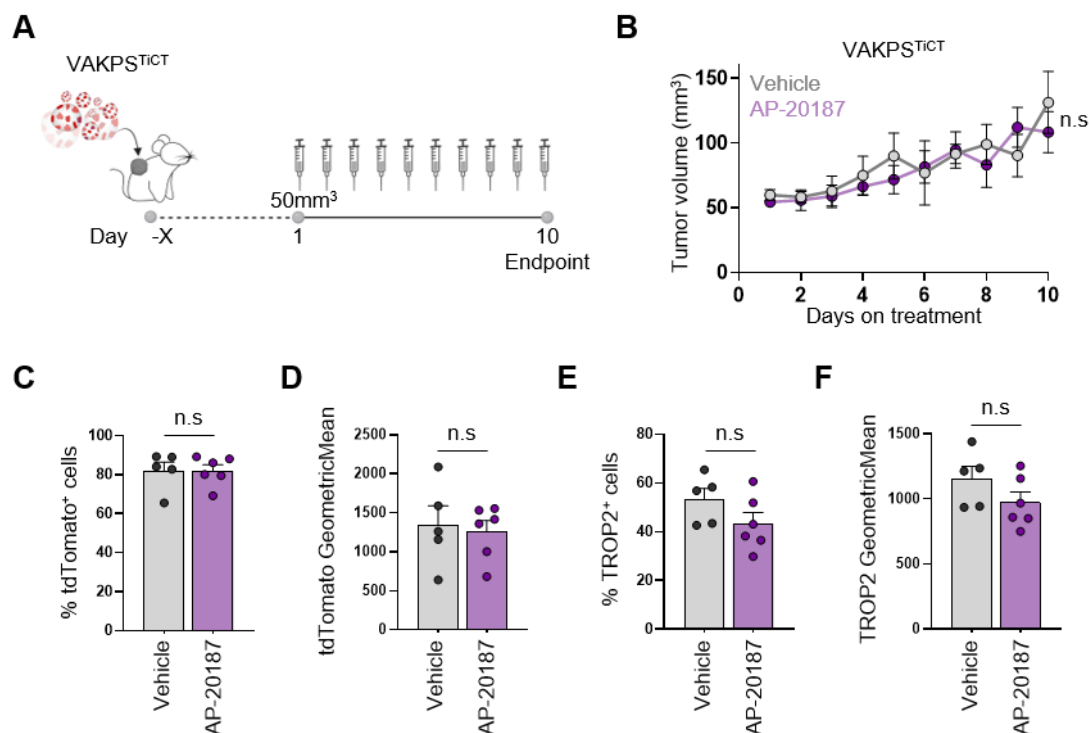


Figure 45. TROP2 expression levels are not sufficient to induce iCaspase 9 dimerization by AP-20187 treatment *in vivo*. **A.** Experimental workflow for AP-20187 treatment *in vivo*. **B.** Tumour volume (mm³) during AP-20187 treatment. **C-D.** Quantification of (**C**) the percentage of tdTomato⁺ cells and (**D**) tdTomato mean signal intensity from VAKPS^{TiCT} tumours after ten days of AP-20187 treatment. **E-F.** Quantification of (**E**) the percentage of TROP2⁺ cells and (**F**) TROP2 mean signal intensity from VAKPS^{TiCT} tumours after ten days of AP-20187 treatment. Statistical analysis was performed using unpaired t-test.

TROP2⁺ cells fuel CRC tumour growth

Limited dilution transplantation assays are a well-accepted and established method to evaluate the tumour initiation capacity of a putative stem cell population (Loh and Ma, 2024). However, this approach requires tumour cell dissociation, sorting and cell inoculation into recipient immunodeficient mice. Furthermore, in this assay, tumour microenvironment and cell-to-cell interactions are overlooked. Thus, to strengthen the statement of defining CSCs additional complementary methods need to be employed. In order to maintain the tumour microenvironment and cell-to-cell interactions I employed genetic-lineage tracing. This method enables the labelling of clonal expansions generated from a specific cell population.

Generation of a GEMM to lineage trace TROP2-expressing cells.

To lineage trace TROP2⁺ cells, in collaboration with the DKFZ transgenic animal facility, I generated the *Tacstd2*^{CreERT2} GEMM. In this model, the promoter of the *Tacstd2* gene drives expression of the Cre recombinase fused to a mutated ligand binding domain of the human estrogen receptor (ERT2) without compromising TROP2 expression (**Figure 46A**). Cre recombination is inducible with tamoxifen treatment. To that end, I designed a targeting vector carrying the "P2A-CreERT2-FRT-NemomycinResistance (NeoR)-FRT" cassette (**Figure 46A**). Flanking this cassette, a 4996 bp of 5' homology arm and 5000 bp of 3' homology arm were introduced to target the insertion right before the TAG stop codon of the *Tacstd2* gene (**Figure 46A**). This CreERT2 knock-in allele was generated by homologous recombination of a Bacterial Artificial Chromosome (BAC) clone in embryonic stem (ES) cells. Neomycin-resistant ES cell clones were expanded *in vitro* and correct insertion of the donor sequence was verified by PCR (**Figure 46B**). Dr. Franciscus van der Hoeven and Brittney Armstrong injected the ES positive clones into C57BL/6N blastocysts and embryo-transferred them into RjOrl:SWISS recipient female mice.

The F0 carrying the *Tacstd2*^{CreERT2-FRT-NeoR-FRT} allele was crossed with the Flipase recombinase-expressing (*FLPe*) mice to remove the NeoR cassette. The offspring (F1) was genotyped for the presence of the NeoR cassette (**Figure 47A**) and the *Tacstd2*^{CreERT2} mouse colony was established from a single founder animal in which the NeoR cassette was flipped-out (**Figure 47B**). In order to lineage trace TROP2⁺ cells, *Tacstd2*^{CreERT2} mice were crossed with the *Rosa26*^{LSL-tdTomato} mice (TcT mice) (**Figure 47A**).

Next, I set out to confirm that the *Tacstd2*^{CreERT2} allele faithfully labels TROP2⁺ cells. To that end, TcT mice were treated with tamoxifen and dissected six days after treatment. Only the skin, which has high TROP2 expression level, was marked by tdTomato, indicating the specificity of the newly generated allele for tracing TROP2-expressing cells (**Figure 48A-B**).

Altogether these results confirm the successful generation of a mouse model to specifically trace TROP2⁺ cells.

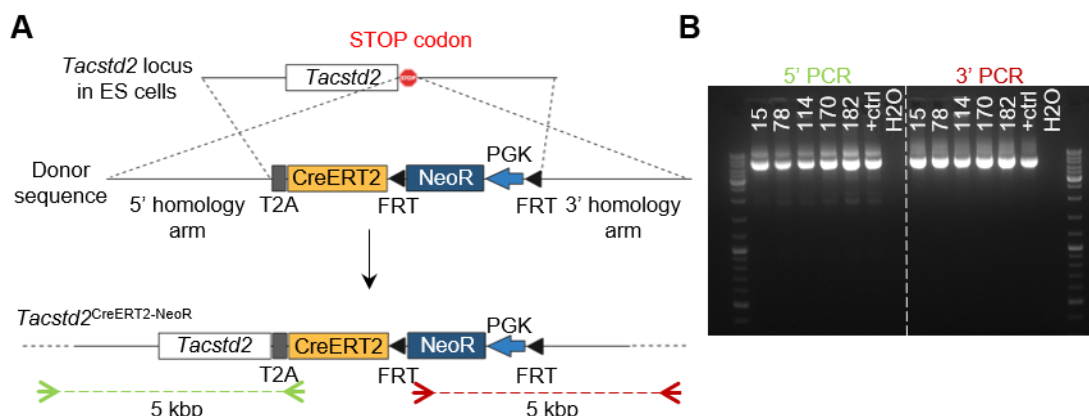


Figure 46. Generation of the *Tacstd2*^{CreERT2} mouse line. **A.** Scheme of the *Tacstd2* gene targeting strategy to knock-in the “T2A-CreERT2-FRT-NeoR-FRT” cassette by homologous recombination in ES cells. The T2A substitutes the STOP codon of the *Tacstd2* gene. The green and red arrows indicate the annealing site of the primers for the 5' and 3' specific PCR, respectively. The green and red dashed lines indicate the PCR products for validating the specific integration of the donor sequence. **B.** PCR products of the 5 positive ES colonies out of the 288 ES colonies tested for the specific integration.

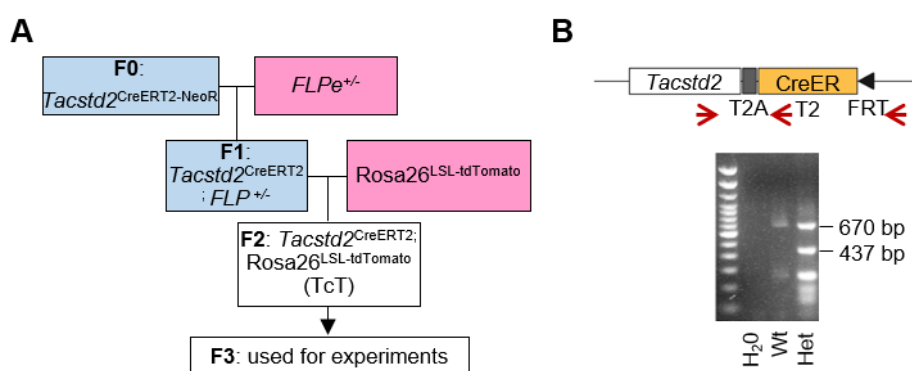


Figure 47. Generation of the *Tacstd2*^{CreERT2}; *Rosa26*^{LSL-tdTomato} (TcT) mouse line. **A.** Breeding scheme for the establishment of the TcT mouse colony. **B.** Scheme of the strategy for genotyping the *Tacstd2*^{CreERT2} mouse line. Red arrows indicate the primers used. Bottom, PCR product of the *Tacstd2*^{CreERT2} allele. Wt, wild-type; het, heterozygous.

Of note, the small intestine and the colon do not have basal TROP2 expression (**Figure 48A**). Similarly, small intestine-derived organoids did not express TROP2, recapitulating the results observed *in vivo* (**Figure 49A**). Indeed, lineage tracing from the TcT small intestine-derived organoids showed no tdTomato⁺ cells, as expected from the absence of TROP2⁺ cells in the organoids (**Figure 49B**). As a positive control for stem cell lineage tracing I used the *Lgr5*^{EGFP-IRES-creERT2}; *Rosa26*^{LSL-tdTomato} (LcT) GEMM. This model allows for the visualisation of the LGR5⁺ cells as well as for the tracing of these cells due to the GFP and CreER cassettes inserted in the *Lgr5* locus, respectively ([Barker et al., 2007](#)). Small intestine-derived organoids

from LcT mice had 10% LGR5-GFP⁺ cells while still no expression of TROP2 was observed (**Figure 49C**). In line with the literature, lineage tracing from LcT small intestine-derived organoids demonstrated that Lgr5-GFP⁺ cells generated progeny, as indicated by the increasing number of tdTomato⁺ cells over time after the 4-OH-tamoxifen (4-OHT) pulse (**Figure 49B**) ([Barker et al., 2007](#)).

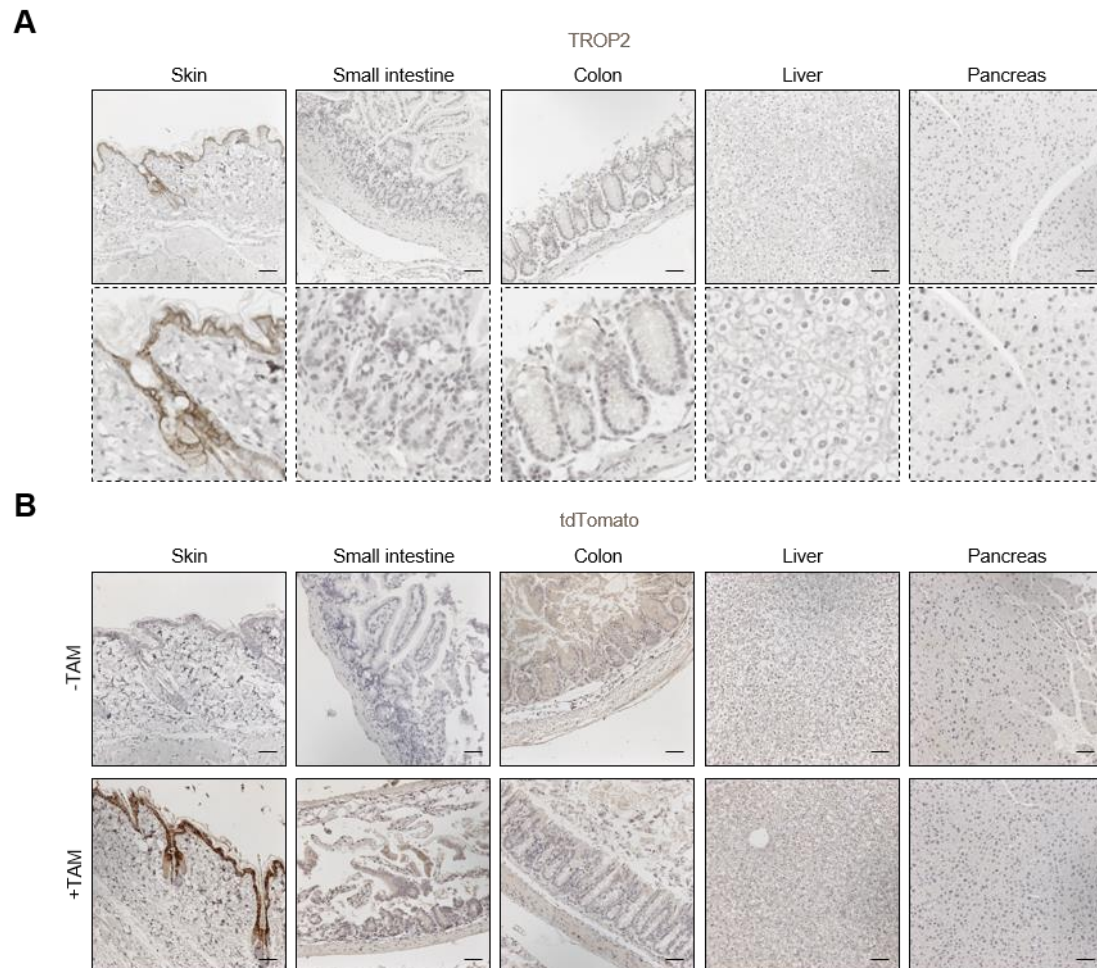


Figure 48. tdTomato labels TROP2⁺ cells in the TcT GEMM. **A.** Representative images of TROP2 IHC across different murine adult tissues during homeostasis. Dashed lines indicate higher magnification. **B.** Representative images of tdTomato IHC six days after tamoxifen induction in the TcT GEMM. Scale bar 50 μ M.

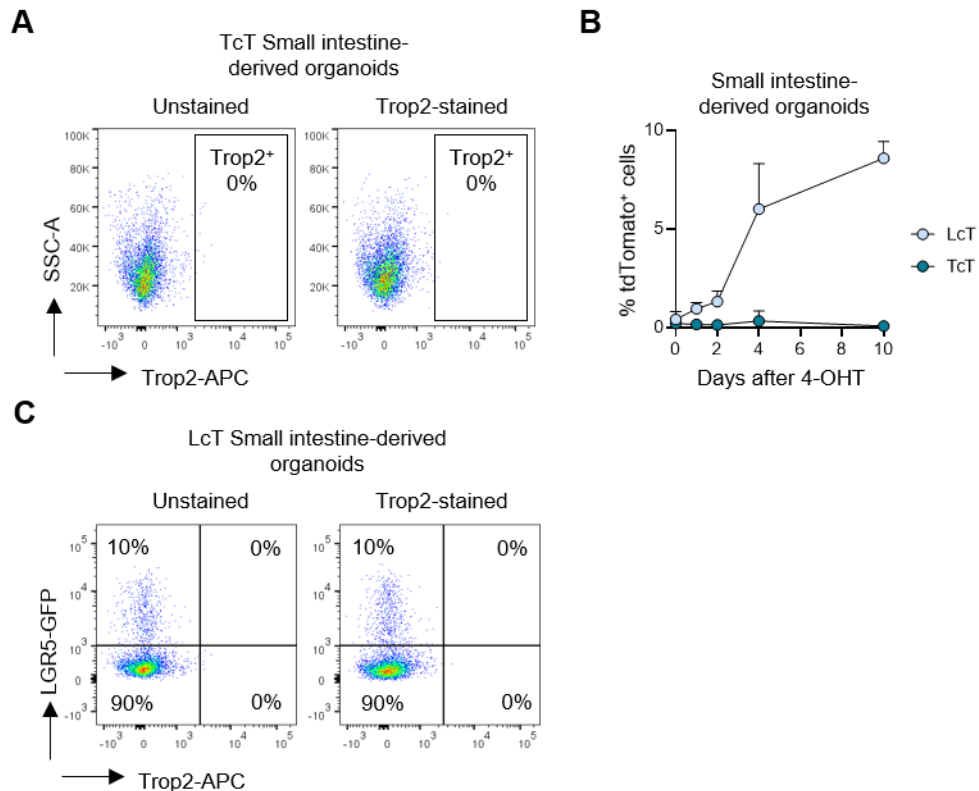


Figure 49. Lineage tracing of TROP2⁺ cells in small intestine-derived organoids. **A.** Flow cytometry plot showing the lack of TROP2 expression in TcT small intestine-derived organoids. **B.** Flow cytometry quantification of tdTomato⁺ cells in TcT and LcT small intestine-derived organoids at different days after the 4OH-tamoxifen pulse. Frequency of populations referred to the number of viable cells. **C.** Flow cytometry plot showing the percentage of TROP2⁺ and LGR5-GFP⁺ cells in LcT small intestine derived organoids.

In vitro transformation of TcT small intestine-derived organoids to carry the CRC-associated oncogenic mutations.

To explore the contribution of TROP2⁺ cells in fuelling colorectal tumour growth I transformed the TcT small intestine-derived organoids *in vitro*. I generated two different organoid lines recapitulating the *Apc*^{mut} and the *Apc*^{wt} CRC subtypes. In order to generate the *Apc*^{mut} CRC line I introduced *Apc* (A) and *Trp53* (P) loss-of-function mutations by CRISPR/Cas9 genome editing technology (TcT-AP line). Additionally, the oncogenic *Kras*^{G12D} (K) mutation was introduced using the sleeping beauty transposase system (TcT-AKP line) (**Figure 50A-G**). To generate the *Apc*^{wt} CRC line I introduced the *Trp53* (P) loss-of-function mutation and the oncogenic *Kras*^{G12D} (K) mutation. Additionally, the Notch1ICD overexpression was introduced by lentiviral infection of a vector encoding for Notch1ICD controlled by the EF1 α promoter (TcT-KPN line) (**Figure 51A-H**). These TcT-AKP and TcT-KPN organoids enabled the lineage tracing of TROP2⁺ cells in advanced CRC models.

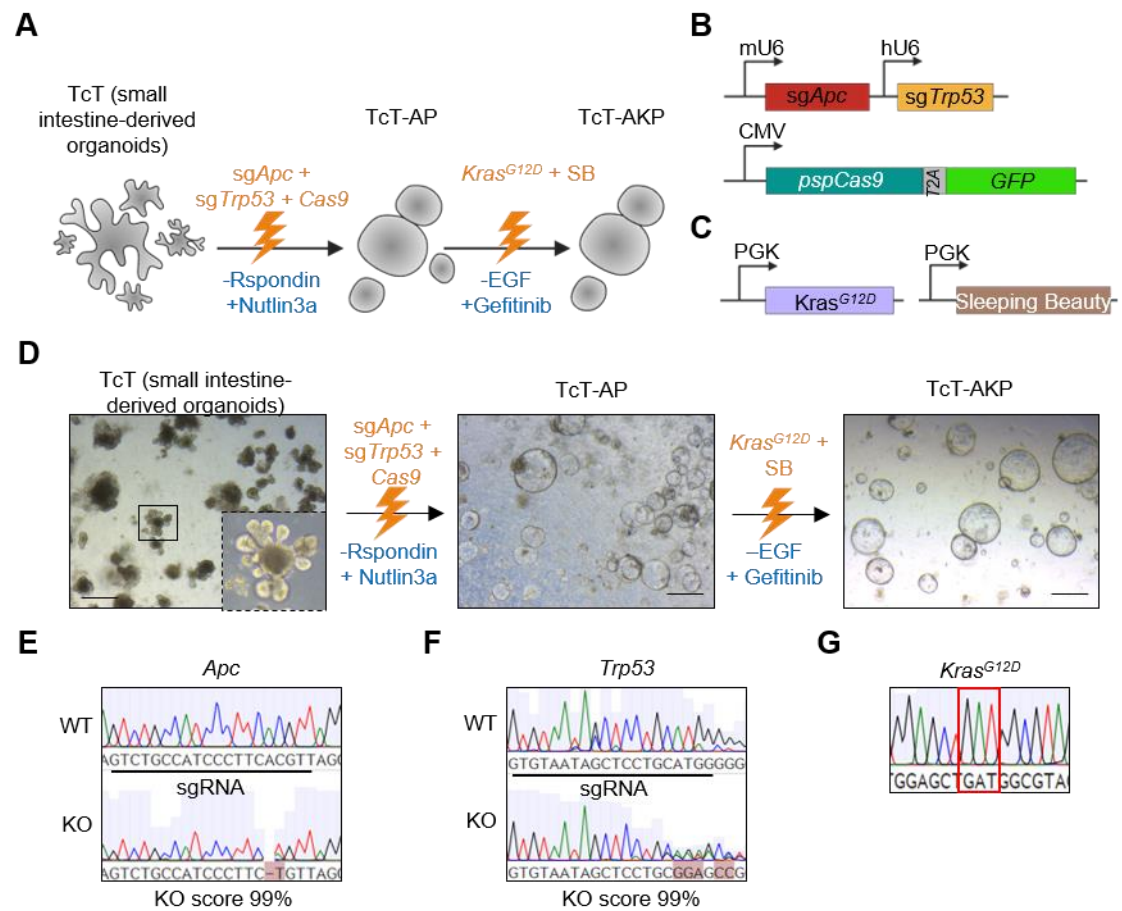


Figure 50. Genetic modification of TcT small intestine-derived organoids to generate TcT-AKP tumour organoids. **A.** Workflow scheme for the generation of the TcT-AKP organoids. SB, sleeping beauty. **B.** Scheme of the vectors used for the generation of the *Apc* and *Trp53* loss-of-function mutations. **C.** Scheme of the vectors used for the generations of the overexpression of the *Kras^{G12D}* oncogenic mutation. **D.** Representative images of the organoids after media selection processes. Scale bar 200 μ m. **E-F.** Sanger sequence for the validation of the (E) *Apc* and (F) *Trp53* knock-outs. **G.** Sanger sequence for the validation of the insertion of the *Kras^{G12D}* oncogenic mutation.

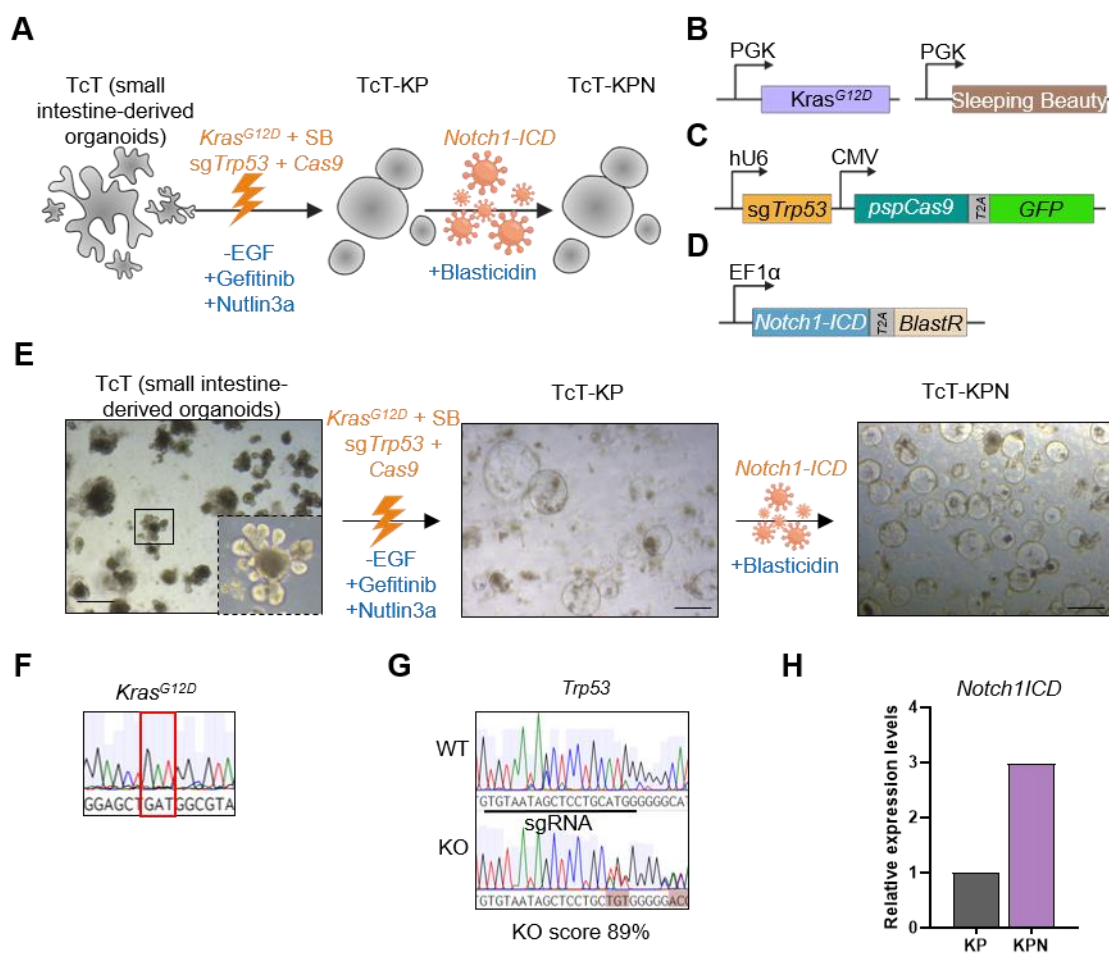


Figure 51. Genetic modification of TcT small intestine-derived organoids to generate TcT-KPN tumour organoids. **A.** Workflow scheme for the generation of the TcT-KPN organoids. SB, sleeping beauty. **B.** Scheme of the vectors used for the generations of the overexpression of the *Kras*^{G12D} oncogenic mutation. **C.** Scheme of the vector used for the generation of the *Trp53* loss-of-function mutation. **D.** Scheme of the vector used for the constitutive overexpression of N1ICD. **E.** Representative images of the organoids after media selection processes. Scale bar 200 μm. **F.** Sanger sequence for the validation of the insertion of the *Kras*^{G12D} oncogenic mutation. **G.** Sanger sequence for the validation of the *Trp53* knock-out. **H.** RT-qPCR confirming the overexpression of N1ICD.

In vitro lineage tracing of TROP2⁺ cancer cells

Once the TcT-AKP and TcT-KPN organoid lines were generated, I performed lineage tracing experiments in both organoid lines *in vitro* (**Figure 52A**). A tdTomato-labelled population emerged two days after the 4-OHT pulse in the TcT-AKP organoids. tdTomato signal did not increased over time but remained stable or even decreased over time, indicating that TROP2 does not fuel tumour growth in this model (**Figure 52B-D**). Unfortunately, I failed to label TROP2⁺ cells in TcT-KPN organoids *in vitro* (data not shown).

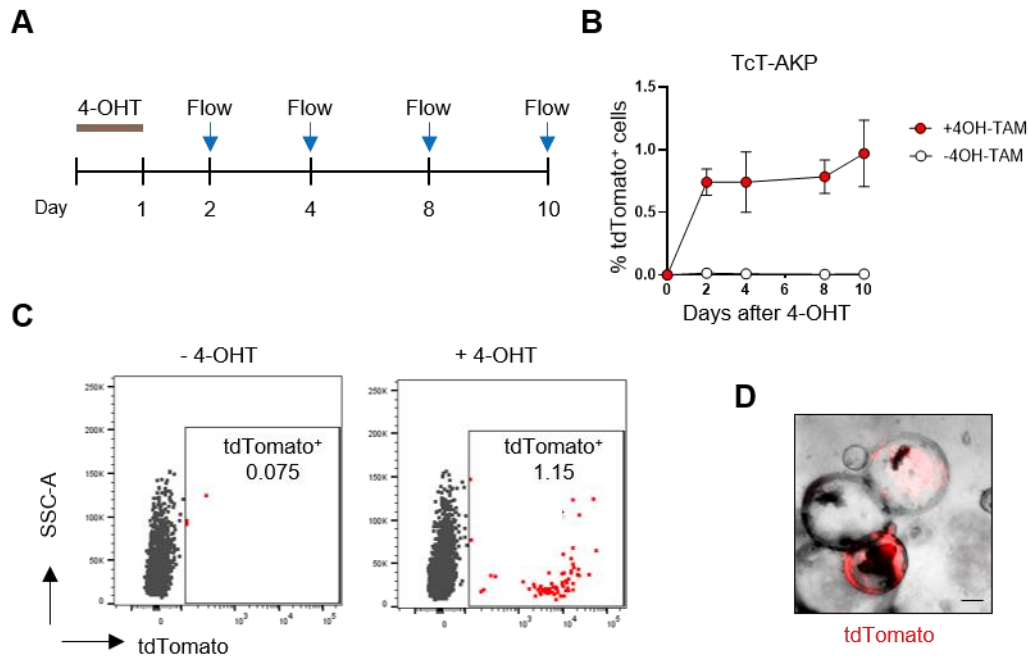


Figure 52. Lineage tracing analysis of TROP2⁺ cells in TcT-AKP organoids. **A.** Experimental workflow for the lineage tracing *in vitro*. **B.** Flow cytometry quantification of tdTomato⁺ cells in TcT-AKP organoids at different days after the 4-OHT pulse. Frequency of populations referred to the number of viable cells (n=3). **C.** Flow cytometry plots of tdTomato⁺ cells in TcT-AKP organoids six days after the 4-OHT pulse. Cell populations referred from the viable cells. **D.** Confocal image of TcT-AKP organoids six days after the 4-OHT pulse. Scale bar 100 μ m.

In order to understand the reason behind the absence of recombination of the *Rosa26*^{LSL-tdTomato} cassette in the TcT-KPN organoids *in vitro*, I electroporated the organoids with a CMV-Cre vector to rule out the possibility that the *Rosa26*^{LSL-tdTomato} cassette was silenced. Fortunately, a high number of tdTomato⁺ cells appeared two days after electroporation, indicating that the *Rosa26*^{LSL-tdTomato} cassette was still functional (**Figure 53**).

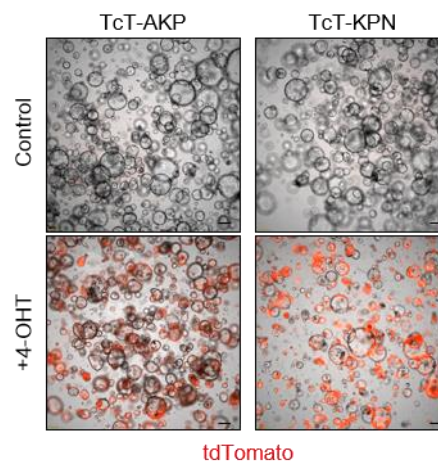


Figure 53. The *Rosa26*^{tdTomato} allele is still functional in the TcT-KPN MTO line. Representative images of the tdTomato signal 48 hours after transfection of the TcT-KPN MTO line with the CMV-Cre vector. The TcT-AKP MTO line was used as a positive control. Scale bar 100 μ m.

Since TROP2 is expressed in the TcT-KPN organoid line (**Figure 54A**), I hypothesized that, similarly to the problem I observed with the iCaspase9 cassette, TROP2 expression

levels, and thus, CreERT2 levels, might not be enough to induce recombination of the *Rosa26^{LSL-tdTomato}* cassette in this cell line. Thus, I checked TROP2 expression levels in the TcT-KPN organoids by RT-qPCR and compared them to the levels in the TcT-AKP organoids, which I used as a positive control of levels needed to recombine the *Rosa26^{LSL-tdTomato}* cassette. Indeed, TROP2 expression levels were highly reduced in the TcT-KPN MTO line compared to the TcT-AKP MTO line (**Figure 54B**), suggesting that these expression levels might not be sufficient to recombine the LoxP-STOP-LoxP cassette.

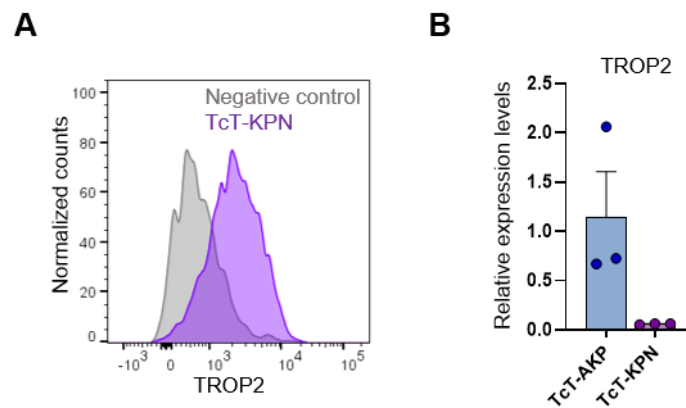


Figure 54. TcT-KPN MTO line has low expression level of TROP2. A. Flow cytometry plot showing the TROP2 level in TcT-KPN MTOs. **B.** RT-qPCR of TROP2 mRNA levels in TcT-AKP and TcT-KPN MTO lines (n=3).

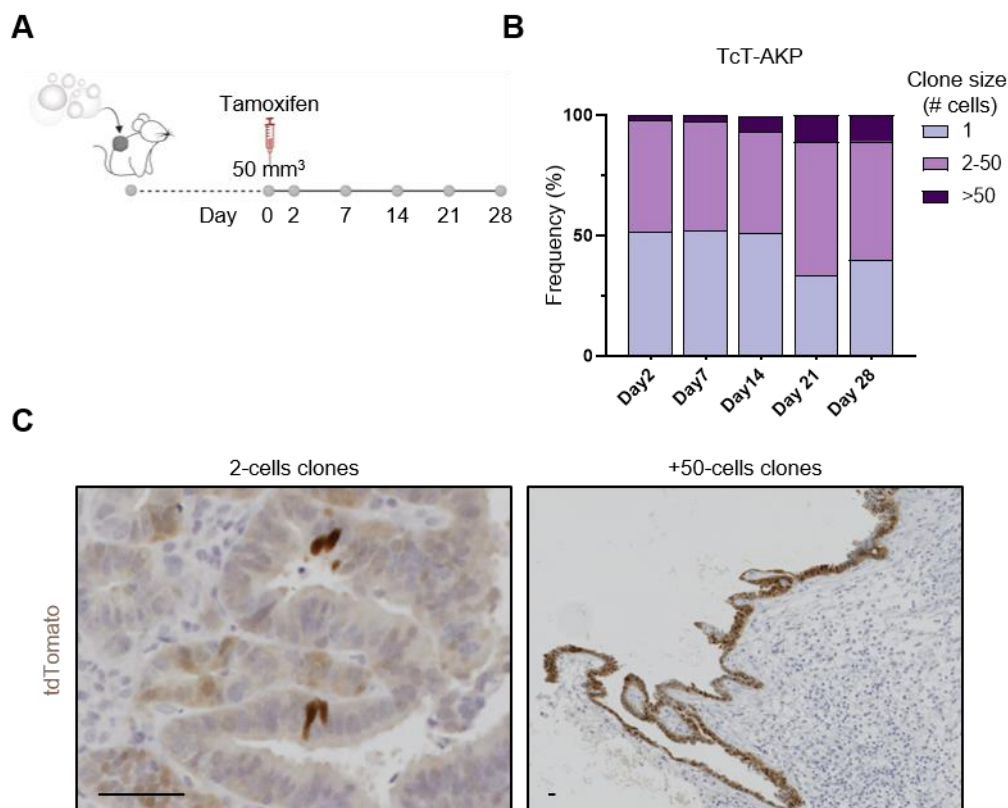


Figure 55. *In vivo* lineage tracing analysis of TROP2⁺ TcT-AKP cells. A. Experimental workflow for the lineage tracing *in vivo*. **B.** Size distribution of clones generated by the *Tacstd2^{CreERT2}* allele in TcT-AKP cells *in vivo*. **C.** Representative immunohistochemistry for tdTomato of a small and a large clone. Scale bar 50 μm.

I next performed lineage tracing experiments of TROP2⁺ cells using TcT-AKP MTOs *in vivo*. To that end, I subcutaneously transplanted TcT-AKP cells in the flank of C57BL/6J mice. First, I determined the tamoxifen dosage needed to recombine only single TROP2⁺ cells. I found that a dose of 1 mg/kg is suitable to induce recombination of the LSL-tdTomato transgene in single TROP2⁺ cells. Having set the parameters, I tracked the TROP2-labelled progenies over time by sampling the animals at different timepoints after the tamoxifen pulse (**Figure 55A**). I then analysed by histology different sections of the tumours and quantified the size of the tdTomato⁺ clones at the different timepoints. Interestingly, I observed an increased number of tdTomato⁺ cells per clone at later timepoints (**Figure 55B-C**). These findings suggest that TROP2⁺ cells contribute to fuel tumour growth *in vivo*. Unfortunately, no tracing was observed for the TcT-KPN cells *in vivo*, due to lack of TROP2 expression in the subcutaneous tumours (data not shown).

Understanding the role of TROP2⁺ cells during CRC progression.

TROP2⁺ cells are the metastasis-initiating cells (MICs) in CRC

In the recent years high research efforts have been focused in characterizing and tracking the MICs. In 2020, Fumagalli *et al.* set out to study the role of LGR5⁺ CSCs during CRC metastasis using intravital imaging. Strikingly, the majority of disseminating tumour cells were LGR5⁻ (Fumagalli *et al.*, 2020a). Furthermore, analysis of micro- and macro-metastatic lesions have shown that restoration of the LGR5⁺ CSC pool was crucial for the progression into macro-metastasis (Canellas-Socias *et al.*, 2022; Fumagalli *et al.*, 2020a; Heinz *et al.*, 2022). These results suggest that an alternative CSC population is important for metastatic dissemination and seeding into the metastatic organ. Hence, I hypothesized that TROP2⁺ CSCs might be crucial during these processes.

Histological analysis in human and mouse tumours revealed that TROP2 is highly expressed at the invasion front as well as in micro-metastatic lesions while LGR5 is absent (**Figure 56A-B**). Furthermore, LGR5⁺ cells reappear at the macro-metastatic stage (**Figure 56C**). In line with this observation, analysis of recently published scRNA-sequencing of different stages of CRC from mouse models showed an enrichment of TROP2⁺ cells in micro-metastatic lesions, suggesting an important role of TROP2⁺ tumour cells in tumour dissemination and metastatic outgrowth (**Figure 56D-F**) (Canellas-Socias *et al.*, 2022).

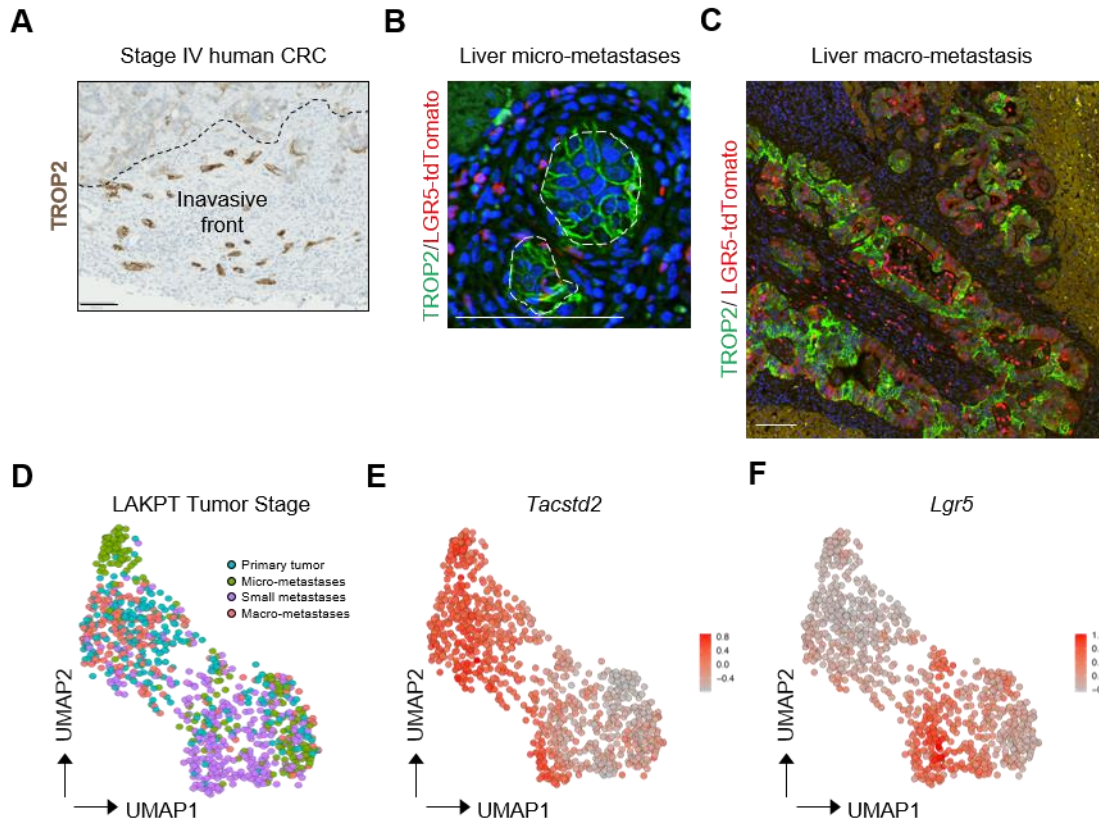


Figure 56. TROP2⁺ cells mark the invasive front and micro-metastases. **A.** Representative TROP2 IHC image of a stage IV human CRC. **B-C.** Immunofluorescence for TROP2 and LGR5-tdTomato of VAKPS^{LICT} liver (**B**) micro-metastases and (**C**) macro-metastases. Scale bar 100µm. **D-F.** UMAP layout from *Lgr5*^{EGFP-IRES-creERT2}; *Apc*^{fl/fl}; *Kras*^{G12D/+}; *Trp53*^{fl/fl}; *Tgfbr2*^{fl/fl} (LAKPT) tumour cells from (Canellas-Socias et al., 2022) colored by (D) metastatic stage (E) *Tacstd2* and (F) *Lgr5* expression levels.

Hence, I further investigated the contribution of TROP2⁺ cells in CRC metastasis. Previous studies showed that LGR5⁻ cells are the metastatic cells in CRC (Fumagalli et al., 2020a; Moorman et al., 2023). I assessed the metastatic potential of the TROP2⁻ and TROP2⁺ cells from both the LGR5⁻ and the LGR5⁺ pools separately. To that end, I sorted the four different populations (LGR5⁻/TROP2⁻, LGR5⁺/TROP2⁻, LGR5⁻/TROP2⁺, LGR5⁺/TROP2⁺) from the VAKPS^{LICT} and VKPN^{LICT} MTO models and transplanted them in the spleen of immunocompromised mice in order to assess their metastatic capacity to the liver (**Figure 57A**).

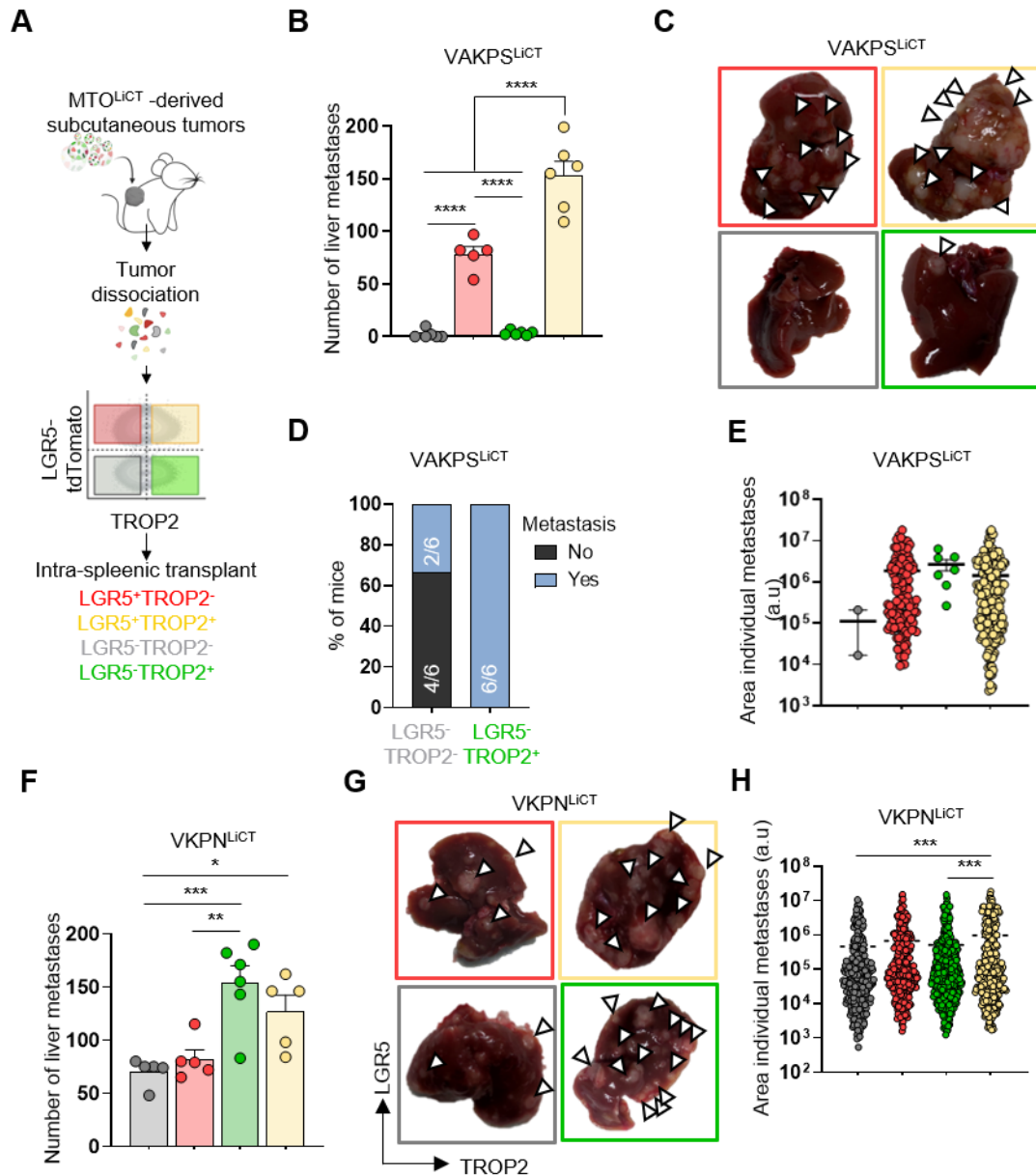


Figure 57. TROP2 marks cancer cells with high metastatic potential in VAKPS and VKPN models. **A.** Workflow scheme for FACS separation of LGR5⁻/TROP2⁻, LGR5⁺/TROP2⁻, LGR5⁻/TROP2⁺, LGR5⁺/TROP2⁺ cell populations derived from subcutaneous tumours for subsequent intra-spleenic transplantation in the flank of secondary recipient immunodeficient NSG mice. **B.** Bar graph showing the number of VAKPS^{LICT} liver metastases originated in NSG mice from the different sorted cell populations in A. Every dot represents one mouse. **C.** Representative images of the livers from B. Arrows indicates metastatic nodules. **D.** Percentage of mice with liver metastases derived from the LGR5⁻/TROP2⁺, LGR5⁺/TROP2⁺ VAKPS^{LICT} sorted cell populations. **E.** Quantification of the area of the individual metastases derived from the four VAKPS^{LICT} sorted cell populations in A. **F.** Bar graph showing the number of VKPN^{LICT} liver metastases originated in NSG mice from the different sorted cell populations in A. **G.** Representative images of the livers from F. Arrows indicates metastatic nodules. **H.** Quantification of the area of the individual metastases derived from the four VKPN^{LICT} sorted cell populations in A. Statistical analysis was performed using Ordinary One-way ANOVA.

Interestingly, in the VAKPS^{LICT} model, LGR5⁺ sorted cell populations had a significant higher metastatic capacity than the LGR5⁻ sorted populations (**Figure 57B-C**). Since I inoculated the cells in the spleen so that they quickly reach the liver through the bloodstream, this technique skipped multiple bottlenecks of the metastatic cascade, explaining why the LGR5⁺ cells (the CSCs in this model) generate more metastases. Nevertheless, when

comparing the metastatic potential of the LGR5⁺/TROP2⁻ and the LGR5⁺/TROP2⁺, I observed a significant increased number of liver metastases in the LGR5⁺/TROP2⁺ (**Figure 57B-C**). Furthermore, when analysing the metastatic capacity of the LGR5⁻ sorted cells, which are the currently accepted metastatic cells, I observed that 100% of the mice transplanted with LGR5⁻/TROP2⁺ developed liver metastases while only two out of six mice transplanted with LGR5⁻/TROP2⁻ cells developed metastases (**Figure 57D**). No significant difference in the size of the metastases was observed across the groups (**Figure 57E**).

In the in the VKPN^{LICT} model, both TROP2⁺ sorted cell populations had a significant higher metastatic capacity than the TROP2⁻ sorted populations regardless of LGR5 level (**Figure 57F-G**). These results reinforce the previous observations where I concluded that in this model TROP2 marks CSCs. Only LGR5⁺/TROP2⁺ derived metastases had a significant higher size compared to the LGR5⁻/TROP2⁺ and LGR5⁻/TROP2⁻ (**Figure 57H**). Taken together, TROP2⁺ cells have a higher metastatic capacity in both VAKPS and VKPN models compared to the TROP2⁻ cells. Interestingly, metastases produced by all the four sorted cell populations contained the other tumour cell types owing to extensive cell plasticity observed in these CRC models (**Figure 58A-B**).

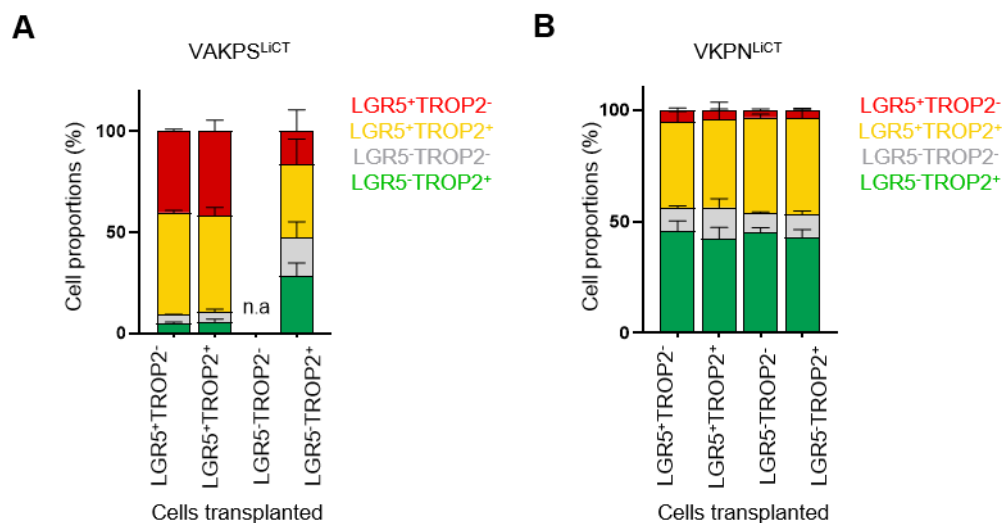


Figure 58. Liver metastases derived from the different sorted cell populations (LGR5⁻/TROP2⁻, LGR5⁺/TROP2⁻, LGR5⁻/TROP2⁺, LGR5⁺/TROP2⁺) restored tumour heterogeneity. A-B. Quantifications of the percentage of LGR5⁻/TROP2⁻, LGR5⁺/TROP2⁻, LGR5⁻/TROP2⁺, LGR5⁺/TROP2⁺ cells from the liver metastases derived from the LGR5⁻/TROP2⁻, LGR5⁺/TROP2⁻, LGR5⁻/TROP2⁺, LGR5⁺/TROP2⁺ sorted cell populations in (A) VAKPS^{LICT} and (B) VKPN^{LICT}.

TROP2 levels are increased in response to chemotherapy treatment.

CSCs play a major role in driving treatment failure largely due to their enhanced plasticity, which allows them to quickly evolve and adapt to harsh conditions such as chemotherapy treatment (Loh and Ma, 2024). As a result, therapeutic strategies to effectively target and eradicate CSCs are on the scope of current research efforts.

Recent publications have inferred that, after chemotherapy, the adult ISC program is downregulated while foetal ISC program is upregulated in CRC (Alvarez-Varela et al., 2022; Vasquez et al., 2022). To infer these results, I treated TcT-AP and TcT-AKP organoid lines with FOLFIRI for 72 hours *in vitro*. Similar to previous observations, markers from the foetal ISC signature, including TROP2, were significantly upregulated upon FOLFIRI treatment. However, I did not observe significant changes in the expression levels of adult ISC markers (Figure 59A-B). Of note, both, the percentage of TROP2⁺ cells and the TROP2 signal intensity per cell were significantly increased after FOLFIRI treatment in both MTO lines (Figure 59 C-F).

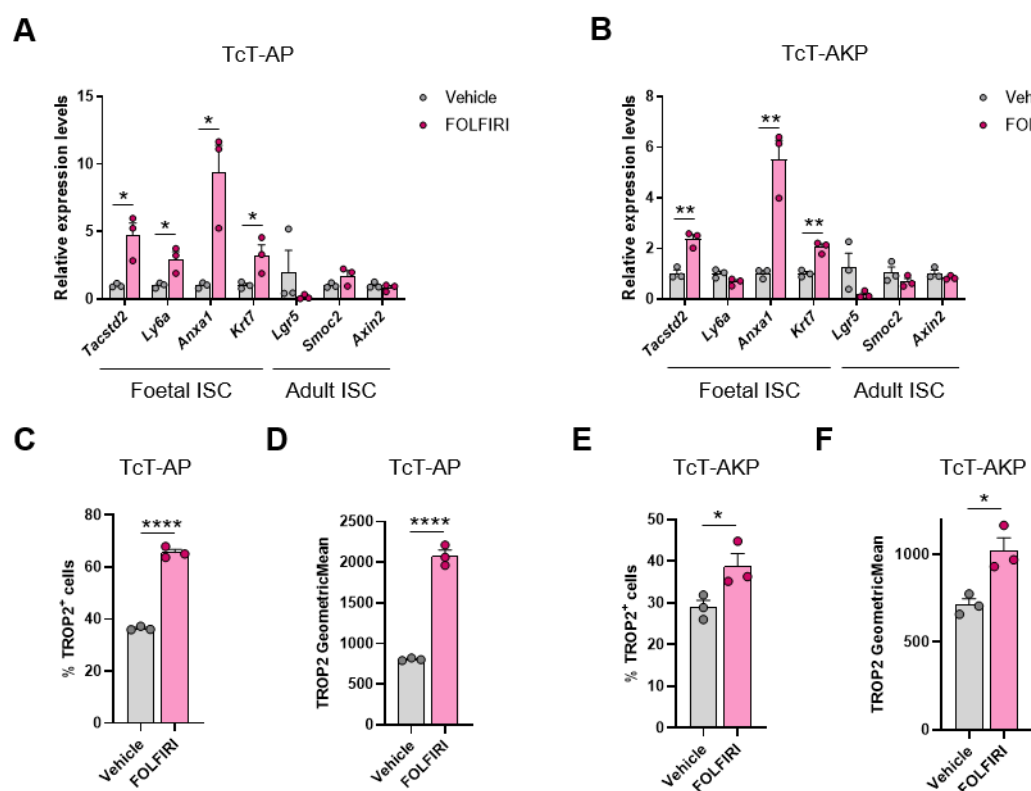


Figure 59. TROP2 expression levels increase after chemotherapy in MTOs. A-B. Relative expression levels of markers from the foetal ISC and adult ISC program after 72 hours of FOLFIRI treatment *in vitro* from (A) TcT-AP and (B) TcT-AKP (n=3). C-D. Quantification of the percentage of (C) TROP2⁺ cells and (D) TROP2 staining intensity from TcT-AP organoids treated with FOLFIRI for 72 hours (n=3). E-F. Quantification of the number of (E) TROP2⁺ cells and (F) TROP2 staining intensity from TcT-AKP organoids treated with FOLFIRI for 72 hours (n=3).

To gain deeper insights into the role of TROP2⁺ cells in chemotherapy resistance I utilized the lineage tracing system. This tool allows to understand whether the pre-existing TROP2⁺ cells within the tumour mass are the drug-persistent cells or if instead, TROP2 expression and the foetal ISC program are acquired by tumour cells in response to chemotherapy treatment as an adaptational mechanism to chemotherapy treatment.

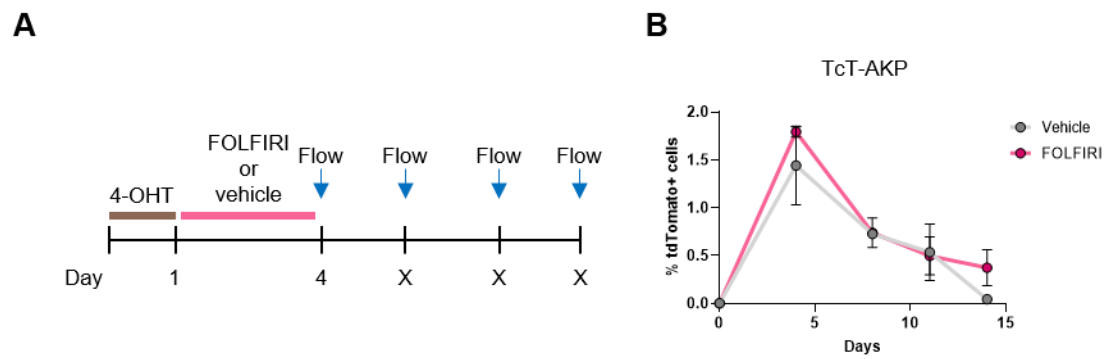


Figure 60. TROP2 does not mark drug-persistent cells. **A.** Experimental workflow for the lineage tracing *in vitro*. **B.** Flow cytometry quantification of tdTomato⁺ cells in **(B)** TcT-AP and **(C)** TcT-AKP MTOs at different days after the 4OH-tamoxifen pulse. Frequency of populations referred to the number of viable cells (n=3).

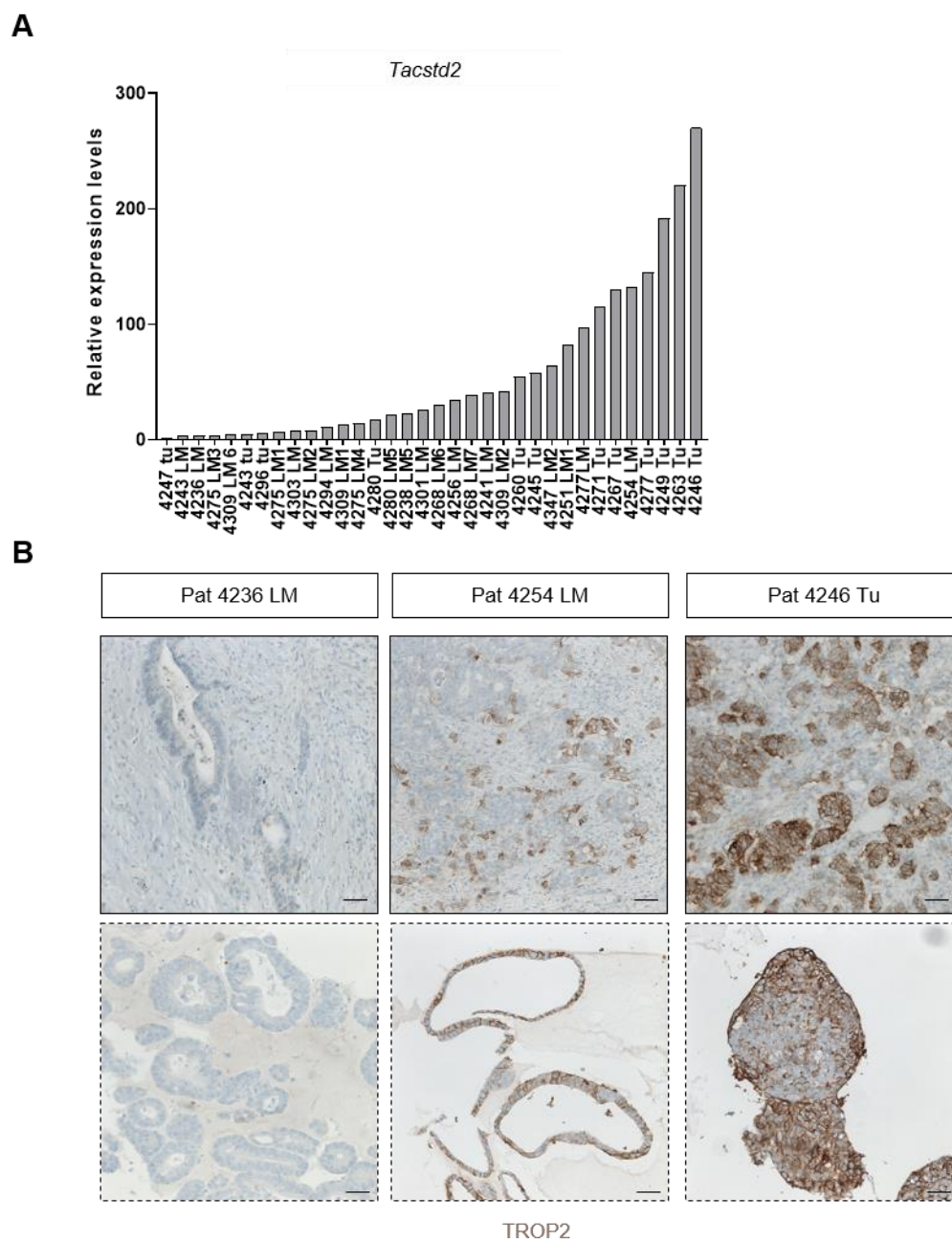


Figure 61. Heterogeneous expression of TROP2 across human CRC patients. **A.** Relative expression level of *TACSTD2* across PDOs. **B.** Representative TROP2 IHC from tumours and PDOs from A. Scale bar 100µm. Pat, patient; LM, liver metastasis; Tu, tumour.

In order to define whether TROP2 marks drug-persistent cells, I treated the TcT-AKP MTO line with 4-OHT 24 hours before treatment with FOLFIRI (**Figure 60A**). The percentage of tdTomato⁺ cells increased in both FOLFIRI and vehicle conditions, however, no difference was observed between both conditions (**Figure 60B**). Furthermore, the percentage of tdTomato⁺ cells decreased over time (**Figure 60B**). Taking together, this data indicated that TROP2⁺ cells are not drug-persistent cells and acquiring TROP2 expression and foetal ISC programs is an adaptive response to FOLFIRI treatment.

Next, I set out to investigate whether these results were also reproduced in PDOs. In our lab, we have generated an extensive CRC PDO biobank that recreates the complex genetic landscape and heterogeneity of CRC. In this biobank, TROP2 is heterogeneously expressed across the different tumour genotypes as well as in samples from primary tumours and liver metastases (**Figure 61A-B**). In line with the data observed in MTO lines, the percentage of TROP2⁺ cells and the TROP2 signal intensity per cell was significantly increased after FOLFIRI treatment in PDO lines with different TROP2 basal expression levels (**Figure 62 A-C**).

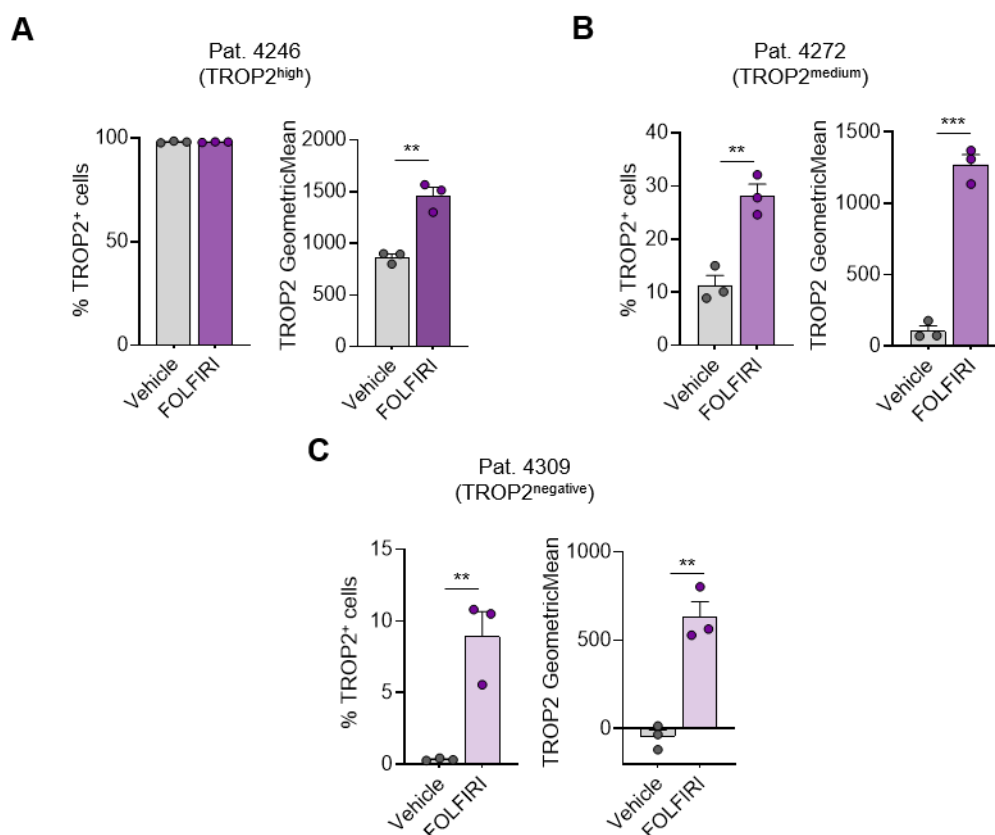


Figure 62. TROP2 expression level increase after chemotherapy treatment in PDOs. **A.** Quantification of the percentage of TROP2⁺ cells and TROP2 staining intensity from PDO from patient 4246 treated with FOLFIRI for 72

hours (n=3). **B.** Quantification of the percentage of TROP2⁺ cells and TROP2 staining intensity from PDO from patient 4272 treated with FOLFIRI for 72 hours (n=3). **C.** Quantification of the percentage of TROP2⁺ cells and TROP2 staining intensity from PDO from patient 4309 treated with FOLFIRI for 72 hours (n=3).

Defining the role of TROP2 in CRC progression.

TROP2 is a driver of tumour initiation in CRC

TROP2 is a transmembrane glycoprotein known for its prominent expression on trophoblast cells. During embryonic development, TROP2 is highly expressed in the intestine, while being absent in the adult intestinal epithelium (Cubas et al., 2009; Lipinski et al., 1981; Mustata et al., 2013). Nevertheless, its re-expression in the adult intestine has been observed during repairing processes and colorectal cancer (reviewed elsewhere (Fey et al., 2024)). TROP2 is also upregulated in various aggressive cancers, such as triple-negative breast, and non-small cell lung cancers, where its expression has been positively correlated with tumour high tumour stage and poor differentiation (Shvartsur and Bonavida, 2015). Yet, its functional role in CRC progression and metastasis remains unclear.

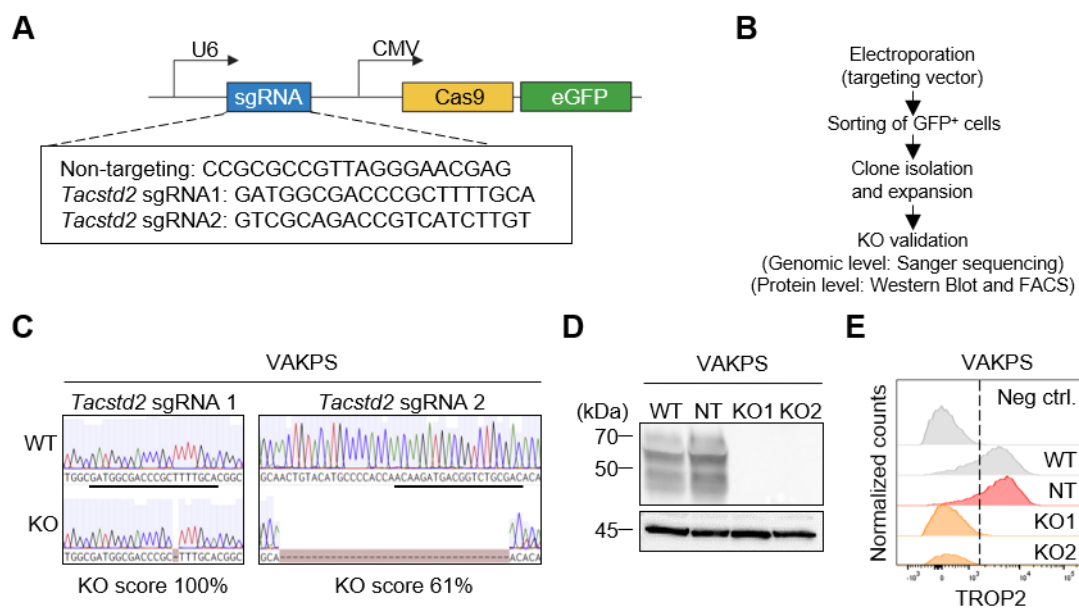


Figure 63. Generation of TROP2 KO VAKPS MTO lines. **A.** Scheme of the targeting vector used for generation of the CRSPR/Cas9-mediated TROP2 KOs. **B.** Workflow for the generation of the CRSPR/Cas9-mediated TROP2 KOs. **C.** Sanger sequence chromatograms confirming the TROP2 KOs in the VAKPS MTOs. Black line indicates the targeting sequencing of the sgRNAs. Data generated by Belén Hackel. **D.** Western-Blot confirming the TROP2 KOs at the protein level. Data generated by Nikolaos Georgakopoulos and Belén Hackel. **E.** Flow cytometry histograms confirming the TROP2 KOs at the protein level. NT, non-targeting; KO, knock-out.

In order to determine whether TROP2 is simply a marker of aggressive CRC cells or is of functional importance in CRC progression, I generated CRISPR/Cas9-mediated TROP2 knock-outs (KOs) in VAKPS MTO lines. To do so, Belén Hackel, a MSc student in the laboratory, electroporated the MTO lines with vectors encoding for Cas9-GFP and the specific sgRNA targeting the TROP2 gene *Tacstd2* (Figure 63A-B). Two days after electroporation, I

FACS separated the GFP⁺ cells and plated the cells *in vitro* for clonal isolation and expansion (**Figure 63B**). The successful knock-out of TROP2 was confirmed at the genomic level by Sanger sequencing and at the protein level by Western-Blot and flow cytometry (**Figure 63B-E**).

Once the TROP2 KO MTO lines were generated, Johanna Kiefer and Belén Hackel assessed the organoid formation capacity *in vitro*. Interestingly, TROP2 KO cells had a significantly lower organoid formation capacity than the non-targeting control (**Figure 64A-B**). Likewise, when subcutaneously transplanting these cells into the flank of NSG mice, VAKPS TROP2 KO cells had decreased tumour initiation capacity and slower tumour growth, indicating that TROP2 expression enhances tumorigenesis (**Figure 65A-C**).

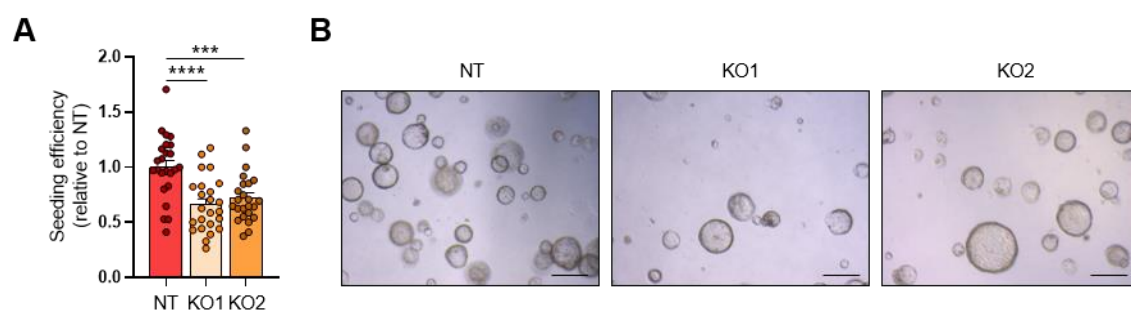


Figure 64. TROP2 deficiency leads to a decrease in the organoid formation capacity *in vitro*. **A.** Quantification of the relative organoid formation capacity of the VAKPS TROP2 KOs five days after seeding 1000 single cells. Every datapoint represent one well. Five to six wells of four independent replicates were quantified. The statistical analysis was performed by using Ordinary on-way ANOVA. **B.** Representative images of the organoids formed five days after seeding. Scale bar 200 μ m. Data generated by Belén Hackel and Johanna Kiefer.

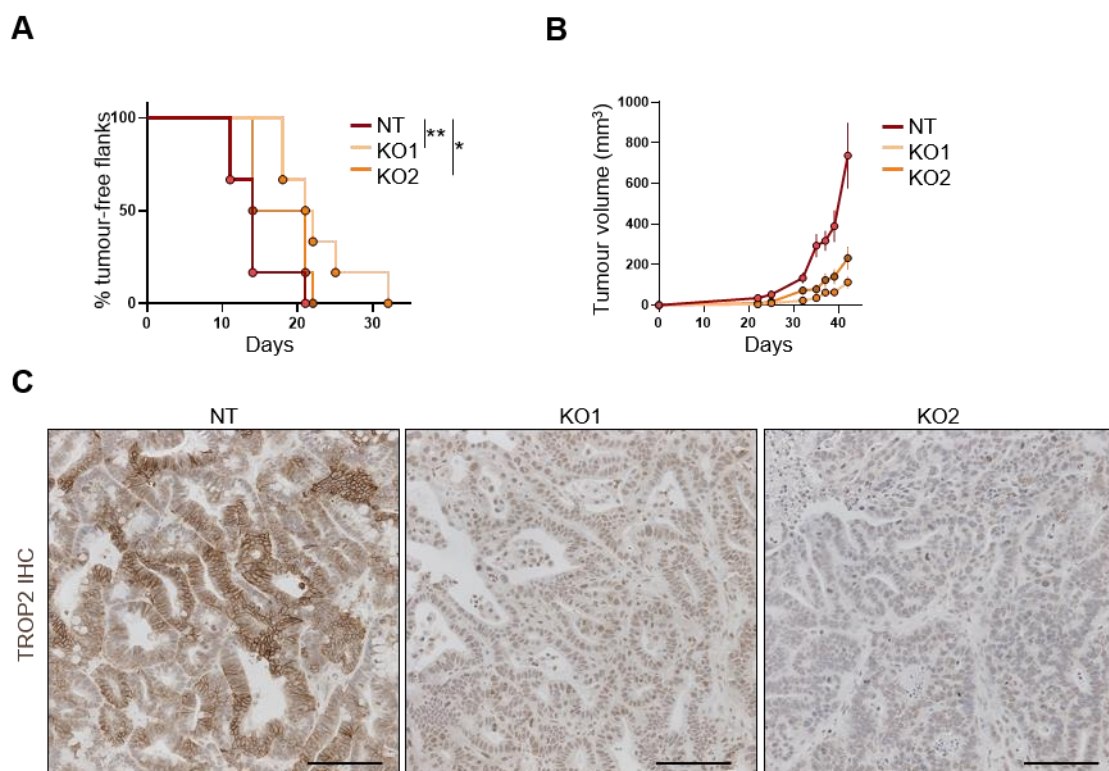


Figure 65. TROP2 deficiency leads to a decrease in the tumour-initiation capacity and tumour growth *in vivo*. **A.** Kaplan-Meier plot representing the tumour initiating capacity of TROP2 KO VAKPS MTO lines. 1000 cells were subcutaneously transplanted in the flank of NSG mice. n=5, 6, 5. Statistical analysis was performed by using unpaired t-test. **B.** Representative IHC images of TROP2 expression in VAKPS tumours. Scale bar 100 μ m.

Additionally, I, with the assistance of Belén Hackel, generated TROP2 overexpressing (OE) MTO lines. To that end, Belén Hackel generated a vector that overexpresses the TROP2 coding sequence together with a blasticidin resistance (BlastR) cassette (**Figure 66A**) and transduced VA (*Villin*^{CreER}; *Apc*^{fl/fl}), VAK (*Villin*^{CreER}; *Apc*^{fl/fl}; *Kras*^{G12D/+}) and VKP (*Villin*^{CreER}; *Kras*^{G12D/+}; *Trp53*^{fl/fl}) MTO lines, which have none or low expression levels of TROP2 (**Figure 66B-C**).

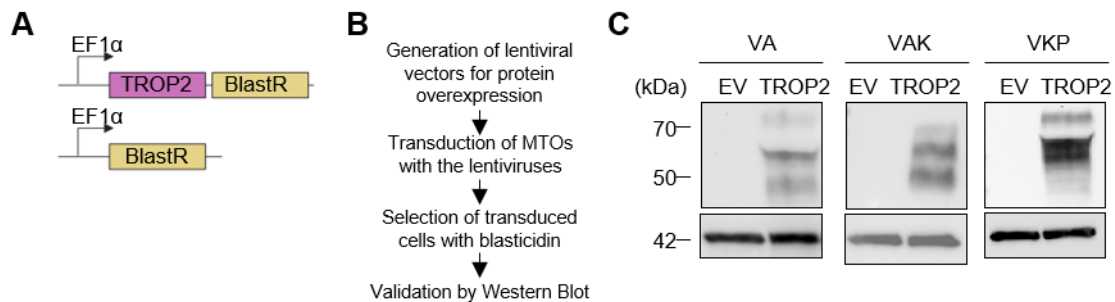


Figure 66. Generation of TROP2 overexpressing MTO lines. **A.** Scheme of the overexpressing vector used for generation of the TROP2 overexpressing cell lines as well as the empty vector (EV) used for the negative control. Plasmids generated by Belén Hackel. **B.** Workflow for the generation of the TROP2 OE MTO lines. **C.** Western-Blots confirming the TROP2 OE at the protein level in the VA, VAK and VKP MTO lines. Data generated by Nikolaos Georgakopoulos and Belén Hackel.

In line with the previous observations, MTO lines overexpressing TROP2 had a significantly higher organoid formation capacity than the non-targeting control *in vitro* (**Figure 67A-D**).

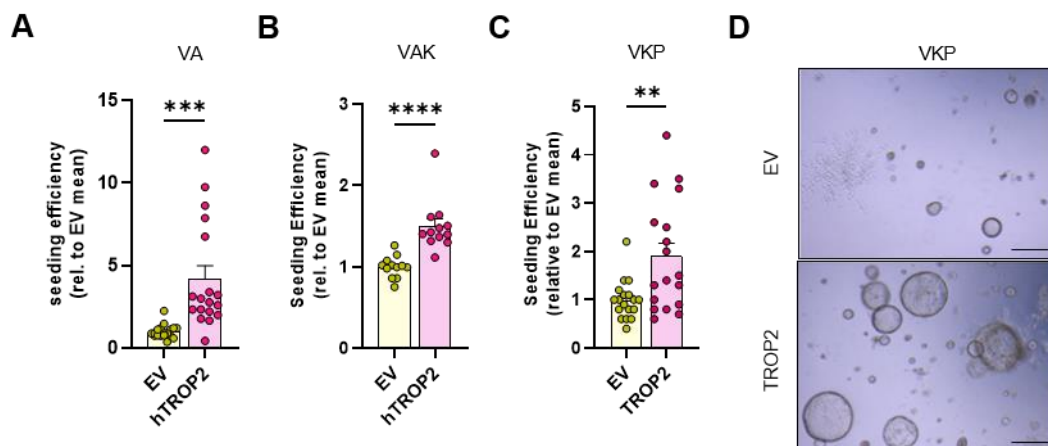


Figure 67. TROP2 overexpression increases organoid formation capacity *in vitro*. **A-C.** Quantification of the relative organoid formation capacity of the (A) VA, (B) VAK and (C) VKP MTO lines overexpressing TROP2 five days after seeding 1000 single cells. Every datapoint represent one well. n=18, 12, 18 individual wells from 3 independent experiments Five to six wells of four independent replicates were quantified. The statistical analysis was performed by using unpaired t-test. **D.** Representative images of the organoids formed five days after seeding. Scale bar 200 μ m. EV, empty vector.

TROP2 is a driver of metastasis in CRC.

Previously, I showed that TROP2⁺ cells were the metastasis-initiating cell. In order to define whether TROP2 protein has a functional role in metastasis, I transplanted intrasplenic the TROP2-deficient VAKPS lines as well as the VA, VAK and VKP lines overexpressing TROP2. TROP2 deficiency in VAKPS MTO lines led to a decreased metastatic burden (**Figure 68A**). Likewise, overexpression of TROP2 increased the metastatic burden of the VKP MTO line (**Figure 68B**). Unfortunately, VA and VAK did not engraft as no splenic tumour or liver metastases were observed in mice transplanted with the EV or TROP2 overexpressing MTO lines. Taking together, these results demonstrate that TROP2 has a functional role in CRC progression.

To gain deeper insight into the molecular mechanisms underlying these phenotypes I performed scRNA sequencing. However, this analysis and further validations are beyond the scope of this PhD thesis.

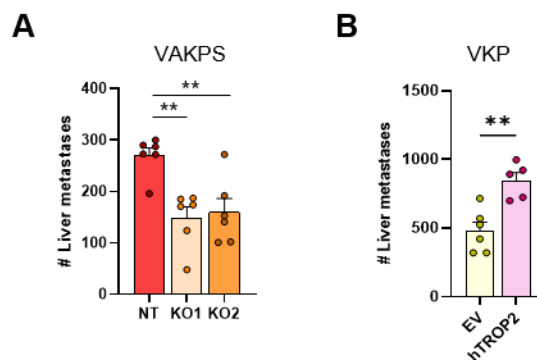


Figure 68. TROP2 is involved in CRC metastasis. **A.** Quantification of the number of liver metastasis derived from the VAKPS TROP2 KO cells four weeks after intrasplenic transplantation in immunodeficient NSG mice. **B.** Quantification of the number of liver metastases derived from the VKP TROP2 OE cells four weeks after intrasplenic transplantation in immunodeficient NSG mice.

DISCUSSION

Tumour heterogeneity as a driver of CRC progression

Half of the CRC patients develop metastasis, which is largely incurable and mainly responsible for the high CRC mortality (Siegel et al., 2020). Yet, dynamics and molecular determinants of metastasis are largely unknown. The advent of next-generation genomic and transcriptomic sequencing has elucidated a high degree of ITH as well as inter-patient heterogeneity in different tumour entities including CRC (Dagogo-Jack and Shaw, 2018; Hu et al., 2019; Hu et al., 2020; McGranahan and Swanton, 2017; Reiter et al., 2020). This ITH refers to the genetic and non-genetic differences between cancer cells across the same tumour mass, conferring them different phenotypes and consequently, different potential to metastasize and survive treatment regimens. Although the term “tumour inhomogeneity” was noticed several decades ago (Huxley, 1958), the absence of advanced study tools has impeded the complete understanding of its functional implications. In this PhD thesis, I studied the two main sources of ITH and their relation with cancer progression and metastasis: the stochastic clonal evolution model and the CSC model.

In the clonal evolution model, several theories have come to light to describe tumour progression, timing and clonality of metastasis (Hu et al., 2019; Hu et al., 2020; Sottoriva et al., 2015). However, all these theories are based on mathematical models and further *in vivo* validation are demanded. In addition, there is a pressing need to overcome the big challenge of obtaining early lesions to decipher novel biomarkers or molecular features that can be predictive of tumour aggressiveness and therapy failure. In contrast, the field of CSC model has been further explored *in vitro* and *in vivo* (Barker et al., 2009; Cortina et al., 2017b; De Sousa E Melo et al., 2017b; Shimokawa et al., 2017). CSC features are linked with poor prognosis and, although LGR5 has been for long proposed as the stem cell marker of CSC in the CRC, alternative CSC programs in LGR5⁻ CRCs still remain unknown.

Clonal evolution in CRC

Cancer evolution is mainly studied within the scope of genomic sequencing data from advanced human CRC samples. However, clonal dynamics at different stages during tumour progression have not been investigated. This is mainly because acquisition of human CRC samples at every stage is impractical. Consequently, the evolutionary dynamics that govern tumour initiation, progression and the onset of metastasis are poorly understood. In addition, systematic analysis on human primary CRC, local and distant metastasis have revealed different levels of genetic diversity (Hu et al., 2020).

Longitudinal studies on disease progression and treatment response, although difficult, are increasingly common and are particularly informative about the dynamics of the different cancer cell populations within the tumour. Indeed, genomic sequencing of primary CRC and matched metastasis have indicated the time and routes of metastasis (Hu et al., 2019; Zhang et al., 2020). A prevailing model posits that metastasis follows a sequential process in which distant metastases arise from lymph node metastases (Naxerova et al., 2017; Reiter et al., 2020). Contrary, the possibility that several subclones co-evolved and present different abilities to invade specific organs has come to light (Ryser et al., 2020).

In this regard, understanding the routes of metastasis and the genotypic-to-phenotypic characteristics of these populations need to be addressed as it can guide cancer therapy. Interestingly, independently of the tumour evolution model, many studies agree that metastases are less diverse than the paired primary tumours, which can be expected considering the complexity of the metastatic cascade and therefore only a few cells or clusters of cells will harbour the ability to survive along this process (Massague and Obenauf, 2016; Reiter et al., 2020).

Modelling clonal evolution in CRC: current limitations

Tumour evolution is governed by stochastic and individual alterations that are inherited to daughter cells followed by selective sweeps leaving unique historical records. Indeed, these mutations are used as genomic scars that can be traced by whole genome sequencing to further reconstruct phylogenetic trees to understand clonal dynamics over time. Yet, since these scars are spread throughout the whole genome, some caveats of this approach rely on (1) the timing and how the tumour is sampled (2) the sequencing resolution as whole genome sequencing is needed (Behjati et al., 2014; McKenna et al., 2016), (3) it is highly expensive due to the high coverage and number of cells needed (McKenna et al., 2016), (4) sequencing artefacts, which hinder the identification of underrepresented subclones (Kebschull and Zador, 2018; Robasky et al., 2014) and (5) insufficiency for a comprehensive characterization of the phenotypic features associated with the selective somatic mutations. Moreover, the spatial distribution is disrupted and tracking the fate of this heterogeneous population in real time at different tumour stages and treatment settings is not feasible with this “retrospective” sequencing technology (Kebschull and Zador, 2018).

The above discussed clonal evolution models on human cohorts are based on computational models derived from bulk sequencing analysis of a snapshot from late stage CRC samples reconstituting the past evolutionary index. Yet, what factors (genetic or non-genetic) determines that a specific cancer cell population metastasizes, has tropism for one specific organ or resists therapeutic regimens still remains elusive. Thus, future experimental

systems are needed to explore the course of tumour progression and the evolutionary process that governs each stage, from adenomas to late metastatic and therapy resistant tumours.

LeGO optical barcoding system reveals niche-dependant clonal selection in CRC

In order to study clonal dynamics during CRC progression, I made use of an optical labelling barcoding system that allows for the stable and longitudinal tracking of individual clones ([Weber et al., 2008](#)). Thus, I generated 21 VKPN LeGO clones and simultaneously transplanted them in a 1:1 ratio orthotopically, intrasplenically and subcutaneously as well as plated them *in vitro* to study the clonal competition and dynamics in the different microenvironments. Consistent with prior studies on mouse models of pancreatic cancer, breast cancer, and squamous cell carcinoma, I found that clonal selection plays a central role in cancer progression ([Berthelet et al., 2021](#); [Maddipati and Stanger, 2015](#); [Reeves et al., 2018](#)). Interestingly, I observed that the clones expanded under *in vitro* conditions and *in vivo* at the different sites differed, suggesting a significant bottleneck at the different sites. Taking together, these findings highlight that clonal selection is niche-dependent, suggesting that distinct TMEs may select clones with superior engraftment or seeding abilities.

Immune-cancer clones crosstalk and their influence on tumour progression and metastatic potential

The role of the immune system in clonal evolution has been inferred ([Grzelak et al., 2022](#); [Westcott et al., 2021](#)). In my experimental setting, no primary tumours were observed when cells were orthotopically transplanted by submucosal colonoscopy guided needle injection into the colon of immunocompetent mice, indicating that the strongest clonal selection occurs in the colon. Previous studies in CRC and breast cancer have shown that tumour rejection was only seen in tumours with high neo-antigen expression ([Grzelak et al., 2022](#); [Westcott et al., 2021](#)). Our findings suggest a possible role of fluorescent protein expression in influencing clonal selection, particularly in the colonic submucosa.

Furthermore, previous studies in CRC cell lines also revealed that a clone's location is more crucial for its growth than intrinsic cellular signals ([Lamprecht et al., 2017](#); [van der Heijden et al., 2019](#)). This was especially pronounced at the tumour edge, pointing to the importance of stromal factors secreted or presented at the tumour-stroma interface. Overall, these insights highlight the pivotal role of the TME in driving clonal selection and tumour progression. However, to further define the role of the immune system in shaping CRC tumour evolution, further multi-omic experiments and clonal evolution studies in immunocompromised mice should be performed.

Phenotypic features associated with selective somatic mutations

Next-generation sequencing has revealed differences between primary and paired metastases although none of those differences have been proven to be the drivers of the metastatic process (Hu et al., 2020). One of the major advantages of the multicolour LeGO optical barcoding system compared to the multiregional sequencing of the tumours is the possibility to not only identify metastatic and/or therapy resistance clones with spatial resolution, but also the further functional characterization of those clones. Indeed, this approach allows to retrospectively study the clones of interest comparing their genotypic and phenotypic characteristics with their counterparts. Furthermore, the LeGO approach will also allow the study of the evolution of a particular clone before, during and after selective pressure. This is possible as the carbon copy I generated at the beginning of the experiments allows for a precise molecular distinction of clones and identification of changes towards metastasis or therapy resistance processes. Further multi-omic analysis of the different clones might shed light on the phenotypic characteristics that endow a particular clone with an advantageous trait.

Defining and targeting CSC in CRC

LGR5 and TROP2 define a different subset of CSCs in CRC

LGR5 marks CSCs in CRC with high WNT pathway activation

Previous studies have demonstrated that LGR5 marks CSCs in human and murine CRCs (Barker et al., 2009; Cortina et al., 2017b; Shimokawa et al., 2017). These studies have been performed in models that recapitulate the classical route of CRC progression tumours, which accounts for approximately 80% of all CRCs and harbour *APC* mutations and high WNT pathway activation (Cortina et al., 2017b; de Sousa e Melo et al., 2017a; Merlos-Suarez et al., 2011; Munoz et al., 2012; Shimokawa et al., 2017). Contrary, the remaining 20% of CRC present low or no levels of *LGR5* expression (Morrall et al., 2020). Serrated adenomas, which are *APC* proficient tumours driven by *KRAS* or *BRAF* oncogenic mutations, are also enriched for foetal stem cell signatures while showing lower levels of WNT pathway activation and adult stem cell programs (Chen et al., 2021; Kawasaki et al., 2020; Leach et al., 2021; Vasquez et al., 2022).

One of the aims of my thesis was to assess the stem cell capacity of LGR5⁺ CSCs in LGR5^{low} tumours. To that end I used two different metastatic CRC mouse models with different levels of WNT pathway activation and LGR5 levels. *In vivo* tumour-initiation experiments revealed that LGR5 only marks CSCs in *Apc*^{mut} tumours, which presents high WNT pathway activation levels. Indeed, while no stem cell potential was observed in LGR5⁺ cells in VKPN tumours, *Apc* mutation reverted this phenotype. These findings suggest that LGR5 marks

CSCs only in Apc^{mut} CRCs whereas in Apc^{wt} CRCs LGR5⁺ cells might not define the CSCs or that at least they have reduced stemness potency.

Foetal-like CRC cells presents stem cell properties

A significant percentage of CRC do not have LGR5⁺ cells (Morral et al., 2020). Thus, I aimed to define whether an alternative stem cell hierarchy was also maintained in those tumours. In particular, I focused on programs that resemble those present during embryonic or foetal intestinal development and that have been described to reappear in adult tissues upon stress conditions or in the context of cancer (Ayyaz et al., 2019; Bala et al., 2023; Karo-Atar et al., 2022; Mustata et al., 2013; Mzoughi et al., 2023; Nusse et al., 2018; Yui et al., 2018). This foetal-like ISC program is characterized by the expression of genes such as *Tacstd2/TROP2*, *Ly6a/SCA1*, *Clu* and *Anxa1* (Mustata et al., 2013). To dissect the stem cell potential of foetal-like cancer cells in CRC I defined TROP2 expression as the best marker for this signature. This allowed for the isolation of the foetal-like CRC cells (TROP2⁺ cells) for functional characterization. *In vivo* tumour-initiation experiments revealed that TROP2 only marks CSCs in Apc^{wt} CRC. Interestingly, tumours derived from TROP2⁻ cells regained TROP2 expression, highlighting the high levels of plasticity in CRC cells and suggesting a possible dependency on TROP2⁺ cell pool restoration for tumour growth.

In sum, I concluded that in CRC there are two mutually exclusive CSC populations, the LGR5⁺ CSCs and the TROP2⁺ CSCs. Indeed, LGR5⁺ CSCs are enriched for the adult ISC program while the TROP2⁺ CSCs enriched for the foetal ISC program. Furthermore, I also demonstrated that while in the Apc^{mut} CRCs the CSCs are marked by LGR5, TROP2 marks the CSCs in the Apc^{wt} “low WNT” CRCs (Figure 69).

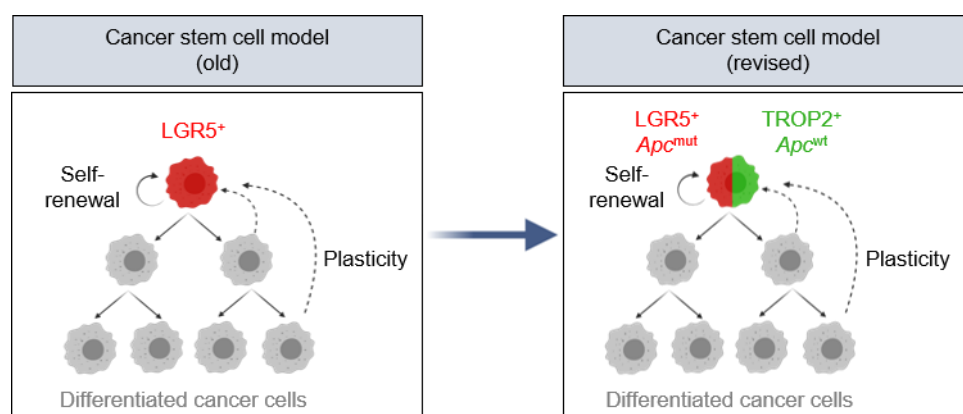


Figure 69. Revised cancer stem cell model in CRC.

Targeting CRC cell plasticity

CRC cells have high degree of plasticity (De Sousa E Melo et al., 2017b; Fumagalli et al., 2018). Indeed, tumours derived from LGR5⁻ or TROP2⁻ sorted cells regained LGR5 and

TROP2 expression, respectively. Thus, to further evaluate the possible dependency on restoring the CSC pools in order to further develop tumours, I took advantage of the iCaspase9 system. Although I successfully established the system for ablating LGR5⁺ and TROP2⁺ cells in different CRC models, no ablation of any of the cell pools was obtained. Nevertheless, I could prove that the reason for this lack of cell ablation was due to the low expression levels of my GOI and thus, expression levels of the iCaspase9. Further systems such as the DT or the DTA system could be further implemented to define the role of the LGR5⁺ cells in *Apc*^{wt} tumours as well as the role of TROP2⁺ cells in *Apc*^{wt} and *Apc*^{mut} tumours.

Establishment of a new model to trace foetal-like CSCs

Lineage tracing is a commonly used method to assess stemness, however, unlike the limiting dilution assay, it does not measure the tumour-initiating capacity of TROP2⁺ cells. Instead, it provides insight into their potency to drive tumour expansion within an already established tumour (Loh and Ma, 2024). Consistent with this, *in vivo* lineage tracing experiments were performed in pre-established tumours, further suggesting a possible role of the TME in influencing the observed phenotype.

Here, I have generated a new GEMM to trace TROP2⁺ cells, the TcT GEMM. Furthermore, I have further developed this model to be able to trace TROP2⁺ cancer cells by transforming the small intestine-derived organoids from the TcT GEMM. *In vivo* lineage tracing analysis of TROP2⁺ cancer cells demonstrated their ability to sustain tumour growth in *Apc*^{mut} tumours. Taken together, while TROP2 marks CRC cells with tumour-initiating capacity in *Apc*^{wt} tumours but not in *Apc*^{mut} tumours, TROP2⁺ cells still have stem cell potential in *Apc*^{mut} as they fuel tumour growth.

Unfortunately, I failed to lineage trace TROP2⁺ cells in TcT-KPN cells. I hypothesized that this could be explained by the low TROP2 expression levels observed in this cell line. Of note, this cell line was transformed *in vitro* and lower proliferation rates and tumour formation capacity were observed when compared with the VKPN MTO lines used in this thesis. Previous data has indicated that some level of activation of the canonical WNT-signalling pathway is required for serrated tumours to metastasize. This alteration might be acquired by additional mutations in the WNT-signalling pathway or alternative gene program regulations (Jackstadt et al., 2019). Thus, further *in vivo* selection for TcT-KPN clones might be needed to enhance TROP2 expression level and study the role of TROP2 in fuelling tumour growth in the TcT-KPN model. Additionally, the *Tacstd2*^{CreERT2} allele has been used in heterozygosis. Thus, using the *Tacstd2*^{CreERT2} allele in homozygosis might also enhance CreERT2 protein levels in tumour cells thus, allowing the tracing of TROP2⁺ cells.

Additionally, further analysis tracing LGR5⁺ cells in the LcT-AKP and LcT-KPN tumour lines would be instrumental as lineage tracing controls in the *Apc*^{mut} (LcT-AKP) and the *Apc*^{wt} (LcT-KPN) model.

TROP2 is associated with tumour aggressiveness

TROP2 is a transmembrane glycoprotein highly abundant in a vast number of epithelial carcinomas and absent in most of healthy adult tissues. Intriguingly, its expression positively correlates with decreased overall survival and increased metastasis in several carcinomas including CRC (Zeng et al., 2016). However, these are only correlational studies and further experimental validations are lacking. Therefore, in this thesis I focused on (1) defining the role of TROP2⁺ cells in CRC progression and (2) deciphering the functional role of TROP2 in CRC progression.

TROP2⁺ cell as the metastasis initiating cell in CRC

Metastasis is a multistep process in which tumour cells escape from the primary tumour, enter into the bloodstream and extravasate to colonize different organs where they can establish macro-metastases. This highly complex process requires enhanced capacity of the tumour cells to quickly adapt to host and unfavourable environments different from the primary tumour (Celia-Terrassa and Kang, 2016; Massague and Obenauf, 2016). Thus, it is not surprising that the metastatic process is highly inefficient and only highly plastic tumour cells that are able to acquire CSC-like properties can overcome these roadblocks and succeed in establishing metastasis (Massague and Obenauf, 2016).

Recent research has focused on characterizing the metastasis-initiating cells in CRC. For years, LGR5 has been recognised as the gold standard “stem cell marker” for CRC (Barker et al., 2009). However, contrary to the expectations that LGR5 would also mark the MIC, it has been shown that the majority of disseminating tumour cells were LGR5⁻ (Fumagalli et al., 2020b). Yet, re-establishing the LGR5⁺ CSC population was crucial for micro-metastases to progress into macro-metastatic lesions. (Canellas-Socias et al., 2022; Fumagalli et al., 2020a; Heinz et al., 2022). These results suggested that while LGR5⁺ CSCs are important to fuel tumour and metastasis growth they are dispensable for early metastatic processes.

In this thesis, I aimed to define the MIC in CRC. A crucial step of the metastatic cascade is the disruption of the lamina propia, enabling the cells to invade and enter into circulation to disseminate to distant organs. Interestingly, these invading cells have been highly associated with regenerative programs (Ganesh et al., 2020). In line with this, I found TROP2 to be highly expressed in the invasive front of primary tumour samples (Figure 70). Furthermore, a recent study has identified a set of genes that is highly enriched at the tumour front and that is also

positively associated with poor prognosis and tumour relapse. In this study they find no significant enrichment of the foetal ISC program in these invading cells. Yet, TROP2 is one of the few canonical markers of the foetal ISC program upregulated in these cells ([Canellas-Socias et al., 2022](#)).

Furthermore, scRNA sequencing data and immunohistochemistry analysis revealed an enrichment of TROP2 micro-metastatic lesions while no LGR5 expression was observed. *In vivo* validation experiments transplanting TROP2⁻ and TROP2⁺ cells showed an enhanced metastatic capacity of the TROP2⁺ cells regardless of the *Apc* status. Furthermore, metastases derived from TROP2⁻ cells regained TROP2 expression. Unfortunately, as I failed to establish a model to block plasticity, I cannot conclude whether regaining TROP2 expression is instrumental for metastasis formation. Overall, this data highlights the enhanced metastasis-initiating capacity of TROP2⁺ cells (**Figure 70**).

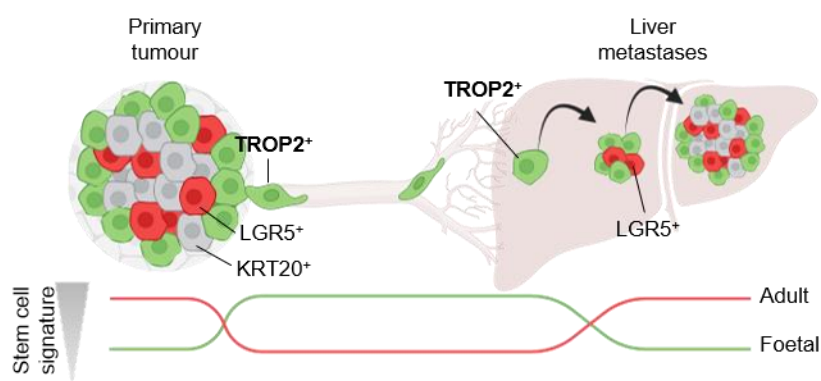


Figure 70. Stem cell dynamic in CRC progression. TROP2⁺ CRC cells are located at the invasive front of the primary tumour. These cells enter circulation and seed to distant organs such as the liver. In order to progress into a macro-metastases, the adult ISC program needs to be activated. Figure adapted from ([Fey et al., 2024](#))

TROP2 has a functional role in CRC initiation and metastasis

Studies in prostate cancers have shown that TROP2 promotes metastatic dissemination by acquiring aggressive neuroendocrine features and interacting with the integrins of the extracellular matrix ([Hsu et al., 2020](#); [Trerotola et al., 2013](#)). Thus, in this thesis, I further sought to determine whether TROP2 serves merely as a marker for aggressive, metastatic CRC cell phenotypes or if it plays an active, functional role in driving tumour aggressiveness. I successfully generated TROP2 loss-of-function and gain-of-function MTO lines and defined that TROP2 plays an important role in tumour initiation as well as in metastasis. Yet, further analysis on the sequencing data and consecutive validations to unravel the mechanisms involved in this phenotype need to be performed.

TROP2 loss-of-function and gain-of-function experiments have been performed in MTO lines derived from aggressive CRC tumour models. Furthermore, the *in vivo* analysis for studying metastasis has been performed in an “artificial” setting where millions of cells are inoculated into circulation, skipping many crucial steps of the metastatic cascade. Thus, I am also generating GEMMs of CRC by crossing the already established VKPN and VAKP CRC models with the *Tacstd2^{fl/fl}* allele. With this setting I would be able to faithfully recapitulate the entire CRC progression cascade to determine the role of TROP2 in tumour initiation and metastasis.

TROP2 expression is enhanced upon chemotherapy expression. A new therapeutic window that can be exploited in the clinics

The standard-of-care for CRC patients consists of the surgical resection of the primary tumour and chemotherapy in a neoadjuvant or adjuvant setting. Although this treatment regimen can be curative in early-stage CRC, 20-40% of the patients will develop metastasis due to an early dissemination of tumour cells (Dekker et al., 2019; Sanchez-Gundin et al., 2018). A major responsible of therapy resistance is cellular plasticity (Loh and Ma, 2024; Vasquez et al., 2022). However, in CRC monitoring the plasticity between cell states have been hindered by the lack of defined programs beyond the canonical adult ISC program.

Previous studies have shed light to the phenotypic switch in CRC cells upon chemotherapy regimens. Indeed, upon chemotherapy, cells downregulate the adult ISC program and activate the foetal ISC program, facilitating temporary drug resistance and survival (Alvarez-Varela et al., 2022; Fey et al., 2024; Vasquez et al., 2022). In line with these findings, I observed that upon chemotherapy, TROP2 expression increased in MTOs and PDOs. Furthermore, by performing lineage tracing analysis on TROP2⁺ cells, I could conclude that TROP2 does not mark drug-persister cells. Instead, TROP2 upregulation is an adaptive mechanism to chemotherapy selective pressures. Yet, it remains to be elucidated whether TROP2 has a functional role in therapy resistance. Taking together, this finding indicates that upon chemotherapy, the stem cell admixture can be shifted towards a foetal stem-like phenotype uncovering a new therapeutic window for targeting these cancer cells that can be exploited in the clinic (**Figure 71**).

Interestingly, these cells are marked by TROP2. In recent years, SG, a TROP2-targeting antibody-drug conjugate (ADC), has shown promising clinical efficacy in breast cancer patients (Bardia et al., 2021; Rugo et al., 2023) and in urothelial carcinoma patients (Tagawa et al., 2021). To my knowledge, at the start of this project, no studies with SG were conducted in CRC patients.

I demonstrated that the foetal ISC program and, in particular, TROP2 is upregulated upon FOLFIRI treatment. Thus, I hypothesized that sequential or combinatorial treatment of chemotherapy and SG will be of benefit to CRC patients and might reduce chemotherapy resistance (**Figure 71**). Furthermore, I observed that upon chemotherapy, TROP2 expression increased even in PDOs with no basal TROP2 expression, suggesting that these patients might also benefit from the new combinatorial therapeutic regimen proposed.

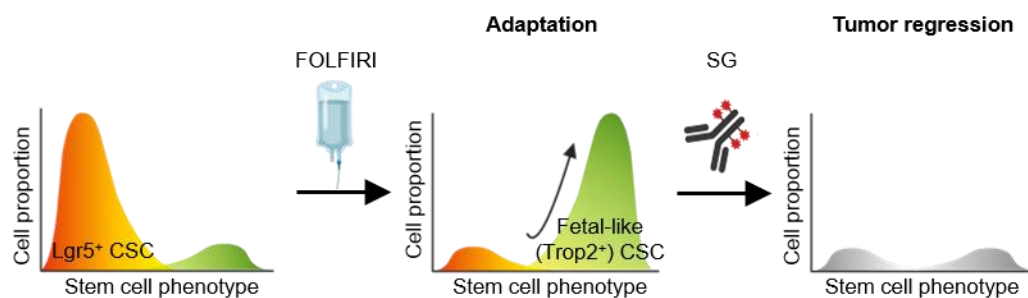


Figure 71. Stem cell dynamics upon therapeutic treatment.

TROPHIT1: an investigator-initiated phase II/III multicentre randomized clinical trial for metastatic CRC

As a result of the research efforts shown in this thesis, TROPHIT1, an investigator-initiated phase II/III multicentre randomized clinical trial (NCT06243393) has been initiated. Here, the clinical benefits of SG as a third line of treatment in metastatic CRC patients will be investigated. Most importantly, the reverse translational research that will be derived from this clinical trial will open new lines of research to uncover whether (1) TROP2 levels will predict tumour response to SG, (2) irinotecan-refractory patients will still benefit from SG and (3) to understand mechanisms of resistance to SG to further improve therapeutic regimens.

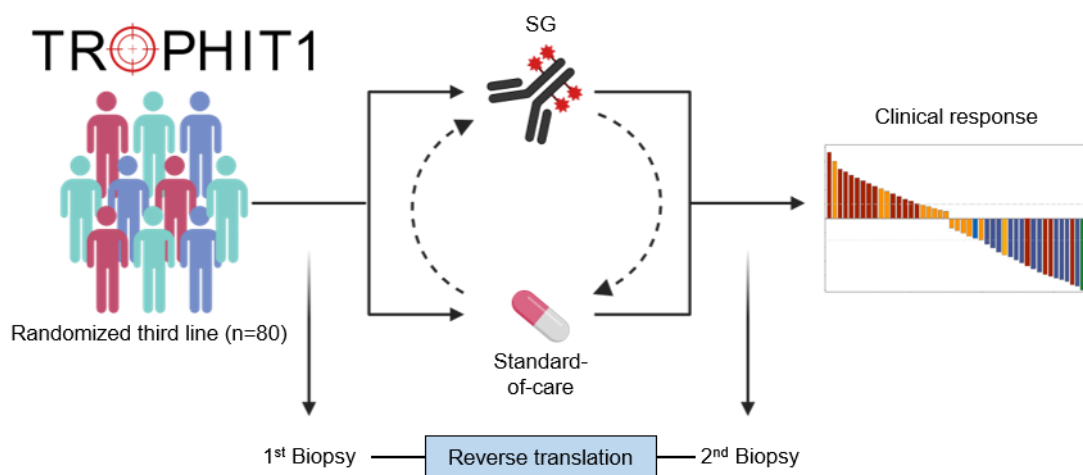


Figure 72. SG as a third line treatment for mCRC. Schematic overview of the treatment plan and reverse translational pipeline for the TROPHIT1 (NCT06243393) clinical trial. Sacituzumab Govitecan (SG); Standard-of-care.

CONCLUSIONS

Understanding clonal dynamics during CRC progression

1. LeGO multicolour barcoding system revealed niche-dependent clonal selection.
2. The colonic submucosa exhibits more robust immune surveillance compared to liver or subcutaneous sites.

Defining the role of foetal-like cancer cells in CRC progression

1. TROP2 identifies foetal-like CSCs in CRC.
2. TROP2⁺ CSCs and LGR5⁺ CSCs are mutually exclusive.
3. LGR5 marks CSCs in CRC with high WNT pathway activation.
4. TROP2 marks CSCs in *Apc*^{wt} CRC.
5. TROP2 expression positively correlates with tumour aggressiveness and lower OS.
6. TROP2⁺ cells are the metastasis initiating cells.
7. TROP2 expression is heterogeneous both across and within individual patients.
8. TROP2 promotes tumour growth and metastasis in MTO and PDO models.
9. Chemotherapy treatment enhances TROP2 expression in CRC, providing a perfect opportunity for efficient combinatorial treatment with SG.

MATERIALS AND METHODS

Organoid Culture

Mouse Tumour-derived organoids

MTOs were derived from intestinal tumours from GEMMs. MTOs were cultured in Cultrex reduced growth factor basement membrane (BME; R&D Systems, #3433-005-01) domes of 20µl. After BME polymerization, media was added. MTOs were grown in Advanced DMEM/F12 (Gibco, #12634028) supplemented with 1% L-Glutamine (Thermo Fisher, #25030024), 1% HEPES (Sigma, #h0887-100), 1x B27 (Gibco, #12585010), 1x N2 (Gibco, #17502048) and 1% penicillin-streptomycin (Sigma, #P4458-100ML) (from now on basic media). Depending on the mutational background of the MTOs, the basic media was additionally supplemented with 50 ng/ml EGF (Peprotech, #AF-100-15-1000), 100 ng/ml of Noggin (Peprotech, #250-38-100) or 100 ng/ml of R-spondin conditioned media (U-Protein Express, kindly provided by Jens Puschhof) (**Table 2**).

MTO genotype	Supplements added to the basic media
<i>Villin</i> ^{CreER} ; <i>Apc</i> ^{fl/fl}	EGF, Noggin
<i>Villin</i> ^{CreER} ; <i>Apc</i> ^{fl/fl} ; <i>Kras</i> ^{G12D/+}	Noggin
<i>Villin</i> ^{CreER} ; <i>Apc</i> ^{fl/fl} ; <i>Trp53</i> ^{fl/fl}	EGF, Noggin
<i>Villin</i> ^{CreER} ; <i>Apc</i> ^{fl/fl} ; <i>Kras</i> ^{G12D/+} ; <i>Trp53</i> ^{fl/fl}	Noggin
<i>Villin</i> ^{CreER} ; <i>Apc</i> ^{fl/fl} ; <i>Kras</i> ^{G12D/+} ; <i>Trp53</i> ^{fl/fl} ; <i>Smad4</i> ^{fl/fl}	-
<i>Villin</i> ^{CreER} ; <i>Kras</i> ^{G12D/+} ; <i>Trp53</i> ^{fl/fl}	Noggin
<i>Villin</i> ^{CreER} ; <i>Kras</i> ^{G12D/+} ; <i>Trp53</i> ^{fl/fl} ; <i>Rosa26</i> ^{N1ICD/+}	Noggin

Table 2. Culture media conditions used for the different MTOs.

MTOs were split every 2-4 days. In brief, BME domes containing the MTOs were detached from the plates and transferred to a 15 ml Falcon. 5 ml of ice-cold PBS was added and samples were centrifuged at 1500 rpm for 5 minutes. The supernatant containing PBS and BME was aspirated and the pellet containing the MTOs was resuspended in 200µL of ice-cold PBS and pipetted vigorously 30-40 times. Subsequently, 5 ml of ice-cold PBS were added and centrifuged for 5 minutes at 1200 rpm. The supernatant was aspirated and the MTO-containing pellet was resuspended in 70% BME (diluted in PBS) and 20 µl domes were plated in pre-warmed plates.

Small intestine epithelial organoids

Organoids derived from the small intestine of GEMMs were generated as previously described ([Sato and Clevers, 2013](#)). In brief, the small intestine was isolated and the first 10 cm were discarded. The rest was washed with ice-cold PBS to remove the faeces and then longitudinally opened. The villi and mucus were scraped off by using a cover slip and the rest was cut into 2-4 mm pieces and transferred to a 50 ml tube with 25 ml of ice-cold PBS. We let the epithelial fragments settle down and remove the supernatant. The process was repeated 3 times. Next, 25 ml of ice-cold PBS with 2 mM EDTA (Thermo Fisher, #AM9260G) were added and gently rocked for 20 minutes at 4 °C. After settling down of the epithelial fragments, the supernatant was then discarded and 5 ml of ice-cold PBS was added and vigorously pipetted up and down to extract the crypts. After settling down, the supernatant was collected. This process was repeated 5-6 times. The supernatants containing the villus fractions were discarded and only the fractions enriched for crypts were passed through a 70 µm cell strainer (Greiner, #542070) and spun down at 600 rpm for 5 minutes. The resulting cell pellets were resuspended in 70% BME (in PBS) and plated forming 20 µl domes. Small intestinal organoids were maintained in basic media supplemented with 50 ng/µl EGF, 100 ng/mL of Noggin and 1 µg/µl of recombinant R-spondin conditioned media (U-Protein Express, kindly provided by Jens Puschhof). The organoids were split every 2-3 days, similarly to the MTOs (described above).

Patient-derived organoids

CRC PDOs were obtained from tumours surgically removed at the University Hospital Heidelberg, Heidelberg, Germany. Patient identity remained anonymous during the course of this research. Tumour-derived cells were grown as organoids in 70% BME and cultured in 50% Advanced DMEM/F12 (supplemented with 1% L-Glutamine, 1% HEPES and 1% penicillin-streptomycin), 50% WRN conditioned media (media generated as previously described ([Miyoshi and Stappenbeck, 2013](#)), 1x B27, 1x N2, 1 mM N-acetyl-L-cysteine (NAC) (Sigma, #A7250), 10 nM gastrin I (Sigma, #G9145), 50 ng/µl EGF, 10µM Y-27632 (Hözel, #M1817), 0.5 µM A83-01 (Sigma, #SML0788), 100 ng/µl IGF-1 (Biolegend, #590908), 50 ng/ml basic FGF (Peprotech, #100-18b), 4 mM nicotinamide (Sigma, #N0636) and 2 µl/ml Primocin (Invivogen, #ant-pm-2). Media was changed every two days. PDOs were passaged every seven days similar to MTOs (described above) but using TrypLE (Invitrogen, #12605010) instead of PBS to break down the organoids into fragments. PDOs were incubated for 5 minutes with TrypLE following a mechanical dissociation by pipetting.

Vectors and cloning strategies

I have designed and generated the plasmids, unless otherwise stated. Plasmids were amplified using competent *E. coli* (Zymo Research, #3001). Bacteria were grown in self-generated YT-Agar plates supplemented with 100 µg/ml carbenicillin (Fisher Scientific, #10396833) and incubated overnight (O/N) at 37°C. Positive bacterial colonies were then grown in YT medium supplemented with 100 µg/ml carbenicillin for 16 hours at 37°C and 220 rpm. Vectors were then isolated using either Qiaprep spin Miniprep kit (QIAGEN, #27106) or Nucleobond Xtra Midi (Macherey-Nagel, #740410.50) according to manufacturer's guidelines.

CRISPR/Cas9 Knock-Out vectors

Single guide RNAs (sgRNAs) were either designed using the web tool <https://chopchop.cbu.uib.no/> or retrieved from the literature. In order to select the most suitable sgRNAs I used the following criteria: a) minimal off-target score, b) high cutting efficiency and c) annealing as close as possible to the transcription start site of the GOI. For efficient transcription of the sgRNAs, these need to start with a guanine, otherwise a guanine was added to the 5'UTR. Additionally, the sgRNAs sequences were flanked by BbsI-specific overhangs to be cloned in at the specific site in the pSpCas9(BB)-2A-GFP (PX458) plasmid (Cong et al., 2013) (sgRNA sequences are detailed in **Table 3**).

Gene of interest	Specie	sgRNA	sgRNA sequence	Source
Non-targeting	n.a	n.a	CCGCGCCGTTAGGGAACGAG	Manuel Mastel
Apc	<i>Mus musculus</i>	n.a	GTCTGCCATCCCTTCACGTT	Manuel Mastel
Trp53	<i>Mus musculus</i>	n.a	GTGTAATAGCTCCTGCATGG	Manuel Mastel
Tacstd2	<i>Mus musculus</i>	1	GATGGCGACCCGCTTTTGCA	Chopchop
		2	GTCGCAGACCGTCATCTTGT	Chopchop

Table 3. sgRNA sequences used for generating CRISPR/Cas9 KO organoid lines.

pSpCas9(BB)-2A-GFP (PX458) plasmid (Addgene, #48138) was used as a backbone to clone in the sgRNAs as previously described (Cong et al., 2013). Briefly, 100 µM oligos containing the sgRNA forward and reverse sequences were phosphorylated and annealed using the T4 Polynucleotide Kinase (PNK) (NEB, #M0201) (the buffer for the T4 Ligase was used instead (NEB, #B0202)) (see **Table 4** for the detailed annealing program). 1 µg of the pSpCas9(BB)-2A-GFP (PX458) plasmid was digested with the BbsI-HF (NEB, #R3539). The annealed and phosphorylated oligo duplex was then ligated to 50 ng of the digested backbone using the Quick Ligase (NEB, #M2200) at room temperature for 10 minutes. To prevent empty-backbone products, the ligation reaction was treated with PlasmidSafe Exonuclease digestion (Biozym, #E3101K) according to manufacturer's recommendations. Insertion of the sgRNA of

interest in the backbone was verified by Sanger sequencing using the primer GACTATCATATGCTTACCGTAA.

°C	37	95	90	85	80	75	70	65	60	55	50	45	40	35	30	25	4
Minutes	30	1	1	1	1	1	1	1	1	1	1	1	1	1	1	1	∞

Table 4. Program used for the annealing of the sgRNAs and shRNA oligo sequences.

Human TROP2 overexpressing vector

To overexpress the human TROP2 protein, a plasmid containing the cDNA sequence of the *TACSTD2* gene under the control of the human elongation factor-1 alpha (EF-1 α) promoter was generated. To that end, the backbone of the Lenti-Cas9-2A-Blast plasmid (Addgene, #73310) was modified replacing the Cas9 sequence for the *TACSTD2* cDNA sequence (Lenti-TROP2-2A-BlastR). In detail, *TACSTD2* cDNA was obtained from HEK-293 cells by PCR amplification using primers containing BamHI-HF and NheI-HF restriction sites at the 5' and 3' ends, respectively (see **Table 5**). Since the vector will present a T2A site after the *TACSTD2* cDNA sequence, the reverse primer lacks the stop codon of the cDNA. Both, the Lenti-Cas9-2A-Blast vector and the PCR amplified *TACSTD2* cDNA, were double-digested with BamHI-HF (NEB, #R3136S) and NheI-HF (NEB, #M0202L) for 1 h at 37°C. The digested backbone (6975 bp) was gel-purified using the QIAquick Gel Extraction Kit and the digested PCR product was PCR-purified using the QIAquick PCR Purification Kit (QIAGEN, #28106). Finally, the PCR-purified *TACSTD2* cDNA sequence was ligated into the open vector using the T4 Ligase according to manufacturer's guidelines. Correct insertion was verified by Sanger sequencing using the following primer: CTGGGAAAGTGATGTCGTG.

Primer Name	Primer Sequence
BamHI-TROP2-Fw	atcgtGGATCCATGGCTCGGGGCCCCG
TROP2(noStopCodon)-NheI-Rv	atagtGCTAGCCAAGCTCGGTTCTTTCTCAACTCCCC

Table 5. Sequence of the primers used for amplification of the *TACSTD2* cDNA amplification. Fw, forward; Rv, reverse.

The empty vector (EV) control plasmid was also generated by Belen Hackel. This plasmid only contains the blasticidin resistance (BlastR) cassette. For its generation, the BlastR sequence from the Lenti-Cas9-2A-BlastR vector was PCR amplified with primers containing BamHI-HF and MluI-HF restriction sites at the 5' and 3' ends, respectively (**Table 6**). Both, the Lenti-Cas9-2A-BlastR vector and the PCR-amplified BlastR sequence, were double-digested with BamHI-HF and MluI-HF (NEB, #R3198S) for 1 hour at 37 °C. The digested backbone (6507 bp) was gel-purified using the QIAquick Gel Extraction Kit and the digested PCR product was PCR-purified using the QIAquick PCR Purification Kit. Finally, the PCR-purified BlastR sequence was ligated into the open vector using the T4 Ligase according

to manufacturer's guidelines. Correct insertion was verified by Sanger sequencing using the following primer: CTGGGAAAGTGATGTCGTG.

Primer Name	Primer Sequence
BamHI-EV-Fw	gcgggatccATGGCCAAGCCTTTGTCTCA
EV-MluI-Rv	gacttaacgcgtTTAGCCCTCCCACACATAAC

Table 6. Sequences of the primers used for the generation of the EV control plasmid. Fw, forward; Rv, reverse.

CRISPR/Cas9 knock-in vectors

pSpCas9(BB)-sgRNA-2A-GFP plasmid construction

sgRNAs were designed using the web tool <https://chopchop.cbu.uib.no/>. In order to select the most suitable sgRNAs I used the following criteria: a) minimal off-target score, b) high cutting efficiency, c) annealing as close as possible to the desired site of insertion of the donor sequence and d) Cas9-mediated double strand break downstream of the STOP codon of the GOI (Cortina et al., 2017a). For efficient transcription of the sgRNAs, these need to start with a guanine, otherwise a guanine was added to the 5'UTR. Additionally, the sgRNAs sequences were flanked by BbsI-specific overhangs to be cloned in at the specific site in the plasmid (Cong et al., 2013) (gRNA sequences are detailed in **Table 7**). Cloning of the sgRNA sequence into the pSpCas9(BB)-2A-GFP (PX458) plasmid was performed as previously described.

Gene of interest	Specie	sgRNA sequence
<i>Lgr5</i>	<i>Mus musculus</i>	GTCTCTAGTGACTATGAGAG
<i>Tacstd2</i>	<i>Mus musculus</i>	CTAGCTTGTAGGTTTCCTGT

Table 7. sgRNA sequences used for generating CRISPR/Cas9 Knock-in organoid lines.

HR180-*Lgr5*-iCaspase9-T2A-tdTomato and HR180-*Tacstd2*-iCaspase9-T2A-tdTomato donor plasmids construction

To introduce the iCaspase9-T2A-tdTomato (iCT) cassette into the *Lgr5* and *Tacstd2* locus, I used the HR180-LGR5-iCT vector (Addgene, #129094). First, an AflIII restriction site was introduced in the PstI restriction site by digesting the vector with PstI (Sibenzyme, #E131) at 30°C for 1 hour and ligating it with previously annealed oligos containing the PstI-specific overhangs and the AflIII restriction site (oligo sequences are detailed in **Table 8**). Next, the 3' HA and 5' HA encoding for the human *LGR5* in the HR180-LGR5-iCT original vector were replaced for the HA specific for the GOI (*Lgr5* or *Tacstd2*). The HAs were amplified from C57BL/6J genomic DNA (gDNA) with primers containing restriction site-specific overhangs (**Table 9**). Next, the 3' HA and the vector were digested with AflIII (NEB, #R0520S) and SphI-

HF (NEB, #R3182S) restriction enzymes for 1 hour at 37°C. The digested backbone was gel-purified and the digested 3' HA was PCR purified for a sequential ligation using the T4 ligase as previously described. Lastly, the 5' HA and the vector were digested with NdeI (Thermo Fisher, #ER0582) and SacI-HF (NEB, #R3156S) (for *Lgr5*) or with NdeI and NsiI-HF (NEB, #R3127S) (for *Tacstd2*) restriction enzymes for 1 hour at 37°C. The digested backbone was gel-purified and the digested 5' HA was PCR purified for a sequential ligation using the T4 ligase as previously described. The correct insertion of the HAs was verified by Sanger sequencing using the following primers: GGCTTAAGCTATGCGGCATCA and GGAAACAGCTATGACCATGATTAC.

Primer	Primer sequence
Fw	GCTTAAGACCGGTAGATA
Rv	CCGGTCTTAAGCCATT

Table 8. Oligo sequences used for the insertion of the AflII restriction site in the HR180-LGR5-iCT vector. Fw, forward; Rv, reverse.

Gene of interest	HA	Primer	Primer sequence	PCR product size (bp)
<i>Lgr5</i>	5'	Fw	gtgcacccatgGCGGTAGTGGACATTCTCATG	1018
		Rv	gaggtaccgagctcCTAGAGACATGGGACAAATGCA	
	3'	Fw	ggcttaagGAGCAGTAGCTAAGAAAAGCTG	1032
		Rv	gaggtaccgagctcCTAGAGACATGGGACAAATGCA	
<i>Tacstd2</i>	5'	Fw	gtgcacccatgGATGACGGTCTGCGACACAA	854
		Rv	gatctgatgcCCTACAAGCTAGGTTTCGCTTCT	
	3'	Fw	ggcttaagGACTTCCTCGGCACCTCAGAC	938
		Rv	gccaaagcttgcGTCATCTCCCACTCCTGTTCA	

Table 9. Primer sequences for the amplification of the homology arms. Fw, forward; Rv, reverse; bp, base pair.

LeGO vectors

To implement the LeGO multicolor barcoding system, 6 vectors encoding for different fluorescent proteins were purchased from Addgene (**Table 10**).

Plasmid	Insert	Source
LeGO-EBFP2	EBFP2	Addgene, #85213
LeGO-S2	T-Sapphire	Addgene, #85211
LeGO-GFP	EGFP	Addgene, #25917

LeGO-V2	Venus	Addgene, #27340
LeGO-mOrange2	mOrange2	Addgene, #85212
LeGO-dKatushka2	dKatushka	Addgene, #85214

Table 10. LeGO vectors.

Electroporation

For the generation of CRISPR/Cas9-mediated knock-ins and knock-outs as well as for the application of the sleeping beauty (SB) system, the PDOs, mouse small intestine-derived organoids and MTOs were electroporated using the NEPA21 electroporator (Nepagene) (program detailed in **Table 11**). The organoids from a confluent well (containing 7x20 μ L BME domes) of a 6-well plate were fragmented with Tryple E and resuspended in 100 μ L Optimem (Life Technologies, #31985062) containing 10 μ g of the vector of interest. After electroporation, the organoids were incubated in suspension for 20 minutes at 37 °C in complete media supplemented with 10 μ M Y-27632. After recovery, the organoids were centrifuged and plated with complete media also supplemented with 10 μ M Y-27632.

Pulse	Voltage (V)	Length (ms)	Interval (ms)	N°	Decay rate (%)	Polarity
Poring	175	5	50	2	10	+
Transfer	20	50	50	5	40	+/-

Table 11. Nepagene program used for organoid electroporation.

CRISPR/Cas9 knock-out generation and selection

For the generation of TROP2 KOs, PDOs and MTOs were electroporated with 10 μ g of the pSpCas9(BB)-sgRNA-2A-GFP vector containing the sgRNA of interest. After 72 hours, electroporated organoids were dissociated into single cells and sorted for GFP⁺. Sorted GFP⁺ cells were plated and incubated for a week in complete media supplemented with 10 μ M Y-27632. Once single-cell derived organoids (clones) were formed, they were isolated with a pipette under a light microscope and expanded.

For the generation of *Trp53* KO I electroporated the murine small intestine-derived organoids with 10 μ g of the pSpCas9(BB)-*Trp53*sgRNA-2A-GFP vector. For the generation of double KO (*Apc* and *Trp53*) murine small intestine-derived organoids, a single vector generated by Manuel Mastel (a PhD student in the lab) containing both sgRNAs against *Apc*, and *Trp53* was used. The small intestine-derived organoids were electroporated with 5 μ g of the double mutant vector together with 5 μ g of the pSpCas9(BB)-2A-GFP vector.

To select organoids with loss-of-function mutations in *Apc*, R-spondin was removed from the small intestine complete medium. To select organoids with loss-of-function mutations

in *Trp53*, organoids were treated with 5 ng/ml Nutlin-3 (MedChemExpress, #HY-10029) for one week.

In order to validate the KO efficiency, the gDNA from the different clones was extracted using the DNeasy Blood & Tissue Kit (Qiagen, # 69506) according to manufacturer's guidelines. The locus where the sgRNA sequence annealed was PCR amplified (primer sequences are detailed in **Table 12**) with the DreamTaq Green PCR Master Mix (ThermoFisher-Scientific, #K1082) following manufacturer's guidelines. PCR program: 95°C 3 min >> 35x (95°C 30 s >> 55°C 30 s >> 72°C 1 min) >> 72°C 10 min >> 4°C hold. The amplified region was submitted to Sanger sequence and the KO efficiency was determined with Synthego webtool (<https://ice.synthego.com/#/>).

Gene	sgRNA	Primer	Primer sequence
<i>Tacstd2</i>	1	Fw	GCAATCTCCCCTGCCTGATTC
		Rv	GAGGCCATCGTTGTCCAGTATC
	2	Fw	CCTCTGGTCTGTAGTTGGAGGT
		Rv	CACTTGGAAGTTAGCGTGGAG
<i>TACSTD2</i>	1	Fw	GCCTACTACTTCGAGAGGGACA
		Rv	CAGTTCCTTGATCTCCACCTTC
	2	Fw	GGCAGGTCGGGTAGAGTATAAG
		Rv	CTGCACACGGTCATCTTGTT
<i>Apc</i>	1	Fw	CTCACAGCTTGACAATAGTC
		Rv	CCATAACTTTGGCTATCTGG
<i>Trp53</i>	1	Fw	TTAACAGCAGTCTCTGGGAG
		Rv	GGGTACAGCTTGTCTCTGG

Table 12. Primer sequences for specific validation of the KO efficiency.

CRISPR/Cas9 knock-in generation and selection

VKPN and VAKPS MTOs were electroporated with 5µg of the pSpCas9 plasmid and 5 µg of the donor plasmid. After 72 hours, electroporated organoids were selected with puromycin (10µg/ml) (Sigma-Aldrich, #P9620) for 4-5 days and Ruby⁺ clones were isolated with a pipette under a fluorescent microscope and expanded. To ensure the specific integration of the donor vector, gDNA from the different clones was extracted using the DNeasy Blood & Tissue Kit according to manufacturer's guidelines. The region of interest was PCR amplified with DreamTaq Green PCR Master Mix following manufacturer's guidelines. PCR program:

95°C 3 min >> 35x (95°C 30 s >> 50°C 30 s >> 72°C 90 s) >> 72°C 10 min >> 4°C hold. For the 5' specific integration, a forward primer located upstream of the 5' HA sequence and a reverse primer located in the integrated cassette were used. Likewise, for the 3' specific integration, a forward primer located in the integrated cassette and a reverse primer located downstream of the 3' HA sequence were used (primer sequences are detailed in **Table 13**).

Knock-in	Region	Primer	Primer sequence
<i>Lgr5</i> -iCT	5' specific	Fw	GCCTTGGTGGCTTTGACCGTG
		Rv	CTCGGATCACCTCCTGCTTGCCTA
	3' specific	Fw	GATCTGATCTTTCCACTCAAAACATATAACT
		Rv	AGAAGCATGCTCCTACTCAGAA
<i>Tacstd2</i> -iCT	5' specific	Fw	GTGTCCTACCCAGCCTGATCCT
		Rv	GGCCTTATTCCAAGCGGCTTCG
	3' specific	Fw	GGATCCAAGGCTGAAAACCT
		Rv	GCCTTCACGTGGTTTAAAC

Table 13. Primers used for the specific integration of the iCT and GFP cassettes.

For the removal of the Ruby-Puromycin resistant cassette, the clones were electroporated as previously described with 10 µg of the AAV-CAG-GFP-Cre vector, kindly gifted from Dr. Mall (DKFZ, Heidelberg). After 72 hours, electroporated organoids were dissociated into single cells and sorted for GFP⁺. Sorted GFP⁺ cells were plated and incubated for a week in complete media supplemented with 10 µM Y-27632. Once single-cell derived organoids (clones) were formed, they were isolated with a pipette under a light microscope and expanded. To confirm the removal of the Ruby-Puromycin resistant cassette, gDNA from the different clones was extracted using the DNeasy Blood & Tissue Kit according to manufacturer's guidelines and the locus was PCR amplified (primer sequences are detailed in **Table 14**) with DreamTaq Green PCR Master Mix following manufacturer's guidelines PCR program: 95°C 3 min >> 35x (95°C 30 s >> 50°C 30 s >> 72°C 90 s) >> 72°C 10 min >> 4°C hold.

Knock-in	Primer	Primer sequence
Generic	Fw1	GATCTGATCTTTCCACTCAAAACAT
	Fw2	CCCGCAACCTCCCCTTCTACGAG
<i>Lgr5</i> -specific	Rv1	GAGTCATCCAACGAGTCTTCTC
<i>Tacstd2</i> -specific	Rv1	GTCCATCTCCCACTCCTGTTCA

	Rv2	GGTGACCTGAGCTCAGCATCT
--	-----	-----------------------

Table 14. Primers used for the validation of the Ruby-Puromycin resistant cassette removal.

Generation of *Kras*^{G12D} mutant small intestine-derived organoids

For the generation of *Kras*^{G12D} mutant organoids, I made use of the SB system (Ivics et al., 1997). To that end, 5 µg of the pPGK-SB13, the SB-coding plasmid, and 5 µg of the pT_EF1a_KRASG12D, the *Kras*^{G12D}-coding plasmid, were used for the electroporation of small intestine-derived organoids as previously described. Plasmids were kindly gifted by Prof. Dr Offringa. To select for organoids carrying the *Kras*^{G12D} mutant protein, EGF was withdrawn from the small intestine complete medium. Additionally, organoids were treated with 1 µmol/L Gefitinib (Selleckchem, #S1025) for a week.

To validate the insertion of the *Kras*^{G12D} mutant sequence in the genome, gDNA from electroporated organoids was extracted after two rounds of splitting and the insert was PCR amplified with DreamTaq Green PCR Master Mix following manufacturer's guidelines. PCR program: 95°C 3 min >> 35x (95°C 30 s >> 55°C 30 s >> 72°C 1 min) >> 72°C 10 min >> 4°C hold (Primer sequences are detailed in **Table 15**). The presence of the G12D mutation was verified by Sanger sequencing.

Primer	Primer sequence
Fw	TCAAGCCTCAGACAGTGGTTC
Rv	CAGTTCTCATGTACTGGTCC

Table 15. Primer sequences used for the amplification of the *Kras*^{G12D} mutant sequence.

Lentiviral production, organoid transduction and selection

Lentiviral production

High-titer lentiviral particles were produced with a protocol optimized by Manuel Mastel. Initially, 15 million of HEK-293T cells were seeded in a 150 mm petri dish and cultured in DMEM (Life Tech, #31966047) supplemented with 10% FBS (Thermo Fisher, #A3382001) and 1% L-glutamine (Thermo Fisher, #25030024) in a 5% CO₂ incubator at 37°C. After 24 h, the media was replaced and the cells were transfected using polyethylenimine (PEI) (polysciences.com, #23966-100). For transfection, a mixture of 5.2 µg of the pMD2.D packaging plasmid (Addgene, #12259), 9.5 µg of the psPAX packaging plasmid (Addgene, #12260) and 8.4 µg of the plasmid of interest (**Table 16**) was prepared in H₂O with 1.5 M NaCl.

This mix was vortexed for 10 seconds with PEI and incubated for 20 minutes at room temperature prior to being added to the cells in a dropwise manner. “The media was changed 12–24 hours after transfection. 50-70 hours after transfection, the supernatant containing the lentiviral particles was harvested and filtered. The lentivirus was concentrated by ultracentrifugation at 25,000 rpm. for 2 hours at 4 °C (Optima L-90K Ultracentrifuge; Beckman Coulter, Krefeld, Germany) with a SW 32 Ti rotor (Beckman Coulter).” (Vaquero-Siguero et al., 2022) Concentrated virus was then re-suspended in 100 µl of Advanced DMEM/F12 and stored at -80°C.

Organoid transduction and selection

The organoids from a confluent well (containing 7x20 µL BME domes) of a 6-well plate were dissociated with TrypLE and resuspended in 500 µl of complete media with 10 µg/ml of Polybrene (Sigma, #TR-1003). 50 µl of the virus were added to the organoid suspension and the mix was spun down at 32°C for 30 minutes and incubated at 37°C for 1 hour. Finally, organoids were plated in 70% BME. 4-5 days after transduction, selection of the transduced organoids was based on the selection marker present in the plasmid of interest: FACS or blasticidin (7 µg/ml) (Santa-Cruz, #sc-495389) (Table 16).

Plasmid	Insert	Selection marker	Source
LeGO-EBFP2	EBFP2	FP	Addgene, #85213
LeGO-S2	T-Sapphire	FP	Addgene, #85211
LeGO-GFP	EGFP	FP	Addgene, #25917
LeGO-V2	Venus	FP	Addgene, #27340
LeGO-mOrange2	mOrange2	FP	Addgene, #85212
LeGO-dKatushka2	dKatushka	FP	Addgene, #85214
Lenti-Blast	n.a	Blasticidin	Dr. Jackstadt's laboratory
Lenti-TROP2-2A-BlastR	human TROP2	Blasticidin	Dr. Jackstadt's laboratory
Lenti-N1icd-2A-BlastR	murine Notch1-ICD	Blasticidin	Dr. Jackstadt's laboratory

Table 16. Vectors used for the lentiviral. FP, Fluorescent protein; ICD, intracellular domain.

Single cell dissociation of organoids

BME domes containing the organoids were detached from the plates and transferred to a 15 ml Falcon. 5 ml of ice-cold PBS was added and samples were centrifuged at 1500 rpm for 5 minutes. The supernatant containing the PBS and BME was aspirated and the pellet

containing the organoids was resuspended in 200 µl of TrypLE and incubated at room temperature for 1 minute (for MTOs) or 5 minutes (for PDOs). Subsequently, 5 ml of ice-cold PBS were added to stop the digestion. The mixture was filtered using the 40 µm EASYSTRAINER filter (Greiner Bio-One GmbH, #542140) and centrifuged for 5 minutes at 1200 rpm. The supernatant was removed and single cells were resuspended in PBS, BME or FACS buffer depending on the experiments.

Clonogenicity assays

MTOs or PDOs were single-cell dissociated as previously described. Subsequently, 1.000 single cells were seeded in 20 µl BME in 24-well plates and incubated for five to ten days until organoids were formed. At endpoint, the number of organoids per well was quantified under the light microscope and organoid size was quantified for one representative image per well using the Fiji software.

In vitro drug treatment

For *in vitro* ablation of iCaspase9 expressing cells, MTOs were seeded and treated with 1 µM or 0.1µM of AP-20187 for 24 hours. After that, cells were collected to assess the efficiency of depletion by flow cytometry or RT-qPCR.

FOLFIRI chemotherapy treatment was performed by treating single cells with (5 mM 5-FU and 5 mM irinotecan) for 72 hours. Subsequently, cells were collected to assess the effect of the treatment on the foetal and adult ISC programs by flow cytometry and RT-qPCR.

In vitro lineage tracing

To induce *in vitro* recombination of the *Rosa26*^{LSL-tdTomato} allele, organoids were treated with 10 µM of 4-Hydroxy-tamoxifen (4-OHT) for 24 hours. 4-OHT was removed from the media and cells were analyzed by flow cytometry to evaluate recombination efficiency at different timepoints.

Organoid and tumour cryopreservation

PDOs or MTOs were mechanically broken into small fragments by pipetting and cryopreserved in freezing media (Life Technologies, #12648010). Tumour and liver metastases were mechanically broken into small fragments and cryopreserved in freezing media (Life Technologies, #12648010). Samples were stored at -80°C or in liquid nitrogen until further use.

Tumour dissociation

For tumour dissociation into single cells, tumour fragments were thawed in 5 ml PBS and centrifuged 5 minutes at 1200 rpm to remove the DMSO present in the freezing media. The fragments were then enzymatically digested with the tumour dissociation kit (Miltenyi, #130-095-929) following manufacturer's instructions. In brief, 5 ml of DMEM GlutaMax was supplemented with 500 µl of the enzyme mix and placed in the gentleMACS C Tube (Miltenyi, #130-096-334) together with the tumour fragments. The tubes were placed in the gentleMACS Octo Dissociator with heaters (Miltenyi, #130-096-427) and dissociated using the default programs 37C_m_TDK_1 (for murine tissue) and 37C_h_TDK_1 (for human tissue). Samples were then filtered using the 40 µm EASYSTRAINER filter (Greiner Bio-One GmbH, #542140) and centrifuged for 5 minutes at 1200 rpm. The supernatant was removed and single cells were stained with different specific antibodies.

FACS and flow cytometry analysis

Single cell samples from human or mouse organoids and tumours were generated as previously described. When indicated in the figure legend, single cells were stained with anti-TROP2 (human: BV605 anti-TROP2 (BD Bioscience, #743274); mouse: APC anti-TROP2 (R&D, #FAB1122A)) (1:100), eFl450 anti-CD31 (eBioscience, #48-0311-82) (1:1000), PB anti-CD45 (Biolegend, #103126) (1:1000), FITC anti-EpCAM (Miltenyi, #130-123-674) (1:100) for 30 minutes at 4°C in the dark. Next, samples were washed with 5 mL FACS Buffer (PBS with 1% FCS) and resuspended in 200 µl FACS Buffer with 4',6-diamidino-2-phenylindole (DAPI) (Biolegend, #422801) or ZombieNIR (Biolegend, #423105), which were used as a death exclusion markers. Samples were analysed on a BD LSR Fortessa and further analysed on FlowJo 10.7.1. For FACS the Fusion cell sorter was used. The LeGO optical barcoded organoids and tumours were analysed on the BD LSR Fortessa with a specific filter configuration (**Table 17**).

Fluorescent protei	Laser (nm)	Dicroic Mirror (nm LP)	Bandpass Filter (nm)
EBFP2	405	-	450/50
T-Sapphire	405	505	525/50
EGFP	488	505	515/20
Venus	488	550	560/40
mOrange2	561	570	586/10
dKatushka	561	735	780/60
ZombieNIR	640	750	780/60

Table 17. Filter configuration on the BD LSR Fortessa to analyze the LeGO optically barcoded cells.

Flow cytometry analysis of tdTomato signal 24 hours after AP-20187 treatment was performed by dissociating the into single cells as previously described. tdTomato^{high} was calculated by gating for the 10% highest tdTomato signal in the non-treated population.

DNA extraction

gDNA from cell pellets was extracted using the DNeasy Blood & Tissue Kit (Qiagen, #69506) following the manufacturer's guidelines. Briefly, cell pellets were resuspended in 200 µL of PBS and 20 µL of proteinase K. Next, 200 µL of buffer AL and 200 µL of 100% ethanol were sequentially added to the pellet and mixed by vortexing. The mixture was transferred to a DNeasy Mini spin column and centrifuged at 8.000 rpm for 1 min. The flow through was discarded and 500 µL of Buffer AW1 was added to the DNeasy Mini spin column and centrifuged at 8.000 rpm for 1 minute. The flow through was discarded and 500 µL of Buffer AW2 was added to the DNeasy Mini spin column and centrifuged at 8.000 rpm for 1 minute. Finally, the DNeasy Mini spin column was centrifuged at 8.000 rpm for 1 minute to remove any residual ethanol. DNA was finally eluted in nuclease-free water.

RNA extraction from cell pellets and tumour tissue

RNA from cell pellets or tissue preserved in RNAlater (Invitrogen, #AM7021) was extracted using QIAGEN RNeasy kit (Qiagen #74104) according to the manufacturer's instructions. Briefly, tissue samples were homogenized with the GentleMACS homogenizer with 600 µl RLT buffer with 10 µl/mL of β-mercaptoethanol in gentleMACS M Tubes (Miltyeni, #130-096-335). Cell pellets were lysed by pipetting in 600 µl RLT buffer. Next, 600 µl of 70% ethanol were added to the lysates and transferred to a RNeasy spin column that was centrifuged for 1 minute at 10.000 rpm. The flow through was discarded and 350 µl of RW1 buffer was added to the RNeasy spin column and centrifuged for 1 minute at 10.000 rpm. For DNA digestion, 10 µl DNaseI (Qiagen #79254) and 70 µl RDD Buffer (Qiagen #79254) were added to the RNeasy spin column and incubated at room temperature for 15 minute. 700 µl of RW1 buffer were added on top and the column was centrifuged for 1 minute at 10.000 rpm and the flow through was discarded. 500 µl of RPE buffer were added and the RNeasy spin column was centrifuged for 2 minutes at 10.000 rpm. The column was transferred to a new tube and the RNA was eluted with RNase-free water and stored at -80°C until further use.

RNA extraction from sorted cells

RNA from a minimum of 40.000 FACS-sorted cells was isolated using the Arcturus™ PicoPure™ RNA Isolation Kit (Applied Biosystems, #KIT0204) following manufacturer's guidelines. DNA digestion was performed as previously described.

cDNA synthesis

RNA concentration was quantified using the NanoDrop spectrophotometer. cDNA was synthesized by reverse transcription of the isolated RNA using the High Capacity cDNA Reverse Transcription kit (Applied Biosystems, #4374966) according to manufacturer's guidelines. Preparation of the reaction mixture is detailed in **Table 18** and the synthesis program used is: 25°C 10 min >> 37°C 120 min >> 85°C 5 min) >> 4°C hold.

Reagent	Volume (μL)
10 X Buffer	2
25 X dNTP Mix (100 Mol)	0.8
10 X RT Random Primers	2
RNAse Inhibitor	1
Reverse Transcriptase	1
RNA (1μg)	X
Nuclease Free Water	up to 20 μL
Total	20 μL

Table 18. Reaction mixture for cDNA synthesis.

For samples with low RNA concentrations (i.e. RNA samples from sorted cells) the cDNA was synthesized with the SuperScript™ VILO™ Master Mix (Thermo Fisher, #11755050) according to manufacturer's guidelines. In brief, 16 μl of RNA were mixed with 4 μl of the SuperScript™ VILO™ Master Mix. cDNA was synthesized using the following program: 25°C 10 min >> 42°C 60 min >> 85°C 5 min) >> 4°C hold.

Real-Time Quantitative PCR (RT-qPCR)

RT-qPCR was performed using the PowerUp™ SYBR™ Green Master Mix (ThermoFisher-Scientific, #A25778) following manufacturer's guidelines. Reaction mixture was prepared as follows (**Table 19**):

Reagent	Volume (μL)
PowerUp™ SYBR™ Green Master Mix	5
cDNA*	2
Fw primer (10 μM)	0.5
Rv primer (10 μM)	0.5
Nuclease-free water	2

Total	10 μL
--------------	-----------------------------

*cDNA was previously diluted 1:5 in nuclease-free water.

Table 19. Reaction mixture for RT-qPCR. Fw, forward; Rv, reverse.

Samples were loaded into a 386-well PCR plate as 3 technical replicates. The plate was sealed and briefly centrifuged before loading into the QuantStudio™ 5 Real-Time PCR System (Applied Biosystems) (program detailed in **Table 20**). The Ct-values of the genes of interest were normalized to the Ct-values of the housekeeping genes (mouse: *Gapdh* or *s18*; human: *GAPDH*, *RPL13A*) (primer sequences are detailed in **Table 21**). Relative expression levels were calculated using the $\Delta\Delta$ Ct method.

Temperature (°C)	Time (seconds)	Cycles
50	120	X1
95	600	
95	15	X40
60	60	
95	15	X1
60	15	

Table 20. RT-qPCR program.

Gene	Specie	Primer sequence
<i>S18</i>	Mouse	Fw: AAGGAGACTCTGGCATGCTAAC Rv: CAGACATCTAAGGGCATCACAGAC
<i>Gapdh</i>	Mouse	Fw: AGCCTCGTCCCGTAGACAA Rv: TGGCAACAATCTCCACTTTG
<i>Lgr5</i>	Mouse	Fw: GACAATGCTCTCACAGAC Rv: GGAGTGGATTCTATTATTATGG
<i>Tacstd2</i>	Mouse	Fw: GAACGCGTCGCGAGAAGGGC Rv: CGGCGGCCCCATGAACAGTGA
<i>Ly6a</i>	Mouse	Fw: AGGAGGCAGCAGTTATTGTGG Rv: CGTTGACCTTAGTACCCAGGA
<i>Anxa1</i>	Mouse	Fw: ATGTTGCTGCCTTGACAAAA Rv: CCAAGGGCTTTCCATTCTCCT
<i>Krt7</i>	Mouse	Fw: AGGAGATCAACCGACGCAC Rv: GTCTCGTGAAGGGTCTTGAGG
<i>Smoc2</i>	Mouse	Fw: GTTCGCACACCGGATCTTC Rv: TTGATCGACTCTCAAGAACGTG
<i>Axin2</i>	Mouse	Fw: GCGACGCACTGACCGACGAT

		Rv: GCAGGCGGTGGGTTCTCGGA
<i>Krt20</i>	Mouse	Fw: AGTTTTTCACCGAAGTCTGAGTTC Rv: GTAGCTCATTACGGCTTTGGAG
<i>tdTomato</i>	n.a	Fw: AGCAAGGGCGAGGAGGTCATC Rv: CCTTGGAGCCGTACATGAACTGG
<i>GAPDH</i>	Human	Fw: GGAGCGAGATCCCTCCAAAAT Rv: GGCTGTTGTCATACTTCTCATGG
<i>RPL 13A</i>	Human	Fw: AAGTACCAGGCAGTGACAG Rv: CCTGTTTCCGTAGCCTCATG
<i>TACSTD2</i>	Human	Fw: ACAACGATGGCCTCTACGAC Rv: GTCCAGGTCTGAGTGGTTGAA

Table 21. Primer sequences used for RT-qPCR. Fw, forward; Rv, reverse.

10x single-cell RNA sequencing

scRNA sequencing from VAKPS and VKPN subcutaneous tumours was performed by Manuel Mastel. Tumour samples were dissociated into single cells as previously described. Live cells were sorted and sequenced following the Chromium Next GEM Single Cell 3' Reagent Kit 3.1 (Dual Index) protocol.

scRNA-seq from patient CRC samples and from PDXs was performed by Dr. Sigrid Fey. Tumour samples were dissociated into single cells as previously described. Patient CRC samples were sorted for live cells whereas PDX samples were sorted for epithelial cells. Samples were sequenced following the Chromium Next GEM Single Cell 3' Reagent Kit 3.1 (Dual Index) protocol. Analysis was conducted by Dr. Bryce Lim, Dr. Maria Puschhof and Manuel Mastel: "The AKPS KPN single-cell RNA-seq data was preprocessed in R using Seurat. Get additional information from person in charge."

Analysis of public datasets

The transcriptome data and clinical metadata of the TCGA-COAD cohort was analysed by Dr. Maria Puschhof. "The transcriptomic data and metadata of the TCGA-COAD cohort loaded through the TCGAbiolinks package 14–16 (v2.25.3) in R (v4.2.0). Gene expression differences across stages were analyzed through pairwise comparisons using a Wilcoxon rank sum test with Holm p-value correction for multiple testing using the `ggpubr::compare_means` function 17 (v0.6.0). For the comparison of all foetal genes, the foetal gene set ([Mustata et al., 2013](#)), converted to human homologues, served as a starting point. Genes with significant positive correlation between expression value and clinical stage in at least 2 out of 6 comparisons were considered putative progression markers".

The transcriptome data and clinical metadata of the SMC and KUL cohorts (Joanito et al., 2022) were analysed by Dr. Maria Pushhof and Dr. Bryce Lim "The epithelial expression data of the SMC and KUL data cohorts was normalized using the Seurat package (v5.0.1). Subsequent analyses were performed as described above."

Gene sets, scores and enrichment analysis

"Gene set scores at single cell level were computed using the `scanpy.tl.score_genes` function. Conversely, GSEA was performed at pseudobulk level on the statistics of differential gene expression results using the decoupler implementation `decoupler.get_gsea_df`" by Dr. Maria Puschhof.

Kaplan-Meier plots from publicly available datasets

Kaplan-Meier plot for CRC patients segregated by *TACSTD2* expression levels were generated in the <https://kmplot.com/analysis/> website. Automatic best cut-off was used and data from 1336 patients was used (Gyorffy, 2024).

Western Blot

Cell pellets from MTOs and PDOs were washed with ice-cold PBS and lysed in ice-cold Radioimmunoprecipitation Assay (RIPA) buffer (Cell Signaling, #9806S) supplemented with the Protease Inhibitor Cocktail (Sigma, #P8340) and 1 mM EDTA pH8 (Invitrogen, #AM9260G) and incubated for 20 minutes on ice. Lysates were centrifuged for 10 minutes at 4°C at 14.000 rpm and the supernatants were transferred into a new tube. Protein concentration was determined using the Pierce BCA Protein Assay Kit (ThermoFisher-Scientific, #23225), using BSA (ThermoFisher-Scientific, #23209) as the standard reference. For protein denaturalization, protein lysates were then boiled for 10 minutes at 95°C with NuPAGE™ LDS buffer (Invitrogen, #NP0007) and NuPAGE™ Sample Reducing Agent ((Invitrogen, #NP0009). Denaturalized proteins were loaded in a precast SDS–polyacrylamide electrophoresis gel (BioRad, #5671084) and ran at 120-150 V until desired protein separation was achieved. Next, proteins were transferred to a nitrocellulose membrane (Cytiva, #GE10600002) using a semi-dry transfer method with the Trans-Blot Turbo Transfer System (Bio-Rad, #1704150) following the "1.5 MM Gel protocol". Correct protein transfer was verified by Ponceau S reversible staining. The membrane was washed with Tris-buffered saline-Tween20 (TBD-T) buffer (**Table 22**) and blocked in 5% milk in TBS-T for 1 hour at room temperature followed by overnight incubation at 4°C with specific primary antibodies (**Table 23**). Membranes were washed 3 times with TBS-T for 10 minutes in gentle agitation at room temperature and incubated with specific HRP-conjugated secondary antibodies (1:10.000 in TBS-T) for 1 hour at room

temperature. Finally, membranes were developed via chemiluminescence using HRP substrate (Bio-Rad, #1705062) and imaged with the ChemiDoc Imaging System (BioRad).

Reagent	Final concentration
NaCl	137 mM
KCl	2.7 mM
Tris-base	19 mM
Tween20	0.05%
Milli-Q water (pH 7.4)	X

Table 22. TBS-T buffer composition

Antibody	Reactivity	Dilution	Species	Supplier	Catalog #
Anti-human TROP2	Human	1:1000	Rabbit	Abcam	ab227691
Anti-mouse TROP2	Mouse	1:2000	Goat	R&D	AF1122
anti- β Actin	Human, Mouse	1:2000	Mouse	Santa Cruz	sc-47778
Anti-Mouse IgG/HRP Conjugated	Mouse	1:10000	Goat	Dako	P0447
Anti-Goat IgG/HRP Conjugated	Goat	1:10000	Donkey	Thermo Scientific	PA128664

Table 23. List of the Western Blot antibodies used.

Histology

Tissue processing

Human and murine tissues were fixed overnight in 10% formalin at 4°C. Tissue samples were processed and embedded by the DKFZ histology facility. Paraffin blocks were cut into 3 μ m thick slices using a microtome (Leica, #ASP300S) by the DKFZ histology facility and placed into Superfrost Plus slides (VWR International, #631-9483). Blank slides were deparaffinized by 2 consecutive washes with Xylene for 3 minutes each followed by a rehydration process by washing the slides with 100%, 95%, 80% and 70% ethanol solutions for 1 minute each. Finally, slides were rinsed with distilled water for 5 minutes.

Haematoxylin & Eosin

After tissue processing, tissue slides were stained with haematoxylin (Sigma, #51275) for 6 minutes and rinsed with running tap water for 1 minute. For cytoplasmic counterstaining, tissue slides were stained with eosin (Sigma, #HT110232) for 1 minute. Finally, slides were dehydrated by sequential washing steps in 95% and 100% ethanol for 1 minute and 15 minutes with xylene and mounted with DPX mounting medium (Sigma-Aldrich, #06522).

Immunohistochemistry (IHC)

After tissue processing, antigen retrieval was performed in a steamer in boiling target retrieval solution (Dako, #S169984) for 30 minutes. Tissue slides were then cooled down for 10 minutes in dH₂O and quenched in 3% H₂O₂ (Sigma #95321) (in PBS) for 10 minutes. Next, the slides were washed for 5 minutes in TBS-T. Samples were blocked in TNB buffer (0.1 M Tris-HCL, pH 7.5, and 0.15 M NaCl with 0.5% w/v blocking reagent (Perkin Elmer, #FP1020)) for 1-2 hours at room temperature and then incubated with specific primary antibodies (**Table 24**) at 4°C overnight or 1.5 hours at room temperature. After incubation, the slides were washed twice with TBS-T and incubated with the corresponding biotinylated secondary antibody (**Table 25**) at room temperature for 1 hour. Next, the ABC avidin–biotin–DAB staining was performed (Vector laboratories, #PK-6100) according to the manufacturer's instructions. The samples were counterstained with hematoxylin for 6 minutes and rinsed with running tap water for 1 minute. Finally, the samples were dehydrated through sequential washings in 70%, 80%, 95% and 100% ethanol and xylene and mounted with DPX mounting medium. Images were acquired using a 20× magnification on the Zeiss Axio Scan.Z1 slide scanner and analyzed with FIJI (ImageJ) or QuPath 0.4.3 softwares.

Antibody	Reactivity	Dilution	Host Specie	Supplier	Catalog #
Anti-human TROP2	Human	1:1000	Rabbit	Abcam	ab227691
Anti-mouse TROP2	Mouse	1:100	Goat	R&D	AF1122
Anti-RFP	n.a	1:50	Rabbit	Rockland	600-401-379
Anti-tdTomato	n.a	1:100	Goat	Sicgen	AB8181-200

Table 24. List of the primary antibodies used for histology.

Antibody	Dilution	Host Specie	Supplier	Catalog #
anti-rabbit IgG (H+L)	1:200	Goat	Vector Laboratories	BA-1000
anti-goat IgG (H+L)	1:200	Rabbit	Vector Laboratories	BA-5000

Table 25. List of the biotinylated secondary antibodies used for IHC.

Immunofluorescence (IF)

After tissue processing, antigen retrieval was performed in a steamer in boiling target retrieval solution (Dako, #S169984) for 30 minutes. Tissue slides were then cooled down for 10 minutes in dH₂O and quenched in 3 % H₂O₂ (Sigma #95321) (in PBS) for 10 minutes. Next, the slides were washed for 5 minutes in TBS-T. Samples were blocked in TNB buffer (0.1 M Tris-HCL, pH 7.5, and 0.15 M NaCl with 0.5% w/v blocking reagent (Perkin Elmer, #FP1020)) for 1-2 hours at room temperature and then incubated with specific primary antibodies (**Table 24**) at 4°C overnight or 1.5 hours at room temperature. After incubation, the slides were washed twice with TBS-T and incubated with the specific secondary antibody (**Table 26**) and

DAPI (1:1000) for 30 minutes at room temperature. Finally, slides were washed twice with TBS-T for 5 minutes and mounted with ProLong Gold Antifade Mountant (ThermoFischer Scientific, #P10144). Images were acquired with Zeiss LSM 710 microscope and analyzed with FIJI (ImageJ).

Antibody	Dilution	Supplier	Catalog #
Alexa Fluor 488 goat anti-rabbit IgG	1:1000	Invitrogen	A11034
Alexa Fluor 488 donkey anti-rabbit IgG	1:1000	Invitrogen	A21206
Alexa Fluor 555 donkey anti-goat IgG	1:1000	Invitrogen	A21432
Alexa Fluor 488 donkey anti-rat IgG	1:1000	Invitrogen	A21208

Table 26: List of the fluorescent secondary antibodies used for IF.

Histological analysis

Evaluation of the metastatic burden was performed on hematoxylin and eosin-stained sections. The area of each individual metastatic nodule was delineated and annotated. Metastatic burden was calculated as the percentage of liver area occupied by metastatic nodules. For quantification of the lineage tracing IHC for tdTomato were used. Number of tdTomato⁺ cells per clone were quantified. Three tissue slides per tumour were used for the quantification.

Mouse Experiments

All mouse experiments described in this thesis were performed according to the German local regulations. The experiments were approved by the local veterinary authorities and by the Regierungspräsidium Karlsruhe, Baden-Württemberg, Germany under the permit numbers G-148-20, G-235-20, G-27-22, G-159-22, G-164-22. Mice were housed according to the local and latest standards at the DKFZ animal facilities with a 12-hour dark and light cycle, a constant temperature (20-24°C) and humidity (45-65%) and were provided with a rodent-specific diet and water *ad libitum*. Mice were weaned at 3-4 weeks old and kept in cages containing up to 6 animals. Animals were monitored according to the animal licenses.

Tacstd2^{CreERT2} GEMM generation

To lineage trace Trop2-expressing cells, in collaboration with the transgenic facility from DKFZ, I generated the *Tacstd2*^{CreERT2} GEMM. To that end, the TAG stop codon of the *Tacstd2* gene was replaced with "P2A-CreERT2-FRT-NeoR-FRT" cassette (construct generated by Gene-H). This CreER knock-in allele was generated by homologous recombination of a BAC clone in ES cells. ES cells were selected with neomycin for 12 days and the 288 resistant

clones were picked and expanded by Dr. Franciscus van der Hoeven and Brittney Armstrong. Correct insertion of the donor sequence was verified by PCR with the Kapa Long Range (Roche, #KK3502) according to manufacturer's guidelines. PCR primers are detailed in **Table 27**. PCR program: 95°C 3 min >> 35x (95°C 30 s >> 60°C 30 s >> 68°C 6 min) >> 72°C 6 min >> 4°C hold. Dr. Franciscus van der Hoeven and Brittney Armstrong injected the ES positive clones into C57BL/6N blastocyst and embryo transfer into RjOrl:SWISS recipient female mice.

Region	Primer	Primer sequence
5' specific	Fw	GCCCCTAATACTAACCACAGACA
	Rv	GCAAATTTTGGTGACGGTCAG
3' specific	Fw	GCCAGAGGCCACTTGTGTAG
	Rv	GTTCTAATTCCAGTCCACCCATG

Table 27. Primer sequences used for specific integration PCR.

Mouse Lines

7-8 weeks old male C57BL/6J mice were purchased from Janvier Labs (Saint-Berthevin, France). NOD-scid IL2R gamma null (NSG) mice were provided by the animal facility at DKFZ. *Lgr5*^{EGFP-IRES-creERT2} GEMM (RRID:IMSR_JAX:008875) was generously provided by Prof. Michaela Frye. *Rosa26*^{LSL-tdTomato} GEMM (B6.Cg-Gt(ROSA)26Sortm14(CAG-tdTomato)Hze/J; RRID:IMSR_JAX:007914) was kindly provided by Prof. Peter Angel. *FLPe* GEMM (B6.Cg-Tg(ACTFLPe)9205Dym/J; RRID:IMSR_JAX:005703) was generously provided by Prof. Dr. Michael Platten. *Tacstd2*^{creERT2} GEMM was generated at the DKFZ by me in collaboration with the transgenic facility led by Prof. Dr. Franciscus van der Hoeven.

All the GEMMs were bred in a C57BL/6J background. *Lgr5*^{EGFP-IRES-CreERT2} and *Tacstd2*^{creERT2} alleles were kept in heterozygosity whereas the *Rosa26*^{LSL-tdTomato} and the *FLPe* alleles were utilized in either homozygosity or heterozygosity. The *Tacstd2*^{creERT2} allele was only used in experiments when the Neomycin resistance cassette was removed.

Mouse Genotyping

To extract DNA for genotyping, mouse ear punches were digested in 25 µl Buffer I (25 mM NaOH, 0.2 µM EDTA) for 15 minutes at 95°C. Following digestion, the reaction was neutralized with 25 µl Buffer II (40 mM Tris-HCl pH 5). DNA was then genotyped for the different alleles using the Green PCR Master Mix following manufacturer's guidelines. Specific primers (**Table 28**) and PCR programs (**Table 29**) for the different alleles were used. Amplicons were separated on a 2% agarose gel containing Ethidium Bromide and visualized under a UV light.

Allele	Primer Sequence	Expected size
<i>Lgr5</i> ^{tm1(cre/ERT2)Cle}	CTGAACCTGTGGCCGTTTAC	wild-type: 386 bp Transgene present: 119 bp
	GTCTGGTCAGAATGCCCTTG	
	CTGCTCTCTGCTCCCAGTCT	
<i>Tacstd2</i> ^{CreERT2}	GAACGCGTCGCAGAAGGGC	wild-type: 670 bp Transgene present: 437 bp
	GCAAATTTTGGTGTACGGTCAG	
	GCCGCTTTCCCATTTCAAACC	
NeoR	CGGTGGGCTCTATGGCTATCAAC	Cassette present: 450 bp
	GCGATGCCTGCTTGCCGAATA	
B6.Cg-Tg(ACTFLPe)9205Dym/J	CACTGATATTGTAAGTAGTTTGC	wild-type: 324 bp Transgene present: 725 bp
	CTAGTGCGAAGTAGTGATCAGG	
	CTAGGCCACAGAATTGAAAGATCT	
	GTAGGTGGAAATTCTAGCATCATCC	
B6.Cg-Gt(ROSA)26Sortm14(CAG-tdTomato)Hze/J	AAGGGAGCTGCAGTGGAGTA	wild-type: 297 bp Transgene present: 284 bp
	CCGAAAATCTGTGGGAAGTC	
	CGGGCCATTTACCGTAAGTTAT	

Table 28. Primer sequences for specific mouse allele genotyping.

Allele	PCR program
<i>Lgr5</i> ^{tm1(cre/ERT2)Cle}	94°C 2 min >> 10x (94°C 45 s >> 65°C (-0.5 °C/cycle) 1 min >> 72°C 1 min) >> 28x (94°C 1 min >> 60°C 45 s >> 72°C 1 min) >> 72°C 5 min >> 4°C hold
<i>Tacstd2</i> ^{CreERT2}	95°C 3 min >> 35x (95°C 30 s >> 55°C 1 min >> 72°C 1 min) >> 72°C 10 min >> 4°C hold
NeoR	95°C 3 min >> 35x (95°C 30 s >> 55°C 1 min >> 72°C 1 min) >> 72°C 10 min >> 4°C hold
B6.Cg-Tg(ACTFLPe)9205Dym/J	94°C 5 min >> 35x (94°C 30 s >> 58°C 1 min >> 72°C 1 min) >> 72°C 7 min >> 4°C hold
<i>Rosa26</i> ^{LSL-tdTomato}	95°C 3 min >> 35x (95°C 30 s >> 55°C 1 min >> 72°C 1 min) >> 72°C 10 min >> 4°C hold

Table 29. PCR programs used for specific mouse allele genotyping.

Murine Colonoscopy-Guided Mucosal Injection

“Murine colonoscopy was conducted using a Karl Storz TELE PACK VET X LED endoscope video unit or a Karl Storz endoscope system consisting of a suction and irrigation device (Karl Storz, vetpump2), documentation system (Karl Storz, AIDA), cold light source (Karl Storz, xenon 175), imaging system (image1 S, Karl Storz, Tuttlingen, Germany), and Hopkins Telescope (part 67030 BA). Mice were anesthetized with isoflurane and organoids were injected using a syringe (Hamilton Inc., Reno, NV, USA, 7656-01), a transfer needle to

take up substances (Hamilton Inc., 7770-02), and an injection needle (Hamilton Inc., 7803-05). The injection needle was placed on the colon mucosa with the bevel facing the mucosa. Afterwards, 70 µl of 4-OHT or organoids was injected into the mucosa to form a bubble. Mice were sacrificed at week 6 or when the endpoint was reached" (Vaquero-Siguero et al., 2022).

Subcutaneous injection and tumour monitoring

Mice were anesthetized with isoflurane and single cells in a final volume of 100 µl (50 µl PBS and 50 µl BME) were injected into the left flank of recipient mice using an insulin syringe needle. Tumour growth was monitored three times per week and experimental endpoint was defined by tumour length >1.5 cm, tumour ulceration, animal distress or end of specific treatment.

To assess the tumour initiation capacity of specific tumour cell populations viable (ZombieNIR⁻), CD45⁻/CD31⁻, EpCam⁺ single cells from dissociated xenograft were sorted and subsequently transplanted subcutaneously into recipient mice. The first day of tumour detection was recorded and tumour growth was monitored as previously described. The experiment was finished when the first animals of the cohort reached a tumour length >1.5 cm.

Intrasplenic injection and tumour monitoring

Mice were anesthetized with isoflurane and single cells in a final volume of 50 µl PBS were injected in the spleen of the mice using an insulin syringe needle. To that end, an incision on the left flank of the mouse was performed and the pancreas was gently pulled out of the abdominal cavity to access the spleen. 10 mg/kg lidocaine and 3 mg/kg bupivacaine were subcutaneously administrated after surgery close to the incision site. Metamizol was administered in the drinking water for three days. Animal weight was monitored 3 times per week. Experimental endpoint was at four weeks after injection of MTOs.

***In vivo* AP-20187 treatment**

To induce cell ablation of cells expressing the iCaspase9 cassette, animals were treated with 10 mg/kg AP-20187 (Tocris, #6297) for ten days by intraperitoneal injection according to manufacturer's guidelines.

***In vivo* lineage tracing**

For *in vivo* lineage tracing of TROP2⁺ cells I subcutaneously transplanted the *Tacstd2*^{CreERT2}; *Rosa26*^{LSLtdTomato} transformed organoids in the flank of C57BL/6J mice. To ensure *in vivo* lineage tracing, 1 mg/kg tamoxifen (Sigma, #T5648) was intraperitoneally

administered. Animals were killed at day 2, 7, 14, 21 and 28 after tamoxifen administration and subcutaneous tumours were fixated in formalin.

Statistical analysis

For statistical analysis the GraphPad Prism software version 9 (GraphPad software) was used. Biological tests used are specified in the figure legends. Data is displayed as mean \pm SEM. Statistical significance is indicated as follows: * $p < 0.05$, ** $p < 0.01$, *** $p < 0.001$ and **** $p < 0.0001$. The number of replicates in every experiment is indicated as n in the figure legends.

Schemes and illustrations

Schemes and illustrations were generated by myself, unless otherwise stated, using Biorender.

Contributions

This thesis has been written by me and proofread by Dr. Rene Jackstadt. ChatGPT (<https://chatgpt.com/>) has been used for grammar corrections. The project has been designed by Dr. Rene Jackstadt and myself. The experiments were conducted by myself unless otherwise stated in the text. The characterization of the functional role of TROP2 was performed together with 2 MSc students, Belén Hackel and Johanna Kiefer. The single-cell RNA sequencing experiments were performed by Manuel Mastel and Dr. Sigrid Fey. Dr. Maria Puschhof, Dr. Bryce Lim and Manuel Mastel conducted the bioinformatic analysis. Additional technical assistance was provided by Dr. Sigrid Fey, Jasmin Meier, Carolin Artmann, Nikolaos Georgakopoulos and Gabriele Schmidt.

BIBLIOGRAPHY

- Aiderus, A., Barker, N., and Tergaonkar, V. (2024). Serrated colorectal cancer: preclinical models and molecular pathways. *Trends Cancer* 10, 76-91.
- Alvarez-Varela, A., Novellademunt, L., Barriga, F.M., Hernando-Momblona, X., Canellas-Socias, A., Cano-Crespo, S., Sevillano, M., Cortina, C., Stork, D., Morral, C., *et al.* (2022). Mex3a marks drug-tolerant persister colorectal cancer cells that mediate relapse after chemotherapy. *Nat Cancer* 3, 1052-1070.
- Armelaio, F., and de Pretis, G. (2014). Familial colorectal cancer: a review. *World J Gastroenterol* 20, 9292-9298.
- Avolio, M., and Trusolino, L. (2021). Rational Treatment of Metastatic Colorectal Cancer: A Reverse Tale of Men, Mice, and Culture Dishes. *Cancer Discov* 11, 1644-1660.
- Ayyaz, A., Kumar, S., Sangiorgi, B., Ghoshal, B., Gosio, J., Ouladan, S., Fink, M., Barutcu, S., Trcka, D., Shen, J., *et al.* (2019). Single-cell transcriptomes of the regenerating intestine reveal a revival stem cell. *Nature* 569, 121-125.
- Bala, P., Rennhack, J.P., Aitymbayev, D., Morris, C., Moyer, S.M., Duronio, G.N., Doan, P., Li, Z., Liang, X., Hornick, J.L., *et al.* (2023). Aberrant cell state plasticity mediated by developmental reprogramming precedes colorectal cancer initiation. *Sci Adv* 9, eadf0927.
- Bardia, A., Hurvitz, S.A., Tolaney, S.M., Loirat, D., Punie, K., Oliveira, M., Brufsky, A., Sardesai, S.D., Kalinsky, K., Zelnak, A.B., *et al.* (2021). Sacituzumab Govitecan in Metastatic Triple-Negative Breast Cancer. *N Engl J Med* 384, 1529-1541.
- Barker, N. (2014). Adult intestinal stem cells: critical drivers of epithelial homeostasis and regeneration. *Nat Rev Mol Cell Biol* 15, 19-33.
- Barker, N., Ridgway, R.A., van Es, J.H., van de Wetering, M., Begthel, H., van den Born, M., Danenberg, E., Clarke, A.R., Sansom, O.J., and Clevers, H. (2009). Crypt stem cells as the cells-of-origin of intestinal cancer. *Nature* 457, 608-611.
- Barker, N., van Es, J.H., Kuipers, J., Kujala, P., van den Born, M., Cozijnsen, M., Haegebarth, A., Korving, J., Begthel, H., Peters, P.J., *et al.* (2007). Identification of stem cells in small intestine and colon by marker gene *Lgr5*. *Nature* 449, 1003-1007.
- Battle, E., and Clevers, H. (2017). Cancer stem cells revisited. *Nat Med* 23, 1124-1134.
- Behjati, S., Huch, M., Van Boxtel, R., Karthaus, W., Wedge, D.C., Tamuri, A.U., Martincorena, I., Petljak, M., Alexandrov, L.B., Gudem, G., *et al.* (2014). Genome sequencing of normal cells reveals developmental lineages and mutational processes. *Nature* 513, 422-425.
- Berthelet, J., Wimmer, V.C., Whitfield, H.J., Serrano, A., Boudier, T., Mangiola, S., Merdas, M., El-Saafin, F., Baloyan, D., Wilcox, J., *et al.* (2021). The site of breast cancer metastases dictates their clonal composition and reversible transcriptomic profile. *Sci Adv* 7.
- Beumer, J., and Clevers, H. (2021). Cell fate specification and differentiation in the adult mammalian intestine. *Nat Rev Mol Cell Biol* 22, 39-53.
- Bhang, H.E.C., Ruddy, D.A., Radhakrishna, V.K., Caushi, J.X., Zhao, R., Hims, M.M., Singh, A.P., Kao, I., Rakiec, D., Shaw, P., *et al.* (2015). Studying clonal dynamics in response to cancer therapy using high-complexity barcoding. *Nature Medicine* 21, 440-448.
- Borowsky, J., Dumenil, T., Bettington, M., Pearson, S.A., Bond, C., Fennell, L., Liu, C., McKeone, D., Rosty, C., Brown, I., *et al.* (2018). The role of APC in WNT pathway activation in serrated neoplasia. *Mod Pathol* 31, 495-504.
- Canellas-Socias, A., Cortina, C., Hernando-Momblona, X., Palomo-Ponce, S., Mulholland, E.J., Turon, G., Mateo, L., Conti, S., Roman, O., Sevillano, M., *et al.* (2022). Metastatic recurrence in colorectal cancer arises from residual EMP1(+) cells. *Nature* 611, 603-613.
- Cardoso, R., Guo, F., Heisser, T., De Schutter, H., Van Damme, N., Nilbert, M.C., Christensen, J., Bouvier, A.M., Bouvier, V., Launoy, G., *et al.* (2022). Overall and stage-specific survival of patients with screen-detected colorectal cancer in European countries: A population-based study in 9 countries. *Lancet Reg Health Eur* 21, 100458.
- Celia-Terrassa, T., and Kang, Y. (2016). Distinctive properties of metastasis-initiating cells. *Genes Dev* 30, 892-908.

Cervantes, A., Adam, R., Rosello, S., Arnold, D., Normanno, N., Taieb, J., Seligmann, J., De Baere, T., Osterlund, P., Yoshino, T., *et al.* (2023). Metastatic colorectal cancer: ESMO Clinical Practice Guideline for diagnosis, treatment and follow-up. *Ann Oncol* **34**, 10-32.

Chen, B., Scurrah, C.R., McKinley, E.T., Simmons, A.J., Ramirez-Solano, M.A., Zhu, X., Markham, N.O., Heiser, C.N., Vega, P.N., Rolong, A., *et al.* (2021). Differential pre-malignant programs and microenvironment chart distinct paths to malignancy in human colorectal polyps. *Cell* **184**, 6262-6280 e6226.

Chen, C., Neumann, J., Kuhn, F., Lee, S.M.L., Drefs, M., Andrassy, J., Werner, J., Bazhin, A.V., and Schiergens, T.S. (2020). Establishment of an Endoscopy-Guided Minimally Invasive Orthotopic Mouse Model of Colorectal Cancer. *Cancers (Basel)* **12**.

Cheung, P., Xiol, J., Dill, M.T., Yuan, W.C., Panero, R., Roper, J., Osorio, F.G., Maglic, D., Li, Q., Gurung, B., *et al.* (2020). Regenerative Reprogramming of the Intestinal Stem Cell State via Hippo Signaling Suppresses Metastatic Colorectal Cancer. *Cell Stem Cell* **27**, 590-604 e599.

Clackson, T., Yang, W., Rozamus, L.W., Hatada, M., Amara, J.F., Rollins, C.T., Stevenson, L.F., Magari, S.R., Wood, S.A., Courage, N.L., *et al.* (1998). Redesigning an FKBP-ligand interface to generate chemical dimerizers with novel specificity. *Proc Natl Acad Sci U S A* **95**, 10437-10442.

Clevers, H., and Nusse, R. (2012). Wnt/beta-catenin signaling and disease. *Cell* **149**, 1192-1205.

Cong, L., Ran, F.A., Cox, D., Lin, S., Barretto, R., Habib, N., Hsu, P.D., Wu, X., Jiang, W., Marraffini, L.A., *et al.* (2013). Multiplex genome engineering using CRISPR/Cas systems. *Science* **339**, 819-823.

Cortina, C., Turon, G., Stork, D., Hernando-Momblona, X., Sevillano, M., Aguilera, M., Tosi, S., Merlos-Suarez, A., Stephan-Otto Attolini, C., Sancho, E., *et al.* (2017a). A genome editing approach to study cancer stem cells in human tumors. *EMBO Mol Med* **9**, 869-879.

Cortina, C., Turon, G., Stork, D., Hernando-Momblona, X., Sevillano, M., Aguilera, M., Tosi, S., Merlos-Suárez, A., Stephan-Otto Attolini, C., Sancho, E., *et al.* (2017b). A genome editing approach to study cancer stem cells in human tumors. *EMBO Molecular Medicine* **9**, 869-879.

Cubas, R., Li, M., Chen, C., and Yao, Q. (2009). Trop2: a possible therapeutic target for late stage epithelial carcinomas. *Biochim Biophys Acta* **1796**, 309-314.

Dagogo-Jack, I., and Shaw, A.T. (2018). Tumour heterogeneity and resistance to cancer therapies. *Nat Rev Clin Oncol* **15**, 81-94.

Davis, H., Irshad, S., Bansal, M., Rafferty, H., Boitsova, T., Bardella, C., Jaeger, E., Lewis, A., Freeman-Mills, L., Giner, F.C., *et al.* (2015). Aberrant epithelial GREM1 expression initiates colonic tumorigenesis from cells outside the stem cell niche. *Nat Med* **21**, 62-70.

de Sousa e Melo, F., Kurtova, A.V., Harnoss, J.M., Kljavin, N., Hoeck, J.D., Hung, J., Anderson, J.E., Storm, E.E., Modrusan, Z., Koeppen, H., *et al.* (2017a). A distinct role for Lgr5(+) stem cells in primary and metastatic colon cancer. *Nature* **543**, 676-680.

De Sousa E Melo, F., Kurtova, A.V., Harnoss, J.M., Kljavin, N., Hoeck, J.D., Hung, J., Anderson, J.E., Storm, E.E., Modrusan, Z., Koeppen, H., *et al.* (2017b). A distinct role for Lgr5 + stem cells in primary and metastatic colon cancer. *Nature* **543**, 676-680.

Dekker, E., Tanis, P.J., Vleugels, J.L.A., Kasi, P.M., and Wallace, M.B. (2019). Colorectal cancer. *Lancet* **394**, 1467-1480.

Douillard, J.Y., Siena, S., Cassidy, J., Tabernero, J., Burkes, R., Barugel, M., Humblet, Y., Bodoky, G., Cunningham, D., Jassem, J., *et al.* (2010). Randomized, phase III trial of panitumumab with infusional fluorouracil, leucovorin, and oxaliplatin (FOLFOX4) versus FOLFOX4 alone as first-line treatment in patients with previously untreated metastatic colorectal cancer: the PRIME study. *J Clin Oncol* **28**, 4697-4705.

Dow, L.E., O'Rourke, K.P., Simon, J., Tschaharganeh, D.F., van Es, J.H., Clevers, H., and Lowe, S.W. (2015). Apc Restoration Promotes Cellular Differentiation and Reestablishes Crypt Homeostasis in Colorectal Cancer. *Cell* **161**, 1539-1552.

Drost, J., and Clevers, H. (2018). Organoids in cancer research. *Nat Rev Cancer* **18**, 407-418.

Dunne, P.D., and Arends, M.J. (2024). Molecular pathological classification of colorectal cancer-an update. *Virchows Arch* **484**, 273-285.

Fazilaty, H., Brugger, M.D., Valenta, T., Szczerba, B.M., Berkova, L., Doumpas, N., Hausmann, G., Scharl, M., and Basler, K. (2021). Tracing colonic embryonic transcriptional profiles and their reactivation upon intestinal damage. *Cell Rep* 36, 109484.

Fearon, E.R. (2011). Molecular genetics of colorectal cancer. *Annu Rev Pathol* 6, 479-507.

Fearon, E.R., and Vogelstein, B. (1990). A genetic model for colorectal tumorigenesis. *Cell* 61, 759-767.

Fey, S.K., Vaquero-Siguero, N., and Jackstadt, R. (2024). Dark force rising: Reawakening and targeting of fetal-like stem cells in colorectal cancer. *Cell Rep* 43, 114270.

Foggetti, G., Li, C., Cai, H., Hellyer, J.A., Lin, W.Y., Ayeni, D., Hastings, K., Choi, J., Wurtz, A., Andrejka, L., *et al.* (2021). Genetic Determinants of EGFR-Driven Lung Cancer Growth and Therapeutic Response In Vivo. *Cancer Discov* 11, 1736-1753.

Fumagalli, A., Drost, J., Suijkerbuijk, S.J., van Boxtel, R., de Lig, J., Offerhaus, G.J., Begthel, H., Beerling, E., Tan, E.H., Sansom, O.J., *et al.* (2017). Genetic dissection of colorectal cancer progression by orthotopic transplantation of engineered cancer organoids. *Proc Natl Acad Sci U S A* 114, E2357-E2364.

Fumagalli, A., Oost, K.C., Kester, L., Morgner, J., Bornes, L., Bruens, L., Spaargaren, L., Azkanaz, M., Schelfhorst, T., Beerling, E., *et al.* (2020a). Plasticity of Lgr5-Negative Cancer Cells Drives Metastasis in Colorectal Cancer. *Cell Stem Cell* 26, 569-578 e567.

Fumagalli, A., Oost, K.C., Suijkerbuijk, J.E., Snippert, H.J., Van, J., and Correspondence, R. (2020b). Plasticity of Lgr5-Negative Cancer Cells Drives Metastasis in Colorectal Cancer. *Stem Cell* 26, 569-578.e567.

Fumagalli, A., Suijkerbuijk, S.J.E., Begthel, H., Beerling, E., Oost, K.C., Snippert, H.J., van Rheenen, J., and Drost, J. (2018). A surgical orthotopic organoid transplantation approach in mice to visualize and study colorectal cancer progression. *Nat Protoc* 13, 235-247.

Ganesh, K., Basnet, H., Kaygusuz, Y., Laughney, A.M., He, L., Sharma, R., O'Rourke, K.P., Reuter, V.P., Huang, Y.H., Turkecul, M., *et al.* (2020). L1CAM defines the regenerative origin of metastasis-initiating cells in colorectal cancer. *Nat Cancer* 1, 28-45.

Garcia, M.I., Ghiani, M., Lefort, A., Libert, F., Strollo, S., and Vassart, G. (2009). LGR5 deficiency deregulates Wnt signaling and leads to precocious Paneth cell differentiation in the fetal intestine. *Dev Biol* 331, 58-67.

Gavish, A., Tyler, M., Greenwald, A.C., Hoefflin, R., Simkin, D., Tschernichovsky, R., Galili Darnell, N., Somech, E., Barbolin, C., Antman, T., *et al.* (2023). Hallmarks of transcriptional intratumour heterogeneity across a thousand tumours. *Nature* 618, 598-606.

Gehart, H., and Clevers, H. (2019). Tales from the crypt: new insights into intestinal stem cells. *Nat Rev Gastroenterol Hepatol* 16, 19-34.

Gerrits, A., Dykstra, B., Kalmykova, O.J., Klauke, K., Verovskaya, E., Broekhuis, M.J.C., De Haan, G., and Bystrykh, L.V. (2010). Cellular barcoding tool for clonal analysis in the hematopoietic system. *Blood* 115, 2610-2618.

Gooding, S., and Leedham, S.J. (2020). Gremlin 1 - small protein, big impact: the multiorgan consequences of disrupted BMP antagonism(dagger). *J Pathol* 251, 349-352.

Gostimskaya, I. (2022). CRISPR-Cas9: A History of Its Discovery and Ethical Considerations of Its Use in Genome Editing. *Biochemistry (Mosc)* 87, 777-788.

Grzelak, C.A., Goddard, E.T., Lederer, E.E., Rajaram, K., Dai, J., Shor, R.E., Lim, A.R., Kim, J., Beronja, S., Funnell, A.P.W., *et al.* (2022). Elimination of fluorescent protein immunogenicity permits modeling of metastasis in immune-competent settings. *Cancer Cell* 40, 1-2.

Guinney, J., Dienstmann, R., Wang, X., de Reynies, A., Schlicker, A., Soneson, C., Marisa, L., Roepman, P., Nyamundanda, G., Angelino, P., *et al.* (2015). The consensus molecular subtypes of colorectal cancer. *Nat Med* 21, 1350-1356.

Gyorffy, B. (2024). Integrated analysis of public datasets for the discovery and validation of survival-associated genes in solid tumors. *Innovation (Camb)* 5, 100625.

Hageman, J.H., Heinz, M.C., Kretzschmar, K., van der Vaart, J., Clevers, H., and Snippert, H.J.G. (2020). Intestinal Regeneration: Regulation by the Microenvironment. *Dev Cell* 54, 435-446.

Hassan, G., and Seno, M. (2022). ERBB Signaling Pathway in Cancer Stem Cells. *Adv Exp Med Biol* 1393, 65-81.

Heinz, M.C., Peters, N.A., Oost, K.C., Lindeboom, R.G.H., van Voorthuijsen, L., Fumagalli, A., van der Net, M.C., de Medeiros, G., Hageman, J.H., Verlaan-Klink, I., *et al.* (2022). Liver Colonization by Colorectal Cancer Metastases Requires YAP-Controlled Plasticity at the Micrometastatic Stage. *Cancer Res* 82, 1953-1968.

Hsu, E.C., Rice, M.A., Bermudez, A., Marques, F.J.G., Aslan, M., Liu, S., Ghoochani, A., Zhang, C.A., Chen, Y.S., Zlitni, A., *et al.* (2020). Trop2 is a driver of metastatic prostate cancer with neuroendocrine phenotype via PARP1. *Proc Natl Acad Sci U S A* 117, 2032-2042.

Hu, Z., Ding, J., Ma, Z., Sun, R., Seoane, J.A., Scott Shaffer, J., Suarez, C.J., Berghoff, A.S., Cremolini, C., Falcone, A., *et al.* (2019). Quantitative evidence for early metastatic seeding in colorectal cancer. *Nat Genet* 51, 1113-1122.

Hu, Z., Li, Z., Ma, Z., and Curtis, C. (2020). Multi-cancer analysis of clonality and the timing of systemic spread in paired primary tumors and metastases. *Nat Genet* 52, 701-708.

Hurwitz, H., Fehrenbacher, L., Novotny, W., Cartwright, T., Hainsworth, J., Heim, W., Berlin, J., Baron, A., Griffing, S., Holmgren, E., *et al.* (2004). Bevacizumab plus irinotecan, fluorouracil, and leucovorin for metastatic colorectal cancer. *N Engl J Med* 350, 2335-2342.

Huxley, J. (1958). Biological aspects of cancer. Institutional Repository at Chittaranjan National Cancer Institute.

Ivics, Z., Hackett, P.B., Plasterk, R.H., and Izsvak, Z. (1997). Molecular reconstruction of Sleeping Beauty, a Tc1-like transposon from fish, and its transposition in human cells. *Cell* 91, 501-510.

Jackstadt, R., and Sansom, O.J. (2016). Mouse models of intestinal cancer. *J Pathol* 238, 141-151.

Jackstadt, R., van Hooff, S.R., Leach, J.D., Cortes-Lavaud, X., Lohuis, J.O., Ridgway, R.A., Wouters, V.M., Roper, J., Kendall, T.J., Roxburgh, C.S., *et al.* (2019). Epithelial NOTCH Signaling Rewires the Tumor Microenvironment of Colorectal Cancer to Drive Poor-Prognosis Subtypes and Metastasis. *Cancer Cell* 36, 319-336 e317.

JE, I.J., Vermeulen, L., Meijer, G.A., and Dekker, E. (2015). Serrated neoplasia-role in colorectal carcinogenesis and clinical implications. *Nat Rev Gastroenterol Hepatol* 12, 401-409.

Joanito, I., Wirapati, P., Zhao, N., Nawaz, Z., Yeo, G., Lee, F., Eng, C.L.P., Macalinao, D.C., Kahraman, M., Srinivasan, H., *et al.* (2022). Single-cell and bulk transcriptome sequencing identifies two epithelial tumor cell states and refines the consensus molecular classification of colorectal cancer. *Nat Genet* 54, 963-975.

Karapetis, C.S., Khambata-Ford, S., Jonker, D.J., O'Callaghan, C.J., Tu, D., Tebbutt, N.C., Simes, R.J., Chalchal, H., Shapiro, J.D., Robitaille, S., *et al.* (2008). K-ras mutations and benefit from cetuximab in advanced colorectal cancer. *N Engl J Med* 359, 1757-1765.

Karo-Atar, D., Ouladan, S., Javkar, T., Joumier, L., Matheson, M.K., Merritt, S., Westfall, S., Rochette, A., Gentile, M.E., Fontes, G., *et al.* (2022). Helminth-induced reprogramming of the stem cell compartment inhibits type 2 immunity. *J Exp Med* 219.

Kawasaki, K., Fujii, M., Sugimoto, S., Ishikawa, K., Matano, M., Ohta, Y., Toshimitsu, K., Takahashi, S., Hosoe, N., Sekine, S., *et al.* (2020). Chromosome Engineering of Human Colon-Derived Organoids to Develop a Model of Traditional Serrated Adenoma. *Gastroenterology* 158, 638-651 e638.

Kebschull, J.M., and Zador, A.M. (2018). Cellular barcoding: lineage tracing, screening and beyond. *Nat Methods* 15, 871-879.

Kemper, K., Rodermond, H., Colak, S., Grandela, C., and Medema, J.P. (2012). Targeting colorectal cancer stem cells with inducible caspase-9. *Apoptosis* 17, 528-537.

Kim, B.M., Mao, J., Taketo, M.M., and Shivdasani, R.A. (2007). Phases of canonical Wnt signaling during the development of mouse intestinal epithelium. *Gastroenterology* 133, 529-538.

Kolev, H.M., and Kaestner, K.H. (2023). Mammalian Intestinal Development and Differentiation-The State of the Art. *Cell Mol Gastroenterol Hepatol* 16, 809-821.

Kopp, A., Hofsess, S., Cardillo, T.M., Govindan, S.V., Donnell, J., and Thurber, G.M. (2023). Antibody-Drug Conjugate Sacituzumab Govitecan Drives Efficient Tissue Penetration and Rapid Intracellular Drug Release. *Mol Cancer Ther* 22, 102-111.

Kreso, A., and Dick, J.E. (2014). Evolution of the cancer stem cell model. *Cell Stem Cell* 14, 275-291.

Lamprecht, S., Schmidt, E.M., Blaj, C., Hermeking, H., Jung, A., Kirchner, T., and Horst, D. (2017). Multicolor lineage tracing reveals clonal architecture and dynamics in colon cancer. *Nat Commun* 8, 1406.

Lange, M.J., Lyddon, T.D., and Johnson, M.C. (2019). Diphtheria Toxin A-Resistant Cell Lines Enable Robust Production and Evaluation of DTA-Encoding Lentiviruses. *Sci Rep* 9, 8985.

Lannagan, T.R., Jackstadt, R., Leedham, S.J., and Sansom, O.J. (2021). Advances in colon cancer research: in vitro and animal models. *Curr Opin Genet Dev* 66, 50-56.

Leach, J.D.G., Vlahov, N., Tsantoulis, P., Ridgway, R.A., Flanagan, D.J., Gilroy, K., Sphyris, N., Vazquez, E.G., Vincent, D.F., Faller, W.J., *et al.* (2021). Oncogenic BRAF, unrestrained by TGFbeta-receptor signalling, drives right-sided colonic tumorigenesis. *Nat Commun* 12, 3464.

Lee, H.O., Hong, Y., Etlioglu, H.E., Cho, Y.B., Pomella, V., Van den Bosch, B., Vanhecke, J., Verbandt, S., Hong, H., Min, J.W., *et al.* (2020). Lineage-dependent gene expression programs influence the immune landscape of colorectal cancer. *Nat Genet* 52, 594-603.

Li, V.S., Ng, S.S., Boersema, P.J., Low, T.Y., Karthaus, W.R., Gerlach, J.P., Mohammed, S., Heck, A.J., Maurice, M.M., Mahmoudi, T., *et al.* (2012). Wnt signaling through inhibition of beta-catenin degradation in an intact Axin1 complex. *Cell* 149, 1245-1256.

Lipinski, M., Parks, D.R., Rouse, R.V., and Herzenberg, L.A. (1981). Human trophoblast cell-surface antigens defined by monoclonal antibodies. *Proc Natl Acad Sci U S A* 78, 5147-5150.

Livet, J., Weissman, T.A., Kang, H., Draft, R.W., Lu, J., Bennis, R.A., Sanes, J.R., and Lichtman, J.W. (2007). Transgenic strategies for combinatorial expression of fluorescent proteins in the nervous system. *Nature* 450, 56-62.

Loh, J.J., and Ma, S. (2024). Hallmarks of cancer stemness. *Cell Stem Cell* 31, 617-639.

Lu, R., Neff, N.F., Quake, S.R., and Weissman, I.L. (2011). Tracking single hematopoietic stem cells in vivo using high-throughput sequencing in conjunction with viral genetic barcoding. *Nat Biotechnol* 29, 928-933.

Maddipati, R., and Stanger, B.Z. (2015). Pancreatic Cancer Metastases Harbor Evidence of Polyclonality.

Madison, B.B., Dunbar, L., Qiao, X.T., Braunstein, K., Braunstein, E., and Gumucio, D.L. (2002). Cis elements of the villin gene control expression in restricted domains of the vertical (crypt) and horizontal (duodenum, cecum) axes of the intestine. *J Biol Chem* 277, 33275-33283.

Malla, S.B., Byrne, R.M., Lafarge, M.W., Corry, S.M., Fisher, N.C., Tsantoulis, P.K., Mills, M.L., Ridgway, R.A., Lannagan, T.R.M., Najumudeen, A.K., *et al.* (2024). Pathway level subtyping identifies a slow-cycling biological phenotype associated with poor clinical outcomes in colorectal cancer. *Nat Genet* 56, 458-472.

Marmol, I., Sanchez-de-Diego, C., Pradilla Dieste, A., Cerrada, E., and Rodriguez Yoldi, M.J. (2017). Colorectal Carcinoma: A General Overview and Future Perspectives in Colorectal Cancer. *Int J Mol Sci* 18.

Massague, J., and Obenauf, A.C. (2016). Metastatic colonization by circulating tumour cells. *Nature* 529, 298-306.

McGranahan, N., and Swanton, C. (2017). Clonal Heterogeneity and Tumor Evolution: Past, Present, and the Future. *Cell* 168, 613-628.

McIntyre, R.E., Buczacki, S.J., Arends, M.J., and Adams, D.J. (2015). Mouse models of colorectal cancer as preclinical models. *Bioessays* 37, 909-920.

McKenna, A., Findlay, G.M., Gagnon, J.A., Horwitz, M.S., Schier, A.F., and Shendure, J. (2016). Whole-organism lineage tracing by combinatorial and cumulative genome editing. *Science* 353, aaf7907.

Merlos-Suarez, A., Barriga, F.M., Jung, P., Iglesias, M., Cespedes, M.V., Rossell, D., Sevillano, M., Hernando-Momblona, X., da Silva-Diz, V., Munoz, P., *et al.* (2011). The intestinal stem cell signature identifies colorectal cancer stem cells and predicts disease relapse. *Cell Stem Cell* 8, 511-524.

Metcalf, C., Kljavin, N.M., Ybarra, R., and de Sauvage, F.J. (2014). Lgr5+ stem cells are indispensable for radiation-induced intestinal regeneration. *Cell Stem Cell* 14, 149-159.

Miyoshi, H., and Stappenbeck, T.S. (2013). In vitro expansion and genetic modification of gastrointestinal stem cells in spheroid culture. *Nat Protoc* 8, 2471-2482.

Mohme, M., Maire, C.L., Riecken, K., Zapf, S., Aranyosy, T., Westphal, M., Lamszus, K., and Fehse, B. (2017). Optical Barcoding for Single-Clone Tracking to Study Tumor Heterogeneity. *Mol Ther* 25, 621-633.

Moorman, A.R., Cambuli, F., Benitez, E.K., Jiang, Q., Xie, Y., Mahmoud, A., Lumish, M., Hartner, S., Balkaran, S., Bermeo, J., *et al.* (2023). Progressive plasticity during colorectal cancer metastasis. *bioRxiv*.

Morral, C., Stanisavljevic, J., Hernando-Momblona, X., Mereu, E., Alvarez-Varela, A., Cortina, C., Stork, D., Slebe, F., Turon, G., Whissell, G., *et al.* (2020). Zonation of Ribosomal DNA Transcription Defines a Stem Cell Hierarchy in Colorectal Cancer. *Cell Stem Cell* 26, 845-861 e812.

Morrison, S.J., and Kimble, J. (2006). Asymmetric and symmetric stem-cell divisions in development and cancer. *Nature* 441, 1068-1074.

Moser, A.R., Mattes, E.M., Dove, W.F., Lindstrom, M.J., Haag, J.D., and Gould, M.N. (1993). ApcMin, a mutation in the murine Apc gene, predisposes to mammary carcinomas and focal alveolar hyperplasias. *Proc Natl Acad Sci U S A* 90, 8977-8981.

Munoz, J., Stange, D.E., Schepers, A.G., van de Wetering, M., Koo, B.K., Itzkovitz, S., Volckmann, R., Kung, K.S., Koster, J., Radulescu, S., *et al.* (2012). The Lgr5 intestinal stem cell signature: robust expression of proposed quiescent '+4' cell markers. *EMBO J* 31, 3079-3091.

Mustata, R.C., Vasile, G., Fernandez-Vallone, V., Strollo, S., Lefort, A., Libert, F., Monteyne, D., Perez-Morga, D., Vassart, G., and Garcia, M.I. (2013). Identification of Lgr5-independent spheroid-generating progenitors of the mouse fetal intestinal epithelium. *Cell Rep* 5, 421-432.

Mzoughi, S., Schwarz, M., Wang, X., Demircioglu, D., Ulukaya, G., Mohammed, K., Tullio, F.D., Company, C., Dramaretska, Y., Leushacke, M., *et al.* (2023). A Mutation-driven oncofetal regression fuels phenotypic plasticity in colorectal cancer. *bioRxiv*.

Nagy, A. (2000). Cre recombinase: the universal reagent for genome tailoring. *Genesis* 26, 99-109.

Naxerova, K., Reiter, J.G., Brachtel, E., Lennerz, J.K., Van De Wetering, M., Rowan, A., Cai, T., Clevers, H., Swanton, C., Nowak, M.A., *et al.* (2017). Origins of lymphatic and distant metastases in human colorectal cancer. *Science* 357, 55-60.

Neal, J.T., Li, X., Zhu, J., Giangarra, V., Grzeskowiak, C.L., Ju, J., Liu, I.H., Chiou, S.H., Salahudeen, A.A., Smith, A.R., *et al.* (2018). Organoid Modeling of the Tumor Immune Microenvironment. *Cell* 175, 1972-1988 e1916.

Nusse, Y.M., Savage, A.K., Marangoni, P., Rosendahl-Huber, A.K.M., Landman, T.A., de Sauvage, F.J., Locksley, R.M., and Klein, O.D. (2018). Parasitic helminths induce fetal-like reversion in the intestinal stem cell niche. *Nature* 559, 109-113.

Ohta, Y., Fujii, M., Takahashi, S., Takano, A., Nanki, K., Matano, M., Hanyu, H., Saito, M., Shimokawa, M., Nishikori, S., *et al.* (2022). Cell-matrix interface regulates dormancy in human colon cancer stem cells. *Nature* 608, 784-794.

Ooft, S.N., Weeber, F., Dijkstra, K.K., McLean, C.M., Kaing, S., van Werkhoven, E., Schipper, L., Hoes, L., Vis, D.J., van de Haar, J., *et al.* (2019). Patient-derived organoids can predict response to chemotherapy in metastatic colorectal cancer patients. *Sci Transl Med* 11.

Peikon, I.D., Kebschull, J.M., Vagin, V.V., Ravens, D.I., Sun, Y.C., Brouzes, E., Correa, I.R., Jr., Bressan, D., and Zador, A.M. (2017). Using high-throughput barcode sequencing to efficiently map connectomes. *Nucleic Acids Res* 45, e115.

Plummer, N.W., Ungewitter, E.K., Smith, K.G., Yao, H.H., and Jensen, P. (2017). A new mouse line for cell ablation by diphtheria toxin subunit A controlled by a Cre-dependent FLEx switch. *Genesis* 55.

Qi, J., Sun, H., Zhang, Y., Wang, Z., Xun, Z., Li, Z., Ding, X., Bao, R., Hong, L., Jia, W., *et al.* (2022). Single-cell and spatial analysis reveal interaction of FAP(+) fibroblasts and SPP1(+) macrophages in colorectal cancer. *Nat Commun* 13, 1742.

Radtke, F., and Clevers, H. (2005). Self-renewal and cancer of the gut: two sides of a coin. *Science* 307, 1904-1909.

Reeves, M.Q., Kandyba, E., Harris, S., Del Rosario, R., and Balmain, A. (2018). Multicolour lineage tracing reveals clonal dynamics of squamous carcinoma evolution from initiation to metastasis. *Nat Cell Biol* 20, 699-709.

Reiter, J.G., Hung, W.T., Lee, I.H., Nagpal, S., Giunta, P., Degner, S., Liu, G., Wassenaar, E.C.E., Jeck, W.R., Taylor, M.S., *et al.* (2020). Lymph node metastases develop through a wider evolutionary bottleneck than distant metastases. *Nat Genet* 52, 692-700.

Robasky, K., Lewis, N.E., and Church, G.M. (2014). The role of replicates for error mitigation in next-generation sequencing. *Nat Rev Genet* 15, 56-62.

Rogers, Z.N., McFarland, C.D., Winters, I.P., Naranjo, S., Chuang, C.H., Petrov, D., and Winslow, M.M. (2017). A quantitative and multiplexed approach to uncover the fitness landscape of tumor suppression in vivo. *Nature Methods* 14, 737-742.

Rugo, H.S., Bardia, A., Marme, F., Cortes, J., Schmid, P., Loirat, D., Tredan, O., Ciruelos, E., Dalenc, F., Gomez Pardo, P., *et al.* (2023). Overall survival with sacituzumab govitecan in hormone receptor-positive and human epidermal growth factor receptor 2-negative metastatic breast cancer (TROPiCS-02): a randomised, open-label, multicentre, phase 3 trial. *Lancet* 402, 1423-1433.

Ryser, M.D., Mallo, D., Hall, A., Hardman, T., King, L.M., Tatishchev, S., Sorribes, I.C., Maley, C.C., Marks, J.R., Hwang, E.S., *et al.* (2020). Minimal barriers to invasion during human colorectal tumor growth. *Nature Communications* 11, 1-10.

Saito, M., Iwawaki, T., Taya, C., Yonekawa, H., Noda, M., Inui, Y., Mekada, E., Kimata, Y., Tsuru, A., and Kohno, K. (2001). Diphtheria toxin receptor-mediated conditional and targeted cell ablation in transgenic mice. *Nat Biotechnol* 19, 746-750.

Saltz, L.B., Clarke, S., Diaz-Rubio, E., Scheithauer, W., Figer, A., Wong, R., Koski, S., Lichinitser, M., Yang, T.S., Rivera, F., *et al.* (2008). Bevacizumab in combination with oxaliplatin-based chemotherapy as first-line therapy in metastatic colorectal cancer: a randomized phase III study. *J Clin Oncol* 26, 2013-2019.

Sanchez-Gundin, J., Fernandez-Carballido, A.M., Martinez-Valdivieso, L., Barreda-Hernandez, D., and Torres-Suarez, A.I. (2018). New Trends in the Therapeutic Approach to Metastatic Colorectal Cancer. *Int J Med Sci* 15, 659-665.

Sato, T., and Clevers, H. (2013). Primary mouse small intestinal epithelial cell cultures. *Methods Mol Biol* 945, 319-328.

Sato, T., Vries, R.G., Snippert, H.J., van de Wetering, M., Barker, N., Stange, D.E., van Es, J.H., Abo, A., Kujala, P., Peters, P.J., *et al.* (2009). Single Lgr5 stem cells build crypt-villus structures in vitro without a mesenchymal niche. *Nature* 459, 262-265.

Shimokawa, M., Ohta, Y., Nishikori, S., Matano, M., Takano, A., Fujii, M., Date, S., Sugimoto, S., Kanai, T., and Sato, T. (2017). Visualization and targeting of LGR5(+) human colon cancer stem cells. *Nature* 545, 187-192.

Shvartsur, A., and Bonavida, B. (2015). Trop2 and its overexpression in cancers: regulation and clinical/therapeutic implications. *Genes Cancer* 6, 84-105.

Siegel, R.L., Miller, K.D., Goding Sauer, A., Fedewa, S.A., Butterly, L.F., Anderson, J.C., Cercek, A., Smith, R.A., and Jemal, A. (2020). Colorectal cancer statistics, 2020. *CA Cancer J Clin* 70, 145-164.

Siegel, R.L., Wagle, N.S., Cercek, A., Smith, R.A., and Jemal, A. (2023). Colorectal cancer statistics, 2023. *CA Cancer J Clin* 73, 233-254.

Snippert, H.J., van der Flier, L.G., Sato, T., van Es, J.H., van den Born, M., Kroon-Veenboer, C., Barker, N., Klein, A.M., van Rheenen, J., Simons, B.D., *et al.* (2010). Intestinal crypt homeostasis results from neutral competition between symmetrically dividing Lgr5 stem cells. *Cell* 143, 134-144.

Sole, L., Lobo-Jarne, T., Alvarez-Villanueva, D., Alonso-Maranon, J., Guillen, Y., Guix, M., Sangrador, I., Rozalen, C., Vert, A., Barbachano, A., *et al.* (2022). p53 wild-type colorectal cancer cells that express a fetal gene signature are associated with metastasis and poor prognosis. *Nat Commun* 13, 2866.

Sottoriva, A., Kang, H., Ma, Z., Graham, T.A., Salomon, M.P., Zhao, J., Marjoram, P., Siegmund, K., Press, M.F., Shibata, D., *et al.* (2015). A Big Bang model of human colorectal tumor growth. *Nat Genet* 47, 209-216.

Tagawa, S.T., Balar, A.V., Petrylak, D.P., Kalebasty, A.R., Loriot, Y., Flechon, A., Jain, R.K., Agarwal, N., Bupathi, M., Barthelemy, P., *et al.* (2021). TROPHY-U-01: A Phase II Open-Label Study of Sacituzumab Govitecan in Patients With Metastatic Urothelial Carcinoma Progressing After Platinum-Based Chemotherapy and Checkpoint Inhibitors. *J Clin Oncol* 39, 2474-2485.

Tan, S.H., Phuah, P., Tan, L.T., Yada, S., Goh, J., Tomaz, L.B., Chua, M., Wong, E., Lee, B., and Barker, N. (2021). A constant pool of Lgr5(+) intestinal stem cells is required for intestinal homeostasis. *Cell Rep* 34, 108633.

Tauriello, D.V.F., Palomo-Ponce, S., Stork, D., Berenguer-Llargo, A., Badia-Ramentol, J., Iglesias, M., Sevillano, M., Ibiza, S., Canellas, A., Hernando-Mombona, X., *et al.* (2018). TGFbeta drives immune evasion in genetically reconstituted colon cancer metastasis. *Nature* 554, 538-543.

Tetteh, P.W., Basak, O., Farin, H.F., Wiebrands, K., Kretzschmar, K., Begthel, H., van den Born, M., Korving, J., de Sauvage, F., van Es, J.H., *et al.* (2016). Replacement of Lost Lgr5-Positive Stem Cells through Plasticity of Their Enterocyte-Lineage Daughters. *Cell Stem Cell* 18, 203-213.

Tian, H., Biehs, B., Warming, S., Leong, K.G., Rangell, L., Klein, O.D., and de Sauvage, F.J. (2011). A reserve stem cell population in small intestine renders Lgr5-positive cells dispensable. *Nature* 478, 255-259.

Tirosh, I., Venteicher, A.S., Hebert, C., Escalante, L.E., Patel, A.P., Yizhak, K., Fisher, J.M., Rodman, C., Mount, C., Filbin, M.G., *et al.* (2016). Single-cell RNA-seq supports a developmental hierarchy in human oligodendrogloma. *Nature* 539, 309-313.

Tomic, G., Morrissey, E., Kozar, S., Ben-Moshe, S., Hoyle, A., Azzarelli, R., Kemp, R., Chilamakuri, C.S.R., Itzkovitz, S., Philpott, A., *et al.* (2018). Phospho-regulation of ATOH1 Is Required for Plasticity of Secretory Progenitors and Tissue Regeneration. *Cell Stem Cell* 23, 436-443 e437.

Trerotola, M., Jernigan, D.L., Liu, Q., Siddiqui, J., Fatatis, A., and Languino, L.R. (2013). Trop-2 promotes prostate cancer metastasis by modulating beta(1) integrin functions. *Cancer Res* 73, 3155-3167.

Turajlic, S., Sottoriva, A., Graham, T., and Swanton, C. (2019). Resolving genetic heterogeneity in cancer. *Nat Rev Genet* 20, 404-416.

Turajlic, S., and Swanton, C. (2016). Metastasis as an evolutionary process. *Science* 352, 169-175.

van der Heijden, M., Miedema, D.M., Waclaw, B., Veenstra, V.L., Lecca, M.C., Nijman, L.E., van Dijk, E., van Neerven, S.M., Lodestijn, S.C., Lenos, K.J., *et al.* (2019). Spatiotemporal regulation of clonogenicity in colorectal cancer xenografts. *Proc Natl Acad Sci U S A* 116, 6140-6145.

van Es, J.H., Haegebarth, A., Kujala, P., Itzkovitz, S., Koo, B.K., Boj, S.F., Korving, J., van den Born, M., van Oudenaarden, A., Robine, S., *et al.* (2012). A critical role for the Wnt effector Tcf4 in adult intestinal homeostatic self-renewal. *Mol Cell Biol* 32, 1918-1927.

Vaquero-Siguero, N., Schleussner, N., Volk, J., Mastel, M., Meier, J., and Jackstadt, R. (2022). Modeling Colorectal Cancer Progression Reveals Niche-Dependent Clonal Selection. *Cancers (Basel)* 14.

Vasquez, E.G., Nasreddin, N., Valbuena, G.N., Mulholland, E.J., Belnoue-Davis, H.L., Eggington, H.R., Schenck, R.O., Wouters, V.M., Wirapati, P., Gilroy, K., *et al.* (2022). Dynamic and adaptive cancer stem cell population admixture in colorectal neoplasia. *Cell Stem Cell* 29, 1213-1228 e1218.

Viragova, S., Li, D., and Klein, O.D. (2024). Activation of fetal-like molecular programs during regeneration in the intestine and beyond. *Cell Stem Cell* 31, 949-960.

Vogelstein, B., Papadopoulos, N., Velculescu, V.E., Zhou, S., Diaz, L.A., Jr., and Kinzler, K.W. (2013). Cancer genome landscapes. *Science* 339, 1546-1558.

Weber, K., Bartsch, U., Stocking, C., and Fehse, B. (2008). A multicolor panel of novel lentiviral "gene ontology" (LeGO) vectors for functional gene analysis. *Mol Ther* 16, 698-706.

Westcott, P.M.K., Sacks, N.J., Schenkel, J.M., Ely, Z.A., Smith, O., Hauck, H., Jaeger, A.M., Zhang, D., Backlund, C.M., Beytagh, M.C., *et al.* (2021). Low neoantigen expression and poor T-cell priming underlie early immune escape in colorectal cancer. *Nat Cancer* 2, 1071-1085.

Winters, I.P., Chiou, S.H., Paulk, N.K., McFarland, C.D., Lalgudi, P.V., Ma, R.K., Lisowski, L., Connolly, A.J., Petrov, D.A., Kay, M.A., *et al.* (2017). Multiplexed in vivo homology-directed repair and tumor barcoding enables parallel quantification of Kras variant oncogenicity. *Nat Commun* 8, 2053.

Wollny, D., Zhao, S., Everlien, I., Lun, X., Brunken, J., Brune, D., Ziebell, F., Tabansky, I., Weichert, W., Marciniak-Czochra, A., *et al.* (2016). Single-Cell Analysis Uncovers Clonal Acinar Cell Heterogeneity in the Adult Pancreas. *Dev Cell* 39, 289-301.

Yao, Y., Xu, X., Yang, L., Zhu, J., Wan, J., Shen, L., Xia, F., Fu, G., Deng, Y., Pan, M., *et al.* (2020). Patient-Derived Organoids Predict Chemoradiation Responses of Locally Advanced Rectal Cancer. *Cell Stem Cell* 26, 17-26 e16.

Yui, S., Azzolin, L., Maimets, M., Pedersen, M.T., Fordham, R.P., Hansen, S.L., Larsen, H.L., Guiu, J., Alves, M.R.P., Rundsten, C.F., *et al.* (2018). YAP/TAZ-Dependent Reprogramming of Colonic Epithelium Links ECM Remodeling to Tissue Regeneration. *Cell Stem Cell* 22, 35-49 e37.

Zeng, P., Chen, M.B., Zhou, L.N., Tang, M., Liu, C.Y., and Lu, P.H. (2016). Impact of TROP2 expression on prognosis in solid tumors: A Systematic Review and Meta-analysis. *Sci Rep* 6, 33658.

Zhang, C., Zhang, L., Xu, T., Xue, R., Yu, L., Zhu, Y., Wu, Y., Zhang, Q., Li, D., Shen, S., *et al.* (2020). Mapping the spreading routes of lymphatic metastases in human colorectal cancer. *Nature Communications* 11, 1-11.

ACKNOWLEDGEMENTS

As this journey comes to an end, I find it hard to express just how grateful I am to my supervisor, **Dr. Rene Jackstadt**. Thank you for believing in me and trusting me with the opportunity to help building your lab from the ground up. I have always said that starting a PhD in a new lab is a risk worth taking. I have gained so much more than just a PhD; I had the privilege of working side by side with you, especially during those early years, when I was able to absorb so much of your expertise. Your enthusiasm and passion for science have been infectious, driving me forward even on the toughest days. You've sparked my desire for independence and nurtured my self-motivation, persistence and resilience. Your mentorship has shaped not only my academic journey but has profoundly influenced my personal growth as well. Thank you for pushing me to be better every day. Now, as I look back, I can see how much I have grown over these years, and I owe so much of that to you.

I would also like to thank my **TAC members**, Prof. Dr. Andreas Trumpp, Prof. Dr. Ursula Klingmüller and PD Dr. med. Bruno Köhler for their time and valuable feedback during our meetings. A special thank you goes to PD **Dr. med. Bruno Köhler**, whose dedication was instrumental in advancing our clinical trial and getting us to this point. To my **PhD examiners**, Prof. Dr. Sergio P. Acebrón, Prof. Dr. Andreas Trumpp, and Dr. Ana Banito, I am truly grateful for your time, support, and for being part of this unique and special moment in my life.

Thank you to **Dr. Bryce Lim** and **Dr. Maria Puschhof** for your instrumental help with the bioinformatic analysis. I would like to extend my thanks to the DKFZ Core Facilities, with special acknowledgment to the animal, microscopy, flow cytometry, and NGS Core Facilities. Their outstanding performance significantly contributed to enhancing the quality of my research.

My deepest gratitude goes to all the past and present members of the lab. I have had the honor of working with each and every one of you, and it has truly been a gift to be part of such an incredible community. We have been more than just lab mates; we have become a team, always ready to support each other and offer help without hesitation. Your kindness, collaboration, and genuine camaraderie have made this experience unforgettable. To the lab technicians **Jasmin** and **Caro**, thank you for your tireless help with mice and histology, respectively. To all the students I had the honour of supervising and mentoring: **Moritz, Belén, and Johanna**. Thank you for your dedication to my project. Your hard work, positivity, and support, especially during my most frustrating moments, made all the difference. I am truly grateful for the time we shared, and I wish each of you the very best of luck in your future careers. To the past and present students from the lab **Estelle, Umberto, Julia, Sara and**

Luzi, thanks for bringing your energy and smiles to the lab every day and for all the experiences we had together inside and outside the lab. To **Manuel**, who embarked on this crazy PhD journey alongside me from the very beginning. Thank you for your support on the project and for always teasing every single one of us, keeping us on our toes and alert for the next challenge. To **Gabriele**, my personal IT guy. Thanks for your patient and help every time my technical problems were more difficult to solve than just switching off and on the computer. To **Aitana** thanks for your kindness and altruism to help always. I wish you the best of luck for your PhD. To **Giannis**, the new member of the TROP2 team, I am really happy that someone as motivated as you takes over this project. I am sure it is in good hands. To **Thorben**, although we shared little time together, I loved your dry sense of humour in every moment we got to share. I wish you all the best with your PhD thesis.

I also want to thank two very important people for my journey that although they stayed in the lab for a short time and they are not anymore here we remain friends. **Sarah**, thanks for being a support in tough times, accompanying me to Dean Lewis concert and have my back when DB stood me up in the middle of nowhere. **Sigi**, you have been like a mentor to me. I am extremely grateful we got to work on the TROP2 project together. The “go-to” person in the lab when I needed advice not only for experiments but for my personal career. Thanks for your incredible support when I was at my lowest by having a ‘girl’s night’. I am so grateful to both of you and I truly wish you all the best.

I want to deeply thank “my person” in the lab, **Niko**. You are, by far, the best reward I take from this journey. We quickly connected at the beginning, when you were here doing a rotation and I was starting my PhD. Both of us lost in a new lab trying to figure ourselves out. Qué heavy!. When I think back, you were present in all the memories and experiences I have from my PhD, from the funny anecdotes to my highest frustration moments. You have been there to listen to me every day, my shoulder to cry and my mate to laugh. I love how we knew what the other one was thinking by just looking at each other. Definitely, I cannot imagine this journey without you. Lab days are always better when you are around. Thank you for using the humour to make my failed experiments and problems in life feel lighter on my shoulders. You have become one of my best friends in life and although I know I will have you forever regardless of which country each of us ends up, I truly wish our paths cross in the future. I could not have imagined a better partner to share this journey with. GRACIAS AMIGO.

To all the **members of Hi-STEM**, for building a network of support. It has been a pleasure to have you all around during these years.

Outside of the lab I got the privilege to form a Spanish Family, those friends that became family when Covid19 hit and we were locked in Germany far away from our relatives:

Alber, Alicia, Damián, Dani, María, Mirian and Paula. Always having each other's back and there to support any situation. All of us, so different but like pieces of a puzzle that fit perfectly together. For all the Spanish meals, birthday celebrations, nights out, trips, movings and advices in life. **Alicia**, the party person, always so welcoming and sweet, you always know how to cheer up every party. **Damián**, my skiing mate, the person all of us go when we need a wise, mature and corporate advice. **Dani**, always late but so caring for everyone's mental health. I have so much to learn from your way of 'flowing' in live. **Maria** la portuguesa, so sweet, so caring and always there when you need her. **Mirian**, the strong-independent woman a role model for perseverance and determination. **Paula**, the holly Paula, still a miracle that she is alive after all the life-threatening experiences she granted us in these years. You definitely make sure our adrenaline levels are high and our glasses full (if not broken) in every experience we ever got to share with you. In sum, you are all true friends and I am so grateful to life for putting you in my way. You make me feel closer to the sunny Spain even during the cold and cloudy winters in Heidelberg.

To **my parents**, Alicia and Toni, who have always been my unwavering support, holding the ladder steady as I climbed up. I hope you feel as proud of me as I do of you. I know how tirelessly you have worked throughout your lives to ensure I never lacked anything, and for that, I am profoundly grateful. Everything I am is because of you. Thank you for teaching me the importance of FAMILY, not just through your own example, but by nurturing my connection with my uncles, aunts, and grandparents. Thank you for being there every step of the way, for supporting and encouraging me, for driving me wherever I needed to go, and for comforting me when times were tough. I cherish the strong bond the three of us share, and it is something I hold dear above all else. I can only hope that the sacrifices I am making now, so far from Spain, will someday bear fruit—allowing me to return home under better working conditions, so I can be close to you once more and no longer miss out on precious moments in your lives. THANK YOU FOR EVERYTHING.

I want to thank my favourite person in this world, mi **Alber**. We have immensely grown in these 8 years together. You are my role model of kindness, hard-work, resilience and perseverance. I admire you so much and I am really grateful to have a partner in life that happens to be my best friend and my biggest pillar. You believed in me when I was lost and you always push me to be the best version of myself. Thanks for always being there when I needed a hug or I needed to recharge my battery, never leaving my hand. Thanks for being my calm when I panicked and my energy booster when I was down. These years have not been easy but your infinite support has been instrumental so that I can be here today defending my PhD thesis. I have no words to describe how lucky I feel to have you in my life. I am

extremely proud of the home we have built and continue building together. We are the best team! TE AMO.

Finally, I want to take a moment to thank **myself**. When I started this PhD, I was focused solely on the exciting science ahead and my aspiration to become a great scientist. I never anticipated the deeper, more personal challenges that would lie beneath the surface. Nearly five years later, I can say with certainty that a PhD is about far more than just the research; it is a test of endurance, resilience, and self-motivation. Throughout this journey, I was fortunate to find incredible people who have become family, a source of strength when I needed it most. But I also faced obstacles that pushed me beyond my limits, revealing the importance of standing up for myself, holding onto my values, and protecting my well-being, even when it felt like everything was against me. Never in a million years would I have imagined the difficulties I had to confront, nor the strength I found within myself to rise above them. I'm proud of the person I've become, not just as a scientist, but as someone who has learned to navigate adversity with courage and integrity.

AGRADECIMIENTOS

Como todo en la vida, esta etapa llega a su fin. Me resulta difícil expresar lo agradecida que estoy a mi supervisor, el **Dr. Rene Jackstadt**. Gracias por creer en mí y darme la oportunidad de ayudar a construir tu laboratorio desde cero. Siempre he dicho que empezar un doctorado en un laboratorio nuevo es un riesgo que vale la pena. He ganado mucho más que un doctorado; tuve el privilegio de trabajar a tu lado, especialmente durante los primeros años, en los que pude empaparme de tus conocimientos y experiencia. Tu entusiasmo y pasión por la ciencia han sido contagiosos, impulsándome incluso en los días más difíciles. Has despertado mi deseo de independencia y has fomentado mi automotivación, perseverancia y resiliencia. Tu apoyo no solo ha moldeado mi trayectoria académica, sino que ha influido profundamente en mi crecimiento personal. Gracias por empujarme a ser mejor cada día. Ahora, echo la vista atrás y puedo ver cuánto he crecido durante estos años. Gran parte de eso te lo debo a tí.

También quiero agradecer a los **miembros de mi TAC**, el Prof. Dr. Andreas Trumpp, la Prof. Dr. Ursula Klingmüller y el PD Dr. med. Bruno Köhler, por su tiempo y valiosos comentarios durante nuestras reuniones. Un agradecimiento especial al **PD Dr. med. Bruno Köhler**, cuya dedicación ha sido fundamental para avanzar en nuestro ensayo clínico y llevarlo hasta este punto. A mis **examinadores del doctorado**, el Prof. Dr. Sergio P. Acebrón, el Prof. Dr. Andreas Trumpp y la Dra. Ana Banito, estoy profundamente agradecida por su tiempo, apoyo y por formar parte de este momento tan especial en mi vida.

Gracias al **Dr. Bryce Lim** y **Dr. Maria Puschhof** por su ayuda con el análisis bioinformático. Quiero extender mi agradecimiento a las instalaciones del DKFZ, con especial mención a las de animales, microscopía, citometría y NGS. Su excelente desempeño ha contribuido significativamente a mejorar la calidad de mi investigación.

Mi más profundo agradecimiento a todos los miembros, pasados y presentes, del laboratorio. He tenido el honor de trabajar con cada uno de vosotros, y ha sido un verdadero regalo formar parte de una comunidad tan increíble. Hemos sido más que compañeros de laboratorio; nos hemos convertido en un equipo, siempre dispuestos a apoyarnos y ofrecer ayuda sin dudar y sin esperar nada a cambio. Vuestra amabilidad, colaboración y auténtico compañerismo han hecho de esta experiencia algo inolvidable. A las técnicas de laboratorio, **Jasmin** y **Caro**, gracias por vuestra incansable ayuda con los ratones y la histología, respectivamente. A los estudiantes a quienes he tenido el honor de supervisar y guiar: **Moritz**, **Belén** y **Johanna**. Gracias por vuestra dedicación a mi proyecto. Vuestro arduo trabajo, positivismo y apoyo, especialmente en mis momentos de mayor frustración, han marcado la

diferencia. Estoy realmente agradecida por el tiempo compartido y os deseo lo mejor en vuestras futuras carreras. A los estudiantes del laboratorio (pasado y presente) **Estelle, Umberto, Julia, Sara y Luzi**, gracias por traer vuestra energía y sonrisas todos los días y por todas las experiencias vividas tanto dentro como fuera del laboratorio. A **Manuel**, quien emprendió esta loca aventura del doctorado junto a mí desde casi el principio. Gracias por tu apoyo en el proyecto y por vacilarnos continuamente a todos, manteniéndonos alerta y preparados para el próximo reto. A **Gabriele**, mi soporte técnico personal. Gracias por tu paciencia y ayuda cada vez que mis problemas técnicos eran más complicados que simplemente reiniciar el ordenador. A **Aitana**, gracias por tu amabilidad y altruismo al ayudar siempre. Te deseo lo mejor en tu doctorado. A **Giannis**, el nuevo miembro del equipo TROP2, me alegra mucho que alguien tan motivado como tú continúe este proyecto. Estoy segura de que lo dejo en buenas manos. A **Thorben**, aunque hemos compartido poco tiempo juntos, me encanta tu sentido del humor siempre sacándome una carcajada en cada experiencia que hemos compartido. Te deseo lo mejor en el doctorado.

También quiero agradecer a dos personas muy importantes en mi trayectoria que, aunque estuvieron poco tiempo en el laboratorio, seguimos siendo muy amigas. **Sarah**, gracias por tu apoyo en los momentos difíciles, por acompañarme al concierto de Dean Lewis y por estar ahí cuando DB me dejó plantada en medio de la nada. **Sigi**, has sido como una mentora para mí. Estoy muy agradecida de haber trabajado contigo en el proyecto TROP2. Siempre has sido la persona a quien acudir en el laboratorio cuando necesitaba consejo, tanto para experimentos como para mi carrera personal. Gracias por tu increíble apoyo cuando estaba en mis peores momentos. Estoy muy agradecida a ambas y os deseo lo mejor de corazón.

Quiero agradecer profundamente a "mi persona" en el laboratorio, **Niko**. Eres, sin duda, la mejor recompensa que me llevo de este 'heavy' viaje. Conectamos rápidamente desde el principio, cuando estabas haciendo una rotación y yo comenzando mi doctorado. Ambos perdidos en un laboratorio nuevo, tratando de encontrar nuestro camino. Al mirar atrás, estás presente en todos los recuerdos y experiencias que tengo de mi doctorado, desde las anécdotas más divertidas hasta mis momentos de mayor frustración. Has estado ahí para escucharme cada día, para consolarme y para compartir risas. Definitivamente, no puedo imaginar este recorrido sin ti. Los días en el lab son mejores cuando tú estas. Te has convertido en uno de mis mejores amigos en la vida, y aunque sé que te tendré para siempre sin importar en qué país terminemos, espero sinceramente que nuestros caminos se crucen en el futuro. No puedo imaginar un mejor amigo con el que haber compartido esta Aventura que tú. ¡GRACIAS, AMIGO!

A todos los **miembros de Hi-STEM**, por crear una red de apoyo. Ha sido un placer tenerlos a todos durante estos años.

Fuera del laboratorio, he tenido la gran suerte de formar mi "Familia Española", esos amigos que se convirtieron en familia cuando llegó el Covid-19 y nos quedamos encerrados en Alemania, lejos de nuestros seres queridos: Alber, Alicia, Damián, Dani, María, Mirian y Paula. Siempre apoyándonos en cualquier situación. Todos tan diferentes, pero como piezas de un puzzle que encajan perfectamente. Por todas las comidas españolas, celebraciones de cumpleaños, noches de fiesta, viajes, mudanzas y consejos en la vida. **Alicia**, la reina de la fiesta, siempre tan acogedora y dulce; sabes cómo animar cualquier situación. **Damián**, mi compañero de esquí, a quien todos recurrimos cuando necesitamos un consejo sabio, maduro y profesional. **Dani**, siempre llegando tarde pero siempre tan pendiente del bienestar mental de todos. Tengo mucho que aprender de tu manera de "fluir" en la vida. **María**, la portuguesa, tan dulce, tan atenta y siempre ahí cuando la necesitas. **Mirian**, la mujer fuerte e independiente, un ejemplo de perseverancia y determinación. **Paula**, la santa Paula, sigue siendo un milagro que sigas viva después de todas las experiencias de alto riesgo que nos has hecho presenciar estos años. Sin duda, te aseguras de que nuestros niveles de adrenalina estén altos y nuestras copas llenas (si no rotas) en cada experiencia compartida contigo. En resumen, amigos verdaderos. Estoy muy agradecida a la vida por haberos puesto en mi camino. Me habéis hecho sentir más cerca de mi tierra incluso durante los inviernos fríos y nublados de Heidelberg.

A **mis padres**, Alicia y Toni, que siempre me han sostenido la escalera para que yo pudiera seguir subiendo. Espero que estéis tan orgullosos de mí como yo lo estoy de vosotros. Sé lo duro que habéis trabajado toda vuestra vida para que nunca me faltara nada, y os estoy profundamente agradecida. Soy quien soy gracias a vosotros. Gracias por inculcarme el valor de la FAMILIA junto a mis tíos y abuelos. Gracias por estar presentes en todos los momentos de mi vida, por apoyarme, animarme, llevarme a dónde sea y consolarme cuando lo he necesitado. Valoro muchísimo la relación tan cercana que hemos construido los tres, y solo deseo que todos estos sacrificios que estoy haciendo lejos de España me permitan, algún día, regresar con unas condiciones laborales dignas para poder estar cerca de vosotros y no tener que perderme ni un momento más de vuestras vidas. ¡GRACIAS POR TODO!

Finalmente, quiero agradecer a mi persona favorita en este mundo, mi **Alber**. Hemos crecido inmensamente en estos 8 años juntos. Eres mi modelo a seguir de bondad, trabajo duro, resiliencia y perseverancia. Te admiro muchísimo y estoy muy agradecida de tener a un compañero de vida que, además, es mi mejor amigo y mi mayor pilar. Creíste en mí cuando

me sentía perdida y siempre me impulsas a ser la mejor versión de mí misma. Gracias por estar siempre ahí cuando necesitaba un abrazo o recargar pilas, sin soltarme la mano. Estos años no han sido fáciles, pero tu apoyo incondicional ha sido fundamental para que hoy pueda estar aquí defendiendo mi tesis doctoral. Estoy inmensamente orgullosa del hogar que hemos construido y seguimos construyendo juntos. Por una vida juntos. TE AMO.

Finalmente, quiero agradecerme a **mí misma**. Cuando comencé este doctorado, solo pensaba en la ciencia que quería hacer y en mi deseo de convertirme en una gran científica. No me imaginaba los desafíos personales que se esconderían tras esa meta. Casi cinco años después, puedo decir con certeza que un doctorado es mucho más que la investigación; es una prueba de resistencia, de resiliencia y de automotivación. A lo largo de este camino, he tenido la suerte de encontrar personas increíbles que hoy considero mi familia, un pilar de apoyo cuando más lo he necesitado. Este camino no ha sido nada fácil. He tenido que enfrentarme a obstáculos que me han llevado al límite, y me han enseñado lo importante que es defenderse a uno mismo, tus valores y proteger tu propio bienestar, incluso cuando parecía que todo estaba en tu contra. Jamás hubiera imaginado las dificultades que tendría que enfrentar ni la fuerza que he encontrado dentro de mí para superarlas. Estoy orgullosa de la persona en la que me he convertido, no solo como científica, sino como alguien que ha aprendido a navegar la adversidad con valentía e integridad.

